

# WATER IMPACT INVESTIGATIONS FOR AIRCRAFT DITCHING ANALYSIS

A thesis submitted in fulfilment of the requirements for  
the degree of Master of Engineering

Sawan A Shah  
B. Eng (Aerospace)

School of Aerospace, Mechanical and Manufacturing Engineering  
College of Science, Engineering and Health  
RMIT University  
January 2010

This page is intentionally blank

## ***Declaration***

I certify that:

- a) except where due acknowledgement has been made, the work is that of the candidate alone
- b) the work has not been submitted previously, in whole or in part, to qualify for any other academic award
- c) the content of the thesis is the result of the work which has been carried out since the official commencement date of the approved research program
- d) any editorial work, paid or unpaid, carried out by a third party is acknowledged
- e) ethics procedures and guidelines have been followed

**Sawan Ashokkumar Shah**

Date: 21-05-2010

This page is intentionally blank

## **ACKNOWLEDGEMENTS**

*I would like to express thanks to my supervisors Dr Jon Watmuff, Dr Adrian Orifici and Dr Javid Bayandor for their support and guidance throughout this research project.*

*My appreciation also goes out to Minki Kim, Anthony Zammit, Andrew Litchfield and Maajid Chishti for their support with the numerical modelling.*

*A special thank you to Chetan Chandra who assisted with the experimental testing and provided valuable insight into the computational work.*

*Last but not least, I would like to thank all the technical staff at RMIT University, friends and family for their support throughout this endeavour.*

This page is intentionally blank

# TABLE OF CONTENTS

<b>ABSTRACT .....</b>	<b>1</b>
<b>Chapter 1 INTRODUCTION .....</b>	<b>3</b>
<b>Chapter 2 PROJECT DEFINITION .....</b>	<b>7</b>
<b>Chapter 3 LITERATURE REVIEW .....</b>	<b>9</b>
3.1 Analytical Models of the Water Entry Problem .....	9
3.1.1 Von Karman Water Impact Theory.....	10
3.1.2 Wagner Water Impact Solution.....	13
3.2 Experimental Testing .....	15
3.3 Crashworthy Structural Concepts.....	17
3.4 Numerical Modelling .....	20
3.5 Critical Review .....	25
3.6 Concluding Remarks .....	27
<b>Chapter 4 SMOOTHED PARTICLE HYDRODYNAMICS .....</b>	<b>29</b>
4.1 SPH Formulation .....	29
4.2 Smoothing Kernel Functions.....	32
4.3 Implementation in LS-DYNA® .....	35
4.3.1 SPH Solution Procedure.....	37
4.3.2 Variable Smoothing Length .....	38
4.3.3 Symmetry Modelling with SPH .....	39
<b>Chapter 5 EXPERIMENTAL INVESTIGATION .....</b>	<b>41</b>
5.1 Experimental Procedure .....	41
5.2 Test Matrix.....	43
5.3 Experimental Setup .....	44
5.4 Video Capture of Water Impact .....	47
5.5 Wedge Accelerations.....	51
5.5.1 Discrete Approximation of Acceleration-Time History .....	51
5.5.1.1 <i>Influence of Time Step on Acceleration – Time History</i> .....	58
5.5.2 Polynomial Approximation of Acceleration – Time History .....	60
5.5.3 Selection of a Suitable Time Step .....	62
5.6 Sensitivity of Results to Displacement Specification.....	65
5.6.1 Selection of Centre of Tracking Point .....	68
5.6.2 Sub-Pixel Enhancement of Video .....	74
5.7 Friction in Guiding Track.....	75
5.8 Evaluation of Impact Force.....	76
5.9 Test Results.....	78
5.9.1 Variation in Deadrise Angle .....	78
5.9.1.1 <i>Light Impactors</i> .....	78
5.9.1.2 <i>Intermediate Impactors</i> .....	79
5.9.1.3 <i>Heavy Impactors</i> .....	79

5.9.2	Variation in Drop Height for the Light Impactors .....	80
5.9.3	Variation in Wedge Masses .....	81
5.10	Concluding Remarks.....	83
<b>Chapter 6</b>	<b>NUMERICAL ANALYSIS.....</b>	<b>85</b>
6.1	Modelling Approach.....	86
6.2	Determination of Basic Model Parameters .....	86
6.2.1	Initial SPH Model.....	86
6.2.2	Combined SPH and Lagrangian Approach .....	88
6.2.3	Wedge Depth Independence .....	92
6.2.4	SPH Particle Density Analysis.....	93
6.2.5	Variations in Particle Smoothing Length.....	95
6.2.6	Solid Lagrangian Element Formulation.....	97
6.2.7	Particle Approximation Theory .....	98
6.3	Material Modelling.....	99
6.3.1	Wedge .....	99
6.3.2	Water .....	99
6.4	Gravitational Acceleration .....	100
6.5	Energy Conservation .....	102
6.6	Basic Model Parameters .....	106
6.7	Simulation Results.....	108
6.7.1	Variation in Deadrise Angle .....	108
6.7.1.1	<i>Light Impactors</i> .....	108
6.7.1.2	<i>Intermediate Impactors</i> .....	109
6.7.1.3	<i>Heavy Impactors</i> .....	109
6.7.2	Variation in Drop Height for Light Impactors.....	110
6.7.3	Variation in Wedge Masses .....	111
6.8	Concluding Remarks.....	114
<b>Chapter 7</b>	<b>EXPERIMENTAL – NUMERICAL COMPARISON .....</b>	<b>115</b>
7.1	Qualitative Comparison .....	115
7.2	Quantitative Comparison.....	118
<b>Chapter 8</b>	<b>DISCUSSION AND RECOMMENDATIONS .....</b>	<b>125</b>
8.1	Experimental Observations.....	125
8.2	Numerical Analysis.....	127
8.3	General Comments .....	128
8.4	Future Work .....	129
<b>Chapter 9</b>	<b>CONCLUSIONS .....</b>	<b>133</b>
<b>Chapter 10</b>	<b>REFERENCES .....</b>	<b>135</b>
<b>Appendix I</b>	<b>Curve Shifting for Experimental Analysis .....</b>	<b>143</b>
<b>Appendix II</b>	<b>Experimental Test Results.....</b>	<b>145</b>
<b>Appendix III</b>	<b>Correlation between Experiment and Simulations .....</b>	<b>153</b>



# LIST OF FIGURES

Figure 1: Differences in load transfer for impacts on rigid surfaces and water.....	3
Figure 2: Schematic of a symmetric wedge entering water.....	10
Figure 3: Factor of increase of the maximum pressure using von Karman’s impact theory .....	12
Figure 4: Pressure distribution along the side of wedge through water entry.....	13
Figure 5: Subfloor beam intersection design .....	17
Figure 6: Sine-wave beams in the fuselage subfloor designed to crush under impact loading .....	18
Figure 7: Tensor-skin panels unfolding under loading .....	18
Figure 8: Airbags on the underside of a rotorcraft.....	19
Figure 9: Deployable Energy Absorber .....	19
Figure 10: Composite fuselage section.....	19
Figure 11: Excessive mesh distortion when using a Lagrangian formulation for the water .....	24
Figure 12: Numerical modelling procedure for SPH.....	29
Figure 13: Support domain of particle $i$ with a radius of $\kappa h$ .....	31
Figure 14: Support domain of a particle with relation to the problem domain .....	32
Figure 15: Cubic B-spline smoothing function.....	33
Figure 16: SPH particle distributions .....	37
Figure 17: SPH solution procedure in LS-DYNA® .....	37
Figure 18: Symmetry modelling for SPH using ghost particles .....	39
Figure 19: Kinematics of a water droplet in freefall.....	42
Figure 20: Schematic of test-rig and wedge specimens.....	45
Figure 21: Experimental set-up .....	45
Figure 22: Cross-sectional view of wedge specimens .....	46
Figure 23: Masses added to wedge specimens to equalise their mass .....	46
Figure 24: Additional masses attached to basic wedge specimen.....	46
Figure 25: Progressive image capture of water impact .....	48
Figure 26: Calculation of velocities and accelerations using discrete displacement data.....	51
Figure 27: Point tracking in Tracker® .....	52
Figure 28: Displacement-time history and the derived velocity and acceleration-time histories .....	54
Figure 29: Progressive images of water entry through the impact zone.....	55
Figure 30: Example of displacement, velocity and acceleration-time histories .....	57
Figure 31: Influence of step size on derived kinematic characteristics .....	59
Figure 32: Polynomial approximation of displacement-time history .....	61
Figure 33: Polynomial approximations of velocity and acceleration-time histories.....	61
Figure 34: 5 <sup>th</sup> and 6 <sup>th</sup> –order polynomial approximations of acceleration .....	62

Figure 35: Polynomial approximations of displacement profile for different displacement step size.....	63
Figure 36: Range of variation in the velocity and acceleration profiles due to different time intervals between displacement measurements .....	64
Figure 37: Variation in kinematic-time histories purely due to subjective judgement.....	65
Figure 38: Variation in acceleration-time histories purely due to subjective judgement.....	66
Figure 39: Effect of a variation of a single point in the displacement data set .....	70
Figure 40: Effect of a variation of two points within the displacement data set .....	71
Figure 41: Variation in the acceleration-time histories for 20° wedge .....	73
Figure 42: Variation in the acceleration-time histories for 40° wedge .....	73
Figure 43: Sub-pixel enhancement of video .....	74
Figure 44: Possible centre of point based on the darkest region of the point’s image .....	74
Figure 45: Freefall accelerations of wedges of varied masses .....	75
Figure 46: Free-body diagram of wedge when impacting water .....	77
Figure 47: Experimental forces for varying deadrise angles for the light impactors .....	78
Figure 48: Experimental forces for varying deadrise angles for the intermediate impactors .....	79
Figure 49: Experimental forces for varying deadrise angles for the heavy impactors.....	79
Figure 50: Experimental forces for varying drop heights for the light impactors .....	80
Figure 51: Experimental accelerations and forces for varying wedge masses dropped from 50 mm .....	81
Figure 52: Experimental accelerations and forces for varying wedge masses dropped from 100 mm .....	82
Figure 53: Water domain represented entirely by SPH formulation.....	87
Figure 54: Evaluation of symmetric modelling approach for purely SPH model.....	88
Figure 55: Water domain represented using both SPH and Lagrangian description .....	89
Figure 56: Evaluation of symmetric modelling approach for SPH+LAG model .....	89
Figure 57: Comparisons between complete SPH and SPH+LAG models.....	90
Figure 58: Influence of varying SPH section width on kinematic predictions of the model .....	91
Figure 59: Influence of varying SPH section depth on kinematic predictions of the model .....	92
Figure 60: Wedge variants in the wedge depth investigations .....	92
Figure 61: Comparison of varying wedge depths on quantitative and qualitative characteristics .....	93
Figure 62: Force predictions with increasing particle densities .....	94
Figure 63: Improvements in qualitative behaviour of water with increasing SPH particle density.....	95
Figure 64: Effect of varying the smoothing length definition parameters .....	96
Figure 65: Effect of varying the Lagrangian section solid element formulation .....	97
Figure 66: Effect of different particle approximation theories on the force-time history .....	98

Figure 67: Fluid flow field for varying particle approximations .....	98
Figure 68: Effect of simulating gravitational acceleration on the impact force.....	100
Figure 69: Behaviour of water under varied gravitational loading cases 20 ms after impact ....	101
Figure 70: Behaviour of water under varied gravitational loading cases 40 ms after impact ....	101
Figure 71: Typical energy loss in SPH models.....	103
Figure 72: Energy loss in the SPH models for all tests configurations .....	103
Figure 73: Differences in energy loss due to different impact energies and deadrise angles....	104
Figure 74: Energy losses when using complete SPH and SPH+LAG approaches.....	105
Figure 75: Trends in energy conservation with increasing SPH particle density .....	106
Figure 76: SPH+LAG model.....	107
Figure 77: Force predictions for varying wedge deadrise angles of the light impactors.....	108
Figure 78: Force predictions for varying wedge deadrise angles of the intermediate impactors.....	109
Figure 79: Force predictions for varying wedge deadrise angles of the heavy impactors .....	109
Figure 80: Force predictions for light impactors at varying drop heights.....	110
Figure 81: Force and acceleration predictions for varying wedge masses dropped from 50 mm.....	112
Figure 82: Force and acceleration predictions for varying wedge masses dropped from 100 mm.....	113
Figure 83: Qualitative validation of SPH model with images from experimental test.....	116
Figure 84: Differences in peak impact forces between experimental and modelling results ....	119
Figure 85: Comparison of force-time histories for 20° and 40° wedge drop tests .....	120
Figure 86: Correlation after impact velocity variation of 20° wedge.....	122
Figure 87: Correlation after impact velocity variation of 40° wedge.....	123
Figure 88: Examples of linear motion guides with reduced friction .....	125
Figure 89: Measuring localised pressures in future experimentation .....	130
Figure 90: Curve shifting for experimental data processing .....	144
Figure 91: Identification of an outlier within an experimental data set .....	144

This page is intentionally blank

# LIST OF TABLES

Table 1: Numerical modelling investigations into ditching .....	22
Table 2: Particle approximations of the mass, momentum and energy conservation equations .....	36
Table 3: Test matrix showing the experimental wedge configurations .....	43
Table 4: Variation in peak accelerations due to operator error .....	67
Table 5: Perception of the centre of tracking points .....	68
Table 6: Variations in point tracking at a single and two points .....	69
Table 7: Variation in acceleration as a percentage of the highest acceleration .....	72
Table 8: Freefall accelerations and frictional forces in the guiding track .....	76
Table 9: Impact characteristics of experimental test configurations .....	85
Table 10: Basic parameters of initial SPH model .....	87
Table 11: SPH section size variation in the SPH+LAG approach .....	90
Table 12: Particle mesh refinement analysis parameters .....	94
Table 13: Variations of the smoothing length definition parameters .....	95
Table 14: Energy loss associated with the SPH domain .....	104
Table 15: Basic model parameters used to simulate all test configurations .....	107
Table 16: Impact velocity variations for 20° and 40° wedges .....	121

This page is intentionally blank

# NOMENCLATURE

Symbol	Units	Description
$a$	$\text{ms}^{-2}$	Acceleration
$a_f$	$\text{ms}^{-2}$	Freefall acceleration of wedge
$F$	N	Force
$h$	m	Smoothing length
$h_0$	m	Initial smoothing length
$h_{min}$	m	Minimum limit of smoothing length
$h_{max}$	m	Maximum limit of smoothing length
$P$	$\text{Nm}^{-2}$	Pressure
$t$	s	Time
$v$	$\text{ms}^{-1}$	Velocity of impactor
$v_0$	$\text{ms}^{-1}$	Impact velocity
$W$		Smoothing kernel function
$\alpha$	$^\circ$	Wedge deadrise angle
$\rho$	$\text{kgm}^{-3}$	Density
$\rho_0$	$\text{kgm}^{-3}$	Initial density

Abbreviation	Description
1D	One-dimensional
2D	Two-dimensional
3D	Three-dimensional
ALE	Arbitrary Lagrangian-Eulerian
FE	Finite Element
FSI	Fluid-Structure Interaction
SPH	Smoothed Particle Hydrodynamics

This page is intentionally blank



# **ABSTRACT**

Passenger safety under dynamic crash loading is of key importance in modern aerospace vehicle design. In particular, crash-landings on water, commonly known as ‘ditching’, are a complex event to understand and account for in structural design for crashworthiness. Structural responses are complex and severe, given the highly dynamic nature of the fluid in the impact zone. Through numerical modelling, a better understanding of the dynamics of the event can be gained and thus lead to the development of efficient structural design tools. Of key importance for ditching investigations is the ability of numerical methods to capture the high deformations of the fluid domain in such events. From the various numerical techniques developed thus far, a particular meshfree numerical method has shown great potential to model water impact problems, namely the Smoothed Particle Hydrodynamics (SPH) method. This thesis investigates the SPH capability available in the commercial Finite Element (FE) code LS-DYNA®, for water impact problems. Experiments have been conducted on rigid wedges impacting water, which were then simulated with the SPH method. Although certain limitations were experienced with the experimental results, a positive correlation was observed with the numerical technique, thus establishing SPH as a promising method for crashworthiness design. The direction of further evaluation of the SPH technique has been identified, with the ultimate aim of developing a simulation methodology for the design and advancement of crashworthy concepts for aerospace vehicles.

This page is intentionally blank

# Chapter 1

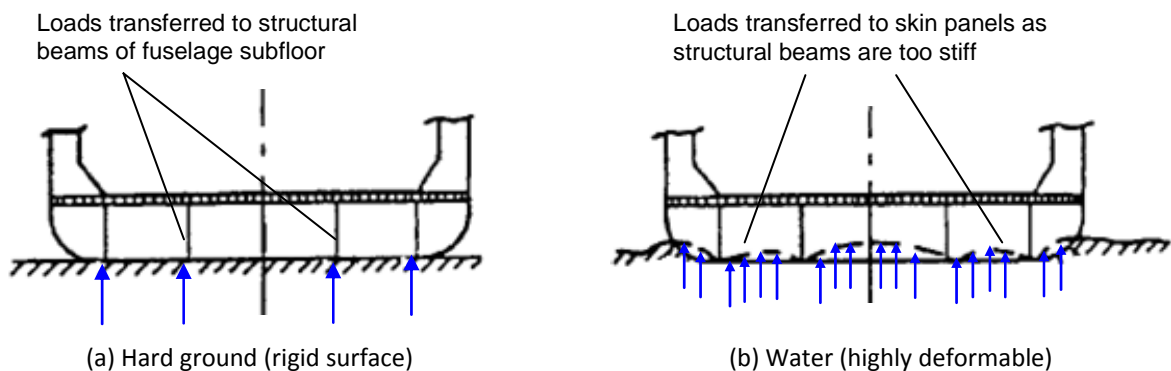
## INTRODUCTION

---

Modern aerospace vehicle design has placed significant emphasis on passenger safety under dynamic crash loading. Increasing occupant survivability is a challenge to engineers due to the wide range of potential crash scenarios and today design for crashworthiness is central to aircraft design.

In the unfortunate event of a crash, aerospace vehicles could collide with hard ground, soft soil or water. The response of the aircraft is highly dependent on the surface upon which it crashes. Structural crashworthiness design aims to improve the energy absorbing capability of aircraft structures whilst maintaining structural integrity of the passenger cabin. Through energy-absorbing damage sequences within the aircraft structure, the loads transferred to the passengers can be minimised during such high energy events.

Crashworthiness design for impact onto rigid surfaces such as hard ground is different to the structural design required to absorb the loading on highly deformable surfaces, particularly water. When crashing onto rigid surfaces, the impact loads are transferred to the frames and beams which absorb significant energy through controlled deformation. This is illustrated in Figure 1a.



**Figure 1:** Differences in load transfer for impacts on rigid surfaces and water

However, when crashing onto water, commonly known as 'ditching', current aircraft structural designs are inefficient in their energy-absorbing mechanisms. The frames and beams which absorb a large proportion of impact energy on impacts with hard ground are too stiff when impacting the softer and highly deformable medium. Moreover, there is complex fluid-structure interaction (FSI) that occurs between structural components and the water. In the ditching case, the impact loads are transferred to the aircraft via pressures that act on the skin panels. Typical skin panels are not designed to withstand out-of-plane impulsive loads, and therefore rupture easily during a water impact. Structural integrity is therefore compromised and large impact forces are experienced by the passengers, generally with fatal consequences.

The study of hydrodynamic impact is of great importance to structural designers and engineers. Maximum impact loads occur during the initial stages of impact over a few milliseconds, and are a crucial parameter for structural design. Decelerations are an important quantity of any impact, since they define the load transfer to the passengers in the vehicle of concern. Additionally, the deformations occurring during an impact are also an important qualitative and quantitative measurement which allow for an estimation of the stresses within a structure. Both these parameters need to be understood and quantified in order to design and develop crashworthy structures.

In recent years, various crashworthy structural designs that improve the impact response in ditching events have been developed. All developed concepts are ultimately tested in controlled experiments to observe the complex structural response due to the highly dynamic nature of the fluid in the impact zone. The high cost and lack of repeatability of full-scale testing has prompted the use of numerical modelling techniques to assist in crashworthiness design.

Numerical modelling provides a platform to evaluate new crashworthy concepts prior to expensive testing programs, and the global research focus is on developing efficient simulation tools, particularly using explicit Finite Element (FE) modelling methods. The challenge with simulating the ditching case is the high deformability of the water, which needs to be modelled effectively to predict the structural response. Conventional FE techniques have considerable instabilities associated with the modelling of highly deformable materials. Despite this, over the previous decade, the Arbitrary Lagrangian-Eulerian (ALE) and Smoothed Particle Hydrodynamics (SPH) techniques are being utilised increasingly to represent the fluid phase in water impact simulations. These techniques have shown great potential for application in water crashworthiness design, by enabling a better understanding of the FSI behaviour through numerical modelling. However, prior to confidently applying these numerical modelling techniques to real-world problems, it is important to evaluate their appropriateness to ditching simulations through simple and fundamental impact scenarios.

The research outlined in this thesis investigates the applicability of SPH, a meshless Lagrangian method, for water impact analysis. The SPH modelling capability within an FE code has been applied to the water impact problem of rigid symmetrical wedges impacting water. This impact case is globally accepted as the fundamental case for understanding and investigating water entry.

Experiments have been conducted whereby rigid wedges of varying geometry and mass were impacted into a trough of water. Through a photographic technique using a high-speed video camera, the kinematic characteristics of the wedge were obtained and images of the impact event were recorded. SPH models of the experimental test configurations were then simulated in the non-linear FE code LS-DYNA® and qualitative and quantitative comparisons with the test results were made. An assessment has been carried out of the modelling approach with recommendations on the direction for further research.

A brief description of the project objectives and scope has been presented, followed by a review of the literary works relevant to the described problem. The fundamental theory behind the SPH technique is then provided. Methodologies and outcomes of the experimental and numerical modelling are discussed, from which conclusions on this investigation have been drawn to lay the foundation for future work.

The investigations carried out through this thesis illustrate that numerical modelling shows great potential to study water impact problems pertaining to ditching events. The SPH modelling capability available to an end user of a commercial FE code has been evaluated. Based on the results of this study, this particular numerical method can be applied to study water impact scenarios by pragmatically investigating its characteristics which gradually account for all the complexities of a full-scale, real-life aircraft ditching case.

This page is intentionally blank

# Chapter 2

## PROJECT DEFINITION

---

This research undertaking investigated the water impact problem for applicability to aircraft crashworthiness design. The focus of the work was within the realm of experimentation and numerical modelling, with the intent of evaluating potential approaches that would assist in structural design improvements to increase crash survivability in ditching incidents.

Specifically, the main objective was to evaluate promising and efficient numerical modelling techniques that can be applied to the design and evaluation of crashworthy structural concepts prior to committing to expensive crash-testing programs.

Within the above project framework, the scope of the research was defined as a quantitative and qualitative evaluation of a numerical modelling technique through a comparison with experimental data from water impact tests. As a preliminary investigation, the experimental study involved the dropping of rigid impactors into a tank of water to generate a 2D fluid flow domain. Acceleration characteristics of the impactors and the evolution of the water profile upon impact were recorded. Numerical models of the water impact tests were then validated against the test results.

The main deliverables of this research included:

- Experimental testing of water impact tests
- Development of a numerical model suitable for simulating the experimental test configurations
- Analysis of the impact kinematic predictions of the numerical model
- Qualitative evaluation of the numerical method
- Correlation study between the experimental results and numerical models
- Evaluation of the modelling methodology within the context of the greater research objectives

This page is intentionally blank



# Chapter 3

## LITERATURE REVIEW

---

This literature review analyses and discusses the work that has been done in the water impact area. It begins with a review on the initiation of the water impact investigations, and identifies the wedge impact as the fundamental case of water entry problem investigations. The progressive development of the initial water impact theories, based on the conservation of momentum, to the relatively accurate and well defined current theories is presented. However, an in-depth review of the analytical solutions to the wedge impact problem is not conducted as further theoretical developments are not the focus of this research.

Experimental testing is still the norm in water crashworthiness investigations, and will remain so for the foreseeable future. Water impact testing programs have been discussed followed by a discussion of several crashworthy structural concepts that have been proposed through advancing simulation tools and materials technology.

The recent popularity of numerical modelling can be attributed to its low cost, increased flexibility, relatively accurate representations of physical systems and their broader scope of applications. An overview of the FE modelling techniques commonly used for water crashworthiness simulations is presented, outlining the results of research in this field pertaining to aerospace structures. Based on this literary survey, specifics of the experimental and numerical aspects of this research were established.

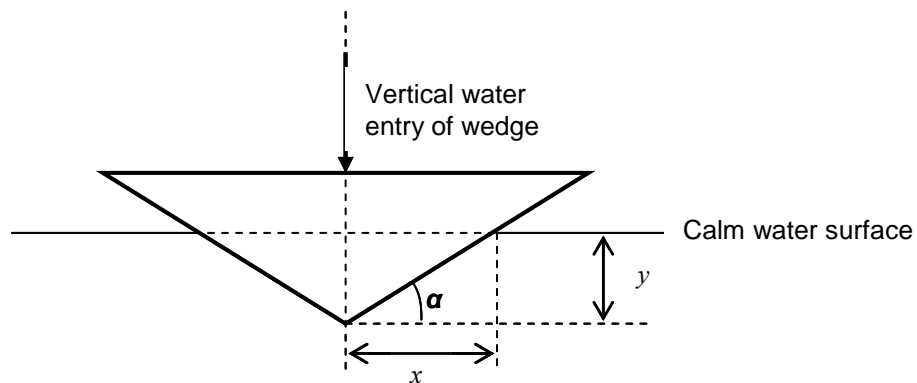
### 3.1 Analytical Models of the Water Entry Problem

The work in the area of water entry and impact of objects was initiated by von Karman (1929) who studied the interaction of seaplane floats with the water. Through his work, von Karman developed an analytical approximation to the impact forces generated during the normal impact of a wedge onto water by the application of conservation of momentum principles and the concept of an associated mass of water. Wagner (1932) also held that the associated mass of water retains all of the transferred momentum from the wedge. In addition to this, Wagner also deals with the sliding and planing motions. These theories in their basic definition predict the

overall impact force acting on the impactor, and have set the foundation for developments in water impact investigations.

### 3.1.1 Von Karman Water Impact Theory

Von Karman's theory states that the momentum associated with the impact was conserved between the impacting wedge and an 'associated' mass of water, which moves at the same velocity as the wedge. Consider a body with a wedge-shaped under surface, which strikes a calm horizontal surface of water as shown in Figure 2.



**Figure 2:** Schematic of a symmetric wedge entering water

From Figure 2,  $\tan \alpha = \frac{y}{x}$ . Therefore,  $2x = 2y \cot \alpha$  is the corresponding breadth of the part of the body in water measured from the original free-surface position. The other variables are described as follows:

$W_i$  – weight of the body per unit depth. The wedge depth is defined as the length of the wedge normal to the cross-sectional view shown in Figure 2

$\alpha$  – deadrise angle i.e. angle of inclination of the sides of the wedge with the horizontal

$y$  – vertical distance through which the body travels in time,  $t$ , from the calm free-surface

At time  $t$ , the original momentum of the body is distributed between the water and the impacting body. The amount of momentum already transferred from the body at time  $t$  depends on  $x$ . This can be approximated by the increase in inertia of the body/water system. It is known that for a long plate of width  $2x$  which is accelerated in a fluid, its inertia is increased by the amount  $\rho x^2 \pi$ , where  $\rho$  is the density of the fluid. This is the concept of associated mass to the impacting body, which indicates the apparent increase in the mass of the plate is equal to the mass of the fluid contained in a circular cylinder of diameter equal to the width of the plate (von Karman 1929).

However, in the case of the aircraft float entering water, the imaginary cylinder will initially be constituted half by water and half by air, due to the varying domains above and below the water free-surface. The impacting float will accelerate the water particles ahead of it, and suck in air behind it. Considering that the effect of air is negligible compared to that of the water, only half the apparent increase in mass is assumed.

The total momentum of the water/body system after impact can then be expressed as:

$$M = \frac{W_i}{g} v + \frac{1}{2} x^2 \rho \pi v \quad (1)$$

where,  $v$  - downward velocity of the system at time  $t$

$$v \text{ can be defined as: } v = \frac{dy}{dt} = \tan \alpha \frac{dx}{dt}$$

Substituting into the system momentum equation (1) and equating to the impactor momentum before impact:

$$\frac{W_i}{g} \frac{dx}{dt} \tan \alpha \left( 1 + \frac{\rho \pi g x^2}{2W_i} \right) = \frac{W_i}{g} v_0 \quad (2)$$

Equation (2) above can be rearranged as:

$$\frac{dx}{dt} = \frac{v_0 \cot \alpha}{1 + \frac{\rho \pi g x^2}{2W_i}} \quad \text{or} \quad \frac{dy}{dt} = v = \frac{v_0}{1 + \frac{\rho \pi g x^2}{2W_i}} \quad (3)$$

The acceleration of the system in the  $y$ -direction can be obtained as:

$$\frac{d^2 y}{dt^2} = \frac{v_0^2 \cot \alpha}{\left( 1 + \frac{\rho \pi g x^2}{2W_i} \right)^3} \left( - \frac{\rho \pi g x}{W_i} \right) \quad (4)$$

From Newton's second law of motion, the force,  $F$ , between the impacting body and the water can be obtained as:

$$F = \frac{W_i}{g} \frac{d^2 y}{dt^2} = \frac{v_0^2 \cot \alpha}{\left( 1 + \frac{\rho \pi g x^2}{2W_i} \right)^3} \rho \pi x \quad (5)$$

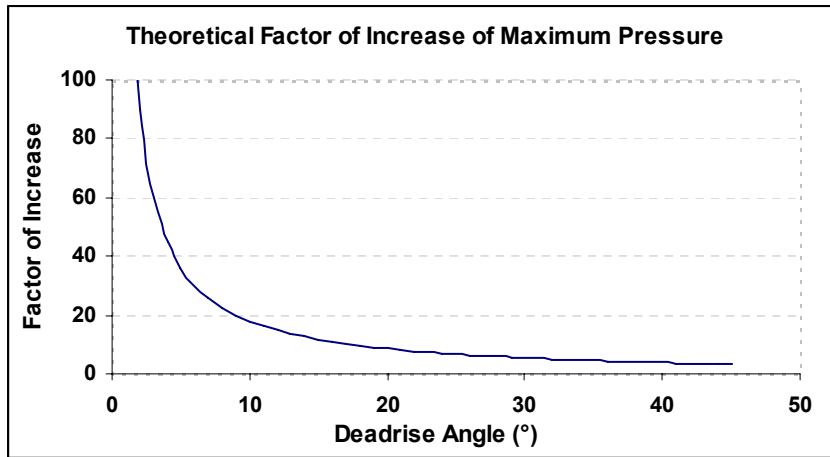
In two dimensions (2D), the pressure,  $P$ , can therefore be obtained as:

$$P = \frac{F}{2x} = \frac{\rho v_0^2}{2} \frac{\pi \cot \alpha}{\left(1 + \frac{\gamma \pi x^2}{2W_i}\right)^3} \quad (6)$$

From equation (6), it is observed that the maximum pressure,  $P_{\max}$ , occurs when  $x \rightarrow 0$ . Theoretically, this indicates that the maximum pressure is at the middle of the impactor at the moment of first impact with the water i.e. when the contact area between the water and wedge is minimal.

$$P_{\max} = \frac{\rho v_0^2}{2} \pi \cot \alpha \quad (7)$$

$\frac{\rho v_0^2}{2}$  represents the dynamic pressure corresponding to the initial impact velocity, and  $\pi \cot \alpha$  is the theoretical factor of increase of the pressure plotted in Figure 3.



**Figure 3:** Factor of increase of the maximum pressure using von Karman's impact theory

As can be observed from Figure 3, there is a sharp decline in the theoretical factor of increase of  $P_{\max}$  as the deadrise angle increases. For deadrise angles less than about  $10^\circ$ ,  $P_{\max}$  tends to increase rapidly as the deadrise angle reduces, resulting in a more 'slamming' effect of the wedge upon impact.

The limitations of the von Karman theory are its inability to model the non-linear free-surface of the water such as the rise of the displaced water along the sides of the wedge, splash, local flow velocity and pressure distribution along the side of the wedge. The above von Karman theory assumes the associated mass of water from the initial calm surface of the water. In reality, the water rises up along the side of the wedge through the impact, as can be seen in Figure 4.

### 3.1.2 Wagner Water Impact Solution

Wagner's (1932) approach accounts for the free-surface elevation by assuming the vertical distance between the highest wetted point on the side of the wedge and the wedge apex to be a factor of  $\frac{\pi}{2}$  of the vertical penetration depth  $y$  as per the von Karman theory shown in Figure 2. Therefore, this translates into a larger associated mass of water compared to that predicted by the von Karman theory, by a factor of  $\left(\frac{\pi}{2}\right)^2$ . Wagner also proposed a solution for the pressure acting along the surface of the impacting wedge, given in equation (8):

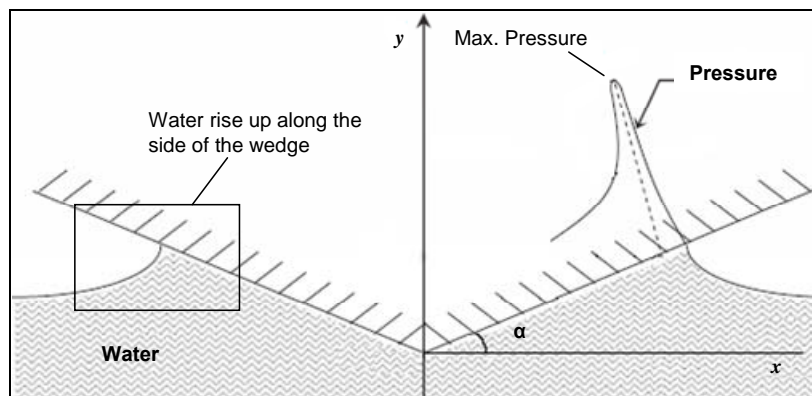
$$P(x) = \frac{1}{2} \rho v^2 \left[ \frac{\pi}{\tan \alpha \left(1 - \frac{x^2}{L^2}\right)^{1/2}} - \frac{\frac{x^2}{L^2}}{1 - \frac{x^2}{L^2}} + \frac{2\ddot{y}}{v^2} (L^2 - x^2)^{1/2} \right] \quad (8)$$

where  $L$  = half wetted breadth of the wedge measured horizontally (see Figure 4)  
 $\ddot{y}$  = vertical acceleration of the wedge

The maximum pressure is obtained by setting  $\frac{dP(x)}{dx} = 0$  which gives:

$$P(x)_{\max} = \frac{1}{2} \rho v^2 \left[ 1 + \frac{\pi^2}{4 \tan^2 \alpha} \right] \text{ at the point } x = L \left( 1 - \frac{4 \tan^2 \alpha}{\pi^2} \right)^{1/2} \quad (9)$$

Figure 4 illustrates the typical pressure distribution for a symmetrical wedge entering the water vertically. The water pile-up is the rise of the free-surface of the water as the wedge penetrates the water, and the highest pressure is observed just before end of the wetted region along the side of the wedge.



**Figure 4:** Pressure distribution along the side of wedge through water entry

In the 2D water impact case of the straight-edged wedge, the assumption was that the momentum of the impactor was transferred into the momentum of an 'associated' mass of water, as per the Von Karman theory. Viscosity, buoyancy and gravitational effects were neglected as they are small when compared to the inertia forces. Nevertheless, buoyancy and skin friction effects prevent the momentum from being completely conserved. Of more significance, however, is the momentum lost in the wake during the water impact, particularly for impactors with a forward velocity. This shortcoming of the classical von Karman and Wagner solutions has been summarised by Monaghan (1952). Impactors with forward speeds have two effects, the importance of which depends on the impact angle:

- They affect the growth of the associated mass of water
- They leave behind an increasing amount of momentum in the wake

Monaghan outlined the modification to the theories by Mayo (1945), Benscoter (1947) and Crewe (1946), who made allowances for both the growth of the associated mass of water as well as the momentum left behind in the wake. These formulae were developed to approximate the forces generated during the impact. Monaghan then proposed approximate design formulae for the maximum deceleration during the water entry of seaplane floats, assuming non-deformable floats with a constant geometry.

Up until 1959, most of the water impact studies extended the initial work done by von Karman and led to the development of mathematical solutions for impact forces. After the 1950s, theoretical developments extended to account for deformable impactors. In his review of water entry investigations up to 1970, May (1970) pointed out that the accelerations observed would be different for rigid and deformable impactors, where they would vary locally throughout the structure. For a scientific approach to define water impact problems, May advised that solutions to the individual structural and fluid domains should be obtained.

One of the first applications of numerical methods to describe the water-entry problem was done by Buyukozturk *et al.* (1974), who applied the finite element method to the space-shuttle solid-rocket boosters. Developments to the analytical solutions to the water entry of various impactors continued and to-date several solutions have been proposed to describe the water entry event and behaviour of the non-linear free surface (Cointe 1989; Korobkin & Pukhnachov 1988; Zhao & Faltinsen 1993). Researchers have used various numerical methods to derive their solutions, the common techniques being:

- a) Boundary element method
- b) Method of asymptotic expansions
- c) Panel methods

An important quantity during the entry of an object into water is the spatial distribution of the pressure along the surface of the object over the period of impact. In most water impact cases, the event is very short and typically lasts for a few milliseconds. Addressing the problems of the non-linear free surface of the water and the structural elasticity are important in order to solve the problems of the fluid-structure interaction (FSI), and this was recognised by the researchers around the 1960s and 1970s. To capture the FSI behaviour in the case of deformable impactors, Zhang *et al.* (1993) formulated a theoretical model by using three sets of coupled dynamic equations for the fluid, structure and the air-gap between the fluid and structure. They observed that the FSI strongly affects the structural response. The FSI behaviour of columns was extended to interaction of flat rectangular plates with water by Cui *et al.* (1999). Donguy *et al.* (2001) developed a numerical method for the analysis of deformable bodies by using a coupling matrix to define the interaction between the fluid and structure.

The analytical developments of the original von Karman and Wagner theories have been extensively validated by comparisons to experimental tests, and very good correlation has been observed over the years. Analytical developments are not the focus of this research, and shall not be referred to in significant detail.

## **3.2 Experimental Testing**

Investigations into the water impact problem became more extensive when the space programmes began in the 1960s. Guidelines on the safe re-entry of space capsules into water were developed and significant experimental testing was carried out with various vehicles. These included experimental tests carried out for the Mercury capsule (McGehee 1959) and the Apollo command module (Stubbs 1967). The first attempt at understanding the structural response on the Apollo module upon entry into water was made by Baker and Westine (1967).

For the case of a rigid wedge entering water, various experimental tests have been conducted by researchers throughout their work (Chuang 1966; Yettou *et al.* 2006). The results from these tests have contributed to empirical refinements of the impact theories and have provided data for the validation of analytical theories. Furthermore, due to the complex nature of the fluid-structure interaction in the case of water impact of deformable structures, most crashworthiness testing in aircraft design has been experimentally based.

More recently, several European research programs have been undertaken to derive methodologies for the design of crashworthy aerospace structures. These have included:

- Commercial Aircraft Design for Crash Survivability (CRASURV 1996-1999) – This program evaluated several designs of composite airframes for crashworthiness on hard ground and water.
- Crashworthiness of Helicopter on Water: Design of Structures using Advanced Simulation Tools (CAST 2000-2003) – This program focused on developing a design methodology and simulation tools that are able to predict the behaviour of rotorcraft during impact onto both hard ground and water. The focus was on the sub-floor design of helicopters to increase their energy absorbing capacity in the event of a crash.
- Crashworthiness of Aircraft for High Velocity Impact (CRAHVI 2000-2004) - A research program aimed at developing a design methodology and simulation tools to predict the behaviour of aircraft structures during high-velocity impact with various obstacles, including the crash response in a ditching event. Various numerical modelling techniques were investigated.

In addition to the above, evaluations into design tools and concepts for crashworthiness were also carried out by Fasanella *et al.* (2003), Bisagni (2002), Hughes *et al.* (2008) amongst others. Due to the impracticality and expensive nature of full-scale drop tests of complete aircraft fuselage structures, most of the experimental testing was conducted on the energy absorbing sections of the fuselage such as the subfloor sections.

The main parameters of the water impact tests included measurements of the pressure variations and accelerations experienced at various locations on the airframes. However, one particular difficulty with the experimental testing is the problem of obtaining consistent pressure-time histories between tests of similar setup. This is due to the difficulties in ensuring precise motion during impact of the large airframe sections being impacted since these airframes are lifted to predefined heights from which they are dropped, usually without guides to ensure controlled motion. This could result in slight differences in the pre-impact conditions which when coupled with the complex deformability of the structures, result in the lack of repeatability within the tests. Pentecote and Kindervater (1999) also claim that pressures obtained through the use of pressure transducers could be different to the actual pressures in a structure absent of the transducers. This is because the experimentally obtained pressures are highly dependent on the local factors, often making it difficult for intricate validation of numerical models whose focus is on the efficient simulation of the water impacts with reasonable predictive accuracy.



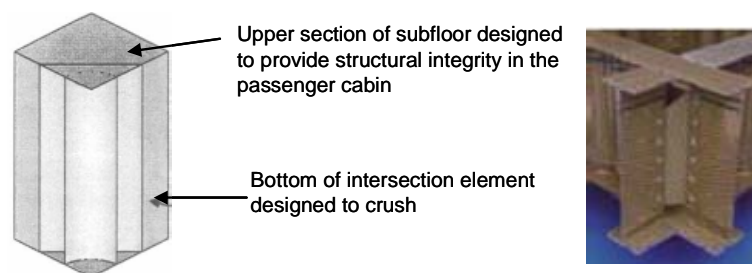
### 3.3 Crashworthy Structural Concepts

The early investigations into water entry were aimed at understanding the pressure distributions on the underside of seaplanes, in order to facilitate better structural design. As discussed, these developments set the foundation for the greater scope of research interest globally pertaining to water crashworthiness.

With commercial air traffic increasing towards the late 1990s, substantial engineering focus was on aircraft crash survivability and as a result various structural designs for crashworthiness onto water have been proposed and tested in the last decade. These structural concepts aim to improve survivability in ditching events, and are based on the concept of energy absorption through the deformation of the structures. In so doing, the objective is to preserve structural integrity of the passenger cabin while reducing the impact loads experienced by the passengers.

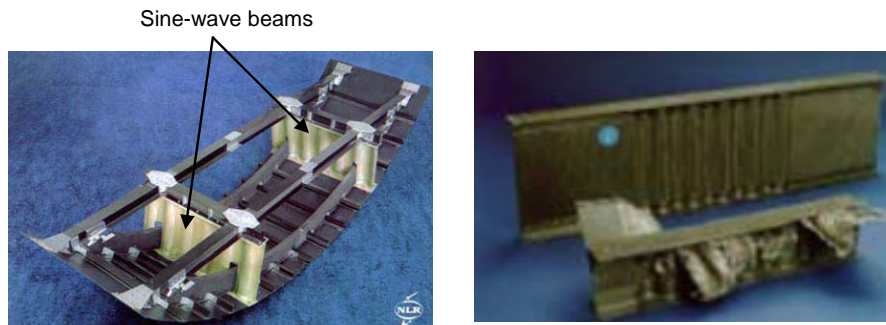
Through the CAST, CRASURV and CRAHVI research programs, various energy absorbing structural designs, particularly of the subfloor structures in helicopters, have been developed. These are largely based on modern advanced composite materials, by exploiting their high energy-absorbing capability under crush loading. Some of the crashworthy structural designs are:

1. Redesign of beam intersection – Typically, in helicopter subfloor sections, the intersections of two beams are stiff points within the structure. During crash-landings on hard ground, these points absorb significant energy. However, they are too stiff to buckle and absorb impact energy during ditching. Figure 5 shows a new design of this intersection incorporating planar and circular webs which allow for deformation of the intersection during both water and hard ground crash-landings (Vignjevic & Meo 2002; Ubels & Wiggenraad 2002).



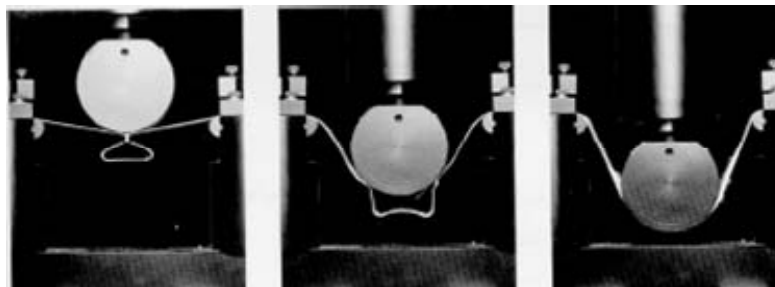
**Figure 5:** Subfloor beam intersection design  
(Source: Vignjevic & Meo 2002; Ubels & Wiggenraad 2002)

2. Sine-wave beams – In aircraft fuselage sections, longitudinal beams made of composite construction have been designed consisting of sine-wave webs (Wiggenraad *et al.* 2001) (see Figure 6). These have shown high energy-absorption properties under controlled impact loading on hard ground, although there is certain difficulty associated with having a controlled crushing process in the actual impact scenario. These designs can be further adopted for water crashworthiness.



**Figure 6:** Sine-wave beams in the fuselage subfloor designed to crush under impact loading  
(Source: Wiggenraad *et al.* 2001)

3. Tensor skin panels – During water impacts, load transfer to the beams in the subfloor is only possible if the skin panels can withstand large deformations without rupturing. A tensor-skin concept (Ubels & Wiggenraad 2002) was developed which unfolds under the pressure of the water upon impact, and then transfers the load to the beams within the structure for further energy absorption (see Figure 7). These tensor skin panels are of composite construction made of polyethylene fibres, Dyneema<sup>®</sup> (DSM 2009), which is impregnated with epoxy resin.



**Figure 7:** Tensor-skin panels unfolding under loading  
(Source: Ubels & Wiggenraad 2002)

4. Rotorcraft External Airbag Protection System (REAPS) – This design shown in Figure 8 involves the deployment of an airbag prior to impact upon water or hard ground, thus relieving the impact loads experienced by the passengers (RAFAEL 2005).



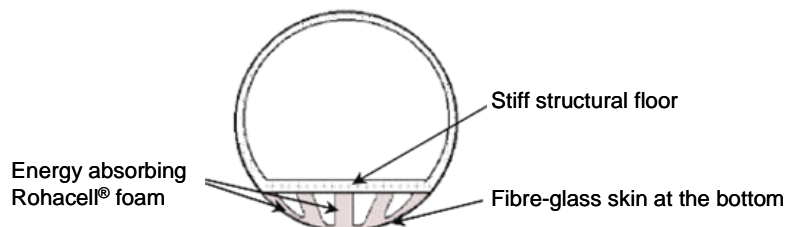
**Figure 8:** Airbags on the underside of a rotorcraft  
(Source: RAFAEL 2005)

5. Deployable Energy Absorber (DEA) – This concept was developed for helicopter water crashworthiness (Jackson & Fuchs 2008). The DEA is based on an expandable honeycomb-like structure which is deployed prior to impact, as depicted in Figure 9. It acts like an airbag upon impact with water by reducing the impact loads experienced by the passengers.



**Figure 9:** Deployable Energy Absorber  
(Source: Jackson & Fuchs 2008)

6. Composite energy-absorbing fuselage sections – This design incorporates the uniform crushing of a composite energy-absorbing fuselage subfloor made of crushable Rohacell® 31-IG foam (Evonik-Industries 2009) overlaid with fibre-glass sheets (Fasanella *et al.* 2003) (see Figure 10).



**Figure 10:** Composite fuselage section  
(Source: Fasanella *et al.* 2003)

### 3.4 Numerical Modelling

The mechanics of the structural and fluid domains have been well understood and defined theoretically. With advances in computational processing capabilities, numerical modelling with Computational Structural Dynamics (CSD) and Computational Fluid Dynamics (CFD) has been increasingly used to simulate physical processes. Since the mid 1990s, the increasing use of numerical modelling has provided a cost-effective and convenient way to investigate the water impact problem. Their popularity has grown and they have provided a platform to develop and evaluate new crashworthy designs prior to conducting expensive testing programs.

Numerical modelling involves representing a physical scenario through mathematical methods. The physical problem can be defined in terms of governing equations which are often expressed mathematically in the form of differential equations or in integral form. In order to model this physical problem, the continuum that is being investigated is first discretised into finite components, followed by a numerical discretisation of the mathematical model. This changes the derivative and integral forms of the governing equations which are continuous, into a discrete form. Numerical discretisation is therefore based on the theory of function approximations.

In general, domain and numerical discretisation results in a set of algebraic equations or ordinary differential equations which can then be solved using numerical methods. These numerical procedures are implemented computationally thus allowing for increasingly complex physical problems to be modelled with relative accuracy.

Although CFD provides a better suited platform to capture the highly-deformable characteristics of the fluid flow field, it is computationally very expensive compared to other methods such as the Finite Element (FE) method. The latter is the more common technique used for efficient water impact analyses and there are several FE approaches that have been developed, each with their own advantages. These can be primarily divided into two groups: mesh based methods which require a grid for the domain discretisation, and meshfree methods.

The main mesh based methods are:

- Lagrangian – the material is fixed to the mesh through nodes, and moves with the grid.
- Eulerian – the mesh remains fixed in space, while the material modelled moves through this mesh
- Combined Lagrangian and Eulerian – this involves a combination of the characteristics of both the Lagrangian and Eulerian formulations to exploit the advantages of each individual method, for example with the Arbitrary Lagrangian-Eulerian (ALE) method.

The dominant numerical techniques employed today are generally mesh based schemes. However, there is an increase in the interest and development of meshfree methods, due to their advantages over certain limitations of the conventional grid-based techniques. The general idea of meshless methods is to provide stable, accurate and reliable solutions to integral or partial differential equations representing a particular physical system without the requirement of mesh connectivity within the domain, and its associated limitations. Meshfree particle methods are a type of meshfree method whereby discrete particles are used to represent a system. Smoothed Particle Hydrodynamics (SPH) is a type of meshfree particle method that has recently been applied to simulate the water impact problem.

The SPH method was first developed by Gingold and Monaghan (1979) for simulating astrophysics problems. It was then applied to the solution of continuum mechanics problems. Over the years, the method has undergone several refinements and its range of application has widened to the modelling of several physical problems. Although it is constantly maturing, SPH has shown significant potential in modelling problems involving fluid flows.

In the SPH method, the continuum is represented by an arbitrary distribution of particles. Each particle is assigned a mass and moves in accordance to the general conservation of mass, momentum and energy equations. Therefore, as per the conventional Lagrangian formulation, SPH is considered to be a meshless Lagrangian method. Within the meshless simulation methodologies, SPH has the advantage of combining the Lagrangian formulation with particle approximations of the field function variables.

The advantages of the SPH method over conventional mesh-based methods are listed below:

- The main advantage of SPH is the absence of physical connectivity between the particles representing the material domain, whilst still retaining the advantage of a Lagrangian formulation. Hence, large deformations can be simulated and captured without the inherent problems of the standard FE method such as severe mesh distortion and tangling. These problems lead to a drastic reduction in the simulation time step, and often an increase in hourglassing energy (energy associated with the excessive shearing of reduced-integration elements, which if substantial indicates that mesh issues need to be addressed) within the model.
- It is often easier to discretise complex geometries than if using a mesh based method.
- It is easier to follow the path and values of physical variables
- When compared to the Eulerian approach, SPH is much more efficient since only the material domain is discretised and not the entire region through which the material may move through the simulation.

On the other hand, the main drawback of the SPH method is its potentially long computational times when compared to other conventional methods. As with other numerical methods, this is largely determined by the mesh distribution and typically compromises have to be made between model accuracy and problem solution times.

Recent investigations have employed three common methodologies within the realm of FE to model the highly-deformable water in ditching investigations. These are the Lagrangian, Arbitrary Lagrangian-Eulerian (ALE) and meshless methods, particularly the SPH method. These modelling capabilities are available in commercial software packages such as LS-DYNA® and PAM-CRASH™.

Each of the afore mentioned modelling approaches have their own advantages. Several researchers have investigated a wide range of water impact problems through these techniques, as summarised in Table 1.

Researchers and Scope	Numerical Modelling Approach for Water
<p><i>Helicopter subfloor structures:</i>            Randhawa &amp; Lankarani (2003)            Candy <i>et al.</i> (2000)            Pentecote &amp; Vigliotti (2003a)            Hughes <i>et al.</i> (2008)            Vignjevic &amp; Meo (2001)            Wittlin <i>et al.</i> (2000)            Climent <i>et al.</i> (2006)            Kindervater <i>et al.</i> (1999)</p> <p><i>Aircraft ditching with forward velocity:</i>            Climent <i>et al.</i> (2006)</p>	<p>Conventional Lagrangian formulation</p> <p>FE packages: LS-DYNA®, MSC.Dytran and PAM-CRASH™</p>
<p><i>Helicopter subfloor structures:</i>            Randhawa &amp; Lankarani (2003)            Candy <i>et al.</i> (2000)            Vignjevic &amp; Meo (2001)</p>	<p>Eulerian formulation</p> <p>FE packages used include: LS-DYNA®, MSC.Dytran and PAM-CRASH™</p>

**Table 1:** Numerical modelling investigations into ditching

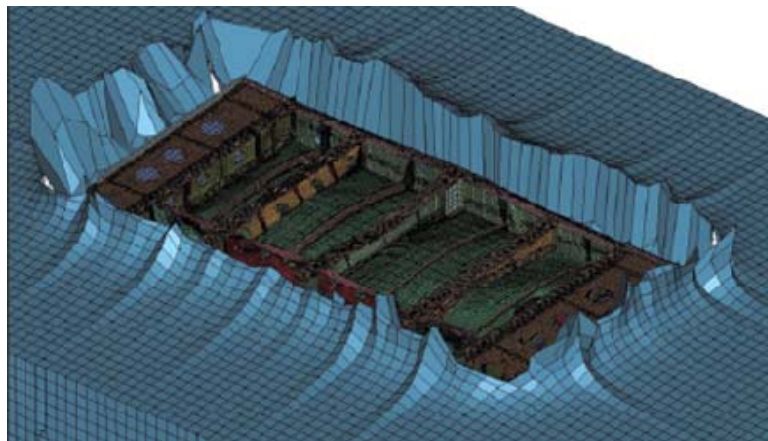
Researchers and Scope	Numerical Modelling Approach for Water
<p><i>Helicopter subfloor structures:</i> Vignjevic &amp; Meo (2001)</p> <p><i>Wedge-water entry:</i> Ortiz <i>et al.</i> (2002)</p> <p><i>Aircraft crashworthy concepts:</i> Jackson &amp; Fuchs (2008) Shoji <i>et al.</i> (2008)</p>	<p>Arbitrary Lagrangian-Eulerian (ALE) formulation</p> <p>FE packages: LS-DYNA®, RADIOSS</p>
<p><i>Helicopter subfloor structures:</i> Anghileri <i>et al.</i> (2007) Pentecote <i>et al.</i> (2003b)</p> <p><i>Wedge-water entry:</i> Pentecote <i>et al.</i> (2003b) Ortiz <i>et al.</i> (2002)</p> <p><i>Aircraft ditching with forward velocity:</i> Climent <i>et al.</i> (2006)</p> <p><i>Aircraft crashworthy concepts:</i> Jackson &amp; Fuchs (2008) Pentecote <i>et al.</i> (2003b) Fasanella <i>et al.</i> (2003)</p>	<p>Smoothed Particle Hydrodynamics (SPH)</p> <p>FE packages: LS-DYNA®, RADIOSS</p>

**Table 1:** Numerical modelling investigations into ditching

For the simulations performed using the conventional Lagrangian formulations for the water, large mesh distortions were observed as the impact event progressed (see Figure 11). This led to excessive hourglassing, a significant reduction in the solution time step and further numerical instabilities. Despite this, good experimental-numerical correlation was observed for the initial moments after impact (Randhawa & Lankarani 2003), prior to the Lagrangian mesh instabilities at the fluid-structure interface. Although computationally efficient, the Lagrangian approach was found to be suitable only for the initial stages of the water impact, prior to the onset of excessive mesh distortion. With these large mesh distortions, the capture of the

intricate FSI behaviour would be questionable since in the standard Lagrangian method, the model results and behaviour are dependent on the mesh and its quality.

With the Eulerian description of the water, the deformation of the water was well captured (Randhawa & Lankarani 2003, Candy *et al.* 2000). Better stability was observed than the Lagrangian approach above and very good correlation with experimental test results was observed (Randhawa & Lankarani 2003). However, the very long computational times when using an entirely Eulerian approach which would prove impractical for full-scale ditching models and, therefore, the global research focus is on investigating alternate efficient numerical modelling techniques.



**Figure 11:** Excessive mesh distortion when using a Lagrangian formulation for the water  
(Source: Hughes *et al.* 2008)

The ALE representation of the water domain generally resulted in very good experimental-simulation correlation (Ortiz *et al.* 2002) although Jackson and Fuchs (2008) highlight that in certain instances poor experimental-numerical correlation is observed. This can be attributed to inaccurate experimental data capture, an issue that is common for all numerical validation studies conducted for water crashworthiness tests. Computational times were dependent on the mesh used for the ALE domain (Jackson & Fuchs 2008). However, even for an appreciable mesh density, the model solution times were less than those of a purely Eulerian formulation. The ALE simulation results, as with most other FE techniques, were highly mesh dependent and certain instabilities occurred in the models with poor mesh distributions (Ortiz *et al.* 2002). ALE has shown strong potential for water impact simulations, and is favoured by many researchers for efficient modelling of highly deformable domains.

Simulations with SPH allowed for modelling the high deformation of the water upon impact. The SPH methodology has been cited as being simple to implement (Vignjevic 2004) and does not suffer instabilities pertaining to mesh-based formulations. In the composite fuselage drop tests



carried out by Fasanella *et al.* (2003), it was observed that refining the SPH particle density did not necessarily result in a convergence of the results, and further investigation into this behaviour was required. On the other hand, investigations by Jackson and Fuchs (2008) concluded that SPH predictions of accelerations and pressures provided the closest match to experimental results, when compared to the ALE method. Despite the positive results obtained thus far with the SPH approach, there is limited information available in the literature on the qualitative capture of the large deformations of the fluid domain associated with water impact problems. This is an important aspect that needs to be adequately captured by numerical models, particularly for modelling the fluid-solid interactive nature of ditching events, hence providing an accurate evolution of the structural deformations through the impact.

In general, although ALE and SPH have their associated limitations, they have been regarded by researchers as promising numerical modelling approaches for water impact problems. The conventional Lagrangian approach is restricted only to simulating the initial milliseconds of impact before instabilities are encountered with the model, whereas the Eulerian approach proves to be too computationally expensive, especially when full-scale ditching simulations need to be simulated.

### **3.5 Critical Review**

The literature review revealed the following key points pertaining to water impact investigations:

- Although theoretical solutions to the fundamental wedge water impact problem are well developed, they are generally case specific and unsuitable to describe the aircraft ditching case involving highly deformable structures.
- Obtaining accurate pressure-time histories is often difficult during experimentation. The pressure is an important parameter that plays a central role in understanding the flow behaviour and structural response during the impact.
- It is difficult to obtain repeatability within tests, particularly when large scale drop tests of deformable structures are performed. This limits the credibility of several experimental-simulation correlation studies as large variability can be observed within the experimental data sets.
- An important consideration when modelling the water for impact conditions is the ability to capture the high deformation that occurs. If this can be accurately captured, then more confidence can be gained in the evolution of the pressure and fluid flow fields during

interaction with a deforming structure. This prompts that meshfree methods would be better suited to modelling water than mesh based methods due to the absence of physical mesh connectivity in the latter technique.

- Within the available literature, the numerical modelling techniques investigated with commercial FE packages often lack validation with simple cases but are directly applied to the simulation of complicated water impact scenarios.
- Qualitative evaluations of the water models upon impact are generally not described in the literature, and the focus is often only on validation with experimentally determined pressures and accelerations. This may suffice for the immediate moments of impact. However, in order to capture the FSI behaviour in deformable structures, an accurate evolution of the fluid flow should be captured by the numerical models which would represent the actual physics of the ditching event.

Of the various FE techniques applied for efficient water impact modelling, ALE and SPH have shown the greatest potential, especially from the numerical stability standpoint that allows stable coupling between the fluid and structural domains for FSI investigations.

As opposed to SPH, ALE is better established and typically more widely applied to high-deformity problems. However, the simulation predictions with ALE are still highly mesh dependent and numerical stability due to mesh consistency is not necessarily guaranteed. SPH, on the other hand, is a relatively new numerical approach that has significant advantages in terms of numerical stability due the absence of a physical mesh.

Although promising results have been demonstrated using SPH by the end users of commercial FE packages, within the scope of the publicly available literature reviewed, a detailed evaluation of these SPH capabilities for interaction between a simplistic rigid body and water is not available in the general literature. This would be the ideal case for a thorough investigation of the modelling method prior to its application for complex simulations with a significantly larger number of influential parameters.

Therefore, following the literature review, the decisions outlined below were made with regards to the approach taken in this research work:

- Rigid symmetric wedges impacting water were selected as the experimental test case in a 2D configuration. This impact case has been accepted as the benchmark problem in water impact investigations, and provides a relatively simple and controlled setup from which quantitative and qualitative data can be generated for numerical model validation.

- This particular research investigated the SPH method for water impact, which is particularly suited to high deformation problems. As mentioned earlier, very little information is available in the general literature on applying the SPH method to simple impact cases, particularly concerning the qualitative behaviour of the water domain. A basic qualitative and quantitative evaluation of SPH for water impact analysis is important prior to its application to FSI occurrences in actual aircraft structures.
- LS-DYNA®, a non-linear FE analysis software package, has been extensively used globally for crashworthiness and impact simulations. The SPH capability is available within this software and can be combined with other FE approaches within a single model, providing engineers a powerful platform for complex impact simulations. Due to its common use throughout industry and research, LS-DYNA® was selected as the simulation platform for this problem.

### **3.6 Concluding Remarks**

Von Karman and Wagner set the foundation for a large portion of the subsequent work in the field of water impact. This preliminary work has been evaluated and improved by other researchers in the field until today. Inclusions have been made in the analytical solutions for impactors with forward velocity, arbitrary shapes and also deformability within the structures.

During the space programs, work began on investigating the water entry behaviour of spacecraft, such as Orbiter modules and also rocket boosters. Several small and full-scale tests were conducted of the water impact of space structures, and this was the primary basis of investigating the crashworthiness of space structures. As energy-absorbing elastic structures became more common in aerospace design, the importance of modelling for structural response was recognised in addition to the peak loads and accelerations of the impact.

The more recent work in this field is mainly focussed within the numerical modelling realm rather than on analytical developments. This is due to the promising results thus far obtained in experimental-numerical model correlation studies. However, it is important to note that the validation of numerical models is only as good as the experimentally obtained data, which is generally difficult to obtain and generate due to the expensive nature of the tests. Moreover, the results from experimental tests are usually confidential. Nevertheless, numerical modelling provides an avenue from which an insight can be gained into the FSI behaviour during water-crash scenarios.

To address design for crashworthiness, several structural concepts have been developed and evaluated for ditching scenarios in aircraft and rotorcraft. These are based on energy-absorbing structures that damage and crush upon impact, and a large proportion of the evaluations have been based entirely on numerical models. Nevertheless, a considerable amount of work is required in model validation since the commonly adopted numerical techniques of SPH and ALE are relatively new and under constant development.

The research work described in this thesis evaluates the promising SPH technique as an efficient and adequately accurate method to apply in the design and analysis of water-crashworthy structures. It builds on arguments put forward in the literature that indicate the applicability of this modelling methodology to the water crashworthiness problem.

The fundamental and simplistic case of rigid symmetric wedges entering calm water was selected for validation with the SPH methodology for the following reasons:

- It allowed for a relatively simple impact case for evaluation of the SPH code from which quantitative and qualitative deductions of the SPH methodology can be made.
- Most data from experimental test programs is confidential and difficult to obtain within publicly available literature. Within the scope of this research, however, inexpensive impact tests could be setup to generate data for validation.
- Based on the outcomes of this research, recommendations can be made on the direction of further evaluations of the SPH approach within the context of water crashworthiness design.
- Although the problem is analytically well defined, the data/knowledge generated through this thesis could potentially be used to complement the analytical solutions of the impact problem in alternate research programs. However, this is not the scope of this research.

As more confidence is gained with this modelling methodology, complexities can be added to the water impact studies in a pragmatic manner. This is important before application of numerical modelling to full-scale crashworthiness design solutions.

# Chapter 4

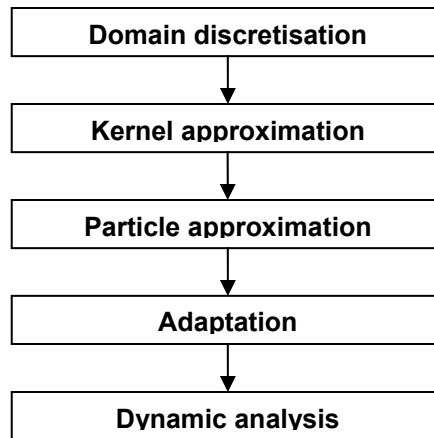
## SMOOTHED PARTICLE HYDRODYNAMICS

---

This section provides an overview of the SPH method and its implementation within LS-DYNA®.

### 4.1 SPH Formulation

Figure 12 outlines the key idea involved with the SPH simulation process:



**Figure 12:** Numerical modelling procedure for SPH

With reference to Figure 12 above:

*Domain discretisation* - Discretisation of the problem domain by a distribution of particles.

*Kernel Approximation* - Kernel approximation (integral representation) of the field function.

*Particle Approximation* - Integration in the kernel approximation is replaced with weighted summations of the values at the neighbouring particles within the support domain of the particle of interest.

*Adaptation* - Particle approximation is conducted at every time step. This depends on the current particle distribution and not on the particle locations in the previous time step.

*Dynamic Analysis* - Direct time integration of the governing equations is performed through an explicit time-integration scheme.

As highlighted above, the numerical discretisation is done in two steps. First, there is the *kernel approximation* whereby the field function is approximated using the integral representation method. This is followed by the *particle approximation* in which the kernel approximation is further approximated with the particles.

The kernel approximation, which is in the form of the integral representation of a function, is given by the integration of the multiplication of the arbitrary function and a smoothing kernel function:

$$f(\mathbf{x}) = \int_{\Omega} f(\mathbf{x}') \delta(\mathbf{x} - \mathbf{x}') d\mathbf{x}' \quad (10)$$

where,  $\mathbf{x}$  is the 3D position vector

$\Omega$  is the volume integral that contains  $\mathbf{x}$

The Dirac delta function is defined by  $\delta(\mathbf{x} - \mathbf{x}') = \begin{cases} 1 & \mathbf{x} = \mathbf{x}' \\ 0 & \mathbf{x} \neq \mathbf{x}' \end{cases}$

In the SPH formulation, the Dirac delta function is replaced by a smoothing function  $W(\mathbf{x} - \mathbf{x}', h)$  as shown in equation (11). The particles have a spatial distance known as the 'smoothing length',  $h$ , over which field variables and properties are approximated by a kernel function. The integral representation in equation (11) is only an approximation provided that  $W$  is not the Dirac delta function.

$$f(\mathbf{x}) = \int_{\Omega} f(\mathbf{x}') W(\mathbf{x} - \mathbf{x}', h) d\mathbf{x}' \quad (11)$$

$\kappa$  is a constant applied to the smoothing length which defines the effective non-zero area of the smoothing function, also known as the support domain. In other words, the smoothing length determines the area of influence of the smoothing function. Therefore, any physical quantity of any particle is obtained by contributions of the relevant property of all the particles which lie within the range of the smoothing kernel, as illustrated in Figure 13.

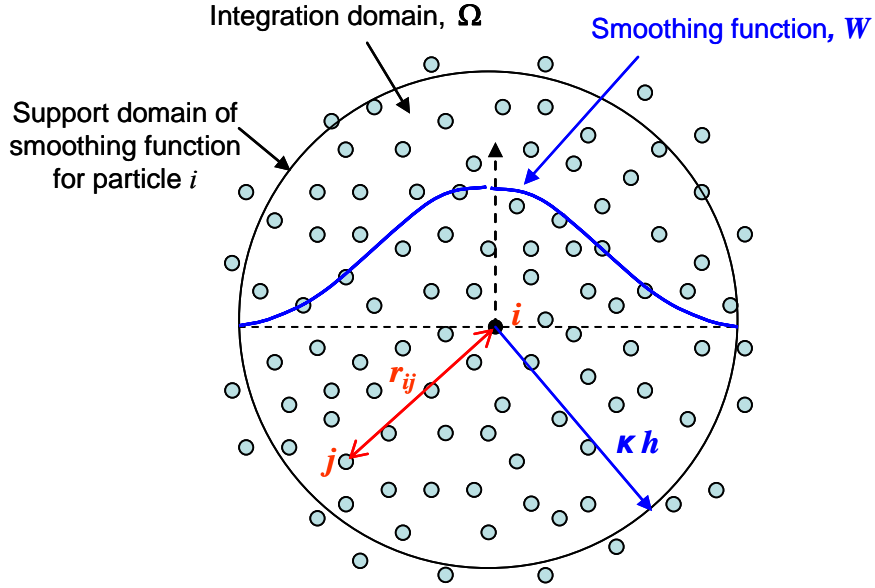


Figure 13: Support domain of particle  $i$  with a radius of  $\kappa h$

In SPH convention, the kernel approximation operator is marked by the angle brackets  $\langle \rangle$ . Equation (11) can therefore be written as:

$$\langle f(\mathbf{x}) \rangle = \int_{\Omega} f(\mathbf{x}') W(\mathbf{x} - \mathbf{x}', h) d\mathbf{x}' \quad (12).$$

The integral representation of the gradient of a function  $\nabla \cdot f(\mathbf{x})$  is obtained by substituting  $f(\mathbf{x})$  with  $\nabla \cdot f(\mathbf{x})$  in equation (12), which gives:

$$\begin{aligned} \langle \nabla \cdot f(\mathbf{x}) \rangle &= \int_{\Omega} [\nabla \cdot f(\mathbf{x}')] W(\mathbf{x} - \mathbf{x}', h) d\mathbf{x}' \\ \therefore \langle \nabla \cdot f(\mathbf{x}) \rangle &= \int_{\Omega} \nabla \cdot [f(\mathbf{x}') W(\mathbf{x} - \mathbf{x}', h)] d\mathbf{x}' - \int_{\Omega} f(\mathbf{x}') \cdot \nabla W(\mathbf{x} - \mathbf{x}', h) d\mathbf{x}' \end{aligned} \quad (13)$$

Using the divergence theorem, the first term on the right hand side of equation (13) can be converted into an integral over the surface,  $S$ , of the domain of integration  $\Omega$ :

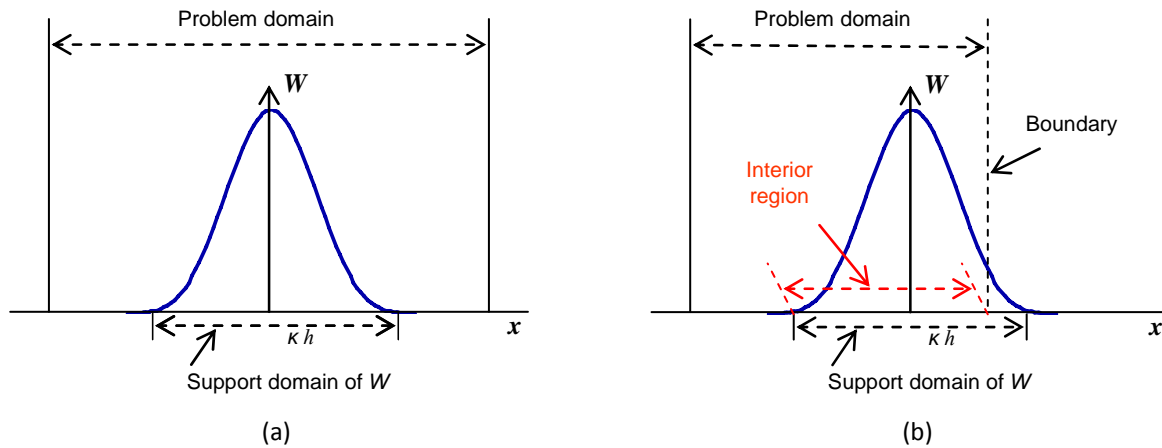
$$\langle \nabla \cdot f(\mathbf{x}) \rangle = \int_S f(\mathbf{x}') W(\mathbf{x} - \mathbf{x}', h) \cdot \vec{n} dS - \int_{\Omega} f(\mathbf{x}') \cdot \nabla W(\mathbf{x} - \mathbf{x}', h) d\mathbf{x}' \quad (14)$$

where  $\vec{n}$  - is the unit vector normal to the surface  $S$

For the particles whose support domain is within the problem domain as shown in Figure 14(a), the surface integral on the right-hand side of equation (14) is zero since the smoothing function,  $W$ , is compact. Therefore, the kernel approximation in equation (14) becomes:

$$\langle \nabla \cdot f(x) \rangle = - \int_{\Omega} f(x') \cdot \nabla W(x - x', h) dx' \quad (15).$$

However, Figure 14(b) shows the case whereby the support domain intersects the problem domain. Now, the smoothing function  $W$  is truncated and the surface integral on the right-hand side of equation (14) is no longer zero. In this case, modifications need to be made to account for the boundary effects.



**Figure 14:** Support domain of a particle with relation to the problem domain

## 4.2 Smoothing Kernel Functions

Various smoothing functions  $W$  are used in the SPH method. The most common smoothing function used within the SPH community, and that which is applicable to most problems modelled with SPH, is the cubic B-spline shown in Figure 15. This is the smoothing function used for the kernel approximation in LS-DYNA®. Smoothing functions should satisfy the following properties:

- The integral of the smoothing function should be unity. This is also known as the normalisation condition, or *Unity* condition.

$$\int_{\Omega} W(x - x', h) dx' = 1$$



- When the smoothing length approaches zero, the smoothing function approaches the Delta function

$$\lim_{h \rightarrow 0} W(\mathbf{x} - \mathbf{x}', h) = \delta(\mathbf{x} - \mathbf{x}')$$

- The smoothing function should be compactly supported i.e.  $W(\mathbf{x} - \mathbf{x}', h) = 0$  when  $|\mathbf{x} - \mathbf{x}'| > \kappa h$
- The *Positivity* condition must be satisfied i.e.  $W(\mathbf{x} - \mathbf{x}', h) \geq 0$  for any point at  $\mathbf{x}'$  within the support domain of the particle at point  $\mathbf{x}$ .
- With increasing distance away from the particle, the smoothing function value should be consistently decreasing.
- The smoothing function should be an even function and sufficiently smooth.

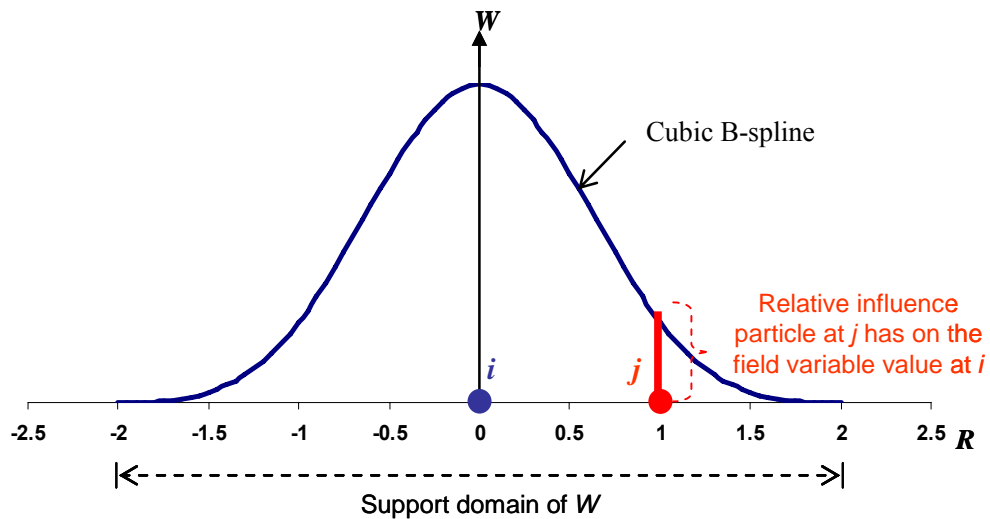


Figure 15: Cubic B-spline smoothing function

The cubic B-spline smoothing kernel function is defined as follows:

$$W(\mathbf{x} - \mathbf{x}', h) = W(R, h) = C \times \begin{cases} 1 - \frac{3}{2}R^2 + \frac{3}{4}R^3 & 0 \leq R \leq 1 \\ \frac{1}{4}(2 - R)^3 & 1 < R \leq 2 \\ 0 & R > 2 \end{cases}$$

where  $C$  is a constant of normalisation which depends on the number of space dimensions i.e. either 1D, 2D or 3D.

In the particle approximation step, the continuous integral representations concerning the kernel approximation are converted into discretised forms of summation over all particles in the support domain.

With reference to Figure 13, the infinitesimal volume  $dx'$  at the location of particle  $j$  is replaced by  $\Delta V_j$ , the finite volume of the particle at  $j$ . This finite volume is related to the mass of the particle,  $m_j$ , by the following expression:

$$m_j = \Delta V_j \rho_j \quad \text{or} \quad \Delta V_j = \frac{m_j}{\rho_j}$$

where  $\rho_j$  is the density of the particle  $j = 1, 2, \dots, N$  in which  $N$  is the number of particles within the support domain of particle  $j$ . Hence, the particle approximation introduces mass and density terms into the equations.

The continuous integral representation of a function  $f(\mathbf{x})$  can therefore be written in following discretised form:

$$\begin{aligned} f(\mathbf{x}) &= \int_{\Omega} f(\mathbf{x}') \mathcal{W}(\mathbf{x} - \mathbf{x}', h) d\mathbf{x}' \\ &\cong \sum_{j=1}^N f(\mathbf{x}_j) \mathcal{W}(\mathbf{x} - \mathbf{x}_j, h) \Delta V_j \\ &\cong \sum_{j=1}^N f(\mathbf{x}_j) \mathcal{W}(\mathbf{x} - \mathbf{x}_j, h) \frac{m_j}{\rho_j} \\ &= \sum_{j=1}^N \frac{m_j}{\rho_j} f(\mathbf{x}_j) \mathcal{W}(\mathbf{x} - \mathbf{x}_j, h) \end{aligned} \tag{16}$$

In summary, the particle approximations for a function and its spatial derivative at particle  $i$  are:

$$\langle f(\mathbf{x}_i) \rangle = \sum_{j=1}^N \frac{m_j}{\rho_j} f(\mathbf{x}_j) \cdot W_{ij} \tag{17}$$

$$\langle \nabla \cdot f(\mathbf{x}_i) \rangle = \sum_{j=1}^N \frac{m_j}{\rho_j} f(\mathbf{x}_j) \cdot \nabla_i W_{ij} \tag{18}$$

where  $W_{ij} = W(\mathbf{x} - \mathbf{x}_j, h) = W(|\mathbf{x} - \mathbf{x}_j|, h)$

$$\nabla_i W_{ij} = \frac{\mathbf{x}_i - \mathbf{x}_j}{r_{ij}} \frac{\partial W_{ij}}{\partial r_{ij}} = \frac{x_{ij}}{r_{ij}} \frac{\partial W_{ij}}{\partial r_{ij}}$$

$r_{ij}$  is the distance between particle  $i$  and  $j$ .

$\nabla_i W_{ij}$  is taken with respect to particle  $i$ .

Equations (17) and (18) state that the value of a function and its derivative at particle  $i$  is approximated using the weighted average of those particular values of the function at all the particles within the support domain of particle  $i$ .

The summation of the particle values for the integral approximation ensures that the SPH method is not dependent on any background mesh during numerical integration. The particles' mass and density are introduced in the basic integral equation and so this makes SPH attractive for hydrodynamic problems, where density is an important variable.

One of the major differences between SPH and the more conventional FE techniques is that in the latter, there is only one parameter for spatial discretisation. However, in the SPH method there are two spatial discretisation parameters, namely the characteristic length of the mesh  $\Delta x$  and the smoothing length  $h$ .

The kernel and particle approximations are applied to the conservation equations of mass, momentum and energy to define a physical domain. The implementation is standard in most SPH algorithms, although slight variations are possible with the conservation of momentum equations. The implementation of these discretised equations in the non-linear dynamic transient solver LS-DYNA® is explained in the section 4.3.

### 4.3 Implementation in LS-DYNA®

The SPH methodology has been implemented in LS-DYNA®, a non-linear FE software which has been widely used for modelling impact scenarios. SPH in LS-DYNA® has been implemented as an explicit scheme and the SPH processor has been developed as an additional layer of the base code. Therefore, the SPH capability can be used with all the other features of the software.

The smoothing kernel used in LS-DYNA® is the cubic B-spline kernel defined in Figure 15. Table 2 summarises the discretised forms of the conservation equations following the particle approximation process.

Conservation Property	Particle Approximation of Equation
Mass	$\frac{\partial \rho_i}{\partial t} = \sum_{j=1}^N m_j \mathbf{v}_{ij} \cdot \frac{\partial W_{ij}}{\partial \mathbf{x}_i} \quad (19)$
Momentum	$\frac{\partial v_i}{\partial t} = \sum_{j=1}^N m_j \cdot \left( \frac{\sigma_i}{\rho_i^2} + \frac{\sigma_j}{\rho_j^2} \right) \cdot \frac{\partial W_{ij}}{\partial \mathbf{x}_i} \quad (20)$
Energy	$\frac{\partial u_i}{\partial t} = \sum_{j=1}^N m_j \cdot \left( \frac{\sigma_i \cdot \sigma_j}{\rho_i \cdot \rho_j} \right) \cdot \mathbf{v}_{ij} \cdot \frac{\partial W_{ij}}{\partial \mathbf{x}_i} \quad (21)$

**Table 2:** Particle approximations of the mass, momentum and energy conservation equations

$\sigma_i$  and  $\sigma_j$  are components of the stress tensor in particle  $i$  and  $j$  respectively.

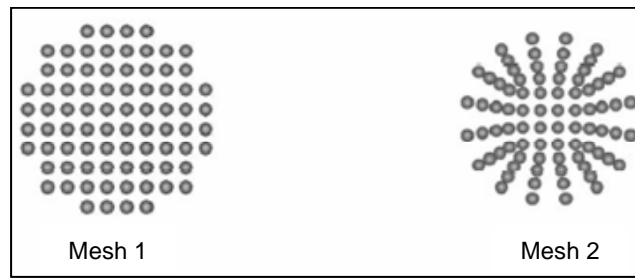
$v_{ij}$  is the component of the relative velocity vector between particle  $i$  and  $j$ .

Various particle approximation theories are available within LS-DYNA®. They differ in their particle approximation theory for the conservation of momentum equation. Other formulations available in LS-DYNA® are the symmetric formulation and ‘fluid’ formulation, whose discretised conservation of momentum equations are shown in equation (22) and equation (23) respectively.

$$\frac{\partial v_i}{\partial t} = \sum_{j=1}^N m_j \cdot \left( \frac{\sigma_i}{\rho_i^2} + \frac{\sigma_j}{\rho_j^2} \right) \cdot \nabla W_{ij} \quad (22)$$

$$\frac{\partial v_i}{\partial t} = \sum_{j=1}^N m_j \cdot \left( \frac{\sigma_i + \sigma_j}{\rho_i \rho_j} \right) \cdot \frac{\partial W_{ij}}{\partial \mathbf{x}_i} \quad (23)$$

Through an investigation described in section 6.2.7, it was observed that differences between the particle approximation theories were minor, although the fluid-formulation for the SPH provided the best qualitative results. Therefore, this particle approximation theory shown in equation (23) was used for the remainder of the models investigated in this research.

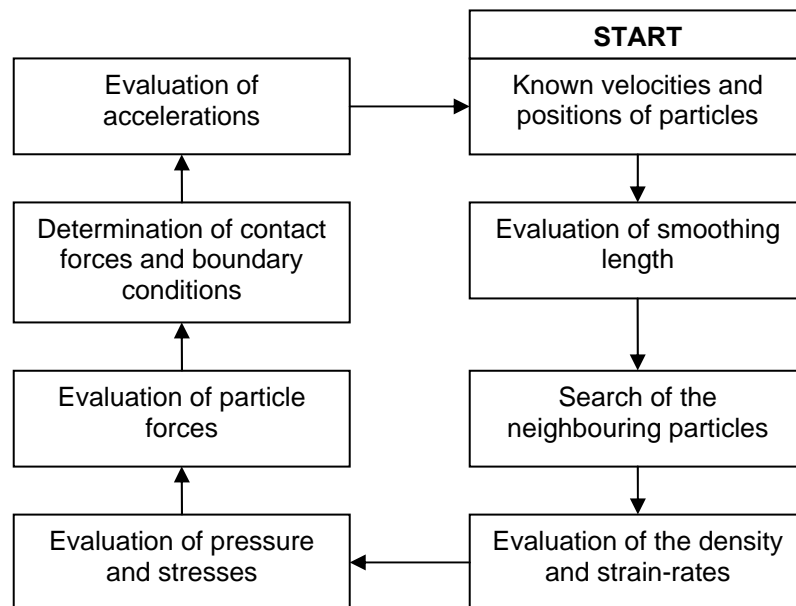


**Figure 16:** SPH particle distributions  
(Source: LSTC 2005)

An important consideration when modelling with SPH in LS-DYNA® is the particle distribution, which should be as regular as possible to maintain the same mass associated between all particles. With reference to Figure 16, Mesh 2 is irregular and depending on the method of particle creation within the pre-processor, could result in unequal particle masses. This coupled with inconsistencies that would be invoked through the automatic initial smoothing length calculation by the SPH solver would result in non-physical model behaviour. On the other hand, Mesh 1 illustrates the recommended particle distribution at the initiation of a model with equal particle masses and the same initial smoothing length that can be applied to all the particles within the entire SPH domain.

#### 4.3.1 SPH Solution Procedure

Figure 17 describes the solution cycle of the SPH integration in LS-DYNA®.



**Figure 17:** SPH solution procedure in LS-DYNA®

### 4.3.2 Variable Smoothing Length

In large deformation problems solved with SPH, one numerical difficulty that could render a model inefficient and unstable is the number of particles within its influence area. The sphere of influence of each particle is  $2h$  and a search of the particles within a certain particle's support domain is conducted at every time step. The initial smoothing length is computed by taking the maximum of the minimum distances between every particle in the SPH domain.

The number of particles within the influence domain of a fixed smoothing length is dependent on the type of loading the material is under. In compression problems, the number of particles within the influence domain increases and this increases the computational processing time. On the other hand, under tensile loading the particles separate away from each other and there are fewer particles in the influence domain which results in low accuracy and leads to stability issues (Vignjevic 2004). A variable smoothing length is therefore used.

Every particle has its own smoothing length which varies over time and space. A variable smoothing length is the default setting in LS-DYNA®, and this scheme is implemented in order to avoid problems of expansion and compression of the material described above. This variation in the smoothing length in 3D is defined by equation (24).

$$\frac{dh}{dt} = \frac{1}{3} h \text{div}(v) \quad (24)$$

where  $\text{div}(v)$  is the divergence of the flow.

The smoothing length increases when the particles separate from each other. The opposite happens when the particles condense together, whereby the smoothing length decreases. This variation in  $h$  keeps approximately the same mass of particles interacting with each other. Additionally, a minimum and maximum value of the smoothing length is also defined for numerical stability and computational efficiency reasons.

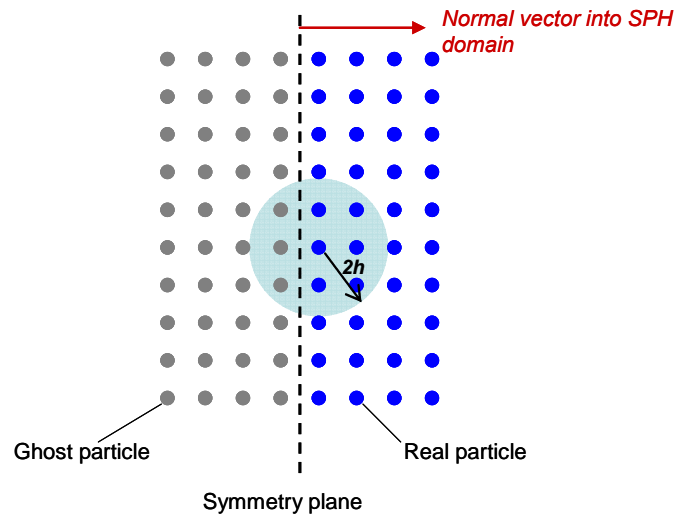
$$h_{\min} < h < h_{\max}$$

These limits of the smoothing length are defined by constants HMIN and HMAX applied to the initial smoothing length,  $h_0$ , calculated at the beginning of a simulation:

$$\begin{aligned} h_{\min} &= \text{HMIN} \times h_0 \\ h_{\max} &= \text{HMAX} \times h_0 \end{aligned}$$

### 4.3.3 Symmetry Modelling with SPH

Symmetry planes for the SPH domain are established by creating ghost particles on the opposite side of the plane. Ghost particles are images of the real particles within a distance of  $2h$  to the plane, and have the same particle mass, pressure and absolute velocity as the real particles. These ghost particles are included in the particle approximation of the real particles, and therefore facilitate the symmetry condition. A schematic of the symmetry plane is drawn in Figure 18.



**Figure 18:** Symmetry modelling for SPH using ghost particles

This page is intentionally blank



# Chapter 5

## EXPERIMENTAL INVESTIGATION

---

### 5.1 Experimental Procedure

The experiments conducted in this research consisted of impacting rigid and symmetric wedges of varying deadrise angles into a trough of water. The motion of the wedges was constrained in the vertical direction so as to closely represent the two-dimensional (2D) impact case. This was facilitated through the design and fabrication of an experimental rig shown in Figure 20.

The aim of the experiment was to capture the following two key data sets:

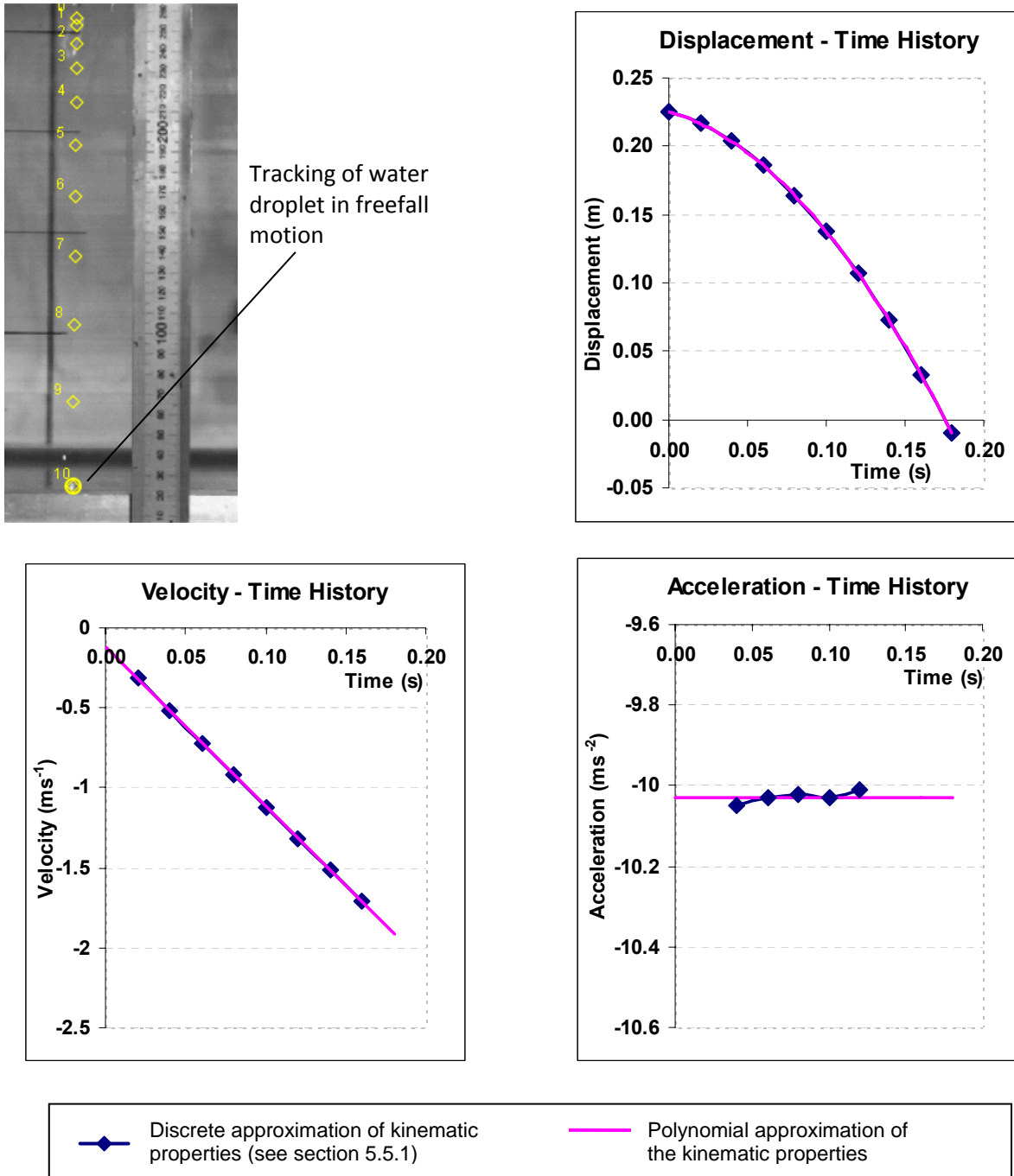
- Kinematic behaviour of the wedges – this included properties such as accelerations and forces of the wedge upon impact.
- Qualitative 2D behaviour of the water – this would be useful in the qualitative validation of the SPH method.

The kinematic behaviour of the wedges was obtained by using a photographic technique, through the filming of the entire impact event with a high-speed video camera. The motion of the wedge was tracked at regular intervals of time to get its displacement-time history. First and second derivatives of the displacement-time history (with respect to time) were then obtained to give the velocity and acceleration profiles, respectively.

The test matrix outlining the range of test configurations is outlined in section 5.2. The specific wedge being impacted was attached to a sliding assembly and raised to the predefined drop height. Once the camera was filming the impact region, the wedge was released from this position. The impact event was captured at a frame rate of 500 frames/second, which was found to be sufficient to visualize a good progression of the impact and water rise-up along the sides of the wedge.

However, prior to performing the wedge water impact tests, the accuracy of this photographic approach was evaluated by tracking the motion of a droplet of water in freefall. Figure 19 shows the results of this initial study. A detailed description of the method adopted to determine the

freefall acceleration is provided in section 5.5.1. Using the displacement-time history of the water droplet under freefall, a quadratic polynomial approximation of the displacement was obtained. This was differentiated twice with respect to time to give a constant acceleration of  $10.03\text{ms}^{-2}$ , which compares well to the known theoretical value of  $9.81\text{ms}^{-2}$  (within 3% of the theoretical value). So, the proposed photographic technique was considered suitably accurate.



**Figure 19:** Kinematics of a water droplet in freefall

## 5.2 Test Matrix

Wedges of five different deadrise angles ranging between 20° and 40°, at regular increments of 5°, were dropped into the water trough. All the wedges were of the same mass and were released from different drop heights. Additional parameters varied during the experiment were an increase in the wedge masses, together with a variation in the level of the water in the trough to observe whether that would have any effect on the impact dynamics. The test matrix is summarised in Table 3.

Drop height above water level	Wedge Deadrise Angle (°)	Wedge Mass		
		1.639 kg	1.852 kg	2.072 kg
50 mm	20	✓	✓	✓
	25	✓	✓	✓
	30	✓	✓	✓
	35	✓	✓	✓
	40	✓	✓	✓
100 mm	20	✓	✓	✓
	25	✓	✓	✓
	30	✓	✓	✓
	35	✓	✓	✓
	40	✓	✓	✓
150 mm	20	✓		
	25	✓		
	30	✓		
	35	✓		
	40	✓		

**Table 3:** Test matrix showing the experimental wedge configurations

For clarity, the wedge masses were designated the following convention which has been used throughout the remainder of the document:

- 1.639 kg – ‘Light’ impactor mass
- 1.852 kg – ‘Intermediate’ impactor mass
- 2.072 kg – ‘Heavy’ impactor mass

The wedge masses specified above consist of the wedge itself, plus the fixed part of the sliding assembly to which the wedge is attached. Three water trough depths were used: 150 mm, 180 mm and 210 mm. Only the light impactors were dropped from a height of 150 mm as the water

trough was too small to contain the splash that would be caused by the heavier impactors dropped from this height.

All the light wedges were dropped into the water trough at the three differing trough depths mentioned. Upon investigation of the results obtained until this stage in the experimental testing, it was observed that the depth of the water trough has no effect on the kinematics of the wedge during the impact phase. Therefore, the drop tests of intermediate and heavy impactors were conducted with a water depth of 210 mm.

Repeatability of the tests was evaluated through three drop tests conducted for each of the test configurations in Table 3. This enabled the identification of any errors that may have affected certain tests and additionally, provides an extended data set that can be averaged during the processing of the results.

The above test configurations were selected for the experimental analysis as they covered a wide range of deadrise angles and impactor energies. Therefore, a larger pool of data would be available for validation of the SPH approach. Although the experiment was performed on a small-scale due to limited financial resources, these tests would provide valuable insight into experimental issues that would need to be addressed prior to conducting larger and more expensive testing programs.

### **5.3 Experimental Setup**

Several ideas were considered in developing a mechanism to ensure vertical motion of the wedge. Considering the scope and budget of the experiment, drawer slides (from here on referred to as 'guiding track') were used which were aligned vertically to provide the required range of motion for the wedges. Although the drawer slides have an appreciable amount of friction (see section 5.7) when compared to freefall motion, all other linear motion systems were financially infeasible for the scale and scope of the experiment.

The experiment was set up so as to generate a 2D flow-field of water upon impact. Considering this experimental setup, 3D effects of the flow would occur at both ends of the wedge. However, by maintaining a very small tolerance of approximately 2 mm between the face of the wedge and the trough window, these 3D effects were found to be negligible and the behaviour of the fluid during the impact can be considered to be sufficiently 2D for a majority of the depth of the wedge.

Figure 20 illustrates the experimental setup with the drop-rig, water trough and the wedge attached to the vertical guiding track. A photograph of the setup is shown in Figure 21.

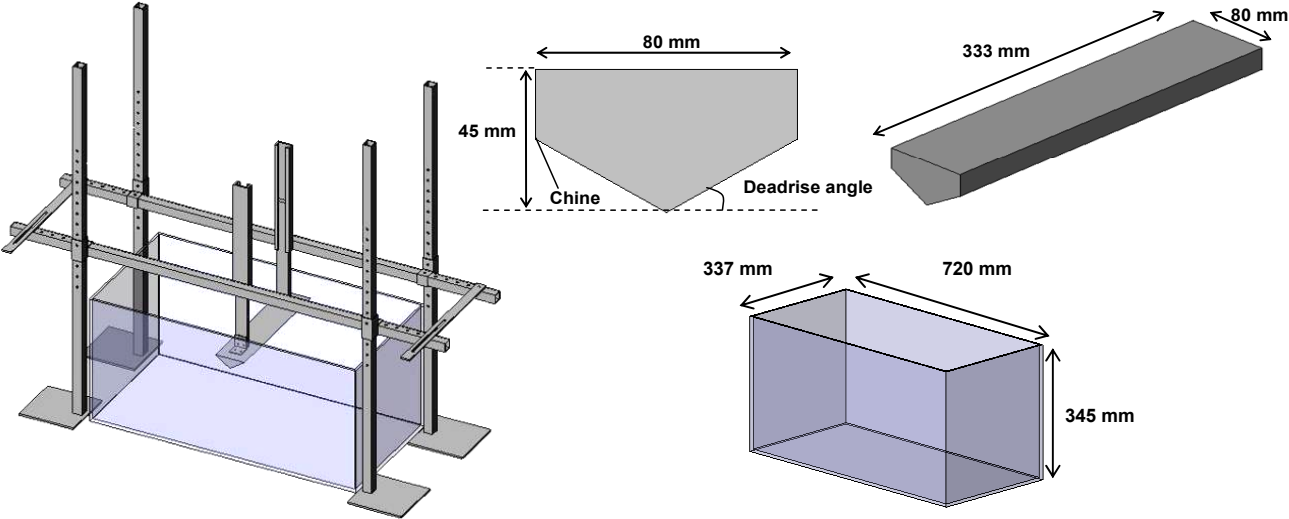


Figure 20: Schematic of test-rig and wedge specimens

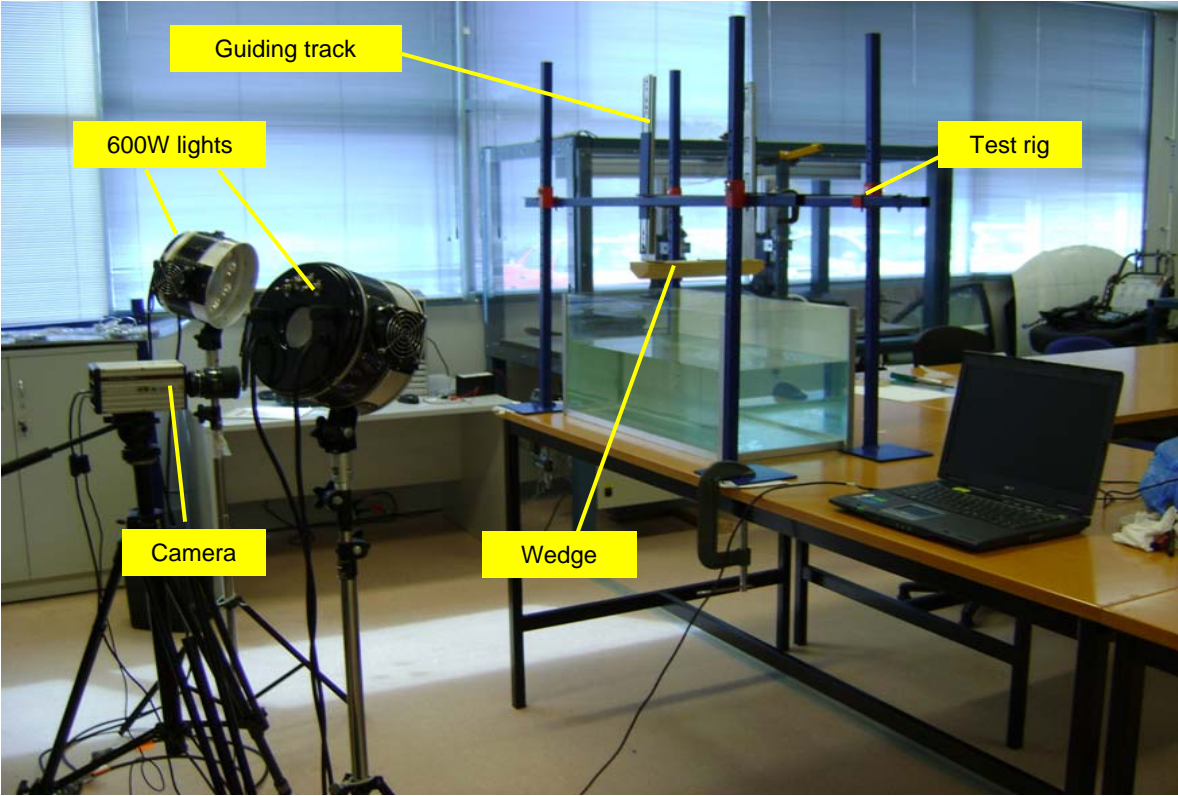
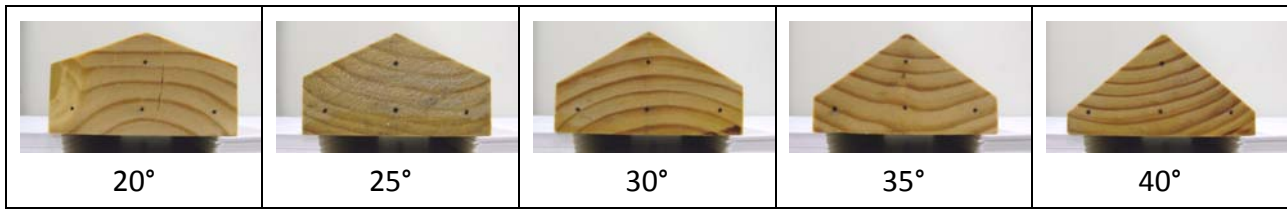


Figure 21: Experimental set-up

The five wedges of differing deadrise angles shown in Figure 22 were machined from a block of pinewood. All the faces were smoothed down and coated with a varnish to prevent the absorption of water into the wood which could distort the physical dimensions of the wedge and affect the consistency of the wedge mass throughout the experiment. In order to

standardise the mass between all wedges, sheet metal was attached proportionately to the wedges as shown in Figure 23. Figure 24 shows the additional mass arrangements for the intermediate and heavy impactors.



**Figure 22:** Cross-sectional view of wedge specimens



**Figure 23:** Masses added to wedge specimens to equalise their mass



(a) Intermediate impactor



(b) Heavy impactor

**Figure 24:** Additional masses attached to basic wedge specimen

A pair of guiding tracks was attached to the horizontal frames of the rig as shown in Figure 21. The wedge was attached at each end to the bottom of the track through a right-angle bracket and screws. This made it easy to interchange the wedges being impacted by simply unscrewing one wedge and attaching another.

The impact event was filmed using a high-speed video camera, identified in Figure 21, at a frequency of 500 frames/second. This translated to an image captured every 0.002 s. The camera was the X-Stream™ XS-4 model manufactured by Integrated Design Tools (IDT), Inc.

Checks were conducted and any necessary adjustments required were made to ensure that the refraction of the light from the impact window did not influence the photographic technique employed to obtain the kinematics of the wedge. Due to the high-frame rate of the video capture, 600 W of lighting was used in addition to the ambient room lighting. These videos were then analysed with the OpenSource software Tracker<sup>®</sup> (Brown 2009) which allows the progressive manual tracking of points in each frame to generate a displacement-time history of the wedge. From this data, the velocity and acceleration-time histories can be obtained.

The base of the experimental rig was clamped down to the table using G-clamps to ensure a rigid setup and provide support during the impact. This was extremely important considering the tolerance between the edge face of the wedge and the glass-trough window was only about 2 mm.

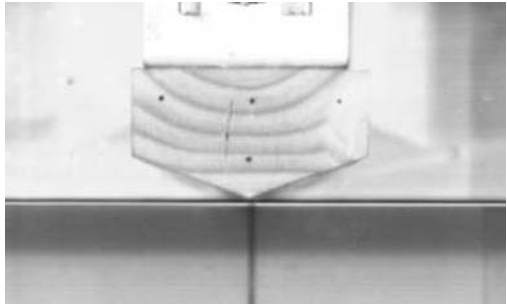
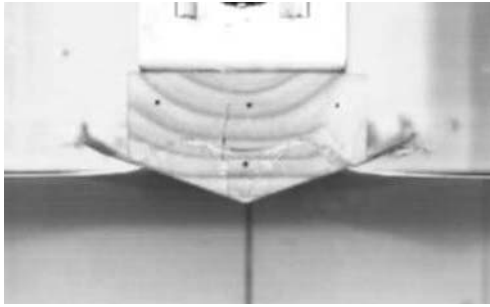
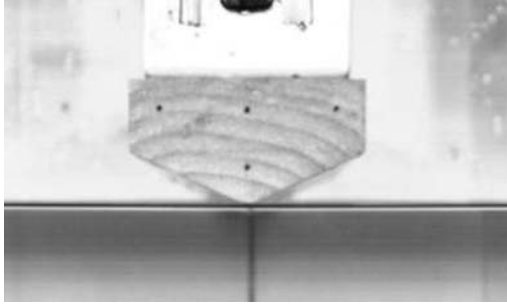
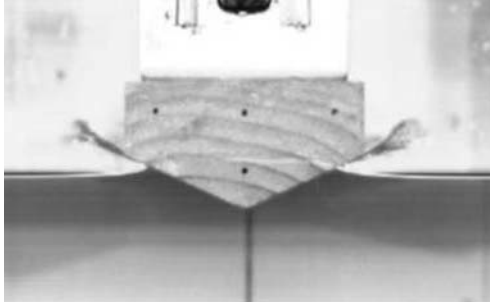
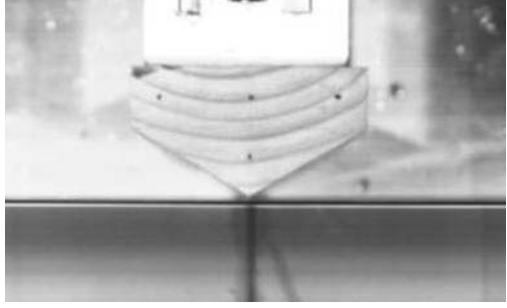
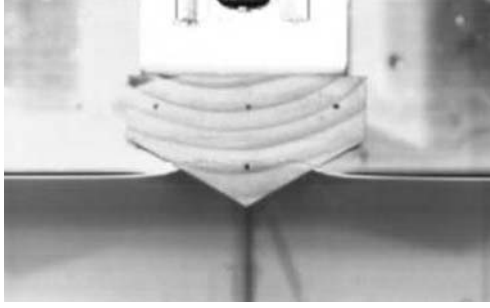
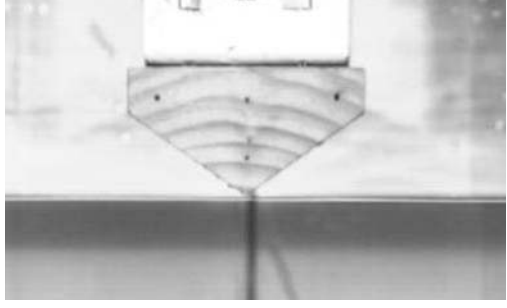
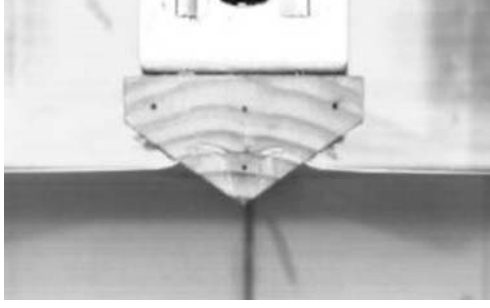
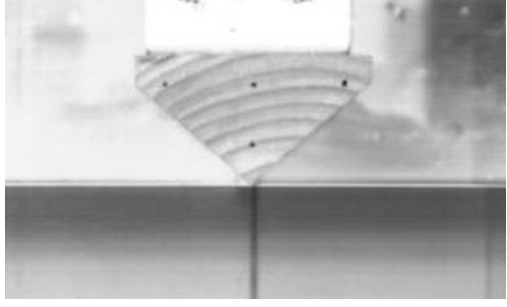
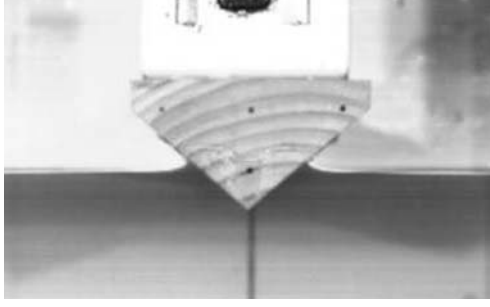
A significant amount of friction was experienced in the guiding track during the experiment. This friction was quantified and factored into the experimental and numerical modelling of the wedge impact scenario, thus allowing for a valid comparison to be made (see section 5.7).

#### **5.4 Video Capture of Water Impact**

Figure 25 shows the progressive images captured for the water entry of all light wedges dropped from a height of 150 mm. The images are presented at intervals of 0.01 s after initial impact with water.

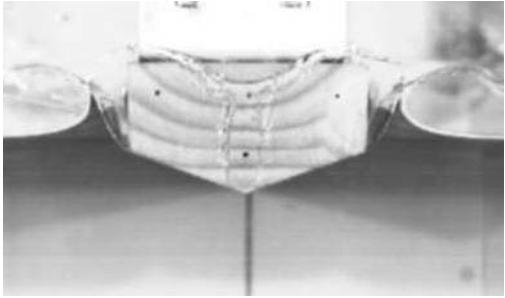
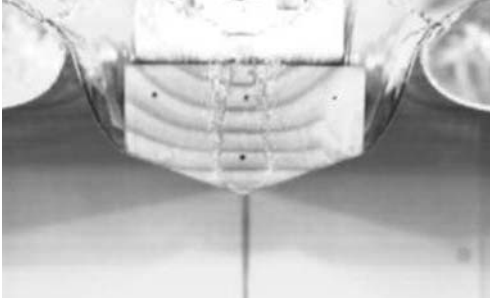
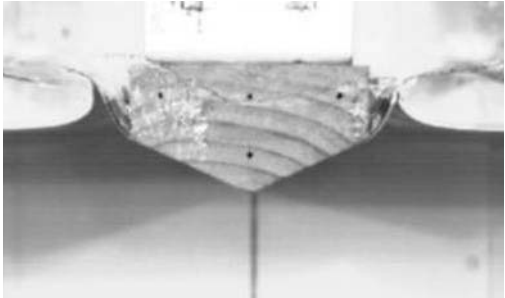
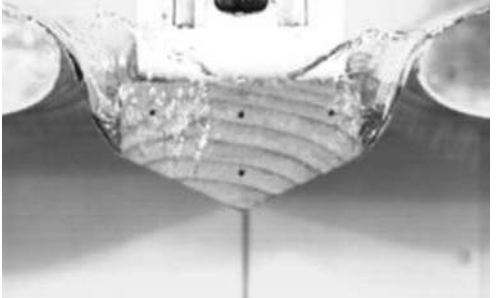
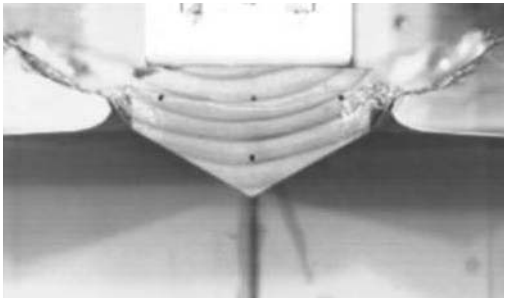
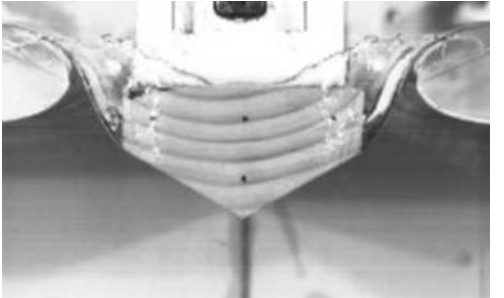
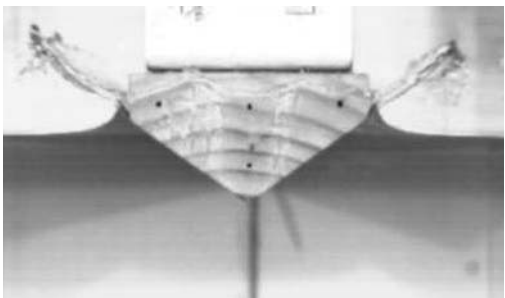
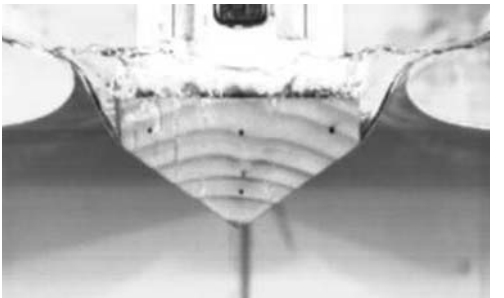
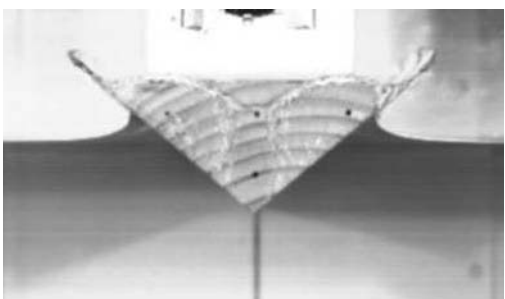
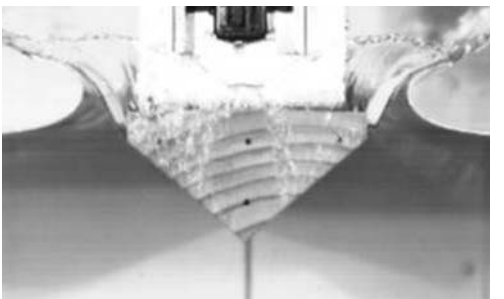
From the images captured, the 2D behaviour of the water is well defined. The rise up of the free-surface can be clearly discerned and symmetric flow patterns are observed along both sides of the wedge. This indicates that the drop-rig was rigid and properly oriented vertically.

3D flow behaviour can also be seen occurring when the water rises in the small gap between the cross-sectional face of the wedge and the trough window. This was expected, however, and is limited to the ends of wedge. The effect of this behaviour on the 2D kinematics of the system is considered negligible due to the majority of the flow along the depth of the wedge being 2D. The wedge depth is defined as the length of the wedge normal to the cross-sectional face.

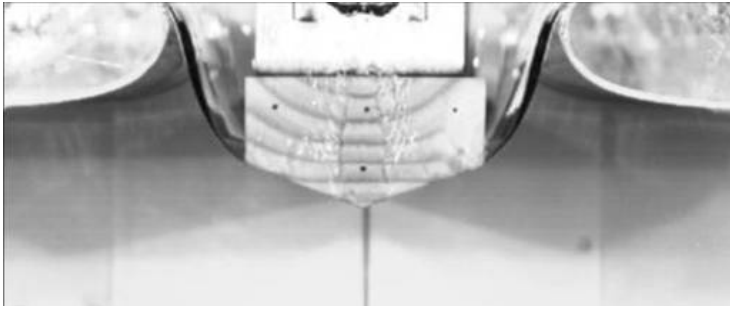
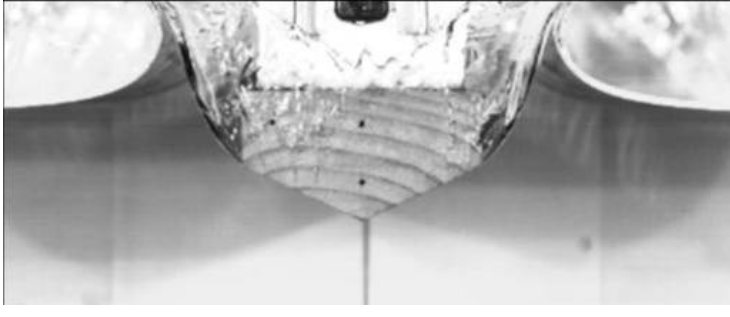
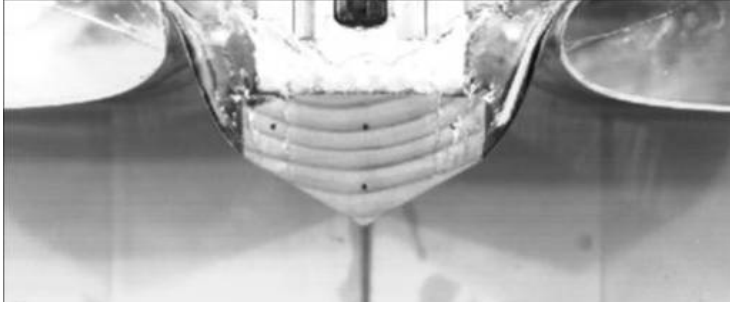

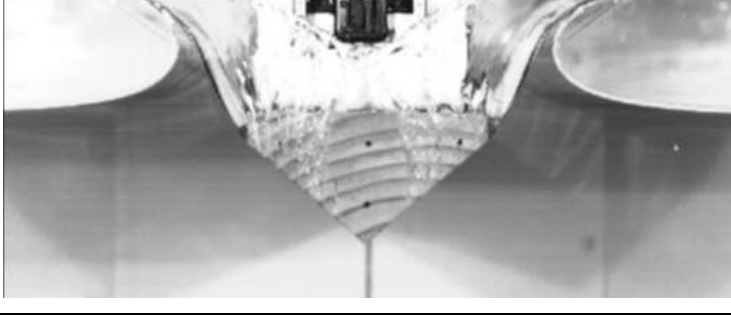
		$t = 0.00 \text{ s}$	$t = 0.01 \text{ s}$
Deadrise Angle	20°		
	25°		
	30°		
	35°		
	40°		

**Figure 25:** Progressive image capture of water impact



		$t = 0.02 \text{ s}$	$t = 0.03 \text{ s}$
Deadrise Angle	20°		
	25°		
	30°		
	35°		
	40°		

**Figure 25:** Progressive image capture of water impact

		$t = 0.04 \text{ s}$
Deadrise Angle	20°	
	25°	
	30°	
	35°	
	40°	

**Figure 25:** Progressive image capture of water impact

## 5.5 Wedge Accelerations

The wedge acceleration was obtained using two methods; a ‘discrete’ method directly using the data from the discrete measurements of the progressive displacements of the wedge, and secondly from the second derivative of a polynomial approximation applied to the initial discrete measurements of the displacement-time history.

### 5.5.1 Discrete Approximation of Acceleration-Time History

The displacement profiles of the impactor were obtained by tracking known positions on the wedge using the software Tracker<sup>®</sup>. This gives a set of discrete displacement data from which the velocity and acceleration of the impactor can be obtained as described below.

The velocity,  $v_n$ , at a given time  $t_n$  is obtained by calculating the distance travelled between  $t_{n+1}$  and  $t_{n-1}$ , and dividing that distance by the time period. This is illustrated in Figure 26.

$$v_n = \frac{\text{displacement}}{\text{time}} = \frac{\Delta s}{\Delta T} = \frac{s_{n+1} - s_{n-1}}{t_{n+1} - t_{n-1}} \quad (25)$$

Since the time-period between each measurement of the displacement is constant, equation (25) simplifies to equation (26).

$$v_n = \frac{s_{n+1} - s_{n-1}}{2\Delta t} \quad (26)$$

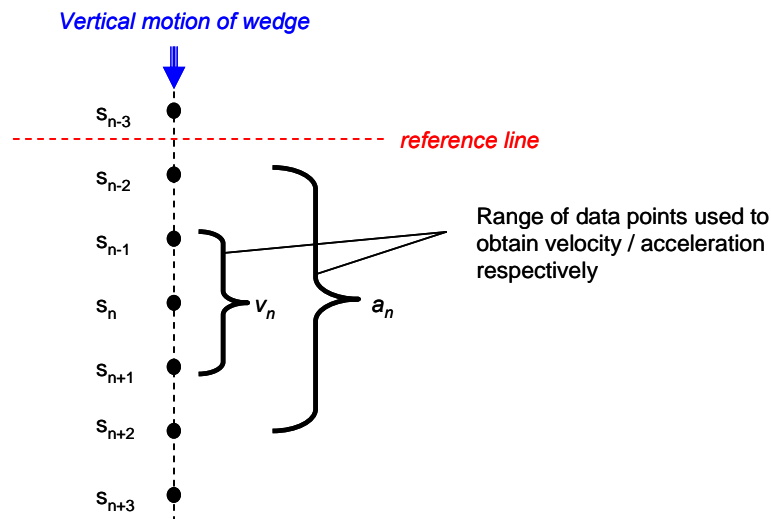


Figure 26: Calculation of velocities and accelerations using discrete displacement data

The acceleration,  $a_n$ , is determined through the second derivative of the discrete displacement profile using the five point central-difference scheme according to equation (27):

$$a_n = \frac{2s_{n-2} - s_{n-1} - 2s_n - s_{n+1} + 2s_{n+2}}{7\Delta t^2} \quad (27)$$

Provided below is an outline of the steps involved in obtaining the accelerations, and hence forces, through numerical differentiation of the manually specified displacements in Tracker<sup>®</sup>.

### Step 1 – Setting Reference Axes and Scale in Tracker<sup>®</sup>

In Tracker<sup>®</sup>, specifying coordinate axes and an appropriate scale provides a reference from which point locations can be specified. The user places the axes anywhere within the image captured, and characterises the scale by using reference points on the image. Figure 27(a) displays the attributes of the axes and scale which was applied to the analysis of all the videos from the experiment.

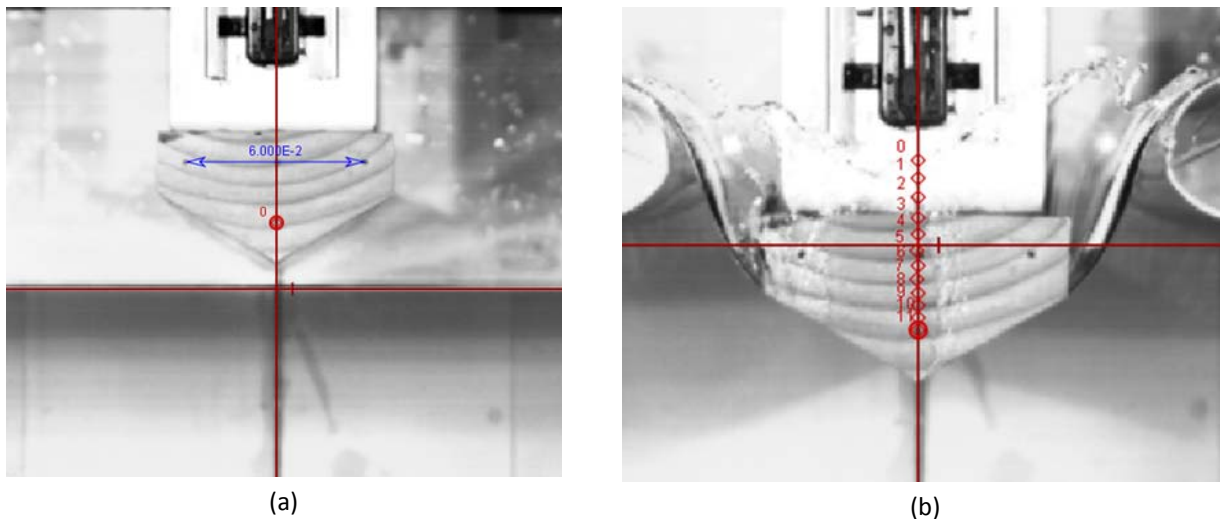


Figure 27: Point tracking in Tracker<sup>®</sup>

### Step 2 – Determination of Video Strip and Time-step

The length of the video clip within which the motion is to be tracked is then specified, together with the frequency of measurements required i.e. the time step between each measurement. For example, given that a frame is captured every 0.002 s, if a displacement is specified every frame then the time step will be 0.002 s. If it is desired to specify a displacement every 5 frames, then the time step between each discrete displacement specification will be 0.01 s.

### **Step 3 – Manual Specification of Displacements**

Once the basic parameters of the video clip are set, the user manually tracks a reference point from the beginning of the selected clip to the end, as shown in Figure 27(b). Black spots were marked on the face of the wedge as can be seen in Figure 22, which were used as the reference points and tracked through the impact event.

From Figure 27(b), it can be seen that the exact specification of the centre of a point is dependent on the judgement of the user. As demonstrated in section 5.6, the acceleration profiles obtained through this discrete method are sensitive to minute variations in the displacement specification, thus often making it difficult to observe intricate trends in the results data set.

### **Step 4 – Evaluation of Wedge Velocity and Acceleration**

From the displacement data set, the velocity and acceleration-time histories of the wedges were obtained by using equations (26) and (27) respectively. An example of the kinematic time histories is shown in Figure 28.

20° Deadrise Angle – Light Impactor– 150 mm Drop

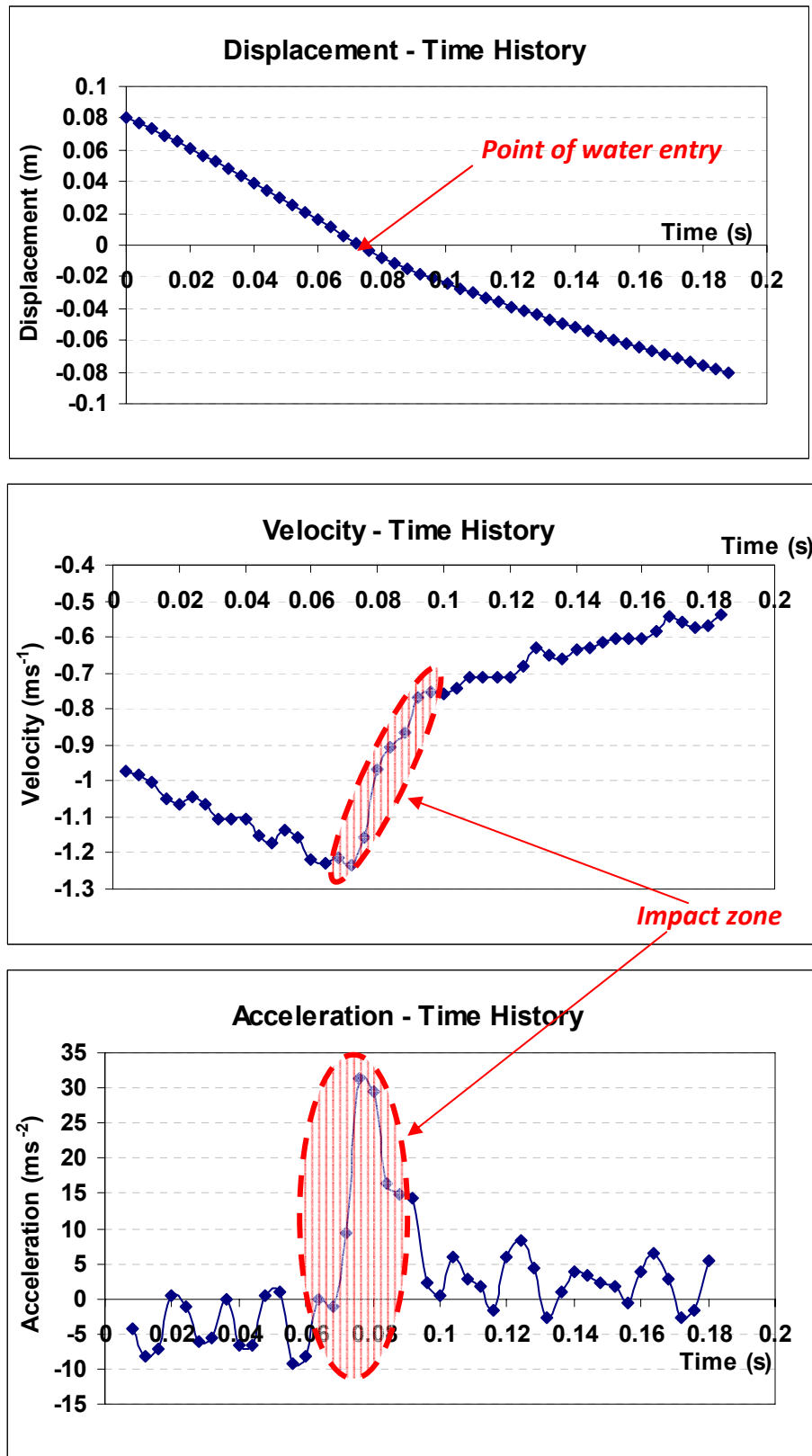


Figure 28: Displacement-time history and the derived velocity and acceleration-time histories

In this investigation, the time-period of interest can be defined as the region where there is the highest rate of loss of kinetic energy upon interaction between the wedge and the water. This corresponds to the period when the largest acceleration, and therefore force, is experienced by the wedge. The impact occurs over a very short time period, typically over 20-30 ms.

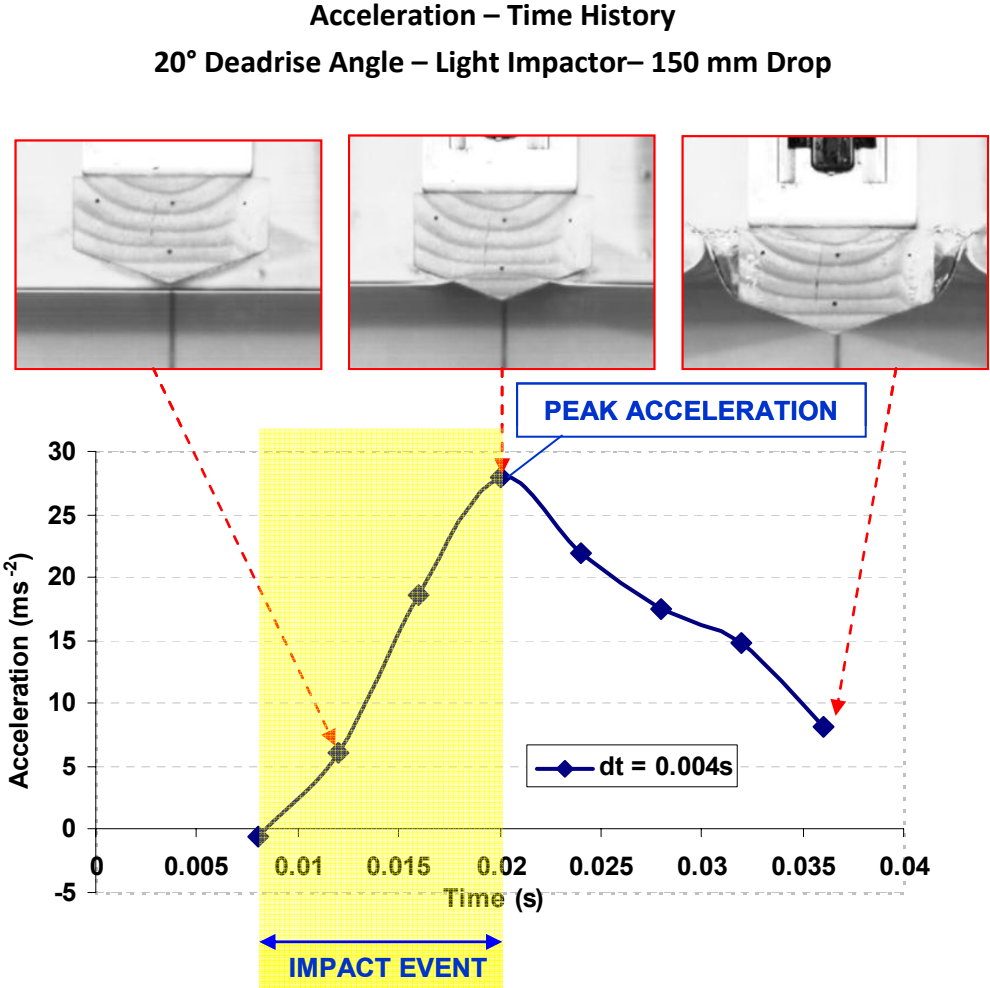


Figure 29: Progressive images of water entry through the impact zone

Within this ‘impact zone’ depicted in Figure 29, the buoyancy effects are considered negligible. Furthermore, from previous research and the literature (von Karman 1929; Wagner 1932; Mayo 1945), the inertial forces dominate the viscous forces through this phase of the water entry and therefore viscosity effects of the water on the force experienced by the wedge can be considered insignificant.

For all the wedges tested, the peak force was observed during the rise up of the water along the side of the wedge, before the free-surface reached the chine i.e. the point where the contour of

the wedge becomes vertical along the side of the wedge away from the centreline. The peak acceleration identified above corresponds to the highest force i.e. the impact force experienced by the wedge. In actual aircraft structures, this would be the instant where the impulsive loading on the structure would cause significant structural deformation and damage followed by complex fluid-structure interaction.

As mentioned earlier, three test runs have been conducted for each test configuration which provides three sets of discrete displacement data. An example of accelerations obtained using the discrete approach for all three test runs of a particular test configuration is shown in Figure 30. The displacement profiles obtained through the point tracking are very similar.

However, since each set would inherently vary due to operator judgement, the three data sets were averaged (excluding any outliers which are considerably disparate from the mean data set) and the final discrete displacement-time histories were used to obtain the acceleration profile illustrated by the solid red line in Figure 30. Despite this averaging, the relatively large variation and randomness in the acceleration profiles obtained using the discrete approach was observed for all the test configurations.

The uncertainty of the peak value of the accelerations makes validation of the simulation results difficult, and an analysis into the extent of this variation is provided in section 5.6.



20° Deadrise Angle – Light Impactor – 150 mm Drop

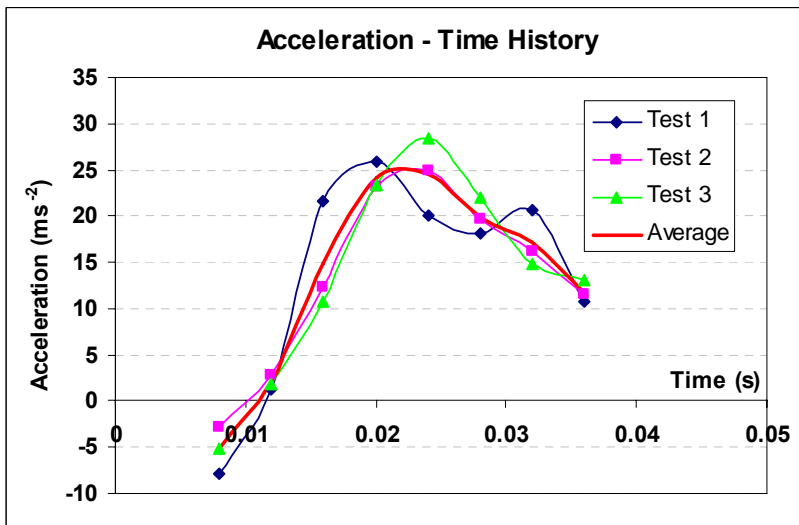
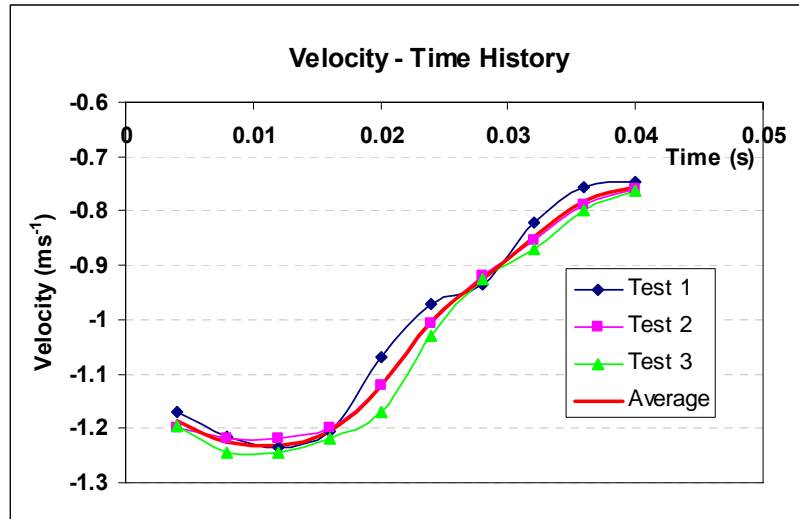
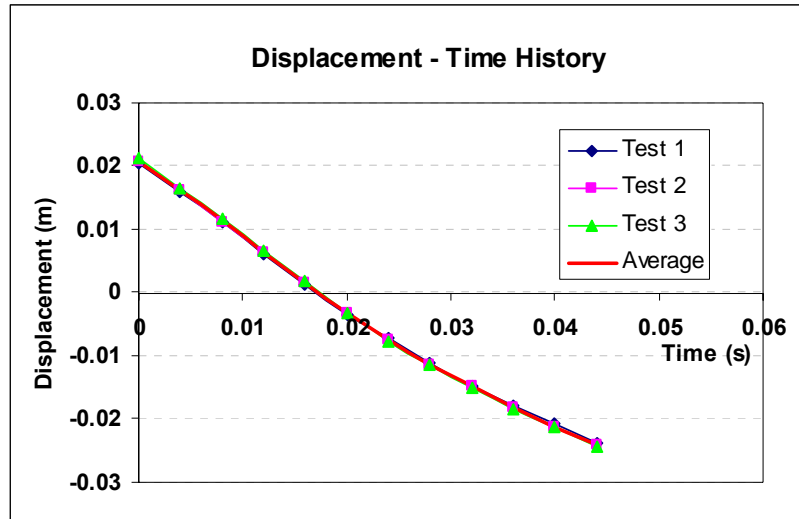


Figure 30: Example of displacement, velocity and acceleration-time histories

### 5.5.1.1 Influence of Time Step on Acceleration – Time History

The selection of the time step greatly influences the acceleration-time histories observed through the discrete approach. To accurately capture the impact event, a time step should be selected such that sufficient discrete displacement data is available to capture a good profile of the acceleration-time history over the impact zone.

In order to obtain realistic acceleration profiles, acceleration-time histories using four different time steps were determined and compared for the light wedge of 20° deadrise angle dropped from a height of 150 mm. This test configuration had the highest impact energy, and consequently the greatest impulsive force represented by the highest acceleration observed of all the configurations tested.

The time-steps selected were:

$\Delta t = 0.002\text{ s}$  - Displacements specified at every video frame

$\Delta t = 0.004\text{ s}$  - Displacements specified every 2 video frames

$\Delta t = 0.01\text{ s}$  - Displacements specified every 5 video frames

$\Delta t = 0.02\text{ s}$  - Displacements specified every 10 video frames

The displacement, velocity and acceleration-time histories at these selected time steps are plotted in Figure 31.

### 20° Deadrise Angle – Light Impactor – 150 mm Drop

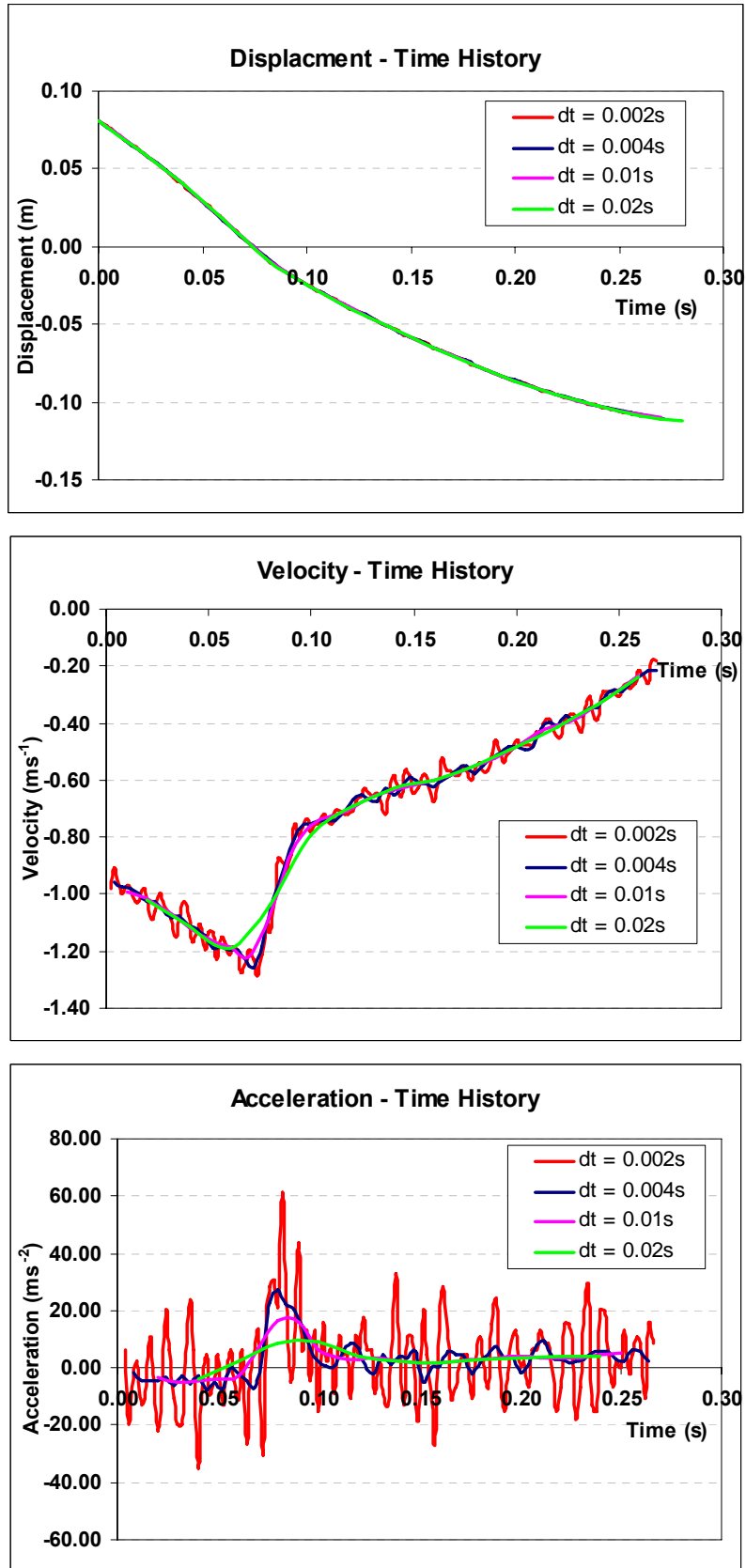


Figure 31: Influence of step size on derived kinematic characteristics

From the acceleration profiles in Figure 31, the region of interest of the impact can be clearly identified where the highest acceleration is experienced. As can be clearly seen, as the time-step between each displacement measurement is reduced, the fluctuations in the acceleration increase, especially since the acceleration is obtained from the second derivative of the displacement data. Also, the 'noise' within the derived acceleration profiles increases with an increasing number of data points for the higher frequency measurements within the same time period.

As the time-step is reduced, the influence of minor differences in the displacement selection increasingly affects the profiles of the velocity and acceleration-time histories. Section 5.6.1 discusses the sensitivity of the acceleration profiles to the specification of the centre of the tracked points.

In reality, the impact event is not characterised by the seemingly random and large fluctuations in acceleration as represented when using the discrete method to derive them. Through further analyses, it can be concluded that these sudden fluctuations are attributed to the specification of the discrete displacement data.

In the actual impact event, the wedges should have a rather smooth transition in their acceleration profiles. To get a smoother approximation of the acceleration profile, a polynomial was used to approximate the trends observed through the differentiation of the discrete displacement data.

### **5.5.2 Polynomial Approximation of Acceleration – Time History**

Polynomial approximations were obtained for the displacement-time history. The advantage of this approach is that these polynomials could be analytically differentiated to obtain the velocity and acceleration profile through the impact.

Figure 30 shows the acceleration profile obtained for all the three test runs of a particular test configuration. It was checked that there were no inflection points over the peak acceleration, and the acceleration profile was representative of a 3<sup>rd</sup>-order polynomial in the impact zone with one trough prior to the impact and a peak in the curve where the maximum acceleration is observed. Therefore, a 5<sup>th</sup>-order polynomial approximation of the displacement function over the impact zone was required. An example of the resulting polynomial approximations is shown Figure 32 and Figure 33.

The polynomial approximation was carried out using the least squares method. Two points prior to and after the prescribed impact zone are included in the data set for the polynomial approximation of the displacement function. This was done to get a good representation of the acceleration profile throughout the impact zone. To reduce the operator error in the manual point tracking, the data set for the polynomial approximation of the displacement-time history consisted of averaged values of the discrete displacement curves from all three test runs, excluding data from any outliers.

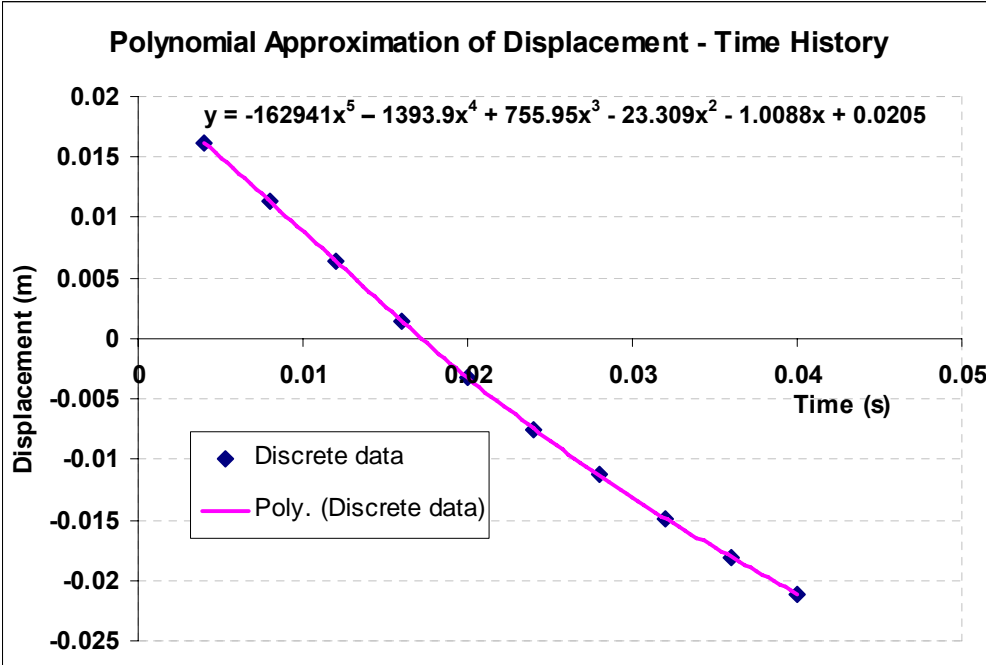


Figure 32: Polynomial approximation of displacement-time history

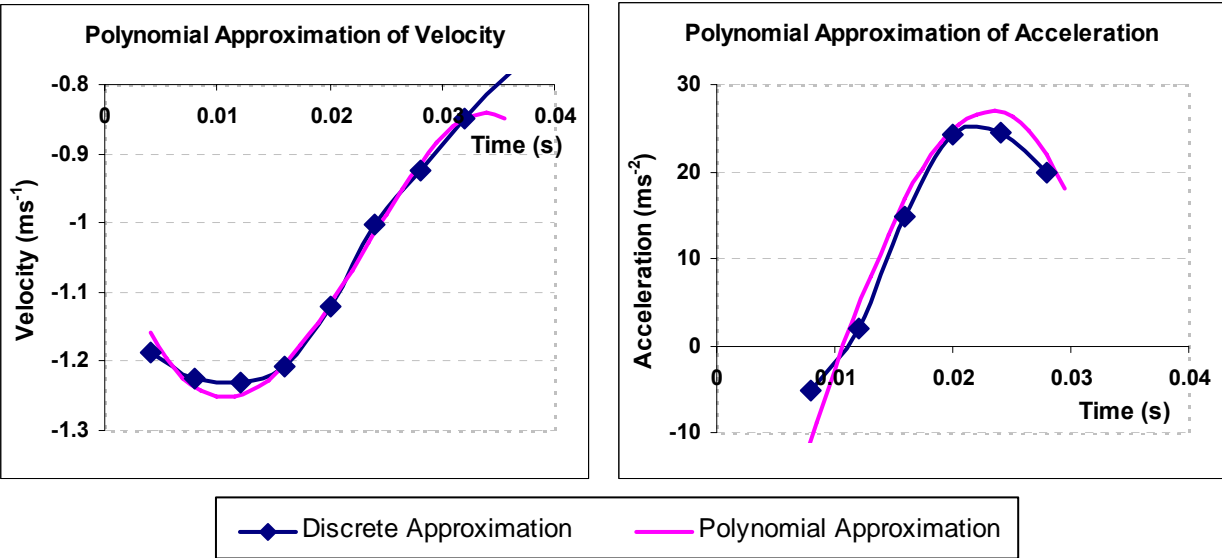


Figure 33: Polynomial approximations of velocity and acceleration-time histories

To further capture the post-impact trough observed in the acceleration profiles, a 6<sup>th</sup>-order polynomial approximation of the displacement-time history was also investigated. Figure 34 suggests that the resulting 4<sup>th</sup>-order polynomial predicted almost identical accelerations as that obtained using a cubic acceleration profile from a 5<sup>th</sup>-order displacement polynomial approximation. As a result, 5<sup>th</sup>-order polynomial approximations of the displacement were used for the rest of the test configurations.

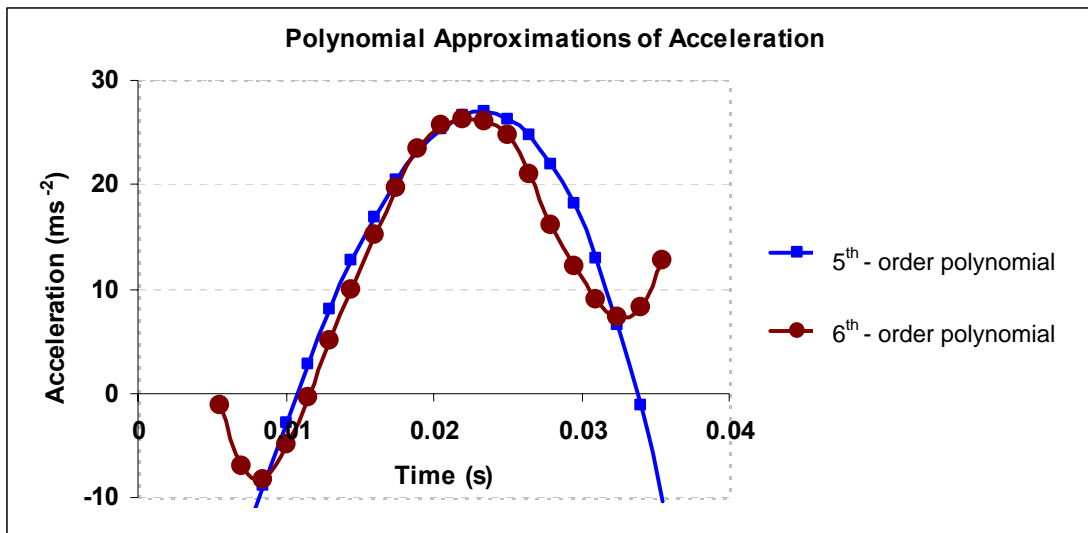


Figure 34: 5<sup>th</sup> and 6<sup>th</sup>-order polynomial approximations of acceleration

### 5.5.3 Selection of a Suitable Time Step

From Figure 31, as the size of the time step is reduced, the variation in the acceleration increases although the displacement-time histories are similar. Since polynomial approximations were to represent the acceleration profiles through the impact zone, polynomial approximations were obtained using the discrete displacement data sets at time steps of 0.002 s and 0.004 s, again for the test configuration with the highest impact accelerations. An example of polynomial approximations from two sets of displacement data at the different time steps are plotted in Figure 35. A comparison of the kinematic predictions allowed for the selection of a suitable time step that could be used to sample the data from all test configurations.

20° Deadrise Angle – Light Impactor – 150 mm Drop

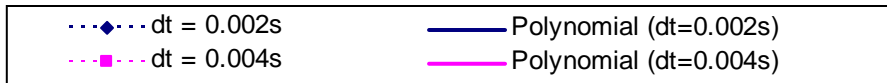
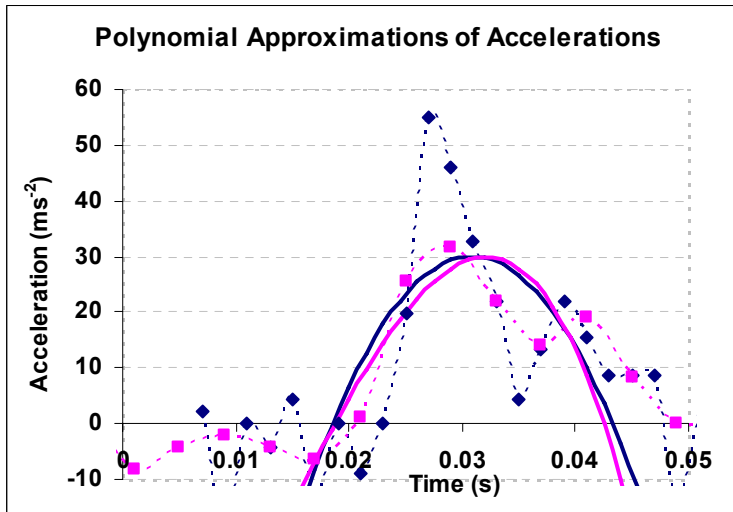
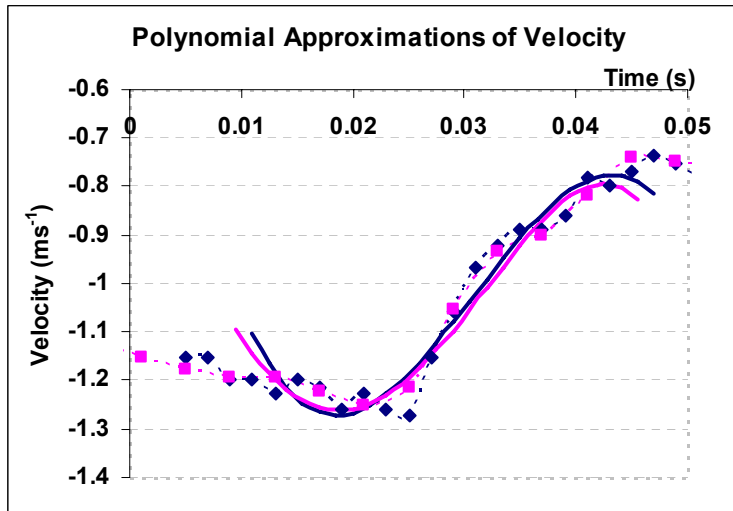
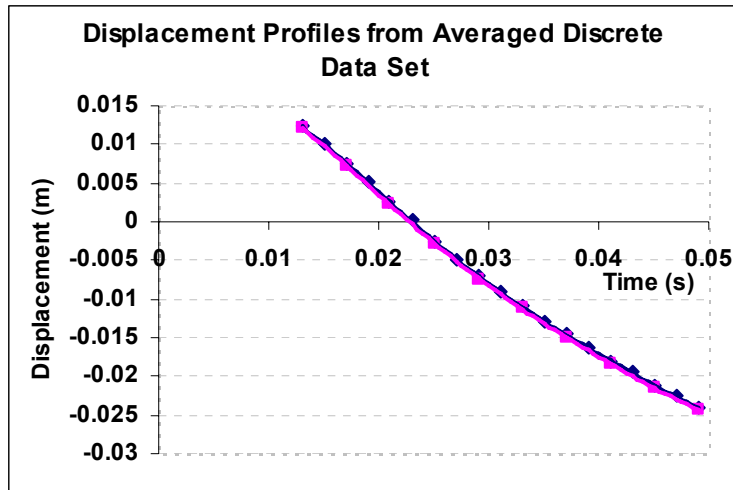
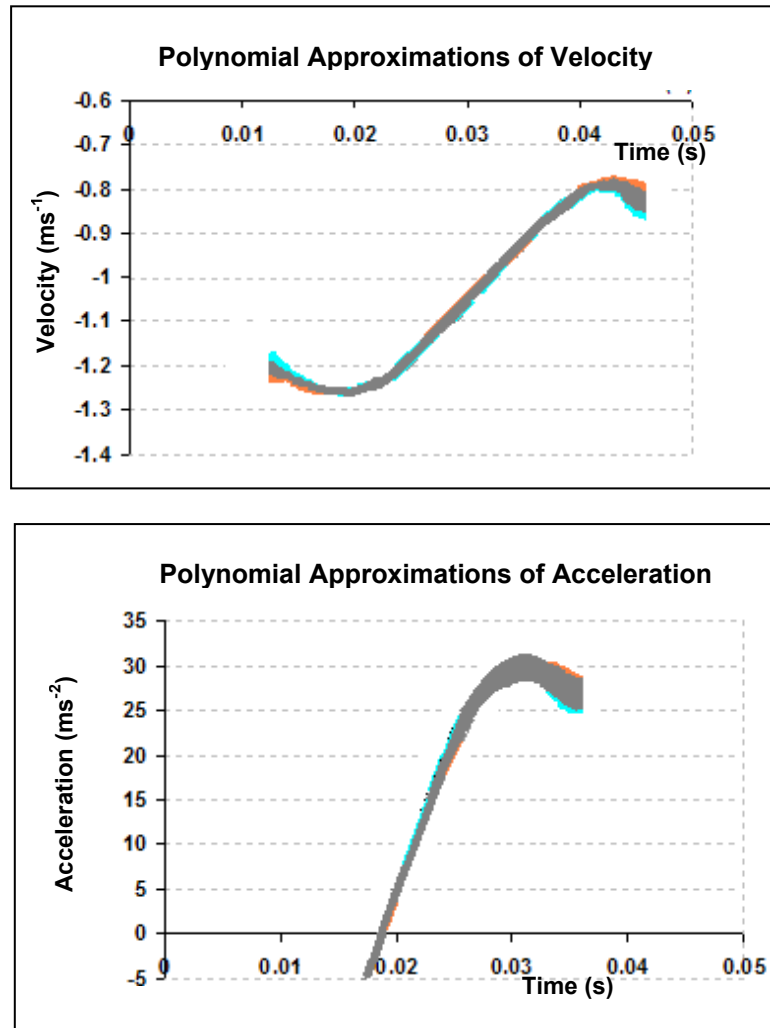


Figure 35: Polynomial approximations of displacement profile for different displacement step size

For each time step, several discrete displacement data sets were obtained in a similar analysis to that presented in section 5.6. Polynomial approximations for each of these data sets were plotted on the same scale, and a range of variation of the predicted kinematic profiles are shown in Figure 36. From a comparison of the plots in Figure 35 and Figure 36, it can be observed that there is not much difference in the polynomial-based derivatives of the displacement-time history when using either a time step of 0.002 s or 0.004 s.



Common range of variation for both  $dt=0.002$  s and  $dt=0.004$  s
  Range of variation for  $dt = 0.002$  s
  Range of variation for  $dt = 0.004$  s

**Figure 36:** Range of variation in the velocity and acceleration profiles due to different time intervals between displacement measurements

Therefore, it was acceptable to use a time step of 0.004 s to define the displacement data set for which the 5<sup>th</sup>-order polynomial can be obtained. Considering there were 35 different test configurations with three test runs each, specifying a displacement measurement every two frames is significantly more efficient than manually tracking the point on the wedge at every single frame.



## 5.6 Sensitivity of Results to Displacement Specification

The manual specification of the displacement profile is subject to judgement of the centre of the tracked point. A study was conducted to investigate how much of an influence this would have on the results.

For three different test configurations, one test run for each was selected i.e. only one video for each configuration. Six sets of discrete displacement data were manually obtained for each of the videos. Therefore, the only difference between the six separate sets of data was entirely due to variation in the point selection. The displacement, velocities and accelerations obtained between all six sets were then compared. Each discrete displacement data set was also approximated with a polynomial to see how much the subjective factor in the displacement specification could influence the analytical prediction of the accelerations experienced by the wedge.

### 20° Deadrise Angle – Light Impactor – 150 mm Drop

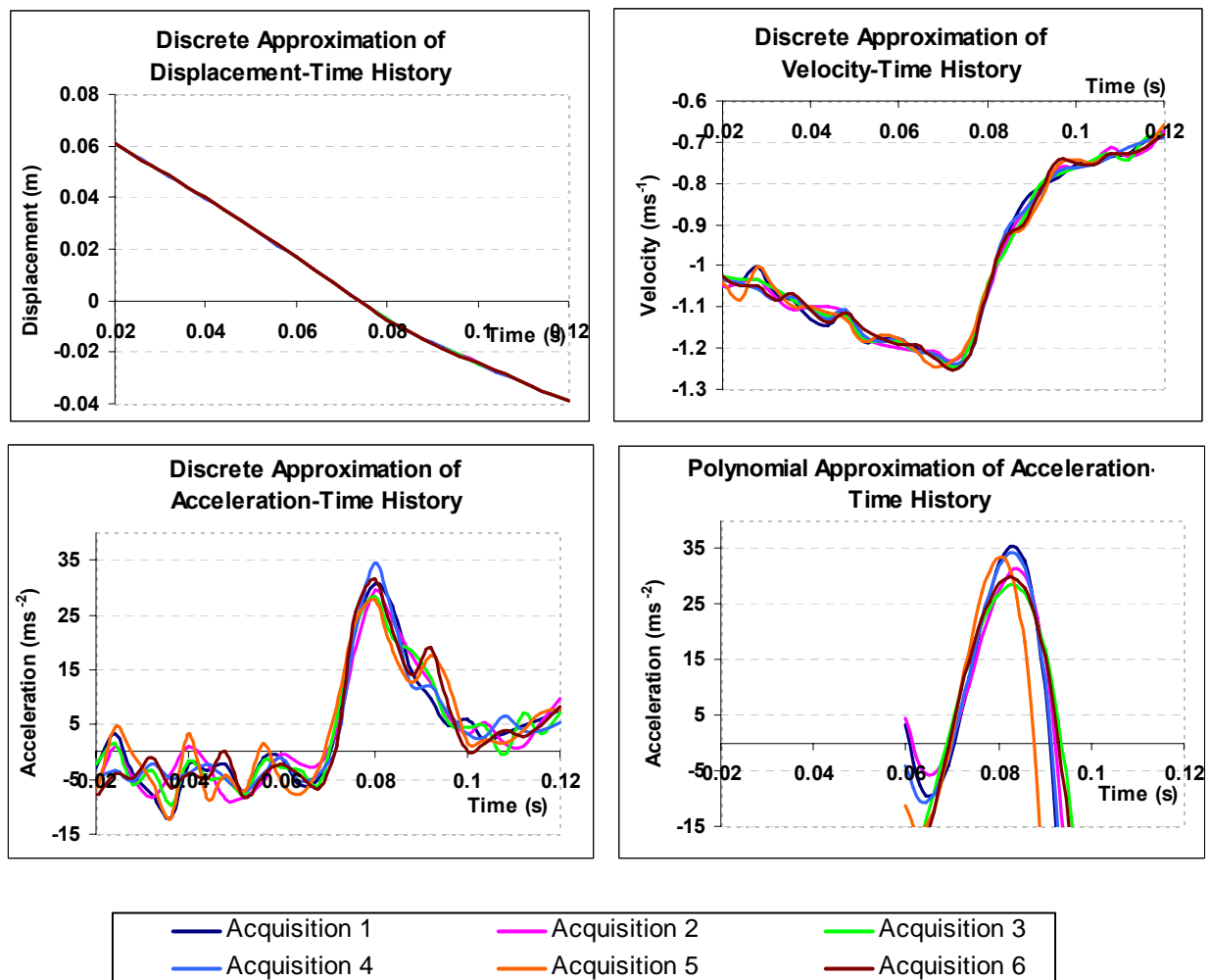
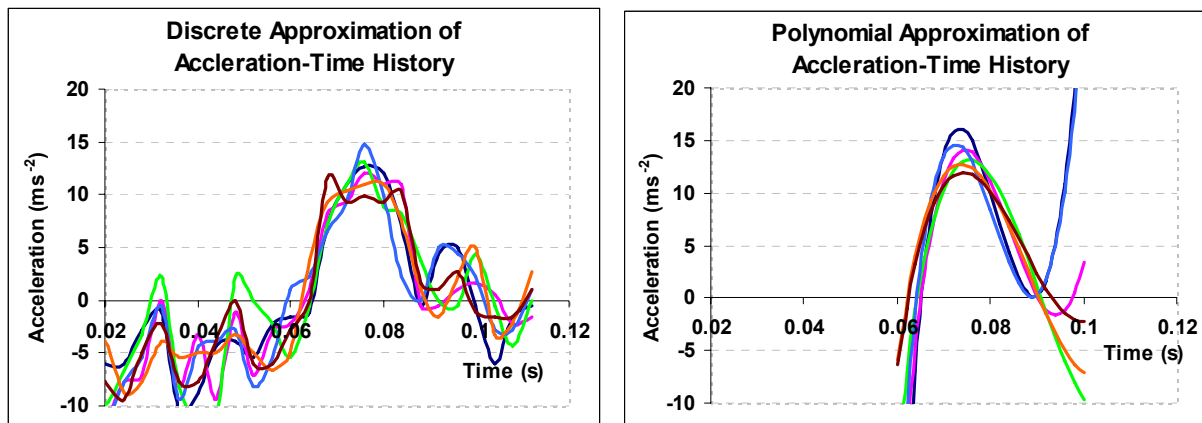


Figure 37: Variation in kinematic-time histories purely due to subjective judgement

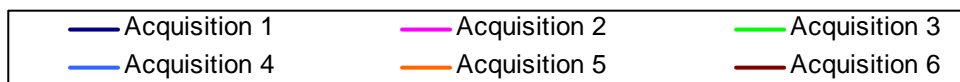
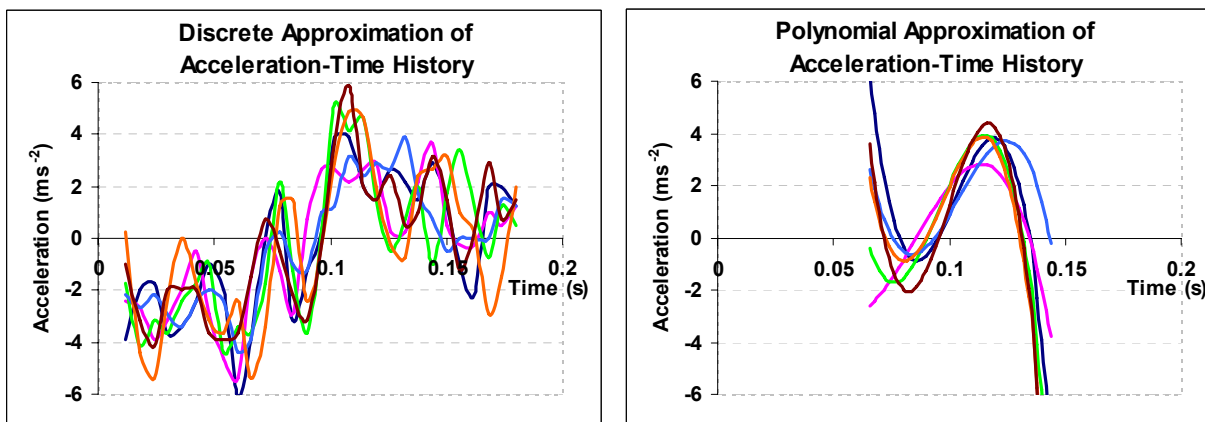
Figure 37 plots results of this investigation for the drop test of the light impactor of 20° deadrise angle dropped from 150 mm. As expected, the displacement profiles were very similar but there are inherent differences in the derived velocity and acceleration profiles. Although a distinct peak acceleration was observed for all the data sets, the peak value predicted using the discrete method varied by  $6.55 \text{ ms}^{-2}$  within the six data sets, which corresponds to an approximate variation of 19% of the largest acceleration prediction.

The same analysis was conducted for two more test configurations: the light impactors of 20° and 40° deadrise angle dropped from 50 mm. Variations in the acceleration profiles for these tests are plotted in Figure 38.

### 20° Deadrise Angle – Light Impactor – 50 mm Drop



### 40° Deadrise Angle – Light Impactor – 50 mm Drop



**Figure 38:** Variation in acceleration-time histories purely due to subjective judgement

The range of variation of the peak acceleration predictions within each of the discrete approach and polynomial approximation have been quantified and summarised in Table 4.

Test Configuration	Discrete Approximation		Polynomial Approximation	
	Variation in Peak Acceleration	% Variation of Peak Acceleration	Variation in Peak Acceleration	% Variation of Peak Acceleration
20° – Light Impactor 150 mm drop	6.55 ms <sup>-2</sup>	19 %	6.91 ms <sup>-2</sup>	19%
20° – Light Impactor 50 mm drop	3.84 ms <sup>-2</sup>	25 %	4.02 ms <sup>-2</sup>	25%
40° – Light Impactor 50 mm drop	2.92 ms <sup>-2</sup>	50%	1.55 ms <sup>-2</sup>	35%

**Table 4:** Variation in peak accelerations due to operator error

The above test configurations were selected for this analysis as the first case involved the highest impact energy and should experience the highest deceleration upon impact, whereas the latter two configurations were of the lowest impact energy tested. In particular, the 40° wedge should result in the least deceleration due to its rather penetrating effect into the water than that experienced by the ‘flatter’ 20° wedge.

The results showed that the accelerations were largely influenced by subjective error and there was the likelihood of significant variations in the prediction of the peak acceleration values, and hence forces, experienced by the wedge. Similar ranges of disparities were observed for both the discrete and polynomial approaches. The extent of fluctuation in the acceleration profiles became more evident as the changes in the velocity through the impact phase became less drastic and severe decelerations were not experienced.


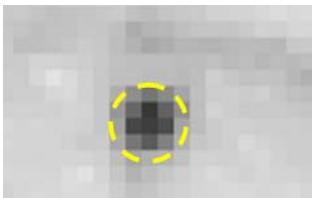
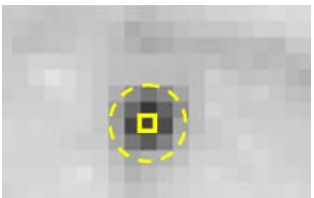

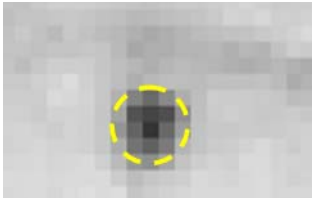
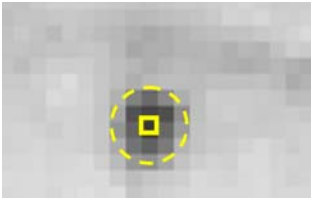
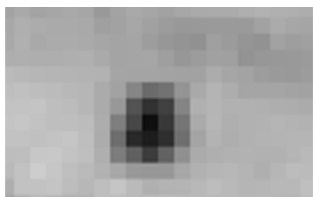
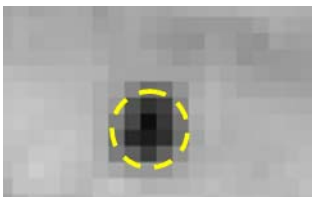
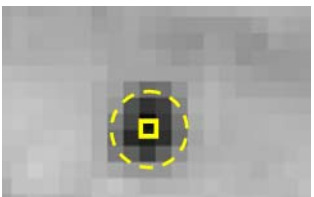
The trend demonstrated through this analysis casts doubt on the accuracy of the peak force predictions that were used for correlation studies of the SPH models. It is clear that precise predictions of the impact forces could not be obtained with the demonstrated data-processing technique and data collected, and several improvements need to be made to the approach. These have been discussed in section Chapter 8. In short, only general trends could be deduced from the test data.

Despite this, the experimental results still provided a platform for qualitative validation and an approximate quantitative comparison for the numerical models. Further deductions on the occurrences observed in the experimental tests, in terms of trends and peak forces observed, could be supplemented by the results of accurate numerical models.

### 5.6.1 Selection of Centre of Tracking Point

As highlighted earlier, the manual specification of displacement points greatly affected the acceleration estimations. In theory, accurate specification of the location of the points would tend to give more consistent approximations for the acceleration.

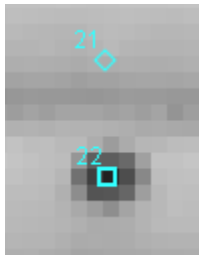
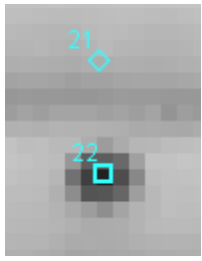
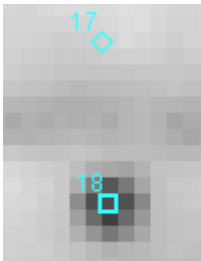

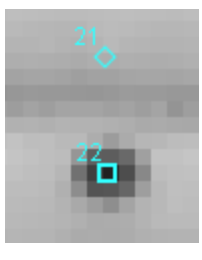
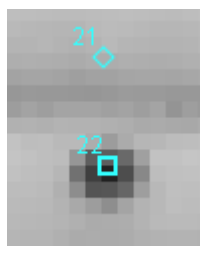
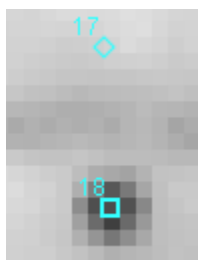

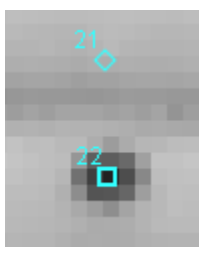
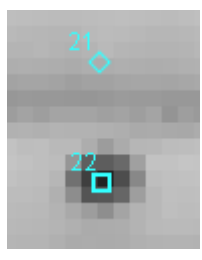
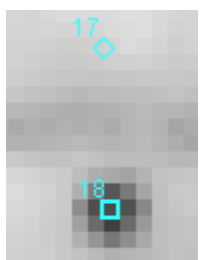

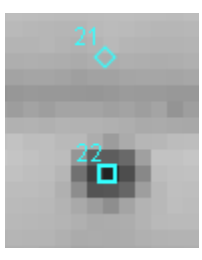
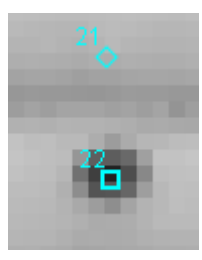
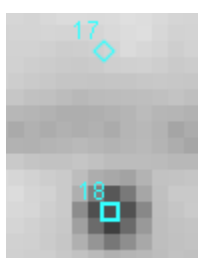

The reason for the large fluctuation in the acceleration predictions was due to the difficulty in determining the exact centre of tracking point that was consistent in progressive frames. One explanation for this variation was the variability in the shadows cast as the wedge dropped with reference to a fixed source of light. This is depicted in the image sequence in Table 5 of the same point.

Time (s)	Original Image	Perceived Boundary	Perceived Centre
0.060			
0.068			
0.084			

**Table 5:** Perception of the centre of tracking points

From Table 5, it is clear that the darkest spot within the image of the tracking point was not necessarily what would be perceived as the centre of the image. Furthermore, once the wedge impacted the water and a thin film of water was present between the wedge-face and trough window, the image became darker due to refraction of the light through this film of water. Depending on the flow field of the water within this film, the image of the tracking point was further distorted thus compounding the difficulty in selecting the exact same centre of the point in progressive frames.

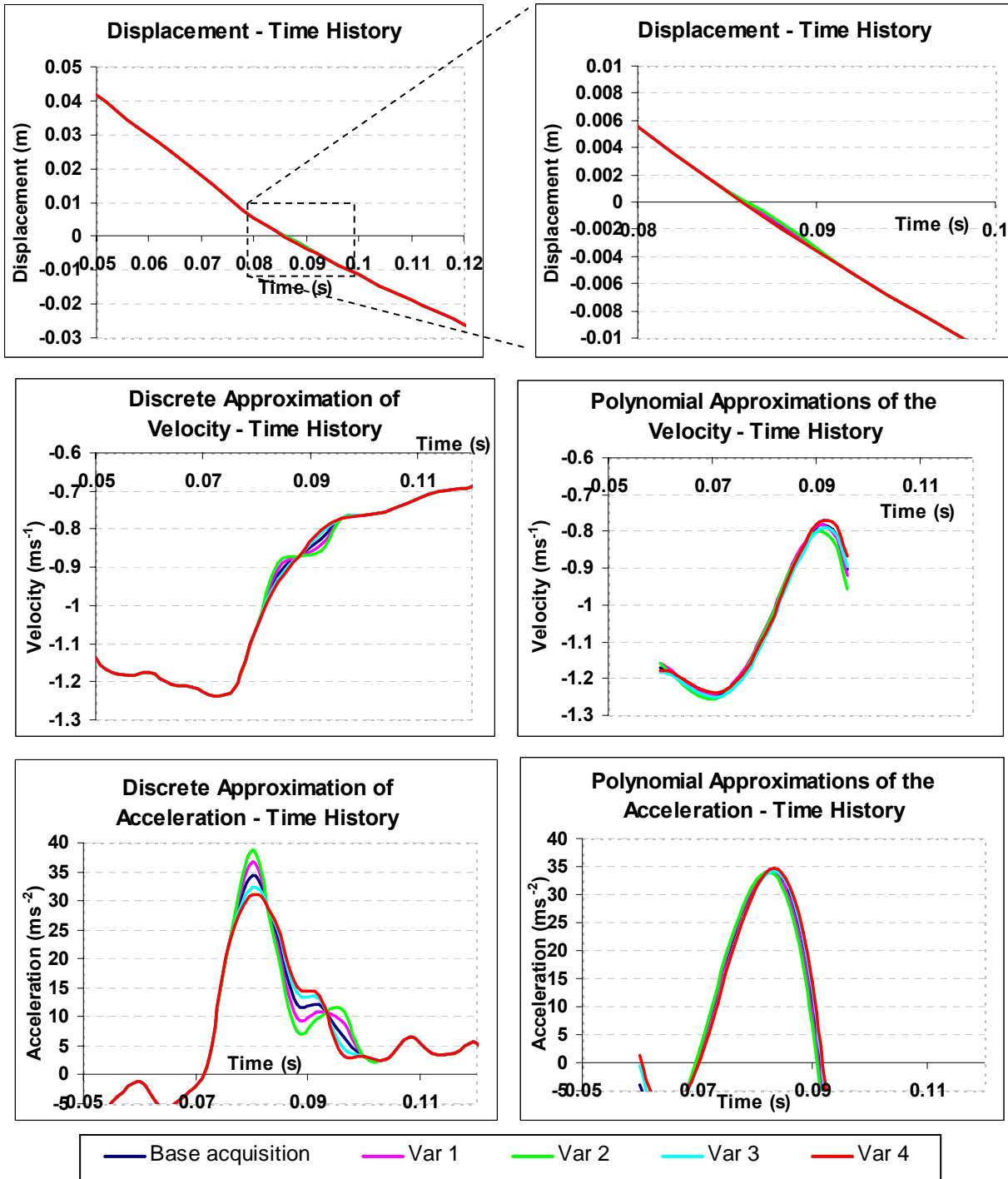
An analysis was conducted, which demonstrated how small variations in the manual point specification could result in measurable fluctuations in the wedge’s acceleration profile. A particular displacement-time history data set was taken, labelled as ‘Base acquisition’. Within this data set, the displacement specification of the centre of a point was varied slightly to what could be plausible selections of the centre based on the user’s judgement. The changes to the specification of point 21 for the highest deceleration case of the light impactor of 20° deadrise angle dropped from 150 mm are given in the left columns of Table 6. The difference in the new point location from the original has been provided.

	Single Point Variation <i>Point ID: 21</i>			Two Point Variation <i>Point ID: 18</i>		
	Base Acquisition	New Position	Distance Moved (mm)	Base Acquisition	New Position	Distance Moved (mm)
Var 1			0.122			0.183
Var 2			0.245			0.245
Var 3			-0.122			-0.122
Var 4			-0.183			-0.245

**Table 6:** Variations in point tracking at a single and two points

Figure 39 plots the displacement and acceleration profiles as a result of the variation of the single point 21 as prescribed above.

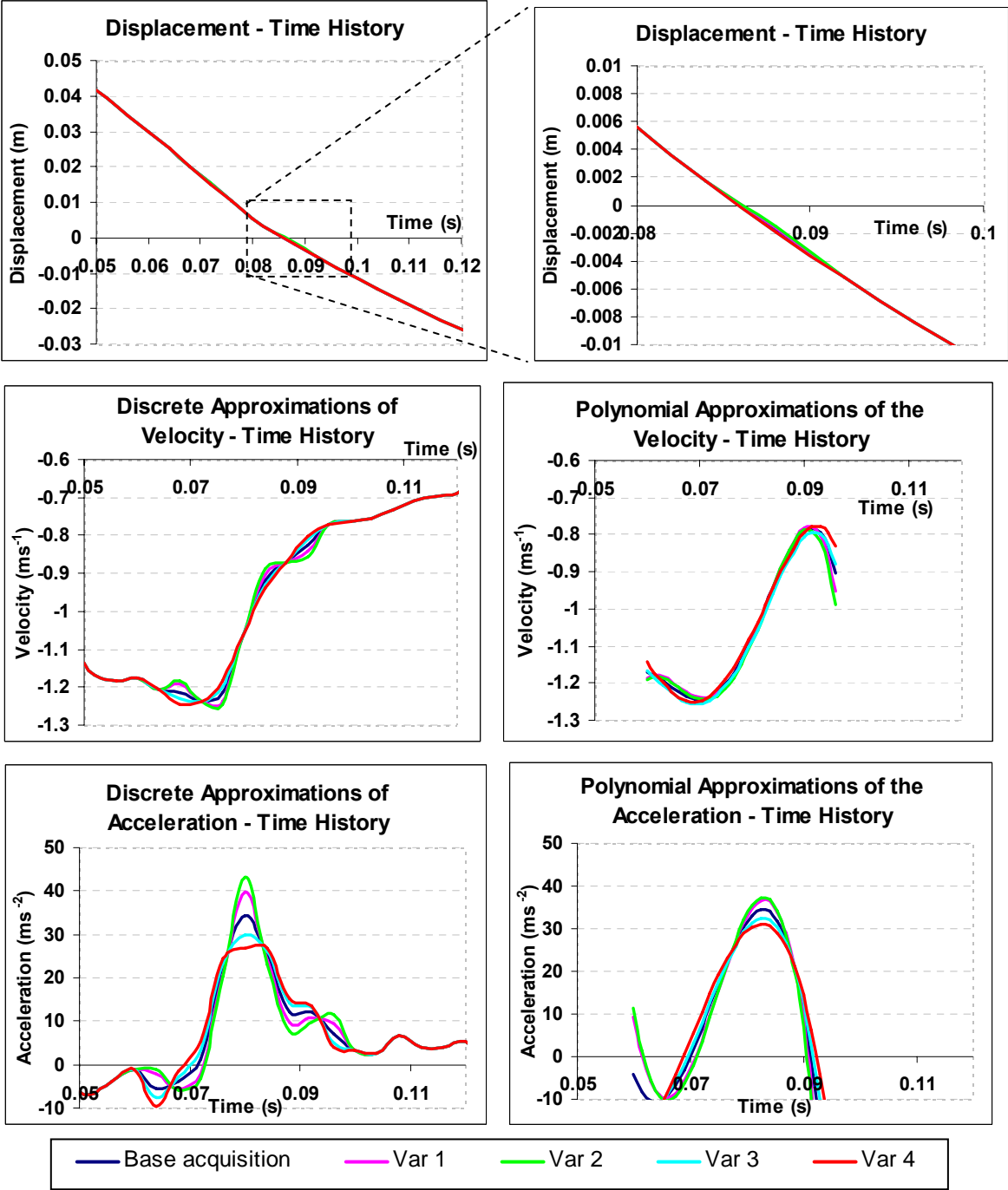
**20 Deadrise Angle – Light Impactor – 150 mm Drop**  
**Variation of Single Data Point (*Point 21*)**



**Figure 39:** Effect of a variation of a single point in the displacement data set

The point variation was extended to another point, namely point 18, within the displacement data set. This was in addition to the original variations of point 21 as outlined in Table 6. Figure 40 plots the trends observed. Table 7 provides a quantitative summary of the disparities observed in Figure 39 and Figure 40.

**20 Deadrise Angle – Light Impactor – 150 mm Drop  
Variation of Two Data Points (Point 21 and Point 18)**



**Figure 40:** Effect of a variation of two points within the displacement data set

The percentage variations calculated in Table 7 were obtained from the acceleration values at the same time-instant when the peak acceleration was expected, for the data sets defined by the point variations Var 2 and Var 4. The difference between the largest and smallest values were taken as a percentage of the largest value.

Test Configuration	% Variation in Acceleration			
	Single Point Variation		Two Point Variation	
	Discrete Approx.	Polynomial Approx.	Discrete Approx.	Polynomial Approx.
20° Deadrise Angle Light Impactor Drop – 150 mm	20%	1.5%	38%	16.4%
20° Deadrise Angle Light Impactor Drop – 50 mm	34%	16.5%	65%	16.5%
40° Deadrise Angle Light Impactor Drop – 50 mm	Difficult to discern	15.6%	Difficult to discern	14.0%

**Table 7:** Variation in acceleration as a percentage of the highest acceleration

The same investigation as described above was conducted for the cases of the light impactors with 20° and 40° deadrise angle from a drop height of 50 mm. The variations observed in the peak accelerations can be compared in Figure 41 and Figure 42. For the case of the light 40° wedge dropped from 50 mm, even though the acceleration profile changed significantly using the discrete approach, the polynomial predictions of the peak acceleration varied within a smaller range.

This analysis indicated the high sensitivity of the derived accelerations to the manual point specification process. However, when considering the polynomial approximations, slight deviations of one or two points within the entire data set did not correspond to peak acceleration differences of the scale observed through the discrete approach.

Therefore, in addition to providing a smoothed and more realistic representation of the impact event, the polynomial approximations provided a more consistent prediction of the acceleration-time history than a discrete approach with different data sets. That said, however, for the highest deceleration case, a variation of 16.4% was observed for the polynomial prediction with two points varied as compared to only 1.5% with a single point varied.



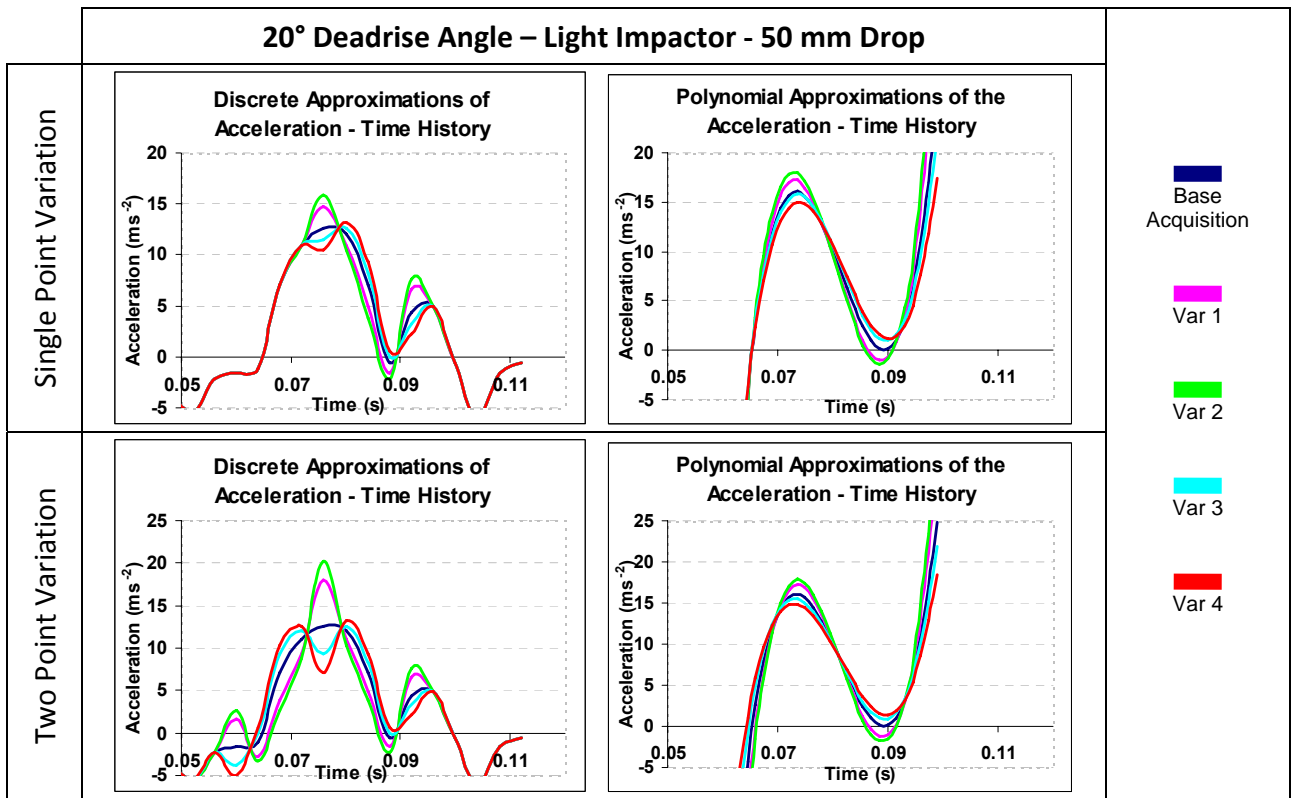


Figure 41: Variation in the acceleration-time histories for 20° wedge

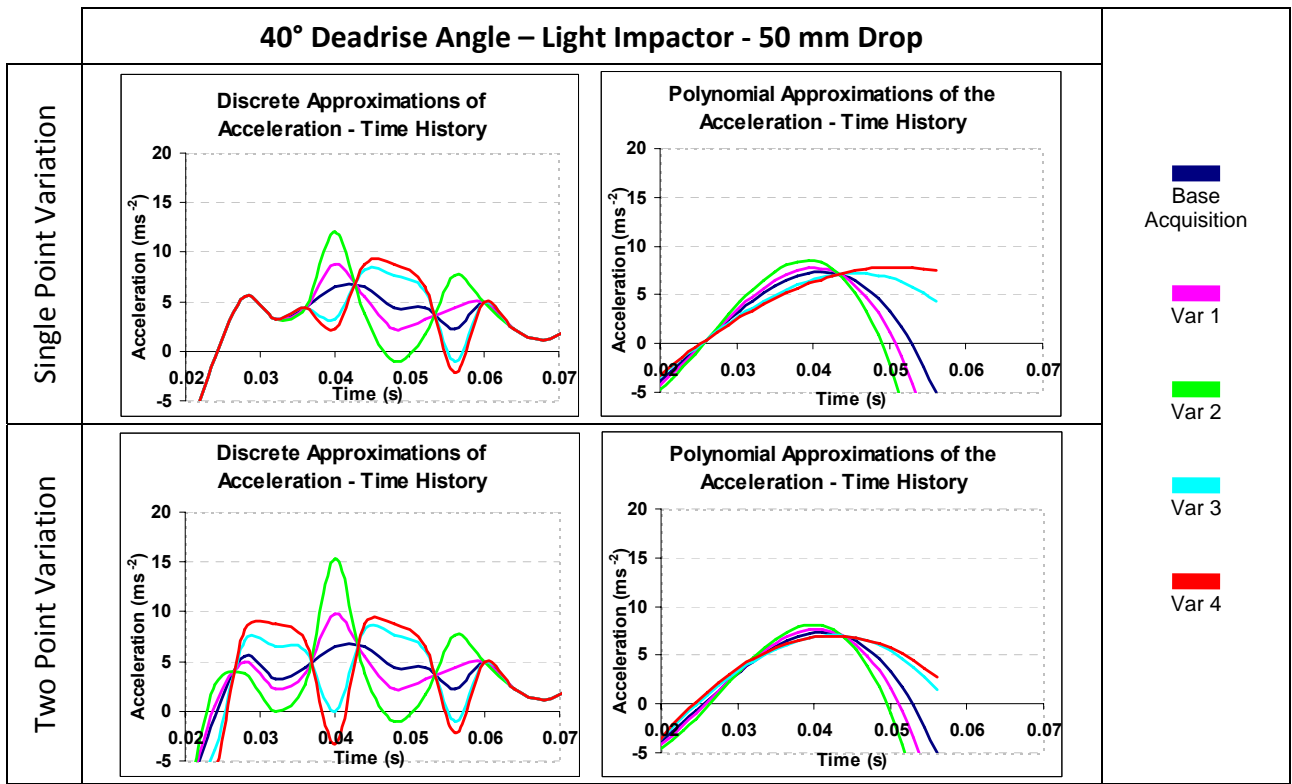


Figure 42: Variation in the acceleration-time histories for 40° wedge

### 5.6.2 Sub-Pixel Enhancement of Video

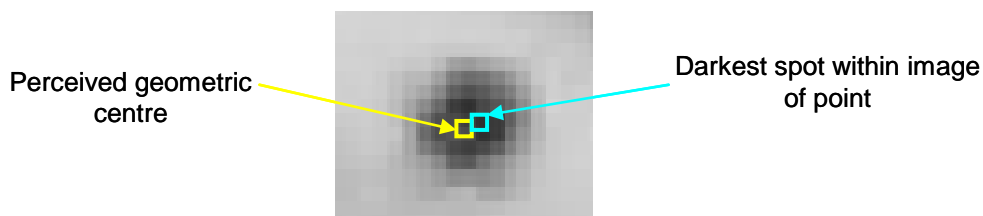
The previous section describes the difficulty and errors induced in the specification of the centre of the tracking points on the wedge. To assist in better defining the centre of these points being tracked, sub-pixel enhancement was performed with Video Enhancer<sup>®</sup> (Dee Mon 2009), a software in which the resolution of the images obtained is increased using mathematical algorithms incorporating information both from contrast scales as well as sequential images from a video.



**Figure 43:** Sub-pixel enhancement of video

Figure 43 illustrates the effect of sub-pixel enhancement using the raw image data. The image file from the camera was of 512 pixels  $\times$  512 pixels resolution which was enhanced two-fold to a resolution of 1024 pixels  $\times$  1024 pixels. Despite the increased resolution, the centre of the point was not necessarily clarified, and in many instances the darker regions tended to be identified away from what was the true centre of the point.

This particularly becomes a problem if image processing algorithms, for example within the MATLAB<sup>®</sup> Image Processing Toolbox (MathWorks 2009), are used to automate the specification of the centre of the point. In this case, the algorithms would select the darkest spot within a specified area to represent the centre of the point, which is different from the true centre. Using the 1024 pixel  $\times$  1024 pixel image, this is depicted in Figure 44.



**Figure 44:** Possible centre of point based on the darkest region of the point's image

This variability in the contrast gradients in the images of the points could have been due to a number of factors associated with the original video. The presence of a film of water between the wedge face and glass wall of the trough, together with lighting effects and shadows resulted

in images where the darkest region within the tracking points was not at what was perceived to be the geometric centre.

In summary, the fundamental problem is explained by the fact that the maximum resolution of the camera, with the desired frame rate and distance from the camera, required that the points marked on the wedge face were solid and large enough to be captured by the camera. If a higher resolution camera was available, then the points marked would have a better definition of the contour of the points as compared to the current 512 pixel  $\times$  512 pixel images. The resulting images of the points would have been more consistent in their definition, and therefore the range of operator error when specifying the displacements would be reduced. This is discussed in more detail in section 8.1.

## 5.7 Friction in Guiding Track

There was a significant amount of friction in the vertical guiding track and this needed to be quantified. This was done through an analysis of freefall drop tests of the wedges of different masses without impact onto water. The objective of these tests was to determine the friction force present in the guiding track. A greater freefall acceleration was expected as the mass of impactor became larger, since the increased inertia of the heavier impactors would more easily overcome the friction present within the bearings of the guiding track.

The photographic technique was employed to track the wedges' freefall motion and consequently determine their freefall acceleration,  $a_f$ . As can be seen from Figure 45, the discrete method predicted a roughly constant acceleration through the range of extension of the track that was required in the experiments.

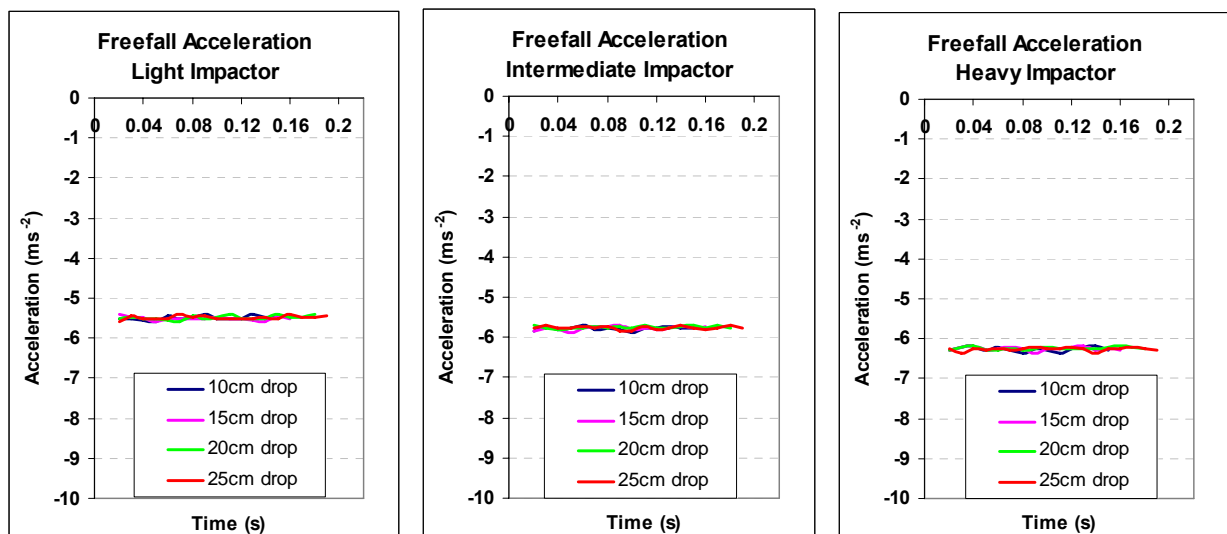


Figure 45: Freefall accelerations of wedges of varied masses

As per the hypothesis, as the mass of the impactor increased, so did its freefall acceleration. Constant acceleration was observed in the case of all three masses, and hence the average freefall acceleration of all drop heights was adopted for each of the mass categories. With reference to Figure 46 and using the simple equation of motion (28) below, the friction force within the guiding track was quantified for the different wedge masses.

$$\begin{aligned}
 (\uparrow +) \sum F &= Ma \\
 F_{friction} - Mg &= Ma_f \\
 \therefore F_{friction} &= M(a_f + g)
 \end{aligned}
 \tag{28}$$

Table 8 summarises the acceleration and friction force associated with the three different impactor masses, from which the impact velocities were estimated.

Mass of Impactor (kg)	Freefall Acceleration (downwards)	Friction Force in Guiding Track
1.6394	5.474 ms <sup>-2</sup>	7.108 N
1.8519	5.757 ms <sup>-2</sup>	7.506 N
2.0722	6.230 ms <sup>-2</sup>	7.418 N

**Table 8:** Freefall accelerations and frictional forces in the guiding track

## 5.8 Evaluation of Impact Force

The impact force was obtained from the equation of motion of the wedge. The impact force,  $F_{impact}$ , consisted of the following components:

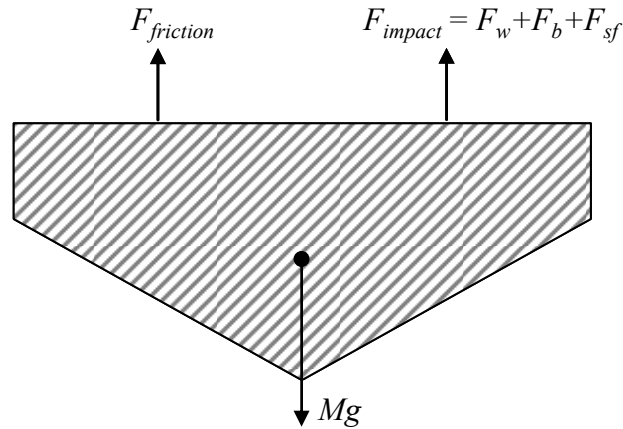
$$F_{impact} = F_w + F_b + F_{sf}$$

where:  $F_w$  - force due to the rate of change of momentum of water

$F_b$  - buoyancy force

$F_{sf}$  - vertical component of skin-friction on the wedge wetted area

Within the impact zone, it was assumed that  $F_b$  and  $F_{sf}$  are negligible compared to the impulsive nature of the force  $F_w$ . The free-body diagram of the wedge during interaction with the water is presented in Figure 46.



**Figure 46:** Free-body diagram of wedge when impacting water

The equation of motion in one-dimension (1D) for the wedge was derived as follows:

$$(\uparrow +) \sum F = Ma$$

$$F_{friction} + F_{impact} - Mg = Ma$$

$$\therefore F_{impact} = M(a + g) + F_{friction}$$

where:  $M$  - mass of the rigid wedge assembly

$g$  - acceleration due to gravity

$a$  - acceleration experienced by the wedge during impact

$F_{friction}$  - friction in the guiding track

## 5.9 Test Results

Due to the sensitivity of the acceleration profiles to subjective displacement specification, accurate force-time histories of the impact could not be interpreted and ascertained with absolute confidence. Recommendations and improvements highlighted in section Chapter 8 need to be incorporated in further tests, with the aim of obtaining more consistency within the results. Despite this limitation, general trends in the impact forces were observed from the wedge drop tests. The force-time histories presented in this section have been normalised with the wedge depth (by dividing the calculated force by the wedge depth of 333 mm) so as to obtain the force per mm along the wedge depth. This facilitates better comparison with the results of the numerical models.

### 5.9.1 Variation in Deadrise Angle

#### 5.9.1.1 Light Impactors

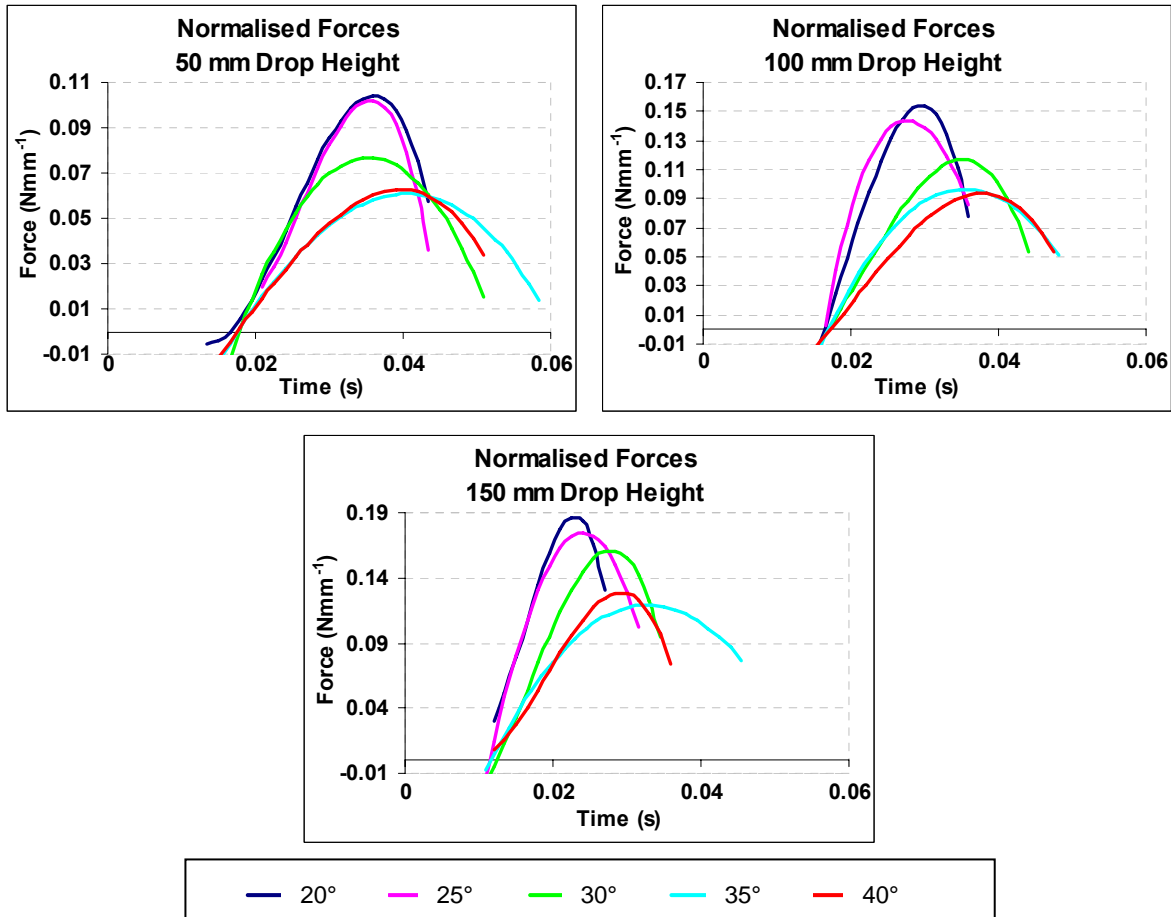


Figure 47: Experimental forces for varying deadrise angles for the light impactors

### 5.9.1.2 Intermediate Impactors

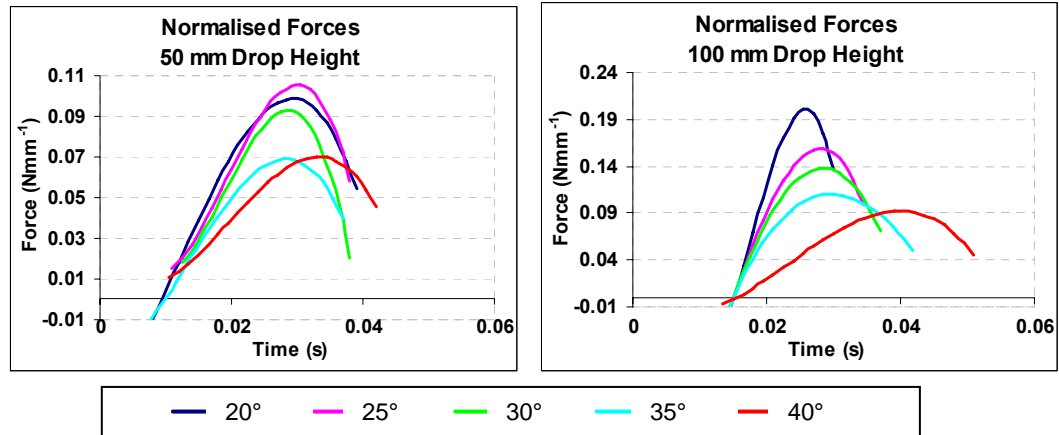


Figure 48: Experimental forces for varying deadrise angles for the intermediate impactors

### 5.9.1.3 Heavy Impactors

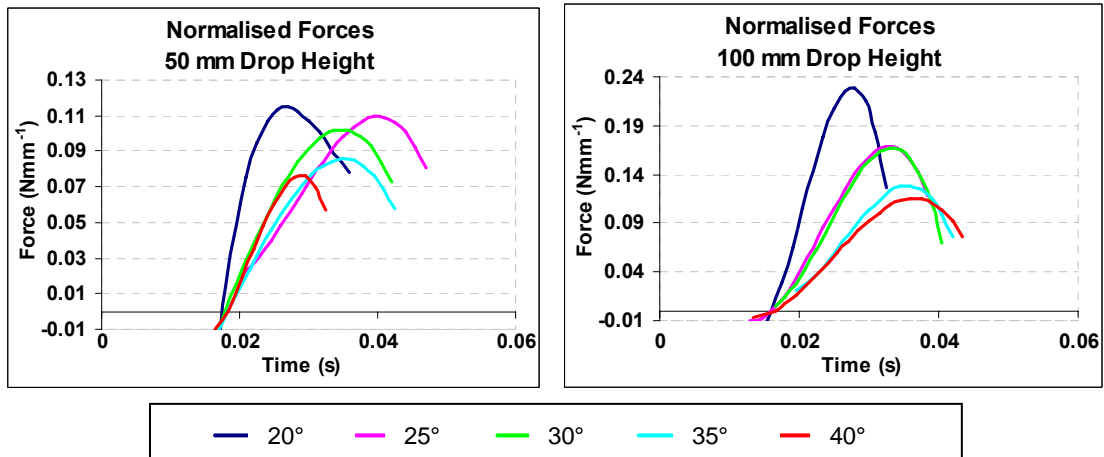


Figure 49: Experimental forces for varying deadrise angles for the heavy impactors

For all the wedge masses, the general observation was a decrease in the peak impact force with increasing deadrise angle. However, in most cases, similar forces were obtained for the 20° and 25° wedges and also 35° and 40° wedge. These trends did not directly agree with the literature. According to Figure 3 and also from a physical standpoint, a distinctly larger force for smaller deadrise angles was expected.

It is very likely that the theoretically defined trends were reflected in the experiments. The sensitivity of the derived accelerations and peak forces with the adopted experimental data processing technique were demonstrated in section 5.6. The indication from the trends plotted in Figure 47, Figure 48 and Figure 49 is that to capture the severe and smaller peak accelerations, a higher resolution and more sensitive data capture and processing technique is required. This is discussed in more detail in section Chapter 8.

A second deduction that was made from the test results was that the ‘impulsive’ nature of the impact decreased with increasing deadrise angle due to a lesser rate of frontal area striking the water surface over the same time period. This was seen through the gentle slope of the acceleration curve for wedges with larger deadrise angles and reflected earlier work done by Pentecote *et al.* (2003b).

### 5.9.2 Variation in Drop Height for the Light Impactors

The variation in drop height has only been shown for the light impactors in Figure 50. As expected, the higher energy impacts corresponding to a higher drop height resulted in larger accelerations due to a larger rate of momentum transfer to the water. This translated into larger impact forces, and wedges of all deadrise angles displayed this trend.

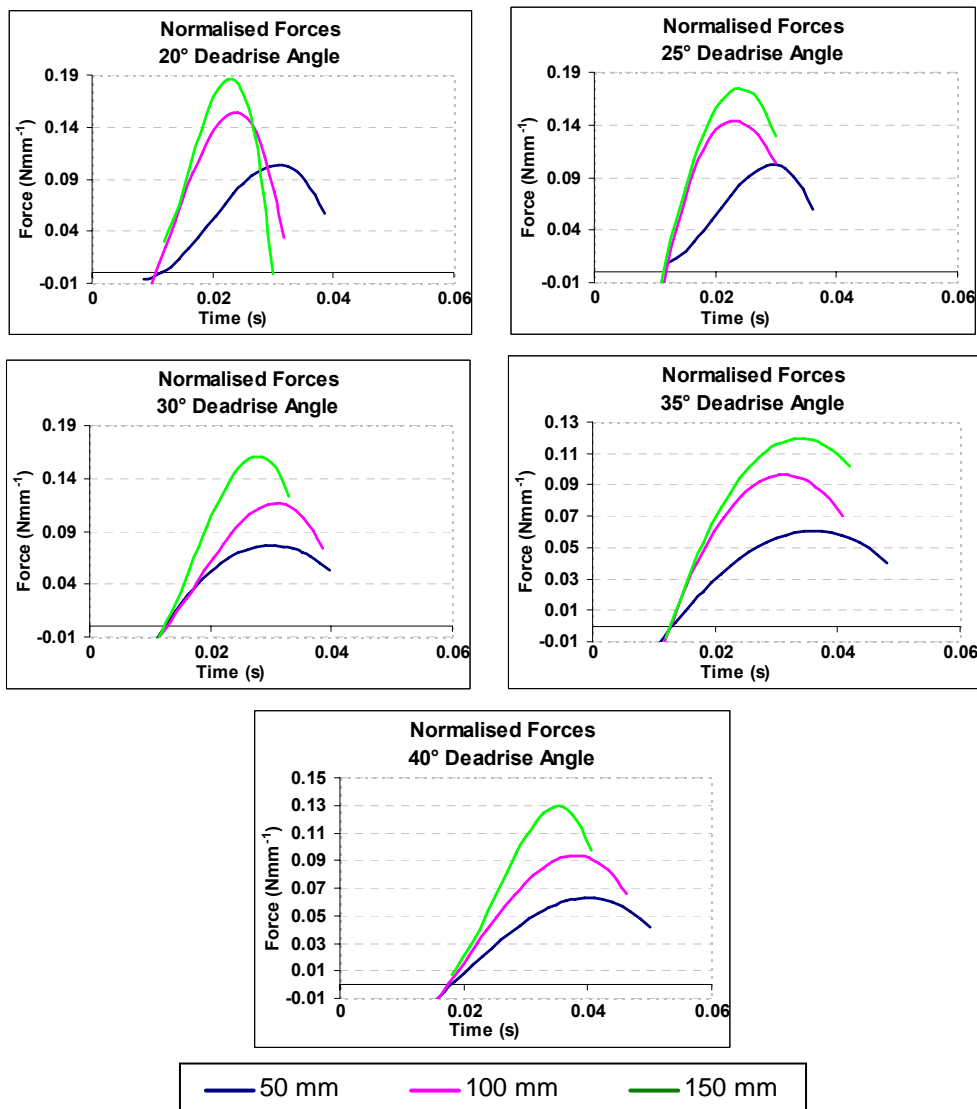


Figure 50: Experimental forces for varying drop heights for the light impactors



### 5.9.3 Variation in Wedge Masses

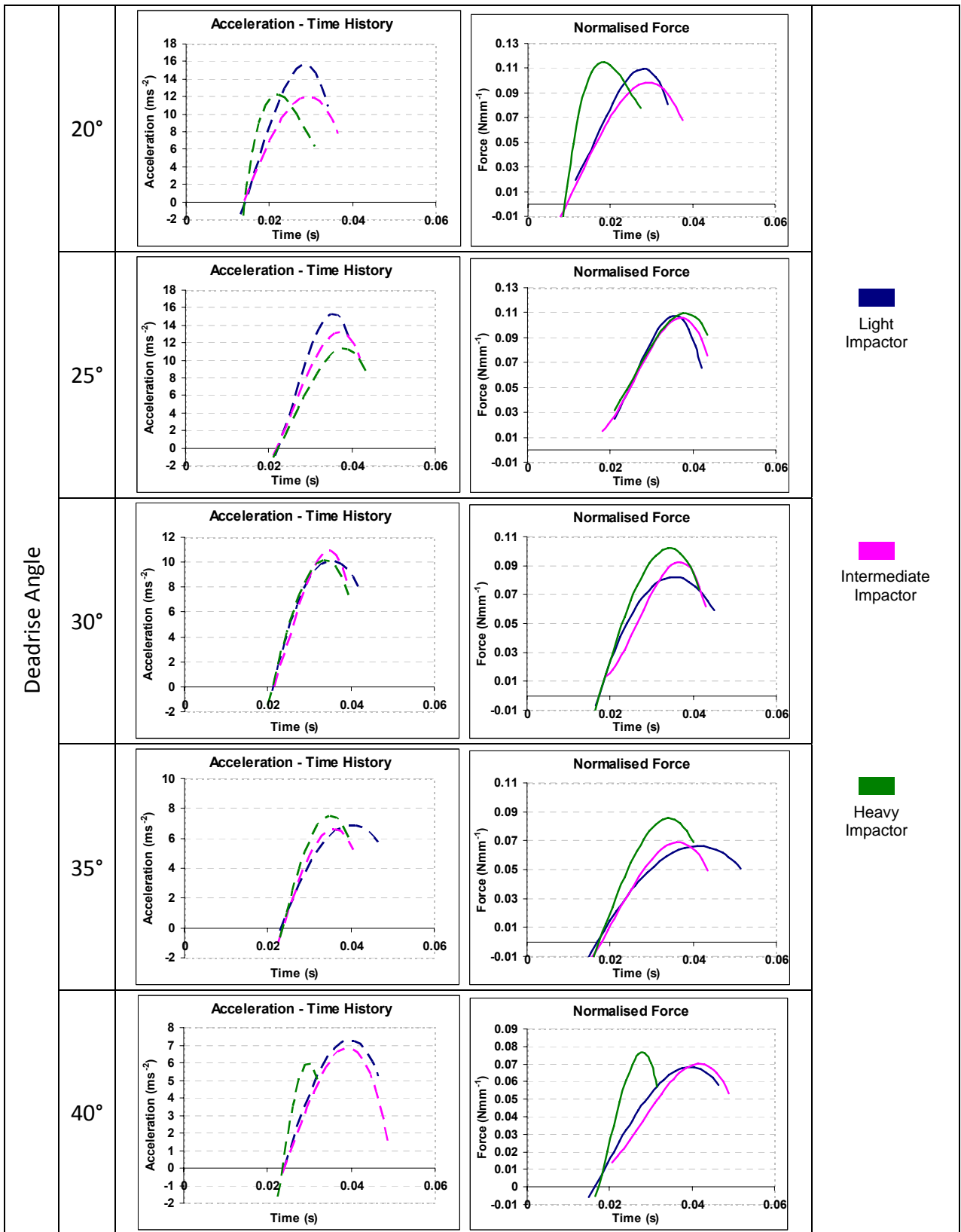


Figure 51: Experimental accelerations and forces for varying wedge masses dropped from 50 mm

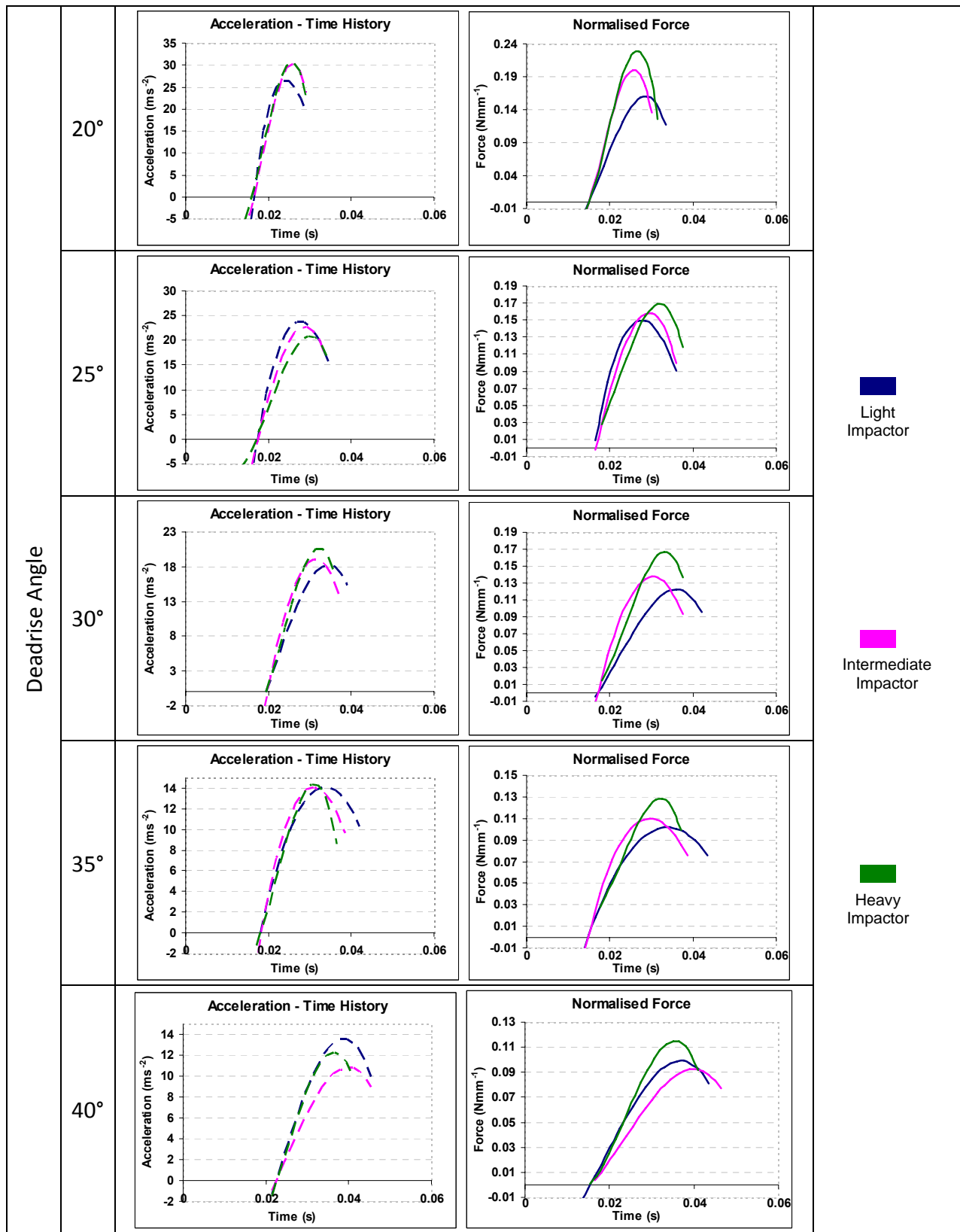


Figure 52: Experimental accelerations and forces for varying wedge masses dropped from 100 mm

The peak accelerations generally fluctuated about a certain value for varying masses of the same deadrise angle. This indicated similar accelerations for impactors of varying mass but with the same deadrise angles. However, the impact force was larger for the higher masses according to Newton's 2<sup>nd</sup> law of motion. This is depicted in the acceleration and force-time histories in Figure 51 and Figure 52. Within the range of masses and impact velocities investigated, the indication was that the acceleration upon impact is determined by the wedge geometry rather than its kinetic energy.

## 5.10 Concluding Remarks

For all the experimental tests conducted, it often remained uncertain as to the exact value to select as the peak acceleration. Despite the improved consistency introduced to the peak acceleration predictions by the polynomial approximations, there was still the possibility of relatively large inherent variations as demonstrated in section 5.6. This made the experimental-numerical validation difficult as it was often unclear on what to use as a benchmark for the quantitative data from the experiment.

The results of the experiment indicated that to use the video analysis technique with sufficient confidence, higher impact velocities are preferred than those generated from a drop height of 50 mm. Clearer and generally distinct acceleration peaks were observed when using the discrete method to obtain acceleration profiles for all drop tests from heights of 100 mm and 150 mm. With higher impact velocities, changes in the impactor velocity immediately after impact are much larger, hence making it clearer to identify peak accelerations experienced by the wedge. On the other hand, it was uncertain as to whether or not the true peak values of the higher deceleration cases were captured, particularly for the 20° and 25° wedges which show similar trends. This can be verified with higher sensitivity data capture methods, for example with the use of accelerometers or higher resolution images preferably with experiments of a larger scale.

Keeping in mind the discussion above, the following points summarise the basic interpretations of the experimental results:

- For 20° and 25° wedges of light and intermediate mass, reasonably clear and distinct peak accelerations were observed for all three drop heights. These wedge profiles with reduced deadrise angles resulted in more of a 'slamming' water entry than for wedges with larger deadrise angles.

- For the 30°, 35° and 40° wedges of light and intermediate mass, there was large variation in the discrete predictions of the peak acceleration, particularly for the 50 mm drop tests. In many cases, no distinct peak could be observed. This often made it difficult to ascertain a reasonable polynomial approximation for the wedge acceleration.
- The discrepancies in the discrete peak predictions were common for wedges of all deadrise angles of the heavy mass from both drop heights of 50 mm and 100 mm.

In summary, application of the video analysis approach to this scale of experiment with the given video resolution resulted in reasonably consistent discrete predictions for an appreciable range of accelerations that are not too large or small. Nevertheless, through the polynomial approximations of the displacement data sets, general trends have been observed which align with the expected behaviour shown through the numerical models in section 6.7 in terms of trends due to variations in deadrise angle, impactor mass and wedge drop height.

# Chapter 6

## NUMERICAL ANALYSIS

The SPH functionality packaged within LS-DYNA® was used to simulate the range of wedge configurations tested in the experimental program. Various parametric studies were conducted to investigate the effect of certain simulation parameters on the results obtained.

All the models used in the numerical analysis were solved with version ls971s of LS-DYNA® installed on a 64-bit Linux workstation. The models were simulated using a single 2.3 Ghz AMD Opteron processor equipped with 4 GB DDR memory.

The simulations were compared to the experimental results and a qualitative and quantitative analysis was conducted as part of the correlation study. From this investigation, deductions were made on the applicability of the SPH technique for water impact, including a discussion of further complexities that could be introduced in further research work. Table 9 provides a summary of the impact conditions of the wedges derived theoretically from the freefall characteristics obtained in section 5.7.

Deadrise Angles (°)	Wedge Mass	Drop height	Freefall Acceleration (ms <sup>-2</sup> )	Impact Velocity (ms <sup>-1</sup> )	Impact Energy (J)
20°	Light Impactor	50 mm	5.474	0.740	<b>0.4489</b>
		100 mm	5.474	1.046	<b>0.8968</b>
150 mm		5.474	1.281	<b>1.3451</b>	
25°	Intermediate Impactor	50 mm	5.757	0.757	<b>0.5306</b>
30°		100 mm	5.757	1.073	<b>1.0661</b>
35°	Heavy Impactor	50 mm	6.230	0.789	<b>0.6450</b>
40°		100 mm	6.230	1.116	<b>1.2904</b>

**Table 9:** Impact characteristics of experimental test configurations

## 6.1 Modelling Approach

Through the experiment, the 2D behaviour of the water upon impact of a symmetrical wedge was observed i.e. the behaviour of the wedge was the same at any location along the depth of the wedge. Due to the consistency of the kinematics of the wedge and water through the depth of the wedge, the entire depth of the wedge was not required to be simulated. A modelling approach using symmetrical planes for the SPH was used to represent the 2D flow behaviour in the 3D domain. The numerical modelling and experimental results could then be compared by normalising the results with the wedge depth, thus rendering them independent of depth.

## 6.2 Determination of Basic Model Parameters

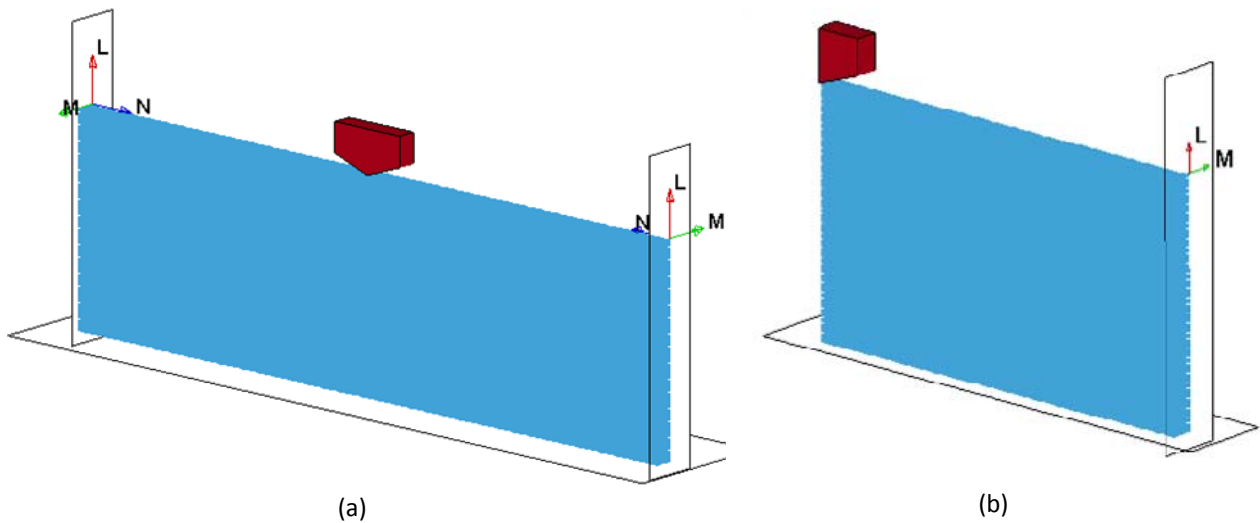
This section outlines the steps undertaken to determine various parameters of the SPH model that constituted a base model with characteristics that were used to simulate all the experimental test configurations.

This base model was derived through the analyses of the following parameters:

- Water trough size variation
- Lagrangian mesh for the water in regions of less deformation
- Wedge depth variation to ensure 2D behaviour
- Particle density variation
- Smoothing length of the discrete SPH particles
- Solid element formulations for the Lagrangian mesh
- Particle approximation theory
- Application of gravity loads

### 6.2.1 Initial SPH Model

A preliminary model was created with a relatively coarse mesh of a full-size water trough modelled entirely with SPH particles. Symmetry planes were used on the front and rear cross-section face for a wedge of 20 mm depth to simulate the 2D behaviour representative of the experiment. The model is shown in Figure 53(a).



**Figure 53:** Water domain represented entirely by SPH formulation

The initial parameters for this model are defined in Table 10.

Wedge depth	20 mm
Particle spacing	4 mm
Particle mass	$6.388 \times 10^{-5}$ kg
Impact velocity	$1.281 \text{ ms}^{-1}$
Water trough size	720 mm $\times$ 208 mm

**Table 10:** Basic parameters of initial SPH model

In this preliminary model, no gravity loads were simulated. The motion of the wedge was constrained in the vertical direction and the walls of the water trough were represented using rigid walls.

The computational time to solve a model increased significantly with an increasing number of particles. The impact scenario was symmetric about the plane of symmetry of the wedge, and this was therefore incorporated into the model as shown in Figure 53(b). Figure 54 demonstrates that the half-width model correctly simulated the impact event as represented by the full-size model, both qualitatively and quantitatively. The half-width model resulted in a 55% reduction in computational time of the 2 hours and 37 minutes taken to solve the full-size model. This would translate into larger savings in computational time for models with more particles within the given SPH trough volume.

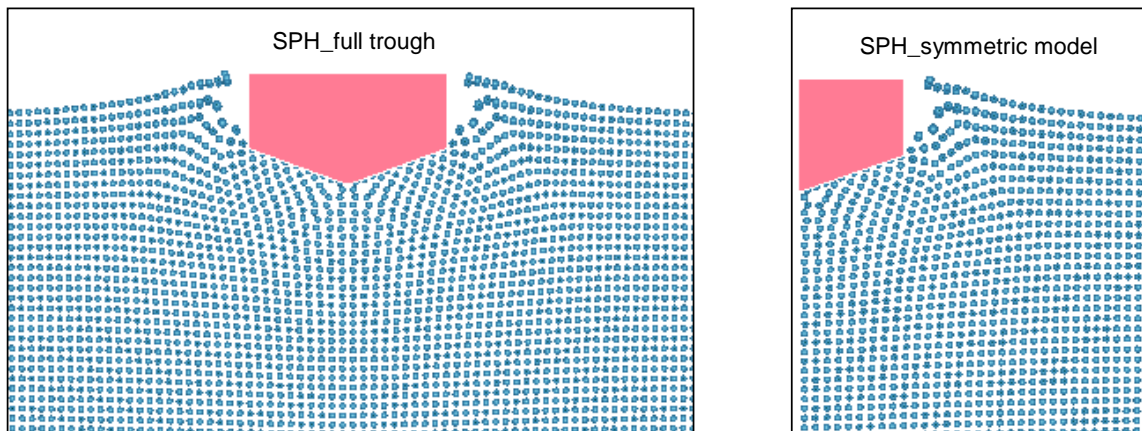
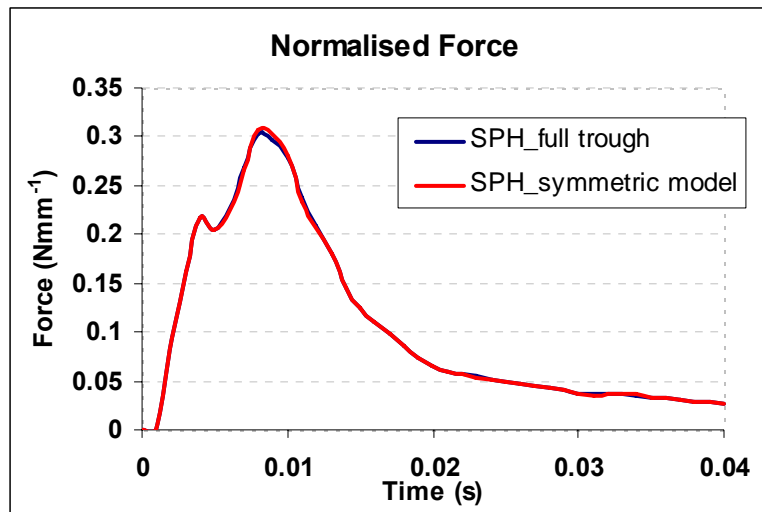


Figure 54: Evaluation of symmetric modelling approach for purely SPH model.

### 6.2.2 Combined SPH and Lagrangian Approach

The SPH technique is suited to modelling high deformation problems which are a limitation of the more computationally efficient Lagrangian approach. During the water impact event, the region of fluid in the immediate vicinity of the wedge underwent significant deformation, which was captured well by the SPH formulation.

However, in the far field region away from the wedge, the water domain did not undergo significant deformation. To make the model more efficient, a Lagrangian mesh was used to model the fluid away from the wedge where there would not be a significant deformation during the impact event (from here on this model is referred to as the SPH+LAG model). A symmetric SPH+LAG model about the wedge centreline was also created and these models are shown in Figure 55 with a comparison of their force and qualitative predictions shown in Figure 56.



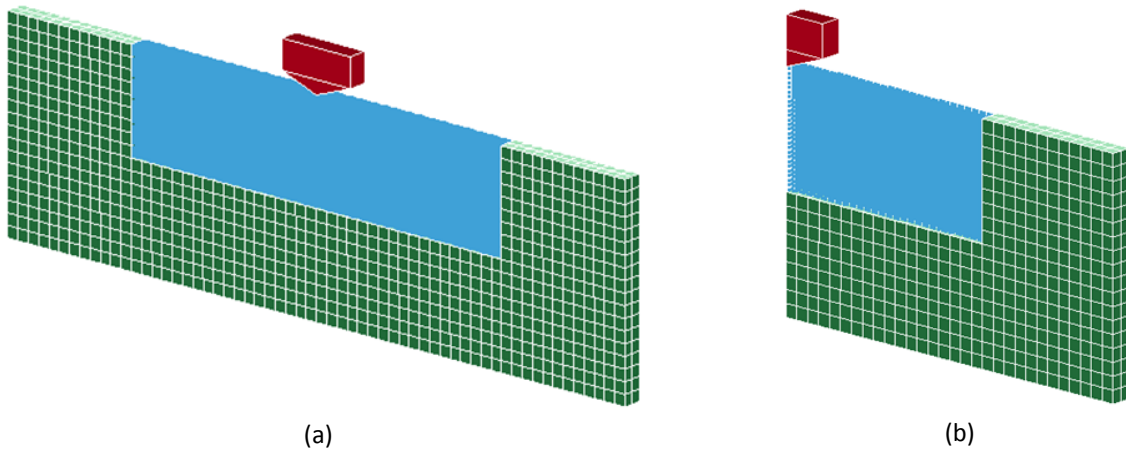


Figure 55: Water domain represented using both SPH and Lagrangian description

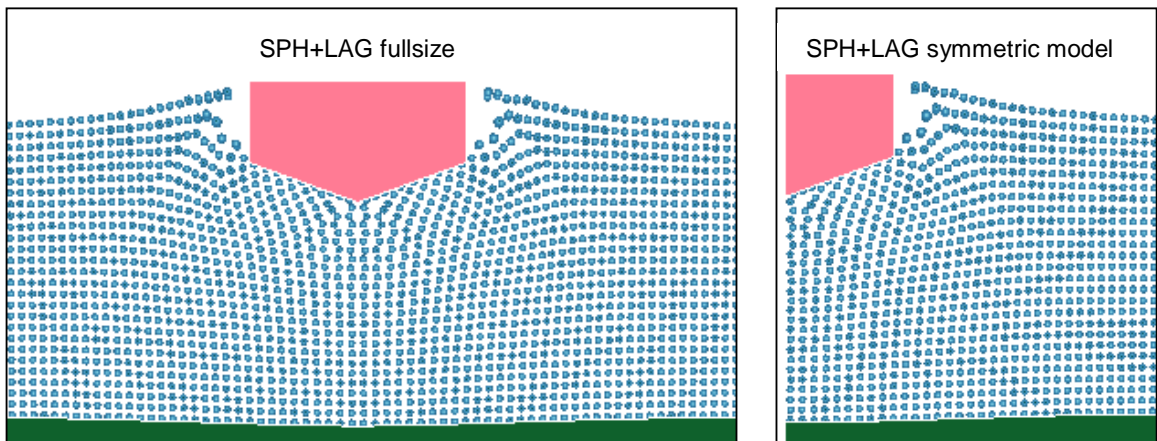
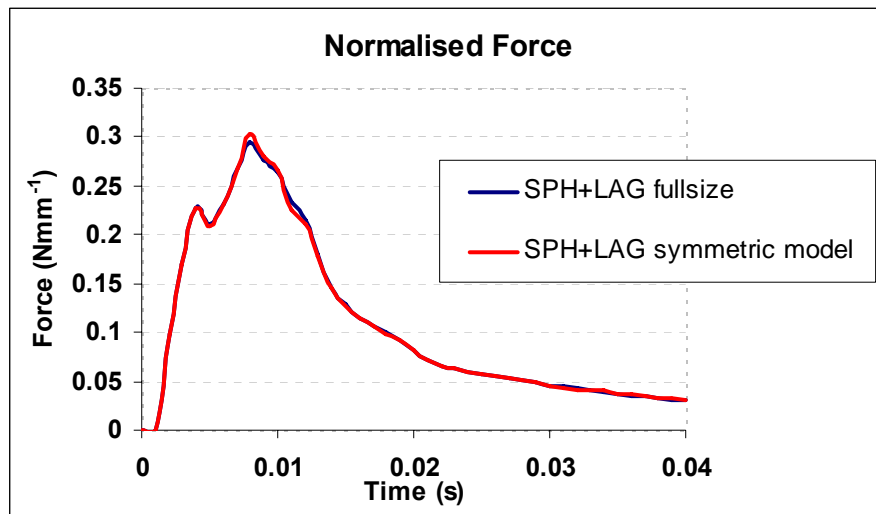


Figure 56: Evaluation of symmetric modelling approach for SPH+LAG model

A saving of approximately 70% was achieved in computational time by using the SPH+LAG approach without a reduction in the accuracy of the result, which can be observed through Figure 57 which compares the force predictions of the complete SPH and SPH+LAG models. This provided a platform for refinement of the particle density in the impact region without a considerable requirement for further computational resources.

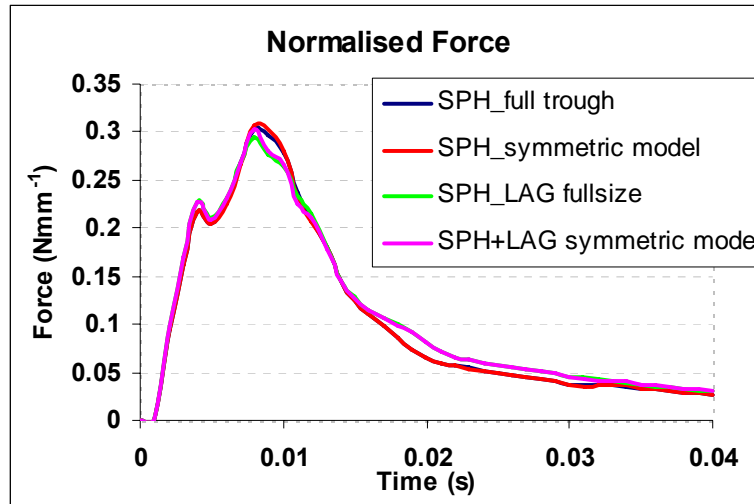
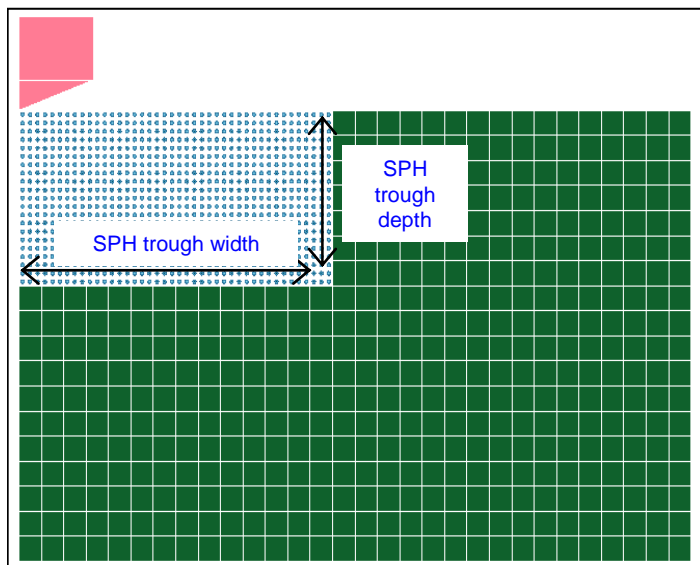


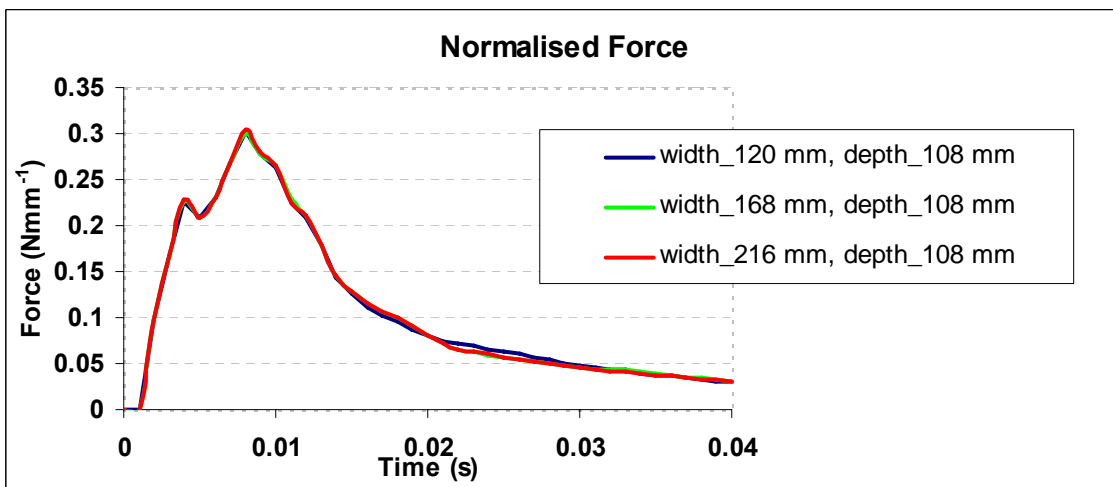
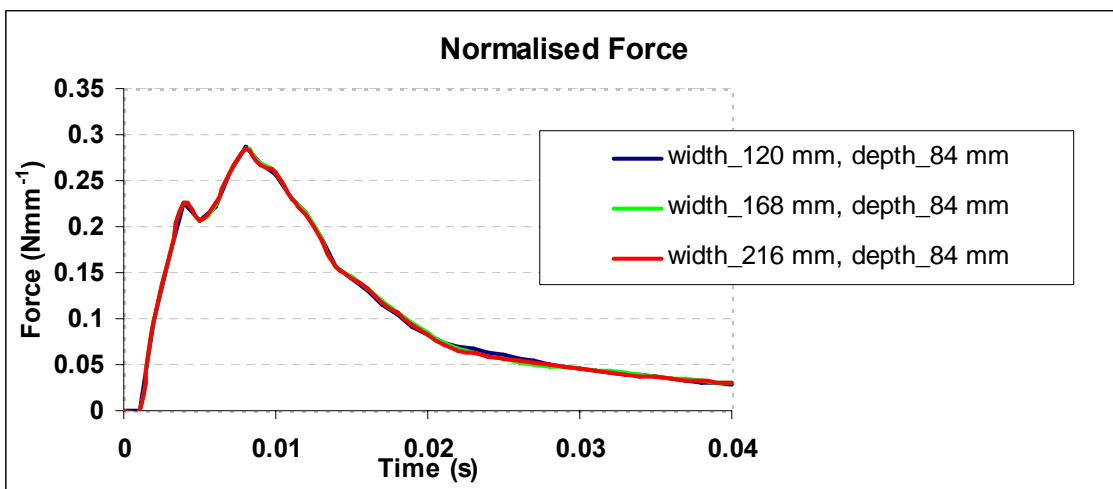
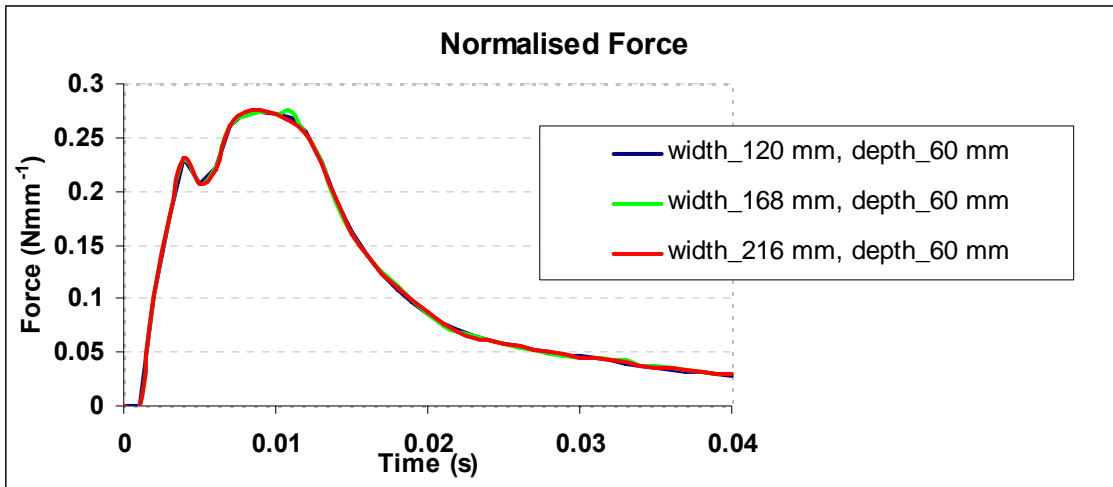
Figure 57: Comparisons between complete SPH and SPH+LAG models

The size of the SPH region was also varied according to Table 11 and compared to the complete SPH model to observe the influence of the reduced SPH domain size on the force predictions and qualitative behaviour of the water. As a result, a suitable minimal size of the SPH domain of the water trough could be determined for better computational efficiency.



SPH Section Width (mm)	SPH Section Depth (mm)
120	60
120	84
120	108
168	60
168	84
168	108
168	132
168	156
168	180
216	60
216	84
216	108

Table 11: SPH section size variation in the SPH+LAG approach



**Figure 58:** Influence of varying SPH section width on kinematic predictions of the model

As can be seen from Figure 58, variation in the SPH trough width does not affect the acceleration predictions of the wedge.

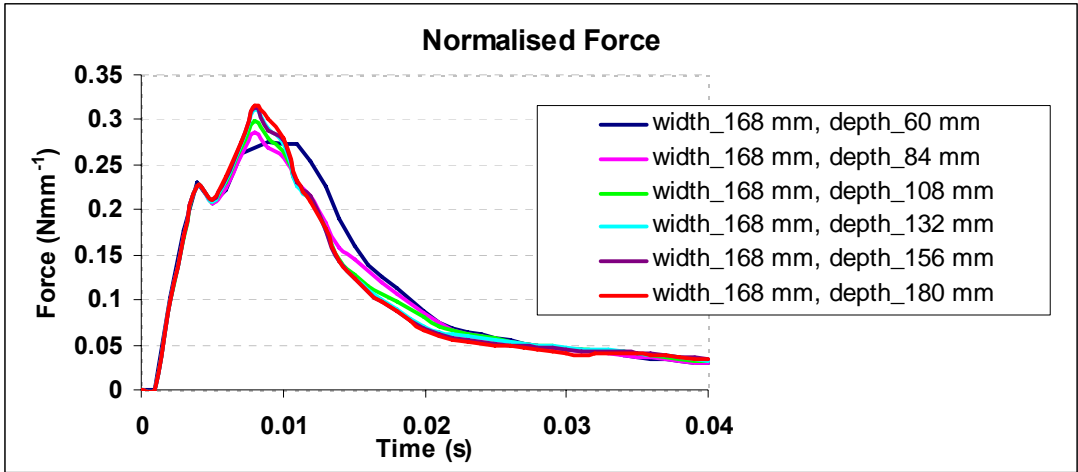


Figure 59: Influence of varying SPH section depth on kinematic predictions of the model

Increasing the depth of the SPH section of the water trough only slightly affected the peak acceleration. The objective was to maintain the SPH trough dimensions as small as possible to minimise computational time which significantly increased with an increasing number of particles. The above trend was observed for a relatively coarse distribution of particles. With particle refinement, variations in the trough depth did not influence the results as much as displayed in Figure 59. Through further analyses, it was concluded that an SPH section of 60 mm depth and 120 mm width was suitable for simulating the initial impact moments of the various test configurations. This allowed for the highly deforming region of the water domain to be captured well and efficiently.

### 6.2.3 Wedge Depth Independence

An investigation was carried out to ensure that the results obtained from the numerical models represented the 2D behaviour of the water throughout the depth of the wedge. Therefore, models with differing wedge depths and corresponding water trough depths were simulated. The results from these models were then normalised with the wedge depth and compared such that they represented the kinematics observed per unit depth (mm) of the wedge.

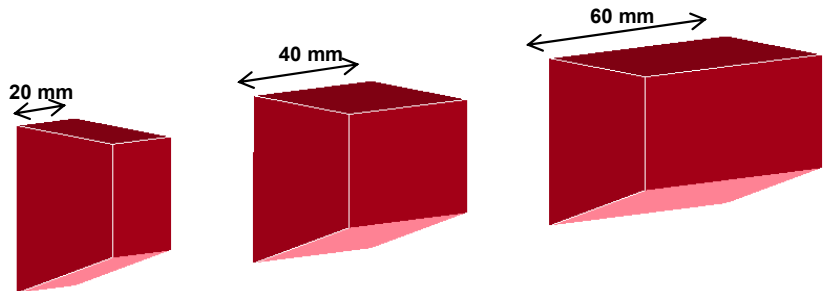


Figure 60: Wedge variants in the wedge depth investigations

Figure 60 shows the variants of the wedge depth simulated. The qualitative and quantitative predictions between these models were compared (see Figure 61) and this confirmed that the 2D flow behaviour was been simulated in the models.

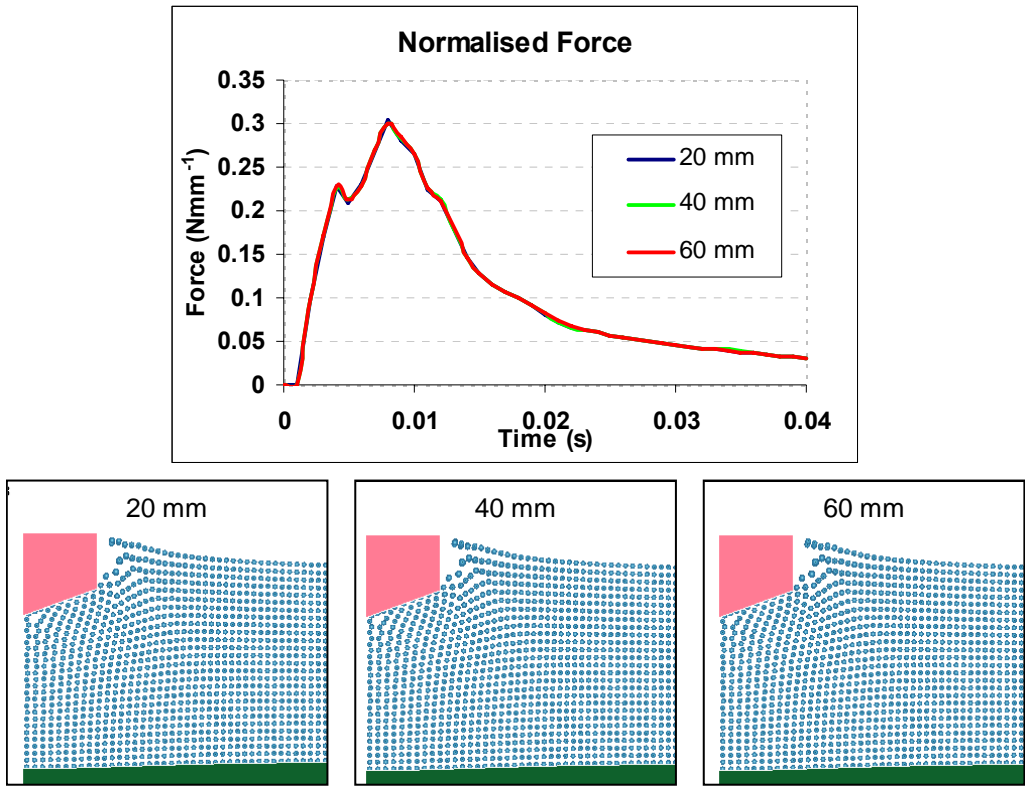


Figure 61: Comparison of varying wedge depths on quantitative and qualitative characteristics

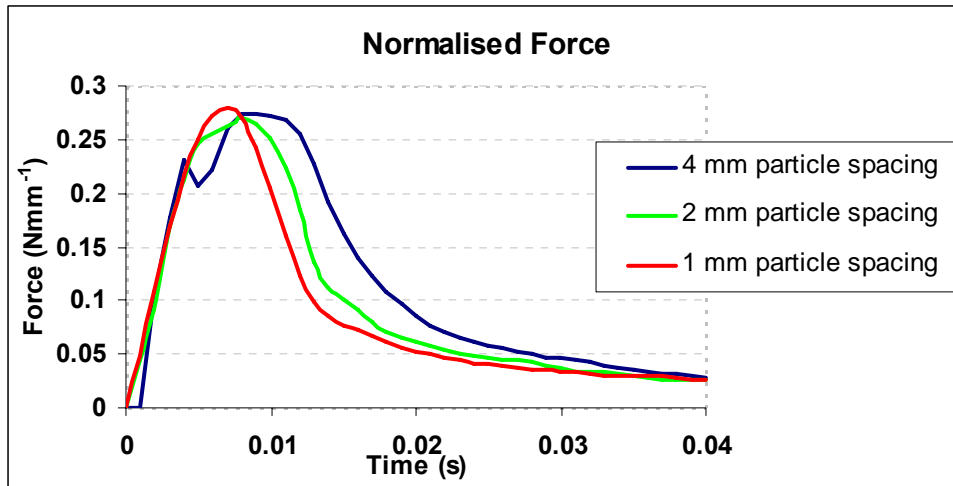
### 6.2.4 SPH Particle Density Analysis

From the above analysis, a symmetric model of a half-wedge and water trough represented by coupled SPH and Lagrangian formulations was achieved. Since the modelling results were independent of the wedge depth, the smallest depth investigated that agreed with the trends observed was selected and the number of SPH particles used to represent the given volume of water was gradually increased. This was to investigate the effect of the particle density on the kinematic predictions of the impact, and also evaluate the ability of SPH to capture the fluid motion of the water upon impact.

From Table 12, increasing the particle density greatly increased the computational time due to a shorter smoothing length of each particle, which in turn reduced the solution time step. Furthermore, increased computational memory is required to solve models with more particles.

Distance Between Particles (mm)	Particle Mass (kg)	Initial Smoothing Length (m)	Solution Time step (s)	Computational Time
4	$6.388 \times 10^{-5}$	0.0048	$4.39 \times 10^{-6}$	22 min
2	$7.986 \times 10^{-6}$	0.0024	$2.19 \times 10^{-6}$	1 hr 34 min
1	$9.982 \times 10^{-7}$	0.0012	$1.10 \times 10^{-6}$	23 hr 10 min

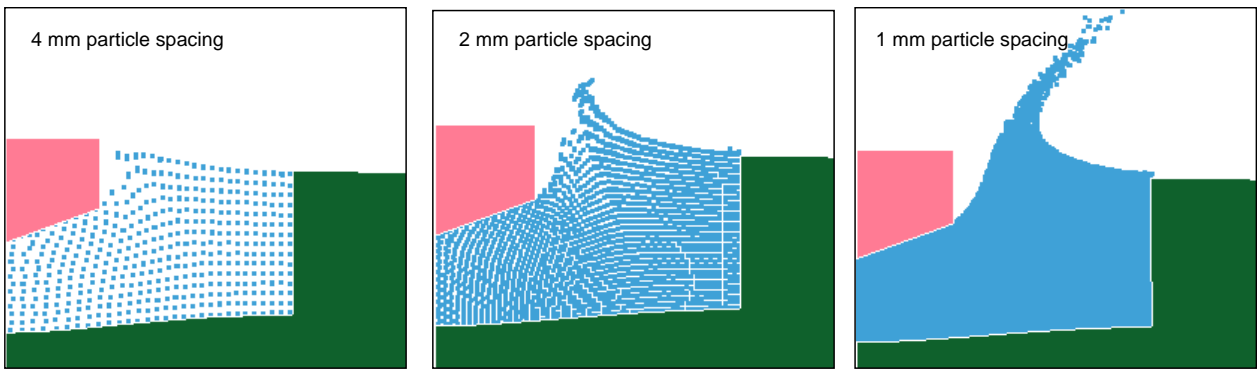
**Table 12:** Particle mesh refinement analysis parameters



**Figure 62:** Force predictions with increasing particle densities

By increasing the number of particles within the SPH domain, there was a significant improvement in both the qualitative and quantitative results. The abrupt peak observed prior to the maximum acceleration was no longer present. This must be due to the improved continuity of the particles within the fluid domain minimizing sudden changes along the fluid-wedge contact interface.

Figure 63 shows that with additional particles, a higher resolution of the free-surface deformation of the water was observed which compared well with the experimental observations. A particle spacing of 1 mm between particles was selected as the specification for simulating the drop tests. Further refinement was unnecessary as it would constitute an impractical increase in the computational time for very little improvements in the kinematic and qualitative predictions.



**Figure 63:** Improvements in qualitative behaviour of water with increasing SPH particle density

As the particle density was increased, the wedge depth investigation was carried out again. This was to determine a suitable wedge depth that could be efficiently used to obtain accurate results independent of the wedge depth by reducing the overall number of particles required in the simulation.

### 6.2.5 Variations in Particle Smoothing Length

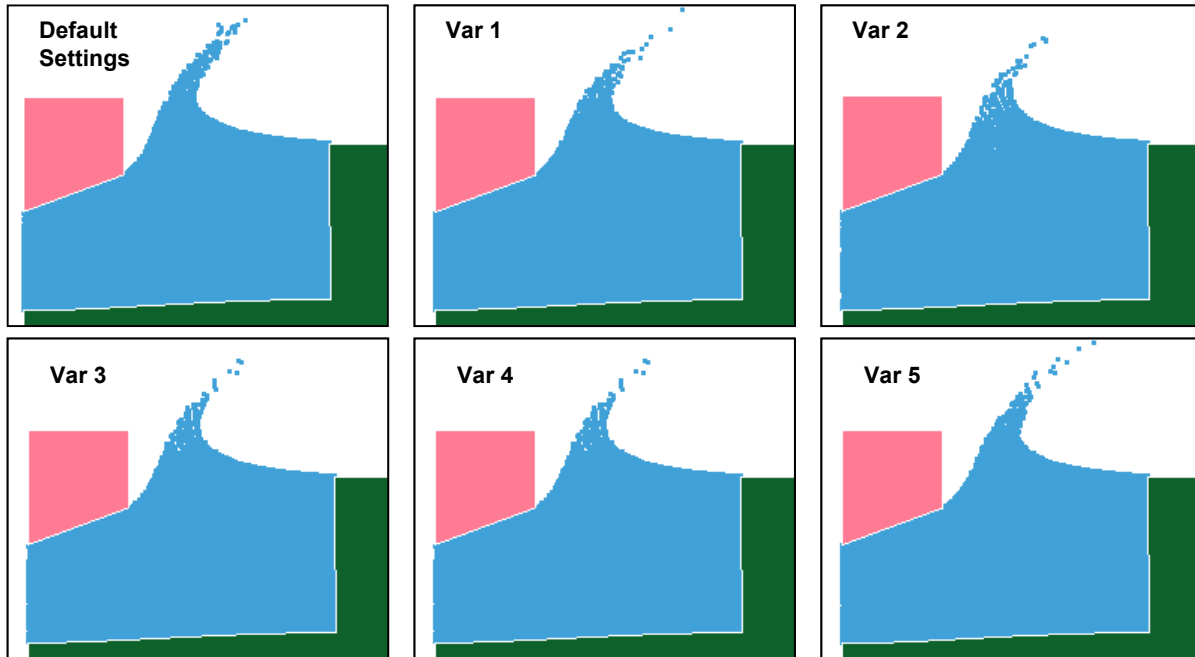
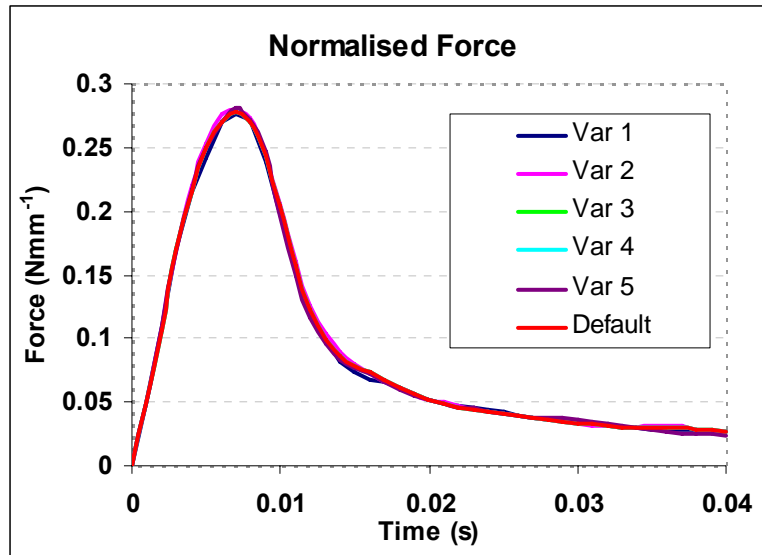
The smoothing length of the particles was automatically calculated by LS-DYNA®, although certain controlling parameters could be set manually as discussed in 4.3.2. Each particle had its own smoothing length which was obtained from the divergence of the flow. Three main parameters of the smoothing length that could be varied in LS-DYNA® are:

- CLSH (Constant applied to the smoothing length)
- HMIN (Scale factor to define the minimum permissible smoothing length)
- HMAX (Scale factor to define the maximum permissible smoothing length)

The variants of the smoothing length parameters are detailed in Table 13.

Name	Parameters Varied		
	CLSH	HMIN	HMAX
Default Model	1.2 (default)	0.2 (default)	2.0 (default)
Var 1	1.05	0.2 (default)	2.0 (default)
Var 2	1.3	0.2 (default)	2.0 (default)
Var 3	1.2 (default)	0.2 (default)	2.4
Var 4	1.2 (default)	0.5	2.0 (default)
Var 5	1.2 (default)	1	1

**Table 13:** Variations of the smoothing length definition parameters



**Figure 64:** Effect of varying the smoothing length definition parameters

From the results shown in Figure 64, it was deduced that varying smoothing length parameters did not influence the qualitative or quantitative results significantly. Although not significant, the prediction of the behaviour of the splash-up region was affected slightly by modifying the smoothing length. Nevertheless, the influences were minimal and it was difficult to subjectively ascertain which variant provided the most accurate representation of the splash-up. Therefore, for the purposes of this investigation, it was decided that the default parameters set in the CONTROL\_SPH card that defined the smoothing length were suitable for accurate results.



## 6.2.6 Solid Lagrangian Element Formulation

The Lagrangian section of the model was not crucial to the impact kinematics and qualitative capture of the highly-deformable region of the water. However, depending on the formulation of the solid elements used to represent the Lagrangian section of the water trough, hourglassing could potentially affect the simulation progression and results. Various formulations were investigated:

- ELFORM = 1 (default setting in LS-DYNA®)
- ELFORM = 2 (fully-integrated S/R solid)
- ELFORM = 3 (fully-integrated 8-noded element with nodal rotations)

For all the above investigated formulations of the solid elements, Figure 65 shows that the results obtained were very similar. However, with fully-integrated elements no hourglassing was present and there was better continuity in the representation of the water free-surface deformation at the SPH-Lagrangian interface, when compared to the default setting.

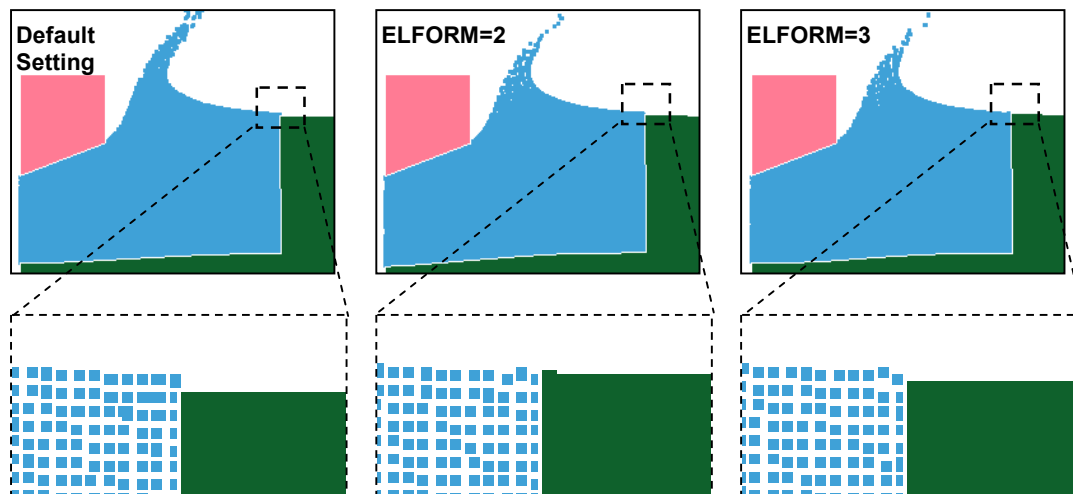
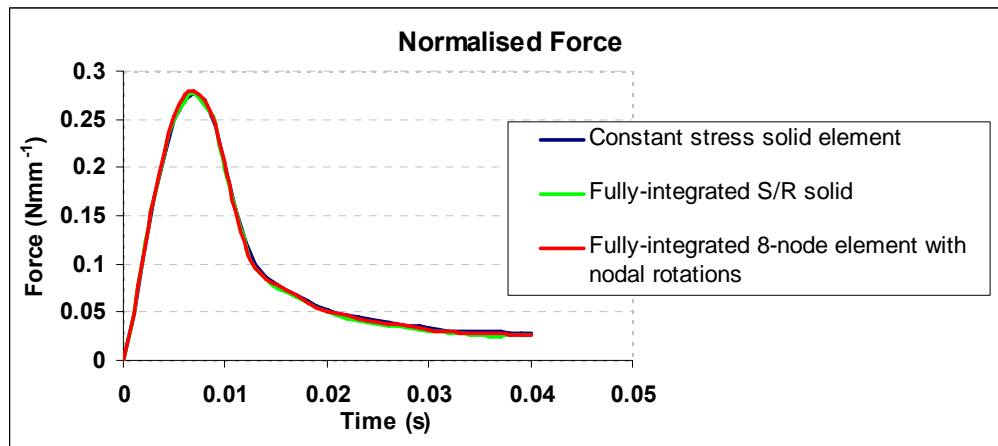


Figure 65: Effect of varying the Lagrangian section solid element formulation

## 6.2.7 Particle Approximation Theory

Depending on the problem being solved, LS-DYNA® provided the option for various particle approximations to be used for the conservation of momentum equation. These were:

- Standard formulation (default)
- Renormalisation approximation
- Symmetric formulation
- Symmetric renormalised approximation
- Fluid particle approximation
- Fluid particle with renormalisation approximation

For water impact modelling, the ideal particle approximation to use is the fluid particle approximation. Nevertheless, all the above approximations were investigated and their comparison is shown in Figure 66.

### 20° Deadrise Angle – Light Impactor – 50 mm Drop – No Gravity Loads

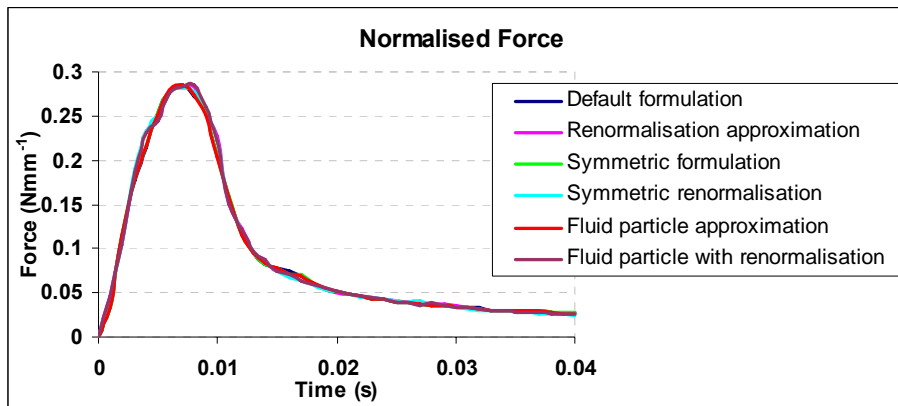


Figure 66: Effect of different particle approximation theories on the force-time history

In terms of the peak forces predicted by the models, there was virtually no difference between the default formulation and the fluid particle approximation. This could be as the impact forces evaluated at the contact interface between the wedge and the SPH section were based on the contact-penalty algorithm which is common across all the particle approximation theories.

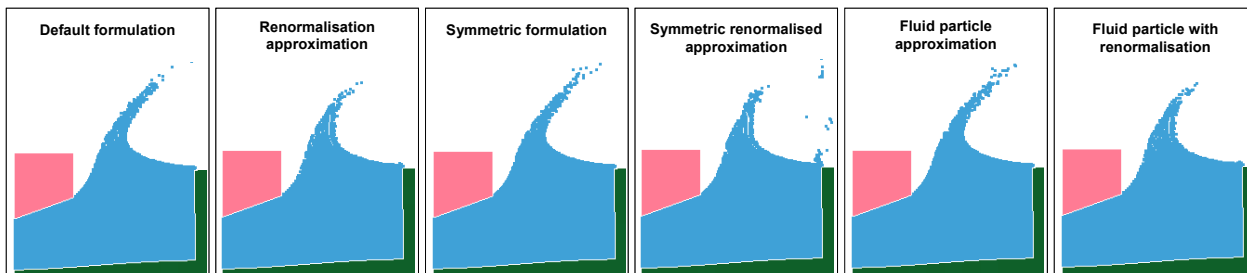


Figure 67: Fluid flow field for varying particle approximations

The particle approximations affected the fluidic behaviour of the SPH particles. It was debatable whether the fluid approximation or the renormalisation showed better qualitative comparisons with the images of the impact. The fluid particle approximation without renormalisation was selected due to its appreciably lower solution time, whereby the approximation with renormalisation required 23% more time to solve than that without renormalisation. For the water impact models that required approximately 22 hours to solve, this translated to significant savings in computational time. For investigations outside the scope of this research project where fluid-structural interaction is present in the physical system, it is important to accurately capture the qualitative behaviour of the fluid and a particle approximation theory has to be selected appropriately.

## 6.3 Material Modelling

### 6.3.1 Wedge

The wedge was modelled as a rigid body using the MAT\_RIGID card in LS-DYNA®. The density of the wedge material was calculated such that it represented the experimental specimens, and hence defined the inertial characteristics of the impactor.

### 6.3.2 Water

The water was modelled using a null material card (\*MAT\_NULL) together with an equation of state to define the pressures within the fluid domain. The material properties of the water defined in the \*MAT\_NULL card were:

$$\rho_0 = 998.2 \text{ kgm}^{-3}$$

Dynamic viscosity – 0.001002 Pa · s

A common equation of state used to represent water in LS-DYNA® is the Gruneisen equation of state (\*EOS\_GRUNEISEN) (Kennedy 2009, pers. comm. 24<sup>th</sup> February). The Gruneisen equation of state for compressed materials is given by equation (29), and by equation (30) for expanded materials (LSTC 2007):

$$p = \frac{\rho_0 C^2 \mu \left[ 1 + \left( 1 - \frac{\gamma_0}{2} \right) \mu - \frac{a}{2} \mu^2 \right]}{\left[ 1 - (S_1 - 1) \mu - S_2 \frac{\mu^2}{\mu + 1} - S_3 \frac{\mu^3}{(\mu + 1)^2} \right]^2} + (\gamma_0 + a\mu)E \quad (29)$$

$$p = \rho_0 C^2 \mu + (\gamma_0 + a\mu)E \quad (30)$$

where:  $\mu = \frac{\rho}{\rho_0} - 1$

To model water at 25° C, the coefficients of the above equation are (Kennedy 2009, pers. comm. 24<sup>th</sup> February):

$C = 1484 \text{ ms}^{-1}$ , which is the speed of sound in water

$S_1 = 1.979$

$S_2 = S_3 = 0$

$\gamma_0 = 0.11$

$a = 0$

$E = 0 \text{ J}$ , which is the initial internal thermal energy.

## 6.4 Gravitational Acceleration

The impact event resulted in an impulsive force and the gravitational force acting on the wedge gave the wedge its inertial properties and contributed to the impact force experienced by the wedge. Once a suitable model was obtained, acceleration due to gravity was applied independently to the wedge and water, and to both the wedge and water.

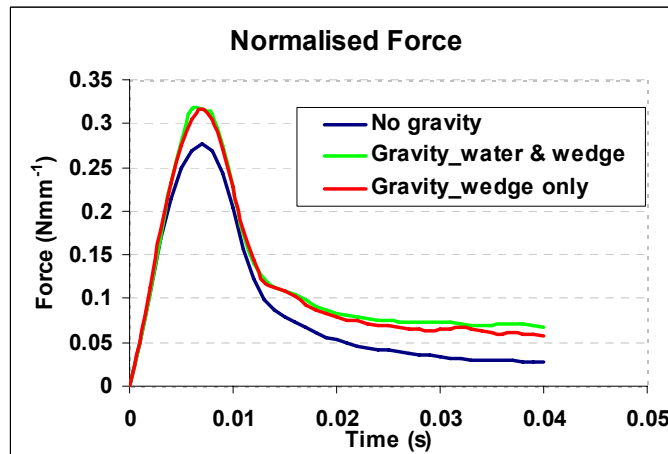


Figure 68: Effect of simulating gravitational acceleration on the impact force

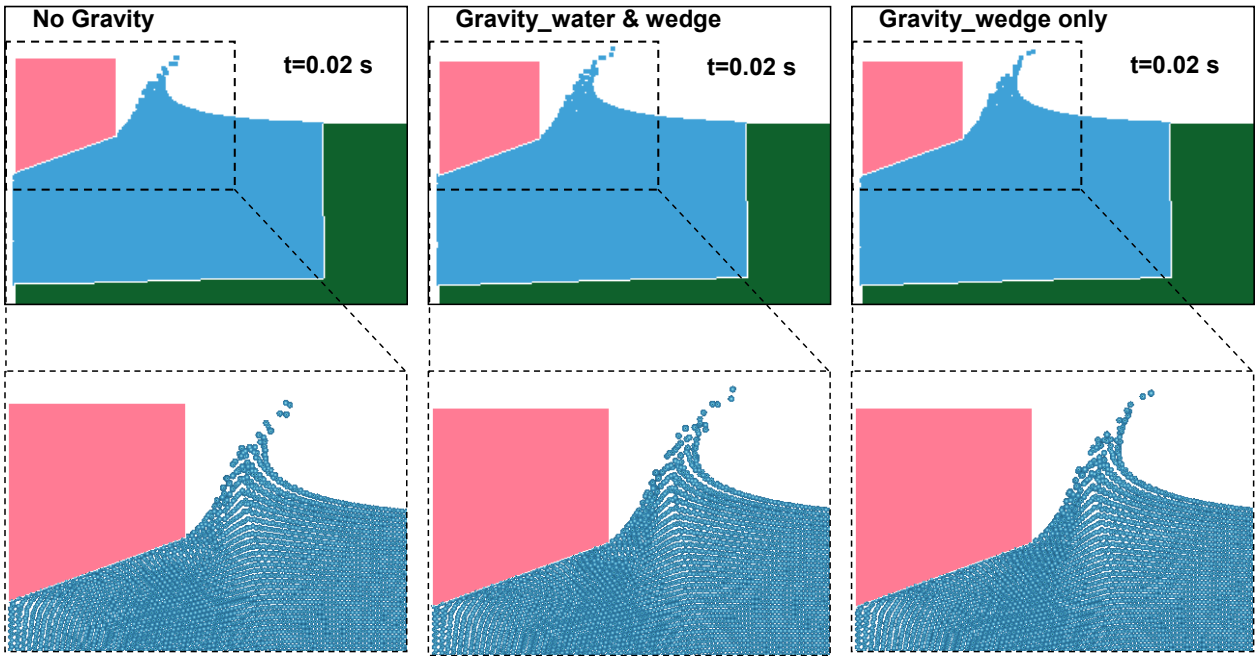


Figure 69: Behaviour of water under varied gravitational loading cases 20 ms after impact

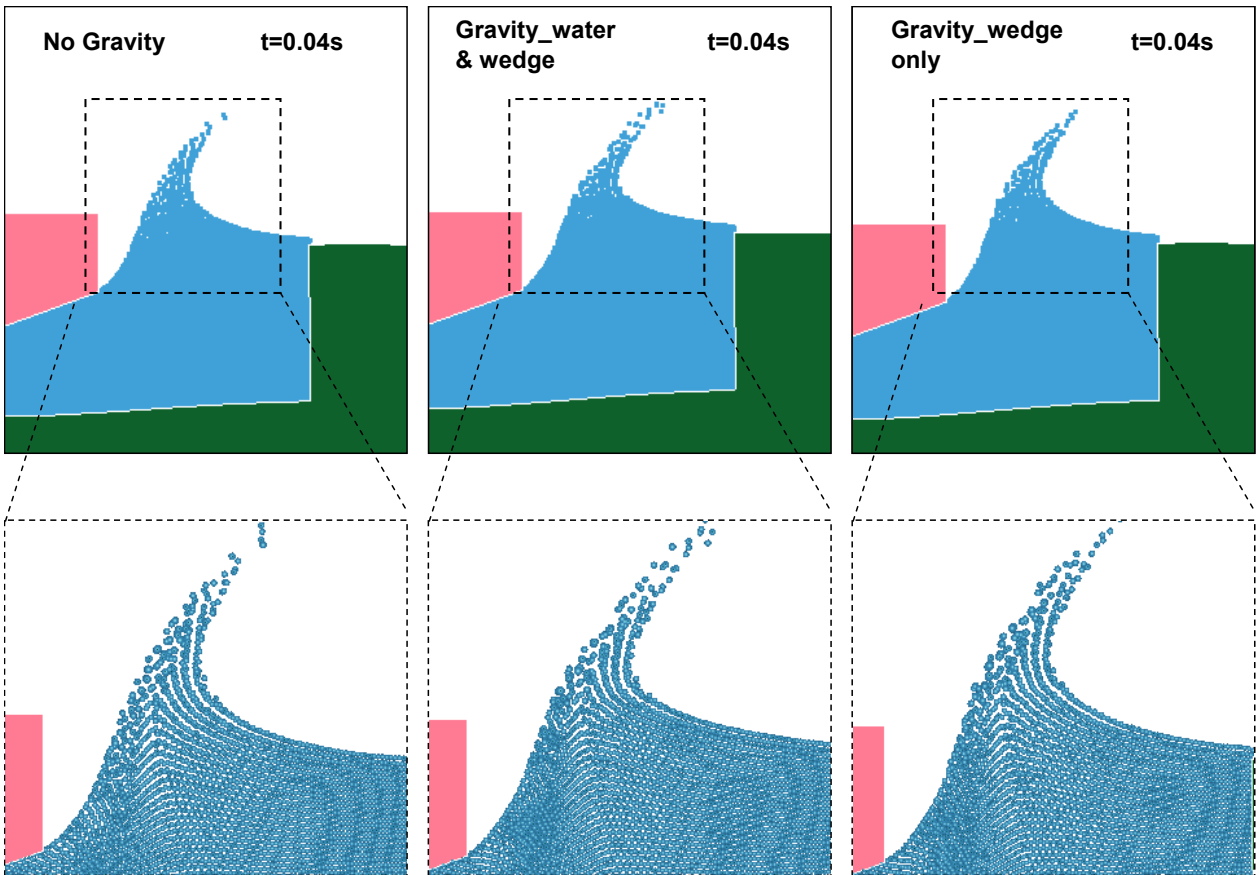


Figure 70: Behaviour of water under varied gravitational loading cases 40 ms after impact

Figure 68, Figure 69 and Figure 70 demonstrate that the quantitative and qualitative results obtained for gravity loads applied to only the wedge and both the wedge and water were very similar over the impact event. Applying a gravitational load to the water alone did not affect the impact force-time history. This was expected since the gravitational loads acting on the water did not affect the wedges' equation of motion.

The computational time required to solve the model increased from approximately 11 hours and 30 minutes for gravitational acceleration applied only to the wedge, to 12 hours and 15 minutes for gravitational loads applied to the entire system. Considering that 35 different models were to be simulated, in the final models gravity was only applied to the wedge and not to both the wedge and water together so as to minimise the computational time. For the immediate moments after impact during the water splash-up, the inertial characteristics of the water to which the wedge momentum was transferred were much more significant than the gravitational loads acting on the individual particles.

If there is interest in capturing the post-impact flow of the water, an efficient proposed approach is to activate gravitational loading for the water particles after the highly dynamic impact event is over i.e. after the peak force has been experienced by the wedge.

## 6.5 Energy Conservation

A major concern of the SPH simulations with LS-DYNA® was the significant reduction in the total energy of the system after impact. This was not observed in a model whereby the water domain was represented entirely by a purely Lagrangian mesh with solid elements. Figure 71 shows the energy loss in the model of the extreme case of the highest impact energy and force. The theoretical total energy,  $E_{total}$ , as shown in equation (31) consists of the initial kinetic energy of the wedge plus the work done on the wedge by the gravitational and friction forces.

$$E_{total} = KE_{init} + M \cdot g \cdot s - F_{fric} \cdot s \quad (31)$$

where:  $KE_{init}$  - Initial kinetic energy of the wedge

$M$  - mass of the wedge

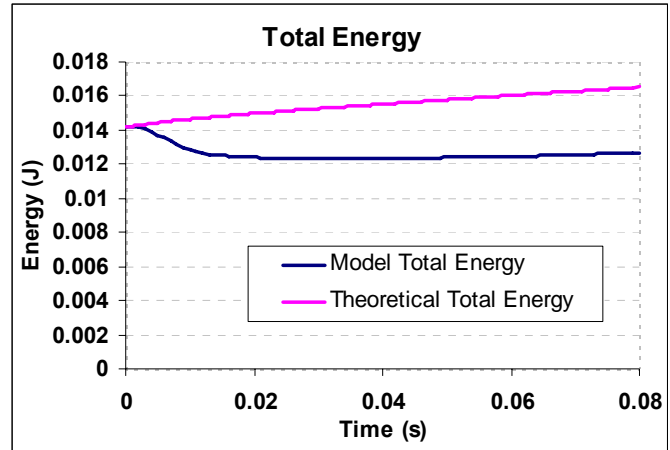
$g$  - gravitational acceleration

$s$  - displacement of wedge

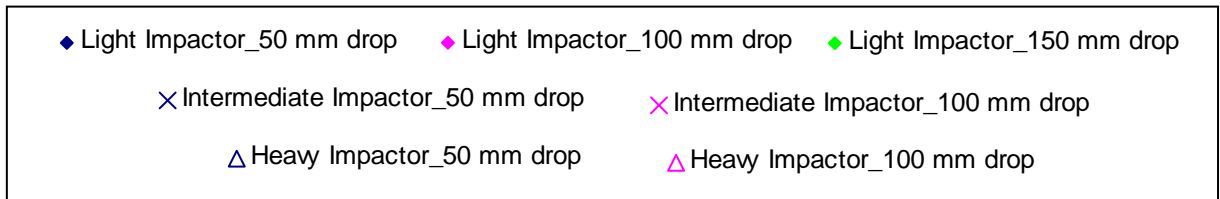
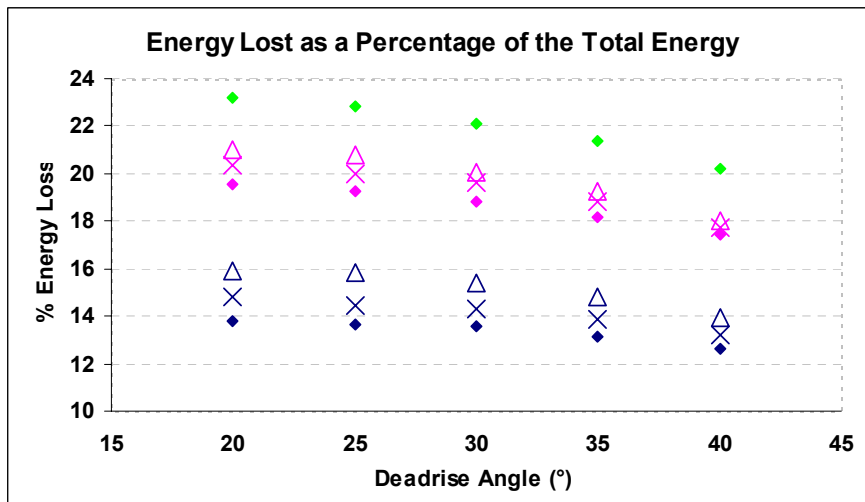
$F_{fric}$  - friction force in guiding track

The displayed trend was observed for all the test configurations (see Figure 72), where the largest rate of energy loss occurred during the initial impact phase when the highest accelerations were experienced by the wedge and SPH particles.

**20 deadrise angle – Light Impactor – 150 mm drop**



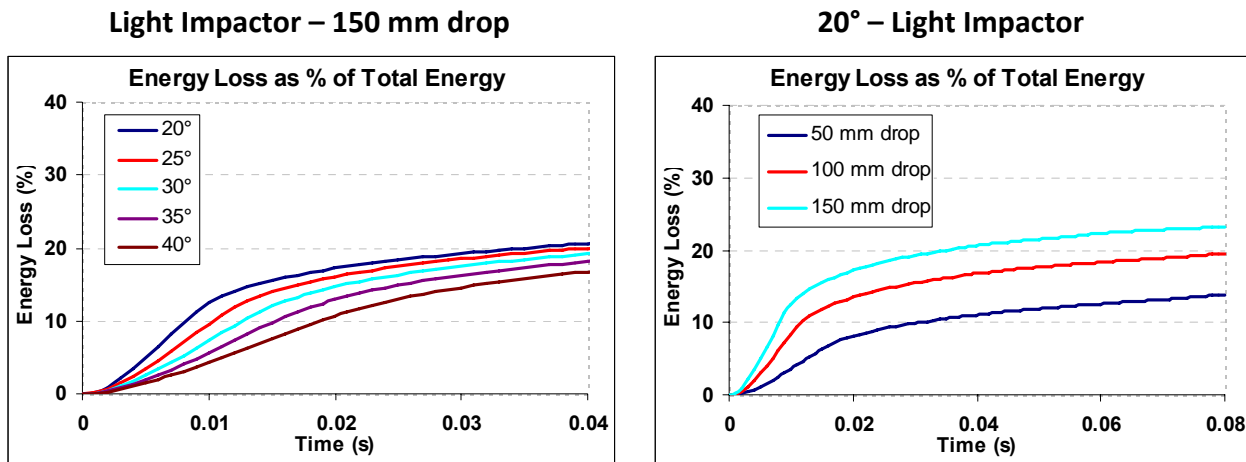
**Figure 71:** Typical energy loss in SPH models



**Figure 72:** Energy loss in the SPH models for all tests configurations

As depicted in Figure 72, there was a direct relation between the percentage of the theoretical total energy lost in a model and the impact accelerations associated with the test configurations. It was established that as the impact energy increases and the deadrise angle reduces, there is an increase in the magnitudes of the peak accelerations and the rates at which

they are reached. As depicted in Figure 73, the percentage of energy lost correspondingly increased as the impact accelerations became more severe.



(a) Different deadrise angles with same impact energy

(b) Variation in drop height

**Figure 73:** Differences in energy loss due to different impact energies and deadrise angles

The energy drop over 0.08 s after impact for the two extreme cases consisting of the highest energy and impact force, and the lowest energy and impact force was quantified and is summarised in Table 14. The range of loss of energy varied between approximately 13% and 23% of the theoretical total energy of the system.

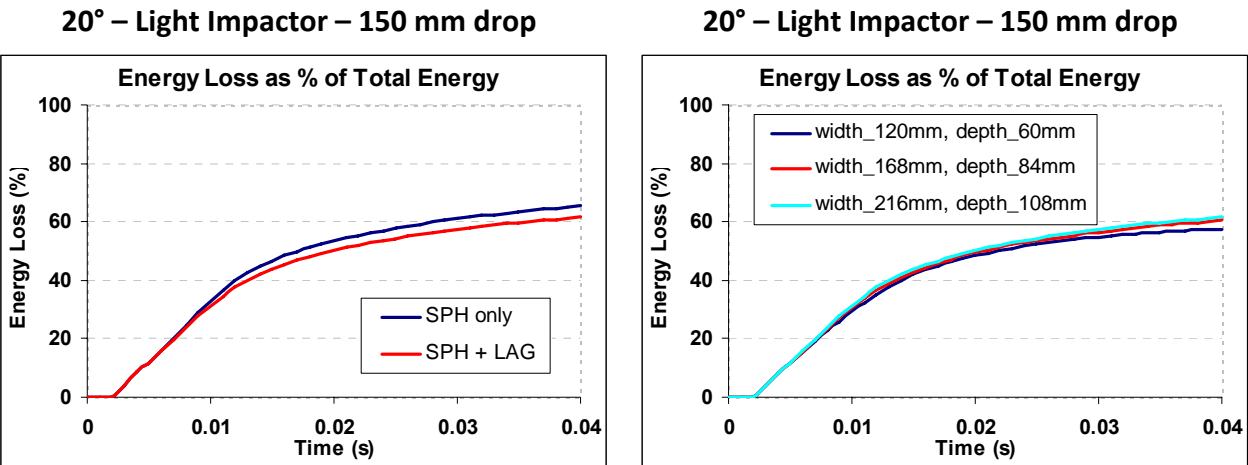
Test Configuration	Impact Energy	Peak Impact Force	Energy Loss as % of Theoretical Total Energy
<b>20° – Light Impactor 150 mm drop</b>	1.3451 J	0.3022 Nmm <sup>-1</sup>	≈ 23 %
<b>40° – Light Impactor 50 mm drop</b>	0.4489 J	0.0568 Nmm <sup>-1</sup>	≈ 13 %

**Table 14:** Energy loss associated with the SPH domain

The energy conservation of the models simulated during the development of the basic model parameters (see section 6.2) was also investigated to identify possible reasons for the energy loss. Note that in the energy conservation plots of these preliminary models (see Figure 74 and Figure 75), the theoretical total energy was constant throughout the simulation as gravity and friction effects were not simulated. Therefore, the percentage of the total energy lost was larger than that quantified for the final numerical models in Figure 72 which incorporated the friction and gravity loads. In this regard, however, the energy losses were very similar when comparing the quantitative values of the energy lost between these initial and final models.



Figure 74(a) shows the difference in energy conservation when the water trough was represented entirely by SPH and using the SPH+LAG modelling approach. Slightly better energy conservation was observed using the SPH+LAG approach rather than a complete SPH trough. However, the SPH regions of both the modelling approaches in Figure 74(a) underwent similar deformations, and therefore resulted in a similar energy loss. Further results are shown in Figure 74(b), whereby the energy conservation tended to improve, if only slightly, with a reduction in the size of the SPH domain. These trends shown in Figure 74 indicated that the energy loss seemed to occur in the high-deformation regions of the SPH domain when the particles underwent rapid acceleration and separated away from each other.



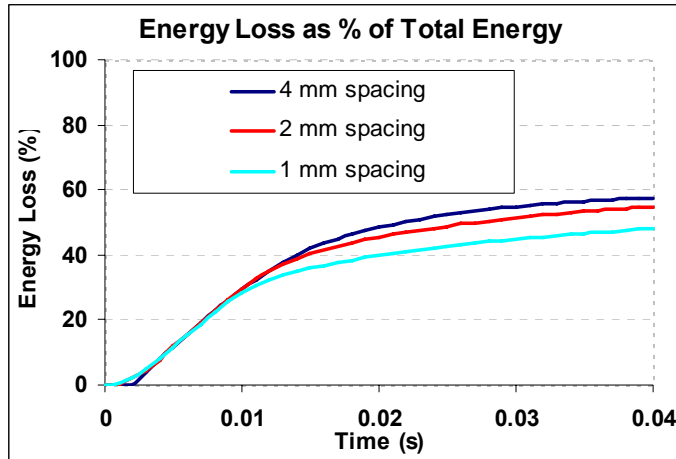
(a) Complete SPH and SPH+LAG approaches for water trough

(b) Variation in SPH section size within the SPH+LAG approach

**Figure 74:** Energy losses when using complete SPH and SPH+LAG approaches

The energy losses associated with an increase in the particle density to define a given volume of water are plotted in Figure 75. It was observed that the overall energy loss decreased as the spacing between particles was reduced. However, the rate of loss of energy over the impact event spanning the initial 10 ms was approximately the same.

## 20° – Light Impactor – 150 mm drop



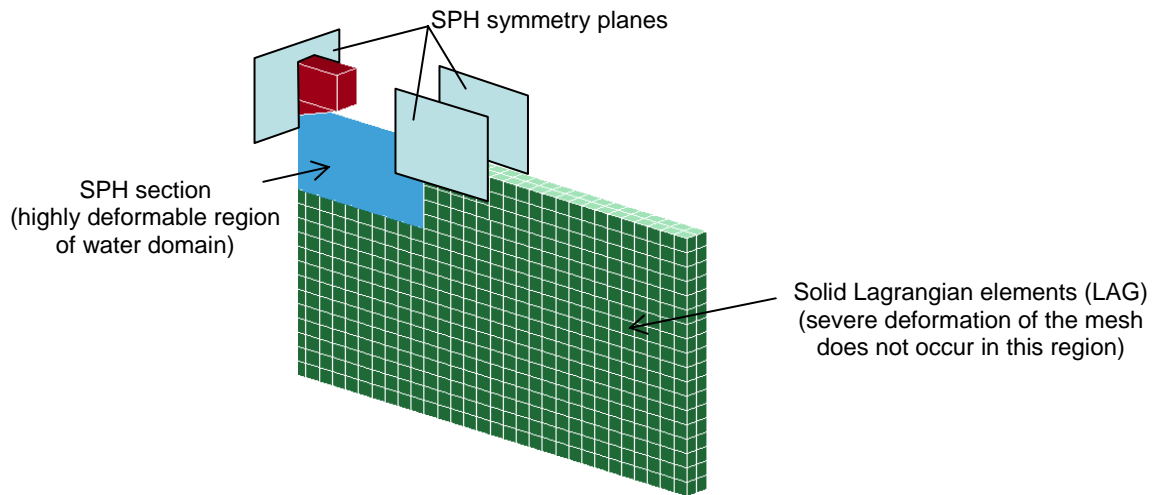
**Figure 75:** Trends in energy conservation with increasing SPH particle density

The problem of energy conservation when using SPH in LS-DYNA® has been observed and cited by Schwer (2009, pers. comm. 24<sup>th</sup> June) and Kennedy (2009, pers. comm. 25<sup>th</sup> June). Areas where the energy loss was occurring could not be identified through the energy control and monitoring outputs available in LS-DYNA®. From discussions (Schwer 2009, pers. comm. 24<sup>th</sup> June; Matthew 2009) it appears as though the loss of energy when using SPH is an inherent problem within the solver, although the results obtained from the simulations suggested an adequate capture of the physics of the impact event.

In theory, the total energy of the system should be conserved as the FE formulation is based around the conservation of energy principles. SPH is still a developing methodology, particularly within commercial FE packages, and this is an important problem that needs to be investigated and addressed by the code developers.

## 6.6 Basic Model Parameters

Following the analysis outlined in section 6.2, the base model shown in Figure 76 incorporated a combined SPH and Lagrangian formulation of the water. Half of the water trough was modelled by using the appropriate symmetry conditions along the wedge centreline. A wedge of 3mm depth was modelled with symmetric boundary conditions applied to the SPH+LAG water domain to replicate 2D flow behaviour that was independent of wedge depth.



**Figure 76:** SPH+LAG model

Table 15 details the simulation parameters that were common between all the models of the complete range of test configurations investigated. The only variation in the various test cases was the wedge geometry, material density (to ensure the correct wedge mass), impact velocity and the constant acceleration acting on the system.

Initial distance between SPH particles	0.001 m
Contact thickness between SPH and LAG for the water domain	0.0005 m
Total trough depth	0.216 m
Total trough half-width	0.360 m
SPH section depth	0.060 m
SPH section half-width	0.120 m
Number of SPH particles	21600
Individual particle mass	$9.98 \times 10^{-7}$ kg
Number of solid Lagrangian elements	490
Simulation termination time	0.08s
Contact type between wedge and water	Soft penalty-based contact
Lagrangian element formulation	Fully integrated solid elements
Smoothing length constant (CSLH)	1.2 (default)
Minimum smoothing length (HMIN)	$0.2h_0$ (default)
Maximum smoothing length (HMAX)	$2h_0$ (default)
Particle approximation theory	Fluid particle approximation

**Table 15:** Basic model parameters used to simulate all test configurations

## 6.7 Simulation Results

The following graphs show the trends observed in the kinematic results through the SPH simulations of the wedge water impacts of the various experimental test configurations.

### 6.7.1 Variation in Deadrise Angle

#### 6.7.1.1 Light Impactors

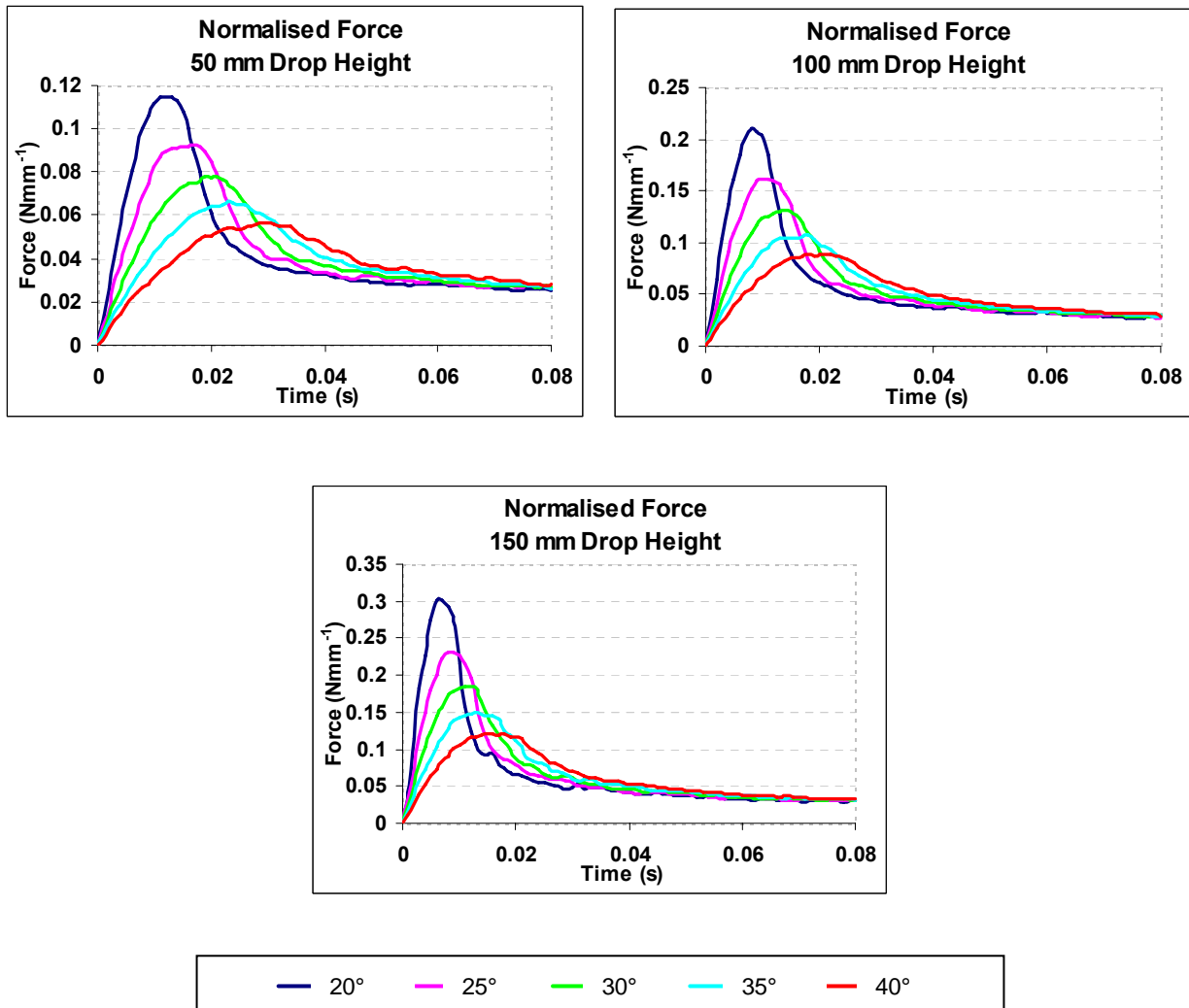


Figure 77: Force predictions for varying wedge deadrise angles of the light impactors

### 6.7.1.2 Intermediate Impactors

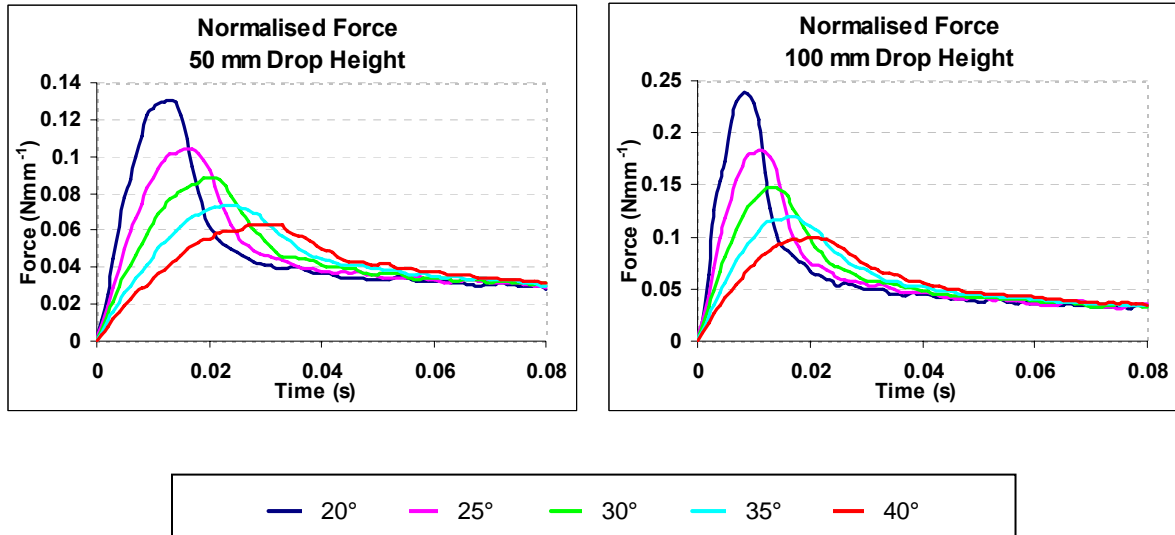


Figure 78: Force predictions for varying wedge deadrise angles of the intermediate impactors

### 6.7.1.3 Heavy Impactors

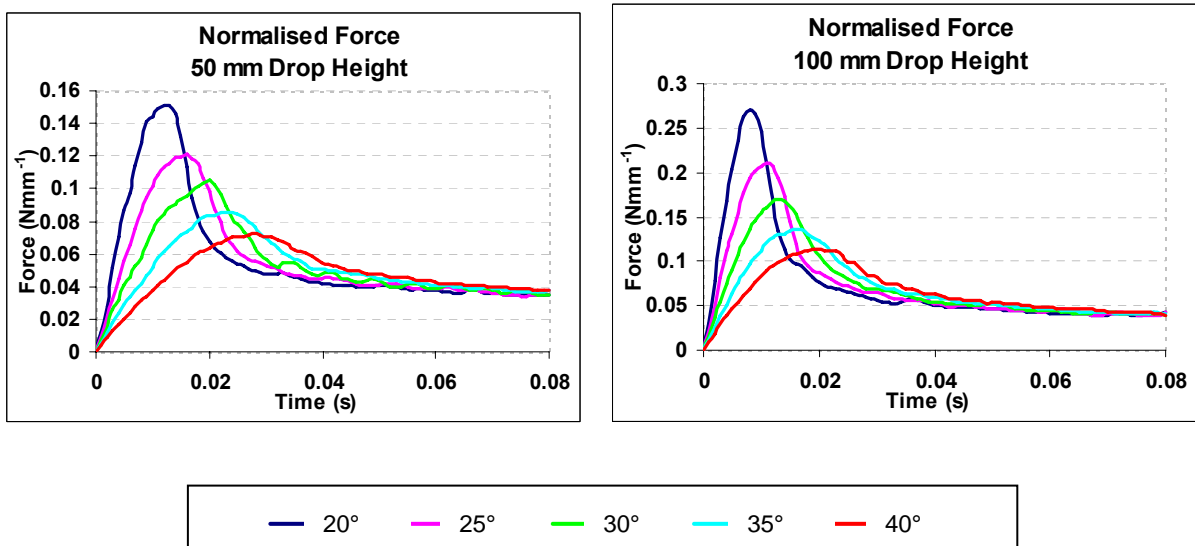


Figure 79: Force predictions for varying wedge deadrise angles of the heavy impactors

Figure 77, Figure 78 and Figure 79 plot the force predictions of the light, intermediate and heavy impactors respectively. For all the masses, as the deadrise angles increased, the peak forces decreased together with the rate at which the peak forces were reached. This was due to a lower rate of change of velocity upon impact, and is consistent with the observations made by Pentecote *et al.* (2003b) and which were in accordance with intuitive expectations of the impact behaviour.

### 6.7.2 Variation in Drop Height for Light Impactors

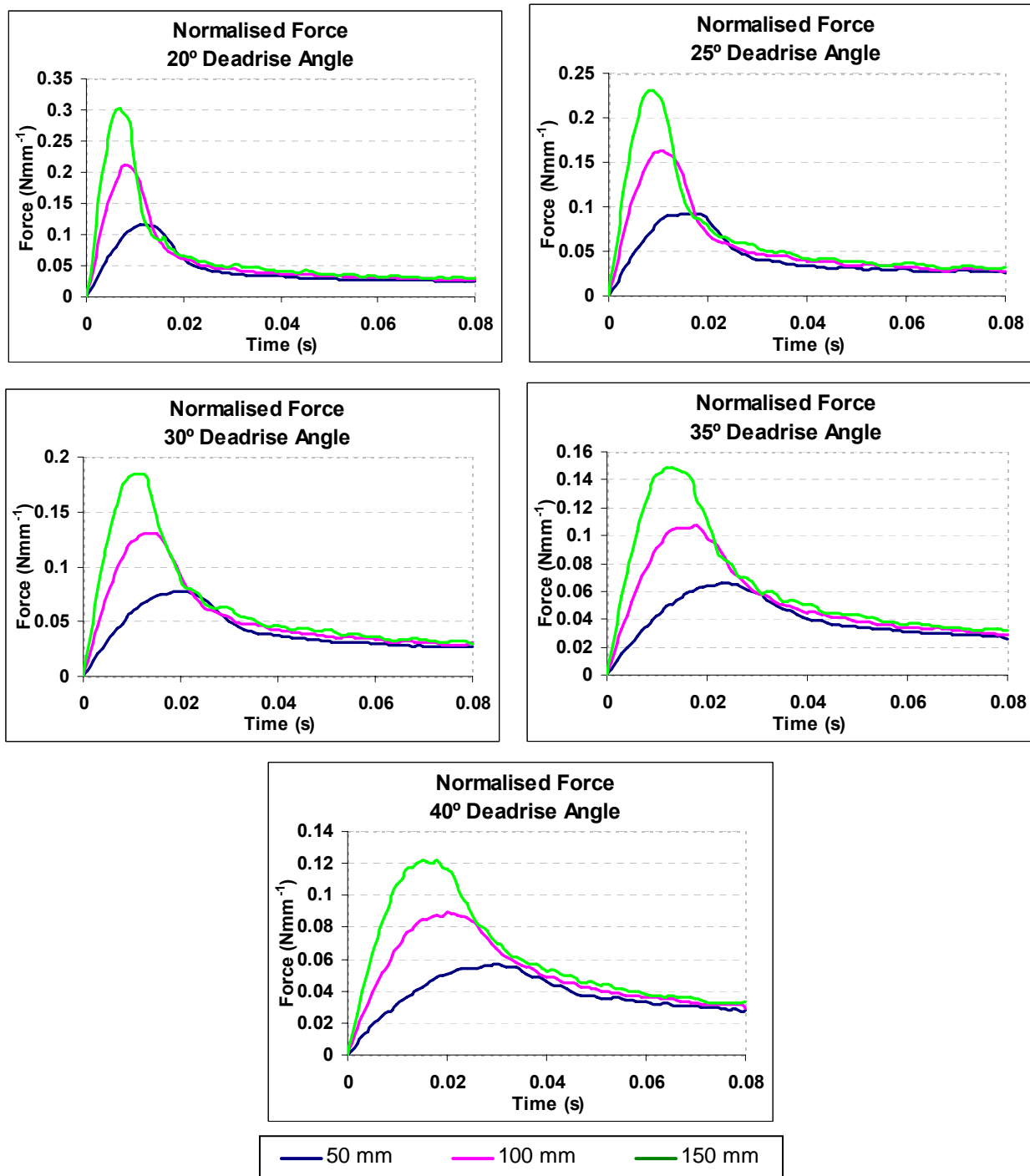


Figure 80: Force predictions for light impactors at varying drop heights

Force-time histories for the light impactors dropped from differing heights are plotted in Figure 80. As expected, the impact forces increased with an increasing drop height represented by higher impacting energies. This same trend was observed for the intermediate and heavy impactors.

### 6.7.3 Variation in Wedge Masses

Figure 81 and Figure 82 plot the results due to a variation in the impactor mass from drop heights of 50 mm and 100 mm respectively. The results were similar to those observed in the experiment, whereby the accelerations for a particular deadrise angle were very similar.

For each of the deadrise angles, the impact velocity varied by approximately 6% between the masses dropped from the same height, as compared to a mass variation of 20%. This suggested that the impact velocity of the wedge, and not the mass of the impactor, was the more influential parameter of the two on the predicted acceleration. However, for the range of impact velocities and masses simulated, the most crucial parameter that affected the impact forces was the deadrise angle of the impactor. This trend was also observed through the experimental tests.

Despite the wedge accelerations being similar, the calculated impact forces are higher for heavier impactors according to Newton's 2<sup>nd</sup> law of motion.

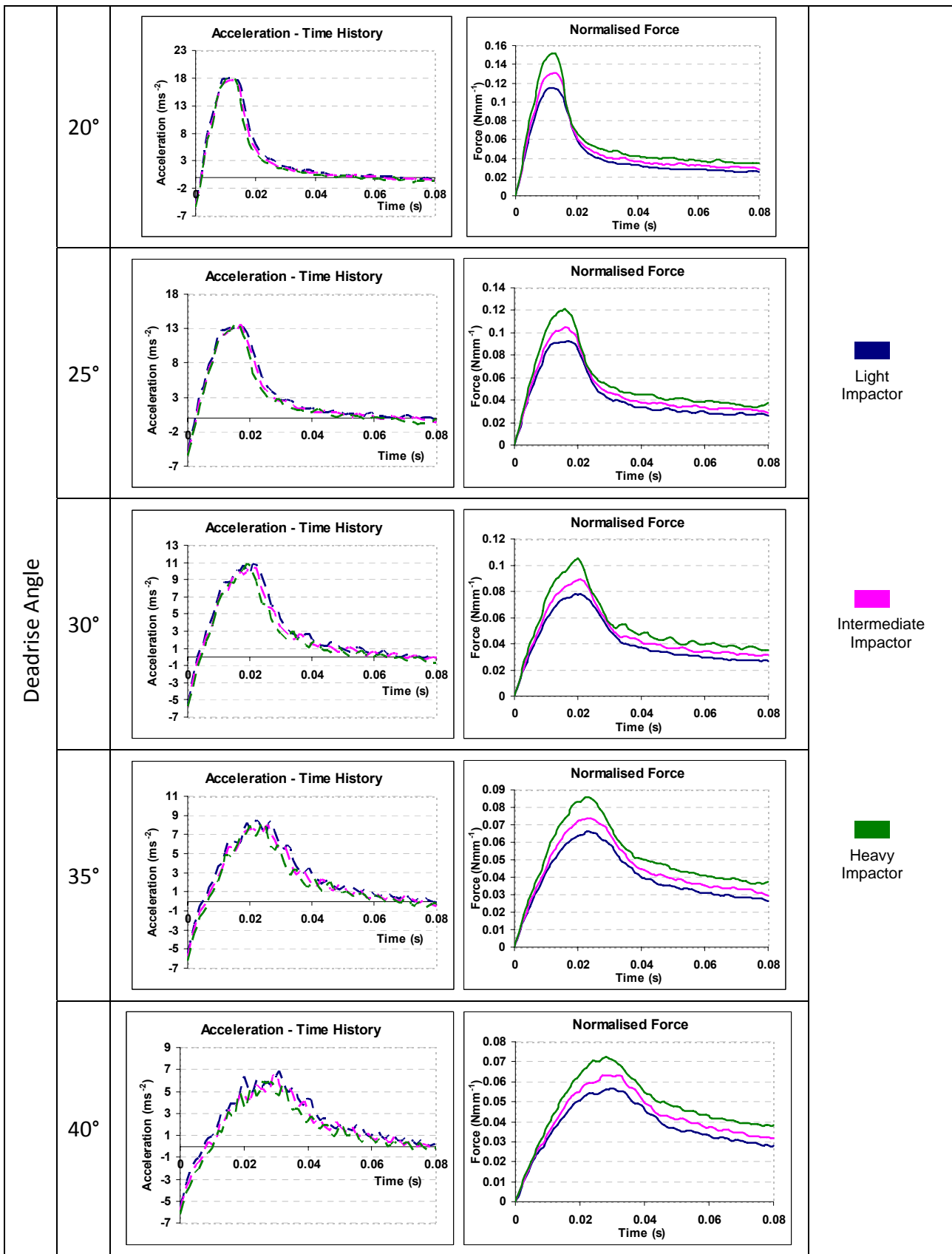


Figure 81: Force and acceleration predictions for varying wedge masses dropped from 50 mm



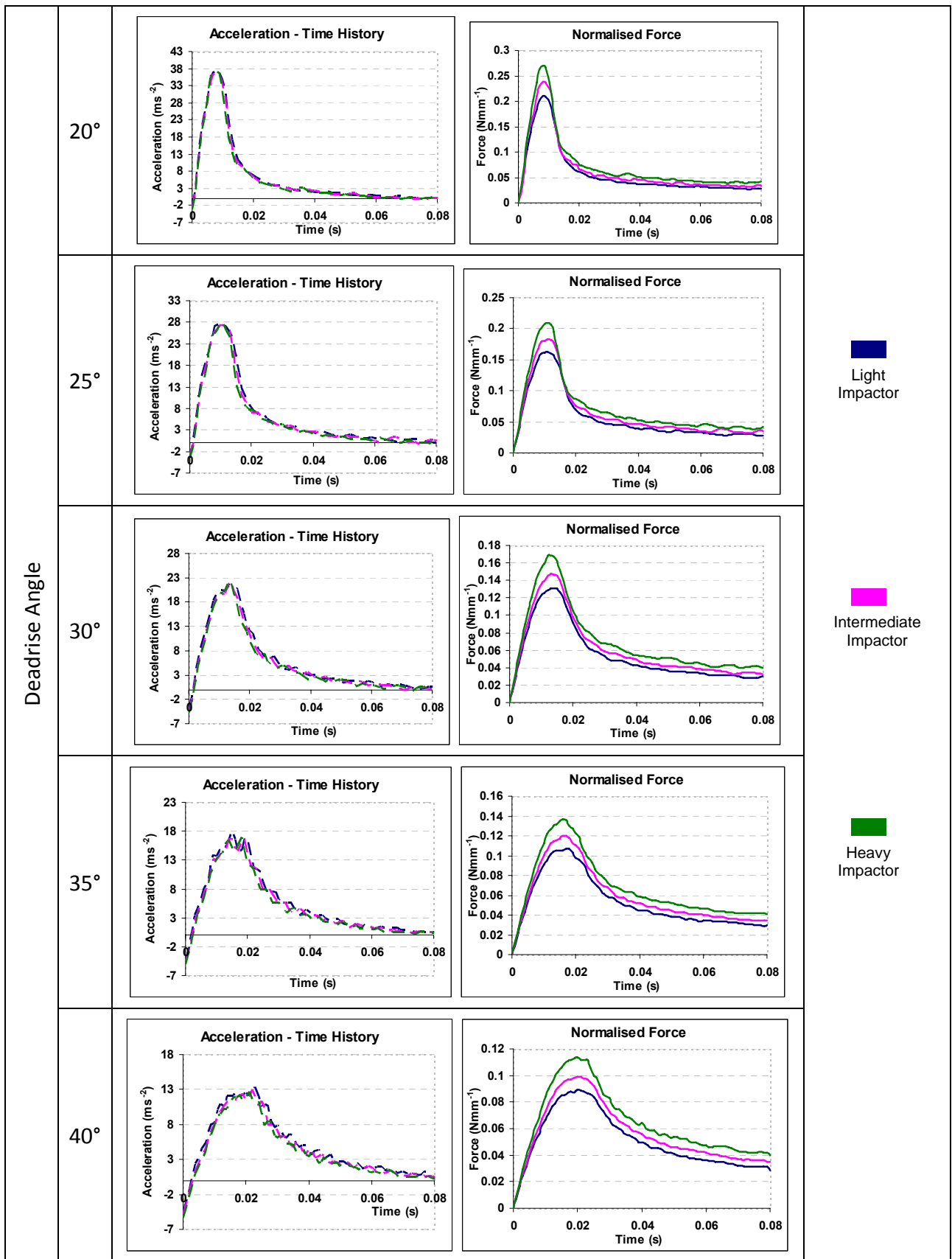


Figure 82: Force and acceleration predictions for varying wedge masses dropped from 100 mm

## 6.8 Concluding Remarks

The experimental test configurations were successfully simulated using a combined SPH and Lagrangian formulation to model the water trough. Despite the high-deformations occurring in the immediate vicinity of the impactors, no numerical instabilities were encountered with the SPH formulation in this region.

Through a preliminary analysis, the basic model parameters were defined which were applicable for modelling the particular water impact tests. A similar approach is recommended to determine the model parameters for other investigations involving the SPH method on larger scale water impact problems.

Despite the problems encountered with the energy conservation in the simulations, the trends identified from the models for variations in the wedge deadrise angle and impact energy suggest a close representation of the physical problem. Further discussion on the predictions of the water impact characteristics and the modelling approach is provided in Chapter 7 and Chapter 8.

# Chapter 7

## **EXPERIMENTAL – NUMERICAL COMPARISON**

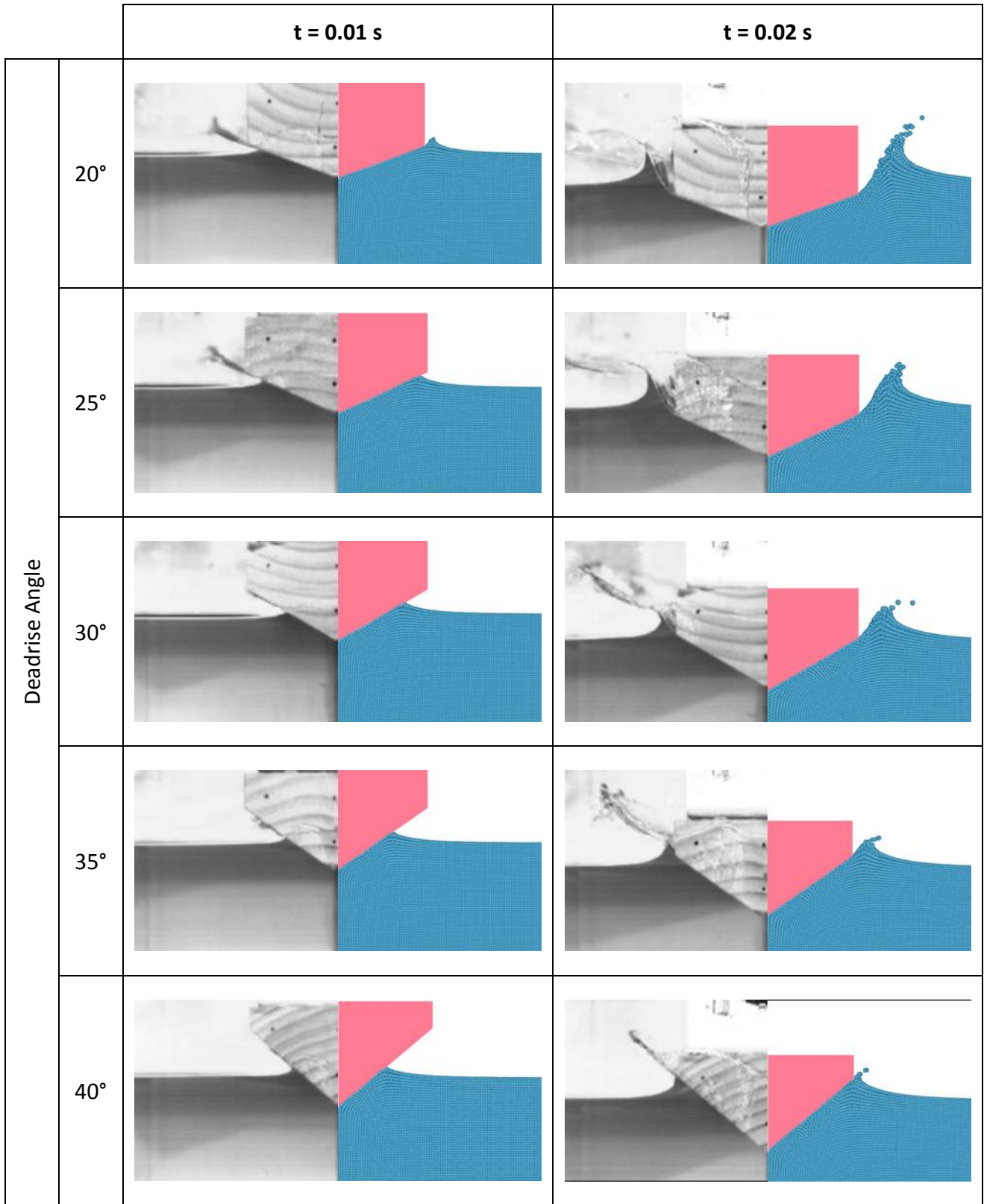
---

### **7.1 Qualitative Comparison**

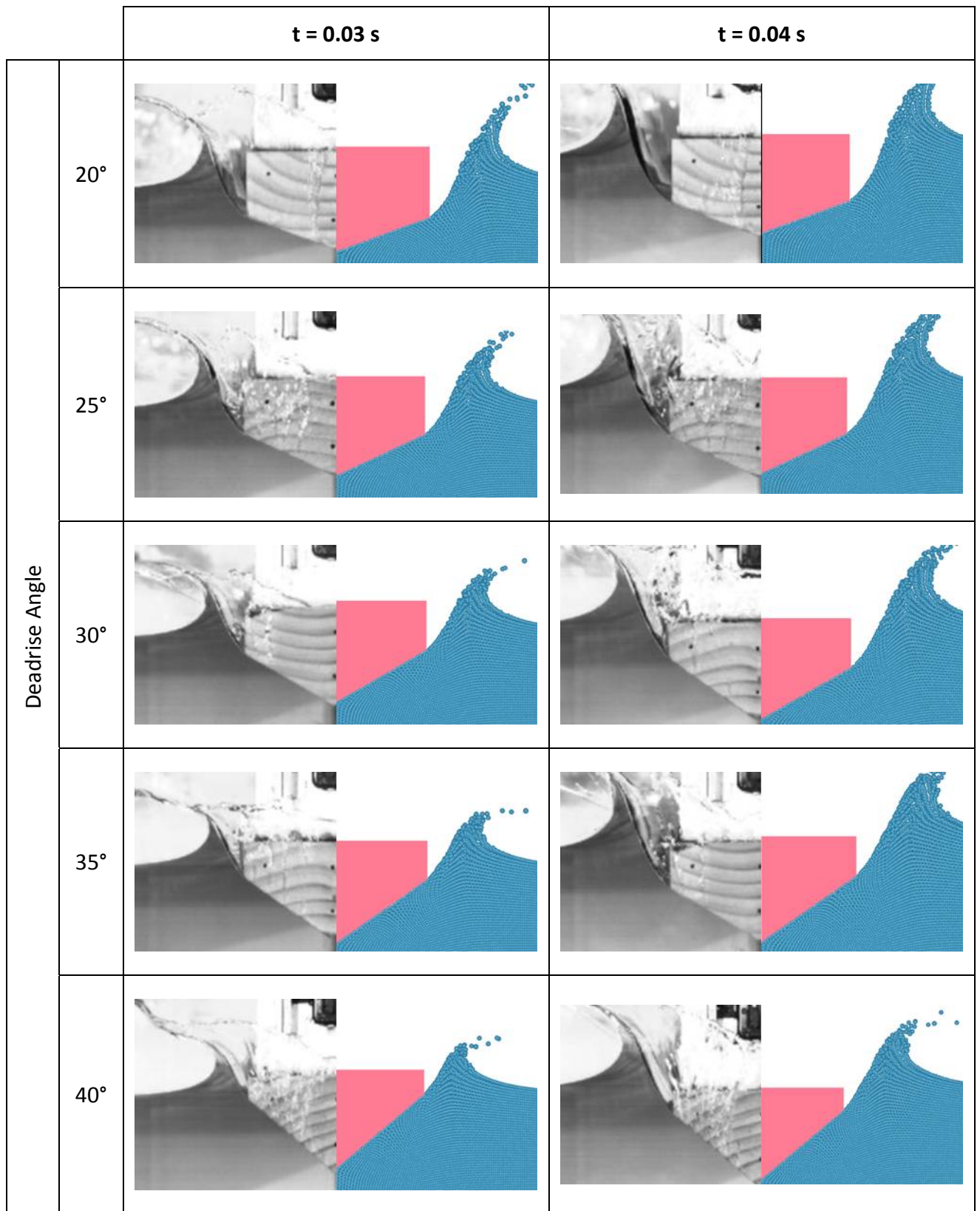
In this section, the physical behaviour of the water impact is compared to that observed through the experimental videos. Qualitative comparisons between the experiment and SPH simulations for the light impactors dropped from a height of 150 mm are displayed in Figure 83, at intervals of 0.01 s after initial impact.

From the screenshots presented in Figure 83, it was observed that the qualitative representation of the water flow field was similar to that predicted by the SPH models. However, it should be noted that the numerical model predictions of the fluid flow showed the water rising up faster along the side of the wedge than what was exhibited in the experiment. This was noticeable for  $t=0.01$  s, particularly for wedges with the lower deadrise angles where the experimental images show a thin film of water that ‘jets’ out at this same time instant, a feature that was not captured by the SPH models. Each SPH particle represented a certain mass (and hence volume) of water and the individual particle masses were possibly larger than the spatially discretised mass of the water jetting out in the experiment.

The water in the jet-flow has a higher velocity than the water rising up the wedge. If the momentum characteristics of the water within the jet and water rise-up region in the experiment could be quantified, this would result in a larger value than the momentum of the water rise-up alone excluding the jet-flow. The flow characteristics of the water predicted by the SPH models appeared to be an intermediate deformation within the bounds of the jet-flow and water rise up observed in the experiment. This indicated that a similar overall momentum transfer to the water had occurred through the impact in both the experiment and SPH models. Through a further increase in the number of SPH particles in this region, the distribution of this momentum is likely to more accurately represent the characteristics observed in the experiment.



**Figure 83:** Qualitative validation of SPH model with images from experimental test



**Figure 83:** Qualitative validation of SPH model with images from experimental test

In general, it was concluded that for the resolution of particles adopted for the simulation, an excellent qualitative representation of the water behaviour was obtained with the SPH approach. Both the rise up of the free-surface and splash up on the sides of the wedge were sufficiently well captured. No numerical instabilities were encountered, which was a major advantage of the SPH method employed for this high deformation problem.

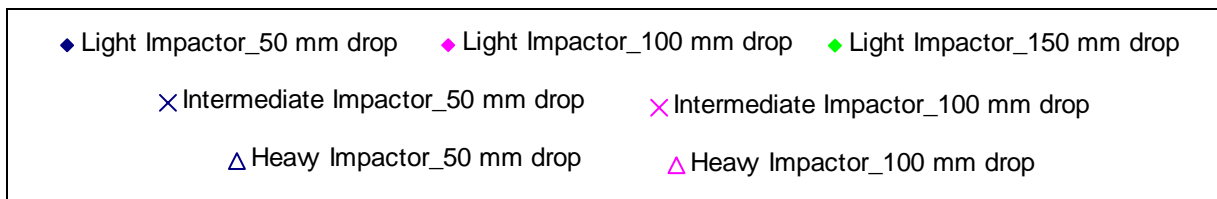
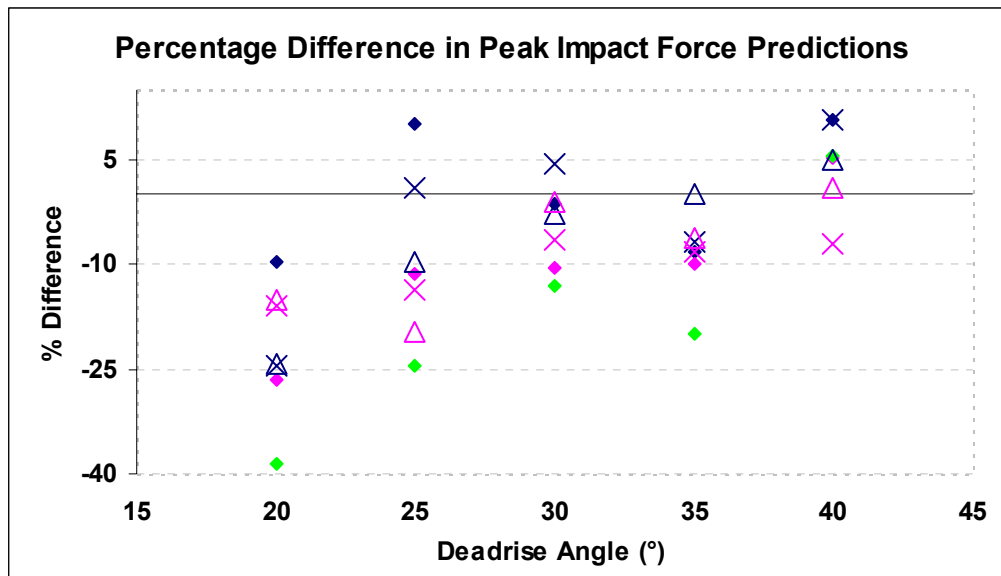
Following the trend observed in section 6.2.4, it is expected that with further refinement of the particle mesh, an improved qualitative representation of the water can be obtained. However, based on the trends shown in Table 12 this will involve significant increases in computational time and processing power than was available for this research. Moreover, a higher level of refinement would not significantly enhance the modelling results.

## 7.2 Quantitative Comparison

Considering the uncertainty associated with the experimentally derived accelerations and impact forces, the SPH simulation results were used as the basis for the quantitative comparison. These numerical models displayed consistency in the trends of the peak force predictions in addition to their excellent qualitative capture of the flow behaviour.

Figure 84 plots the difference in peak impact forces obtained experimentally and predicted by the numerical models for all the test configurations. The difference is measured as a percentage of the peak force predicted by the SPH models for that particular configuration, according to equation (31). A negative percentage difference indicates that the experimental derivation of the peak force was lower compared to the numerical prediction of the same, whereas a positive percentage difference shows that the experimentally derived force prediction was larger than that of the numerical models.

$$\% \text{ Difference} = \frac{\text{Peak Force}_{\text{experiment}} - \text{Peak Force}_{\text{SPH}}}{\text{Peak Force}_{\text{SPH}}} \times 100 \quad (32)$$



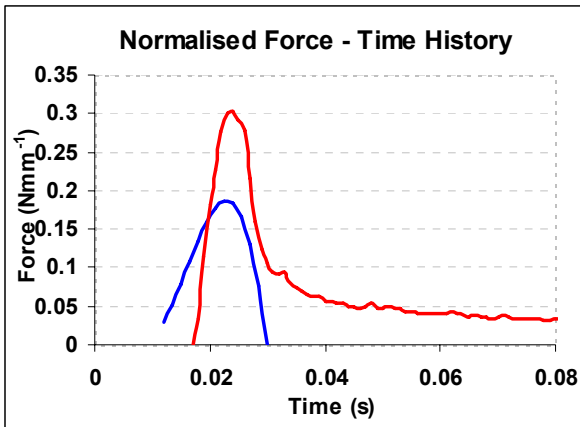
**Figure 84:** Differences in peak impact forces between experimental and modelling results

Larger differences between the experiment and numerical results are observed for the lower deadrise angles. In most cases, the experimentally obtained forces were lower than their numerical counterparts except for the 40° case whereby the numerical models generally predicted lower peak impact forces than the experiment.

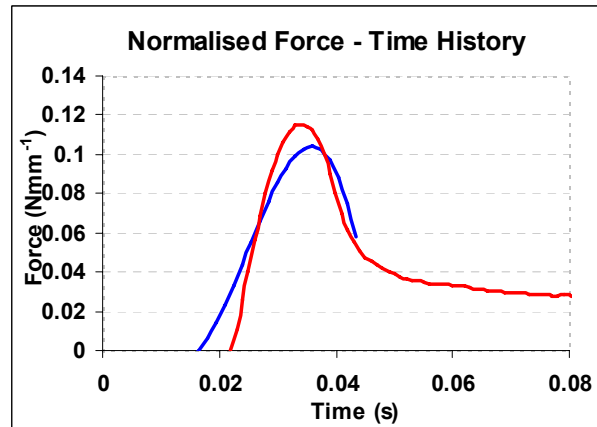
In addition to the above, Figure 85 shows the correlation between the experimentally derived force-time histories and the simulation results for two extreme configurations of the 20° and 40° wedges. The experimental result for the smaller deadrise angle of 20° under-predicted the impact force, whilst the opposite was observed for the 40° wedge. The lower peak force values obtained through the experiment for the 20° wedge could be attributed to the difficulties in the method used to obtain experimental accelerations, which did not seem to accurately capture the very large accelerations demonstrated by the high energy impacts of lower deadrise wedges. Appendix III and Figure 84 show that this trend was observed throughout the predictions for wedges with lower deadrise angles.

Nevertheless, although there were often significant differences in the force-time histories between the experiment and simulations, there was a good basic correlation which suggested that the SPH methodology adequately captured the physics of the impact event whilst an improved accuracy of acceleration approximations is required from the experiments.

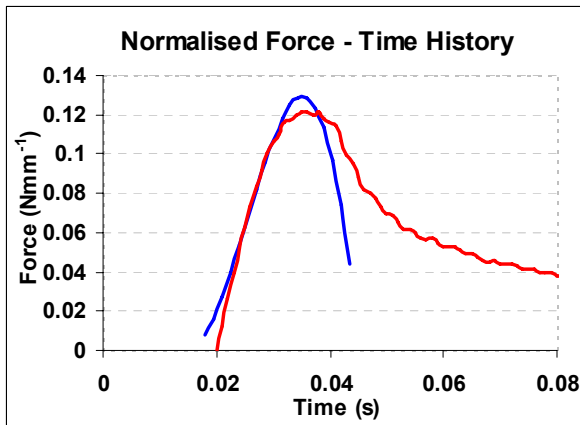
**20° Deadrise Angle – Light Impactor  
150 mm Drop**



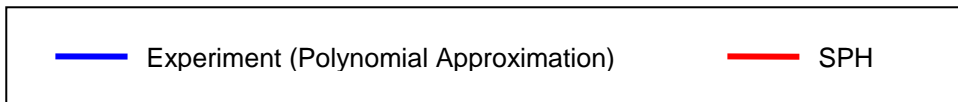
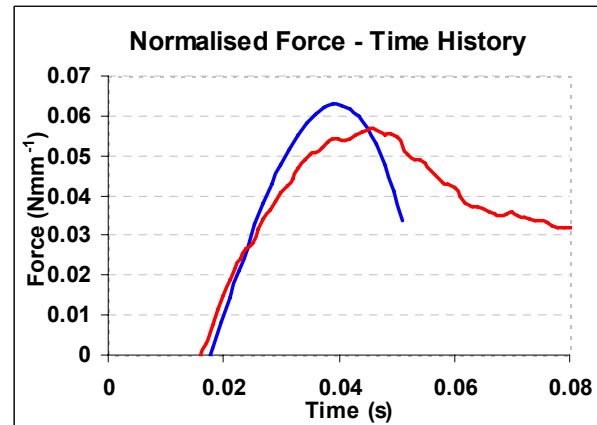
**20° Deadrise Angle – Light Impactor  
50 mm Drop**



**40° Deadrise Angle – Light Impactor  
150 mm Drop**



**40° Deadrise Angle – Light Impactor  
50 mm Drop**



**Figure 85:** Comparison of force-time histories for 20° and 40° wedge drop tests

Furthermore, from the graphs in Appendix III, it can be seen that the polynomial approximation for the impact velocity of the wedge increased as the deadrise angle increased. This general trend was observed for every mass category and drop height. This occurred since the displacement approximations were based on the discrete displacement data. As the deadrise angle increased, for the same time period after the first point of contact with the water, the 40° wedge penetrated deeper into the water than the 20° wedge which experienced a much larger deceleration. This translated into larger velocity approximations at the point of impact for wedges with progressively increasing deadrise angles.



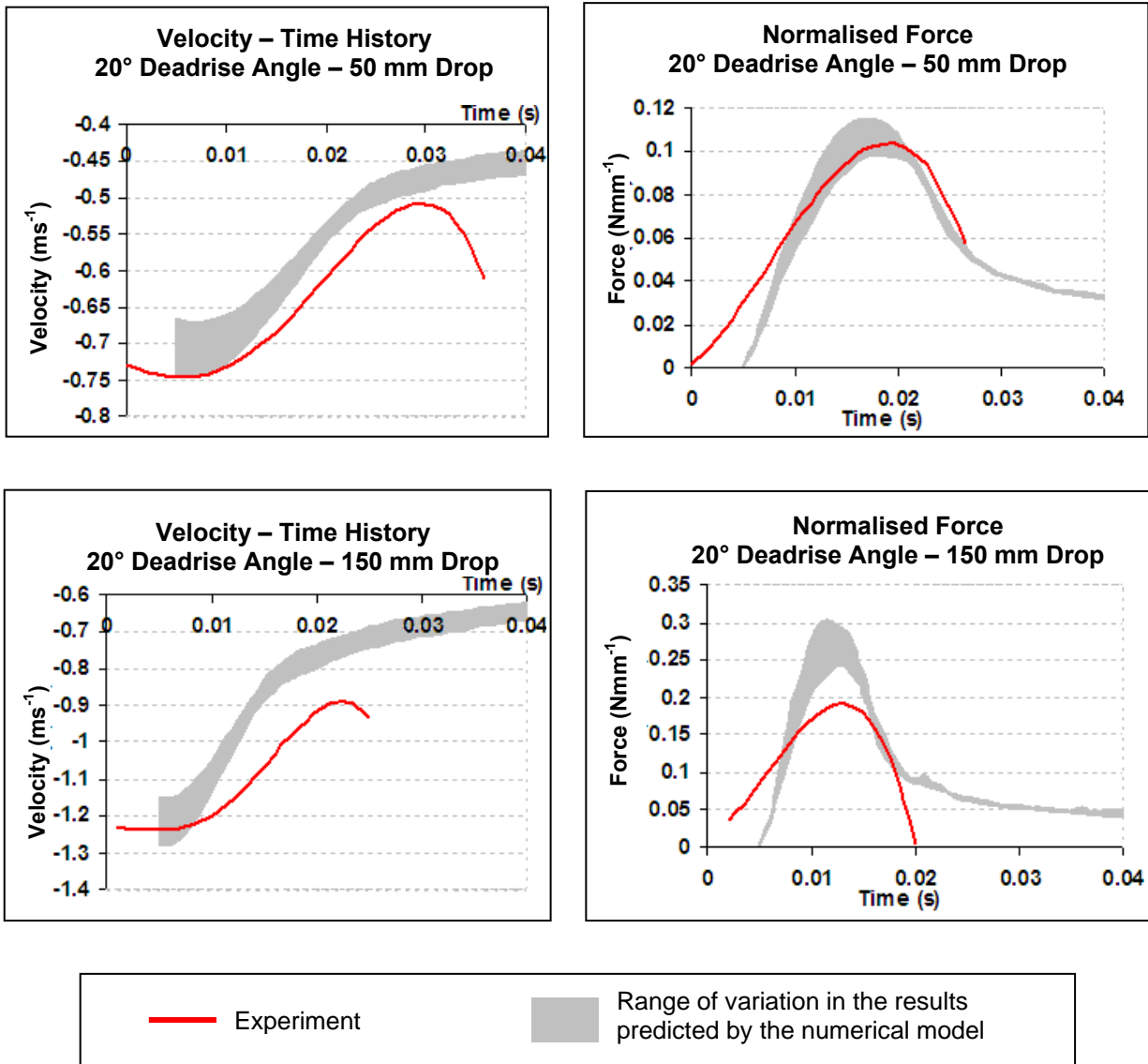
Theoretically, the impact velocity should have been the same for all the wedges of the same mass and drop height. The effect of variations of the impact velocity on the peak forces predicted by the simulations was investigated. An analysis was conducted for two extremes of the all the test configurations, namely the light impactor of 20° deadrise angle dropped from a height of 150 mm, and the light impactor of 40° deadrise angle dropped from a height of 50 mm. The former case theoretically had the highest impact energy and experienced the largest impact force, while the latter had the lowest impact energy and experienced the least impact force of all the test configurations. Additionally, velocity variations were also simulated for the same 20° wedge dropped from a height of 50 mm, and the same 40° wedge dropped from a height of 150 mm.

The velocity of the 20° wedge cases was reduced by 10% while that for the 40° wedge cases was increased by 10%. Table 16 details the range of impact velocity variation followed by the results in Figure 86 and Figure 87, which are presented as a range of variation of the kinematic-time histories due to a 10% variation in impactor velocity.

Velocity Variant	Variation in Velocity (%)	20° Deadrise Angle – Light Impactor	
		50 mm Drop Impact Velocity (ms <sup>-1</sup> )	150 mm Drop Impact Velocity (ms <sup>-1</sup> )
<i>Base model</i>	0	0.7400	1.281
Variant 1	-2	0.7252	1.255
Variant 2	-4	0.7104	1.230
Variant 3	-6	0.6956	1.204
Variant 4	-8	0.6808	1.179
Variant 5	-10	0.6660	1.153

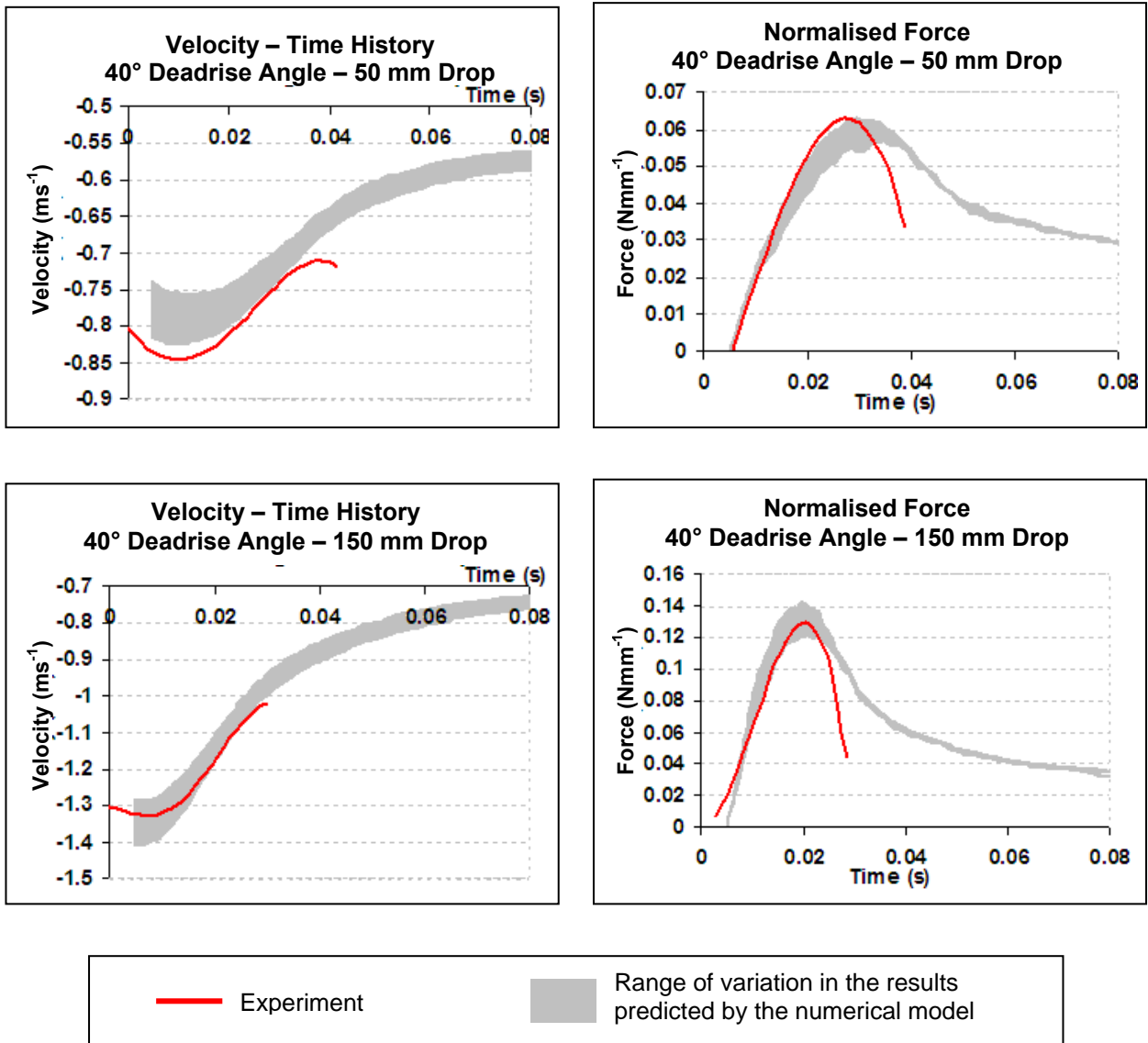
Velocity Variant	Variation in Velocity (%)	40° Deadrise Angle – Light Impactor	
		50 mm Drop Impact Velocity (ms <sup>-1</sup> )	150 mm Drop Impact Velocity (ms <sup>-1</sup> )
<i>Base model</i>	0	0.7400	1.281
Variant 1	+2	0.7548	1.307
Variant 2	+4	0.7696	1.332
Variant 3	+6	0.7844	1.358
Variant 4	+8	0.7992	1.383
Variant 5	+10	0.8140	1.409

**Table 16:** Impact velocity variations for 20° and 40° wedges



**Figure 86:** Correlation after impact velocity variation of 20° wedge

For the 20° wedge case, reducing the impact velocity by 10% resulted in a reduction in the peak acceleration of 15% and 19% for the 50 mm and 150 mm drops respectively. An improved correlation was achieved between the experiment and SPH models in the case of the lower drop height. However, the SPH model still predicted a larger impact acceleration for a 20° wedge released from a height of 150 mm, than that obtained through the experimental technique.



**Figure 87:** Correlation after impact velocity variation of 40° wedge

In the case of the 40° wedge, improved correlation trends were observed through an increase in the impact velocity for both drop heights of 50 mm and 150 mm.

This page is intentionally blank

## Chapter 8

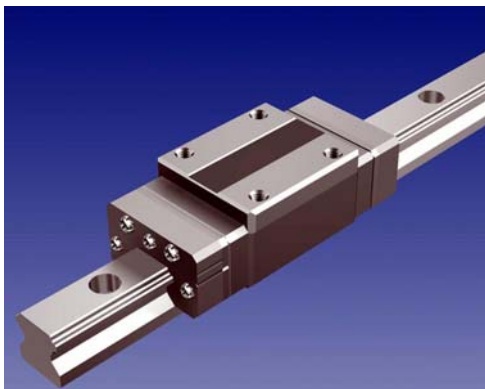
# DISCUSSION AND RECOMMENDATIONS

---

### 8.1 Experimental Observations

From the wedge water impact experiments conducted, several important issues have been highlighted and discussed as follows:

- There was a significant amount of friction in the guiding track. Although the frictional force was quantified as a constant based on the acceleration profiles obtained from the track under freefall, in reality the frictional force varies depending on the extension of the guiding track. This is because along different sections of the track, varied resistance is encountered by the ball bearings within the track. Considering the small scale of the experiment, guiding systems with reduced friction should be sought for future experiments to eliminate the force's effect on the kinematic response of the impacting wedges. Examples of potential guiding systems are the linear motion rail guides shown in Figure 88, or even air bearings which utilise a thin film of air between the two sliding surfaces. Although substantially more expensive than the mechanism adopted for this research, these advanced guiding systems are manufactured to high precision and quality in order to minimize friction and provide smooth and consistent motion through the range of movement.



(Source: ThomasNet 2009)



(Source: THK 2006)

**Figure 88:** Examples of linear motion guides with reduced friction

- Smooth variations occur in the physical system of the wedge impacting the water, which were not adequately represented by the discrete approximations in the data analysis of the experiment. Often, large discrepancies were observed in the acceleration predictions using the discrete approach, and therefore the polynomial approximations of the same provided a smoothed transition of the kinematic characteristics over time. The polynomial derivations of the velocity and acceleration profiles were, however, originally obtained from the discrete displacement data set and the polynomial accuracy was ultimately only as good as the point specification performed on the sequential images.
- As seen in section 5.5, large variations in the derived acceleration profiles, and hence force-time histories may have occurred for a given test configuration. These variations were observed throughout the test results and were sensitive to small inconsistencies in the displacement specification of tracking points. As a result, operator judgement had an appreciable influence on the experimentally derived results through the photographic approach used in this work.

The key problem with specifying the centre of the tracking point's image was the inconsistency of the image in sequential frames of the video capture due to a combination of lighting and shadow effects. A higher resolution camera could potentially alleviate this problem by capturing a sharper image of the point boundary that should result in more accurate definitions of the point images between frames.

Through a more consistent image of the point in progressive frames, the centroid of the area of the point can be obtained. In the 8 bit images captured, each pixel is assigned a particular greyscale value ranging from 0 to 255, with 0 representing white and 255 representing black. A threshold can be set such that greyscale values above this particular threshold would correspond to pixels associated with the point. This image can then be converted into black and white format, with the black area spanning the area of the point. The location of the centroid of the black area can then be obtained and specified as the centre of the point.

Further improvement in the point specification can also be obtained by increasing the point size on the wedge which would therefore cover more pixels in the image. With the current video resolution, coupling the larger point area with the centroid specification approach mentioned above should significantly reduce the variation in point specification. Through this, it is expected that the large variations in the peak acceleration predictions discussed in 5.6 would be considerably reduced.

These recommendations to improve point tracking should reduce the effect of operator judgement on the displacement specification and hence the experimentally derived results in general. The need for polynomials may be eradicated altogether or at the very least, better polynomial approximations could be obtained with less inherent variability due to the subjective factor.

An additional benefit of this is a significant reduction in the data-processing time that can be achieved by implementing the technique in a computational algorithm, for example with MATLAB<sup>®</sup> (MathWorks 2009), as opposed to the manual point specification performed in this research.

In conclusion, the following key issues have been identified that need to be addressed in future experiments of a similar nature:

- Friction within the impactor guiding systems should be minimised.
- The scale of the experiment should be increased so as to make the effects of minute variations in experimental test parameters more distinct.
- Accelerometers should be adopted for a good quantitative capture of the acceleration-time history, as opposed to using a photographic technique.
- Depending on the scale of the experiment, pressure transducers can pragmatically be incorporated into the testing (See section 8.4).

## **8.2 Numerical Analysis**

Excellent qualitative comparisons of the SPH models with the experiments of the wedge water impacts were observed. This highlighted the numerical method's ability to adequately represent the physics of the water through the impact event, and gave confidence to the quantitative predictions of the kinematics of the wedge.

Numerical instabilities were not encountered when capturing the high deformations occurring in the fluid domain in the close vicinity of the wedge. The combined approach of a SPH and Lagrangian formulation to represent the water trough was efficient and suitable to capture the kinematics of the system in the impact window of interest.

One of the major concerns with the numerical models was the loss in the energy of the system within the SPH domain. This loss in energy was not encountered when using a complete Lagrangian formulation, and accounted for approximately 13% to 23% of the total energy of the

wedge-water system. It was observed that the amount of energy lost increased as the severity of the impact increased causing larger accelerations within the SPH domain. As with all numerical modelling approaches, conservation of mass, momentum and energy form the cornerstone of the physical discretisation process, and this is the case with SPH.

For this reason, the loss in energy noticed in the models is unexpected and the source of this loss cannot be discerned through the available energy-monitoring controls in LS-DYNA®. This occurrence of energy loss with SPH in LS-DYNA® is not a unique case, and various users of the code reflect this problem (for example Schwer 2009). The physics of the impact, however, are sufficiently captured with the SPH method and the loss in energy could simply be an error within the algorithm that monitors the energy balance. In any case, this is an important aspect of the modelling that requires further investigation.

Through this research, the following suggestions have been proposed for adoption in future numerical analysis with SPH:

- For computational efficiency, SPH should be limited to regions of high deformation. The low-deformation regions of the water domain can be modelled using the standard Lagrangian formulation.
- A particle density analysis should always be carried out to observe its effect on the representation of the physics of the system. This is particularly important as the scale of the experiment increases, where a lower particle density to that selected in this thesis may be sufficient to maintain the efficiency and accuracy of the modelling approach.
- Gravitational loads applied to the water domain do not affect the qualitative and quantitative predictions of the impact kinematics for the immediate moments after impact. However, in extended analysis, particularly with deformable structural domains, this should be implemented to represent realistic post-impact fluid behaviour.
- The fluid formulation of the SPH particle approximation in LS-DYNA® should be adopted for further ditching simulations. The standard approximation and that with renormalisation should be continually evaluated and the differences between them would become more evident as complexities are introduced in the problem being modelled. A suitable particle approximation theory can thereby be selected for larger scale investigations representative of ditching scenarios.

### **8.3 General Comments**



Experimental force-time histories obtained through the video analysis approach in this research only provided an approximate representation of the physical system. It was often unclear as to the accuracy of these profiles for the higher and lower deceleration cases due to the small scale of the experiment and difficulties associated with the point specification. Higher resolution data acquisition is required to be able to capture the intricate variations through the wedge impacts. This could be facilitated through the use of accelerometers to quantitatively and more accurately measure the impact kinematics.

In summary, a better set of experimental data is required for a more accurate comparison of the peak impact forces between the SPH model predictions and experimental derivations. Preferably, the experiment should be conducted on a larger scale which would make the experiment less sensitive to minor variations in the setup and data capture techniques. The experimentally derived results in this research cannot be deemed entirely accurate, and therefore intricate behaviours and patterns occurring within the experiment cannot be discerned. Logical and smoother trends were observed through the SPH simulations of the impacts, and these results can supplement the shortcomings of the experiment.

In general, the SPH modelling approach evaluated with LS-DYNA® showed excellent qualitative comparisons with the test results and strongly favourable quantitative predictions. The characteristic behaviour of the water was represented well with this numerical modelling technique. This aligns with the objective of applying the SPH technique to develop water-crashworthy structures where an accurate evolution of the water domain over time is important when simulating ditching events, particularly when complex fluid-structure interactions are present due to deformable structural design.

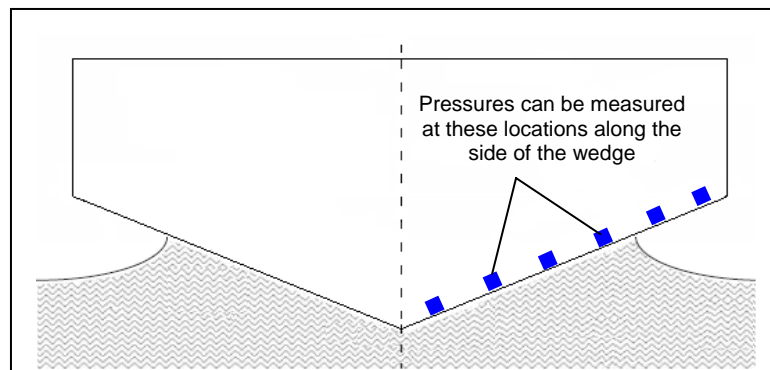
## **8.4 Future Work**

The work carried out through this research has shown that SPH has great potential to efficiently simulate the ditching case with adequate accuracy. However, due to the lack of confidence in the experimentally derived results, it is suggested that further experiments be conducted to generate accurate quantitative data in terms of local pressures and accelerations. These tests should incorporate the improved data acquisition techniques outlined in section 8.1.

With regards to the problem of energy conservation with the SPH models in LS-DYNA®, alternate FE codes with SPH modelling capabilities, for example PAM-CRASH™, should be used to simulate the test configurations in this research. A comparison between LS-DYNA® and the

other FE codes would identify whether the problem of energy loss is inherent only within the LS-DYNA® solver. Work should be directed towards determining the source of this energy loss, and understanding its effect on the interpretation of the modelling results.

A recommended follow through of this work would be to conduct similar experiments of rigid wedges impacting water on a larger scale. Important considerations in the development of these tests pertain to minimizing the friction effects of any implemented guiding systems, whilst incorporating advanced and sophisticated data acquisition techniques to obtain accurate pressure-time histories and wedge accelerations.



**Figure 89:** Measuring localised pressures in future experimentation

In addition to experimentally determining the overall force experienced by the wedge upon impact, a similar testing program to that presented and discussed by Yettou *et al.* (2006) should be followed to capture the localised pressure variation along the sides of the wedge as the wedge penetrates the free surface (see Figure 89). The SPH method can then be applied to model this problem and evaluated on its predictions of localised pressures.

The range of testing parameters can be extended from those investigated in this thesis to smaller deadrise angles and impactors with higher impact velocities, introducing possible compressibility effects into the modelling equation. Other rigid impactors such as non-symmetrical wedges, cylinders and spheres can be investigated in experimental tests and SPH models through quantitative and qualitative comparisons. This would provide for further evaluations of the numerical method through studying a wider range of water impact configurations. Fundamentally, this would establish the confidence with SPH modelling and provide a framework of modelling techniques and parameters that need to be adopted for simulating water impacts of deformable structures.

Following this, the next step would be to assess the ability of the numerical modelling technique for rigid body-fluid interaction whereby the impactor is still constrained to move vertically but can rotate freely in the 2D plane. Attention should be paid to the qualitative behaviour of the

entire system, as this would give an insight and set the foundation for the subsequent investigations into fluid-structure interaction (FSI) problems.

As more confidence is gained with the SPH method's applicability for accurate capture of the physics of fluid-body interaction, deformity can progressively be introduced into the impacting structures. The fluid-structure interaction can therefore be investigated both at the experimental level and numerical modelling platform through an evaluation of the SPH method on its interaction with deformable Lagrangian domains. This would be representative of the actual occurrence during an aircraft ditching event, where large deformations of the fluid and structural domains are common.

As discussed previously in the literature review, ALE is another popular numerical modelling technique used for water impact modelling. This technique should also be evaluated in a similar research structure to that discussed above for the SPH approach. A comparative study of these numerical methods should be conducted and their strengths and weaknesses further identified.

Through the above outlined progressive approach, a numerical modelling methodology can be developed and rigorously evaluated for simulating high deformation problems pertaining to impacts onto water. Additionally, on the global scale, it is also important to ensure that accurate numerical models of structures that can adequately predict the material response are coupled with the favourable water modelling approach. This would evolve into a wholly predictive modelling methodology applicable to water crashworthiness design.

This page is intentionally blank

# Chapter 9

## CONCLUSIONS

---

The fundamental wedge water impact problem has been investigated in this research through experimentation and numerical modelling. Impact tests of rigid wedges into a tank of water were successfully conducted. A sufficiently 2D fluid-flow was generated through the experimental setup and excellent progression of the impact was captured on video.

Quantitative derivatives of the experimental results involved considerable variations and were sensitive to slight inconsistencies in the data processing methods. This was due to the small scale of the experiment coupled with the sensitivity of the acceleration predictions through the photographic technique employed. A discussion of the associated issues with this preliminary investigation into water impact is presented in this thesis and improvements to be adopted in further experimentation have been identified.

Numerical models of the experimental tests were successfully simulated using the Smoothed Particle Hydrodynamics capability in LS-DYNA®. Difficulties were associated with the quantitative validation of the models due to the variability encountered within the experimental results. Furthermore, poor model energy conservation was identified with the SPH solver. This is an important issue that needs to be investigated. Despite this, excellent qualitative and favourable quantitative validation with the experimental tests shows that the SPH method captures the physics of the rigid body impact onto water sufficiently well.

The objectives of this particular research project have been achieved, and recommendations on the future direction of applying the SPH technique for water crashworthiness problems have been presented. Through this pragmatic approach, it is envisaged that an SPH modelling methodology will be developed to provide the capability of accurately representing and developing crashworthy structural concepts to improve passenger survivability in aircraft ditching events.

This page is intentionally blank

# Chapter 10

## REFERENCES

---

- Anghileri, M., Castelletti, L. M.-L. and Francesconi, E. 2007, 'Water impact: experimental tests and numerical simulations using meshless methods', 6<sup>th</sup> European LS-DYNA Users' Conference, 29-30 May, Gothenburg, Sweden
- Anghileri, M. and Spizzica, A. 1995, 'Experimental validation of finite element models for water impacts', 2<sup>nd</sup> International Crash Users Seminar, Cranfield, UK
- Baker, W. E. and Westine, P. S. 1967, 'Model tests for structural response of Apollo command module', *Journal of Spacecraft and Rockets*, vol.4, no. 2, pp. 201-208
- Belytschko, T., Krongauz, Y., Organ, D., Fleming, M. and Krysl, P. 1996, 'Meshless methods: An overview and recent developments', *Computer Methods in Applied Mechanics and Engineering*, vol. 139, no. 1, pp. 3-47
- Bensch, L., Shigunov, V. and Beuck, G. 2001, 'Planned ditching simulation of a transport plane', KRASH User's seminar, Phoenix, Arizona, USA
- Benscoter 1947, *Impact theory for seaplane landings*, U.S. Navy Structures Project, Report No NACA-TN-1437
- Bisagni, C. 2002, 'Crashworthiness of helicopter subfloor structures', *International Journal of Impact Engineering*, vol. 27, no. 10, pp. 1067-1082
- Breder, J. 2005, *Experimental testing of slamming pressure on a rigid marine panel*, Master of Engineering Thesis, The Royal Institute of Technology, Stockholm, Sweden
- Brown, D. 2009, *Tracker - Free video analysis and modelling tool for physics education*, <<http://www.cabrillo.edu/~dbrown/tracker/>>
- Buyukozturk, O., Hibbit, H. D. and Sorensen, E. P. 1974, *Water impact analysis of space shuttle solid rocket motor by the finite element method*, Marshall Space Flight Center, NASA-TR73-7, Alabama, USA
- Candy, E. G., Kirk, N. E. and Murrell, P. 1998, 'Helicopter water impact analysis using LS DYNA3D', *Institution of Mechanical Engineers*, vol. 9, pp. 115-126
- Candy, E. G., Kirk, N. E. and Murrell, P. J. 2000, 'Airframe water impact analysis', *International Journal of Crashworthiness*, vol. 5, no. 1, pp. 51-62

Chuang, S.-L. 1966, *Slamming of rigid redge-shaped bodies with various deadrise angles* David Taylor Model Basin, Department of the Navy, Report 2268

Clarke, C. W. and Shen, Y. 1998, 'The development of a rotorcraft water impact methodology', AHS/SAFE Crashworthiness Specialists Meeting on Crash Safety, 14-17 September, Phoenix, Arizona, USA

Climent, H., Benitez, L., Rosich, F., Rueda, F. and Pentecote, N. 2006, 'Aircraft ditching numerical simulation', 25<sup>th</sup> International Congress of the Aeronautical Sciences, 3-8 September, Hamburg, Germany

Cointe, R. 1989, 'Two-dimensional water solid impact', *Journal of Offshore Mechanics and Arctic Engineering*, vol. 111, pp. 109-114

Crane, C. L. 1961, *A photographic study of water impact parameters and flow*, Master of Science Thesis, Stevens Institute of Technology, Hoboken, New Jersey, USA

Crewe 1946, *A proposed theory to cover water impacts of seaplanes in which the craft has constant attitude and a tangential to keel velocity relative to the water*, Aeronautical Research Council, Report No ARC-10492, HMSO London

Cui, S., Cheong, H. K. and Hao, H. 2000, 'Experimental study of dynamic post buckling characteristics of columns under fluid solid slamming', *Engineering Structures*, vol. 22, pp. 647-656

Dee Mon (2009). *Video Enhancer*®. Infognition Co. Ltd.  
<<http://www.thedeemon.com/VideoEnhancer/>>

Donguy, B., Peseux, B., Gornet, L. and Fontaine, E. 2001, 'Three dimensional hydroelastic water entry: preliminary results', 11<sup>th</sup> International Offshore and Polar Engineering conference, 17-22 June, Stavanger, Norway, 324-330

DSM 2009, *Dyneema, the world's strongest fiber*,  
<[http://www.dsm.com/en\\_US/html/hpf/home\\_dyneema.htm](http://www.dsm.com/en_US/html/hpf/home_dyneema.htm)>

Engle, A. and Lewis, R. 2003, 'A comparison of hydrodynamic impact prediction methods with two dimensional drop test data', *Marine Structures*, vol. 16, pp. 175-182

Evonik-Industries 2009, *ROHACELL*, <[www.rohacell.com](http://www.rohacell.com)>

Faltinsen, O. M. 1990, 'Water impact and entry', in *Sea Loads on Ships and Offshore Structures*, Cambridge University Press, pp. 282-315

Faltinsen, O. M. 2000, 'Hydroelastic slamming', *Journal of Material Science and Technology*, vol. 5, pp. 49-65



- Fasanella, E. L., Jackson, K. E., Sparks, C. E. and Sareen, A. K. 2003, 'Water impact test and simulation of a composite energy absorbing fuselage section', American Helicopter Society 59<sup>th</sup> Annual Forum, 6-8 May, Phoenix, AZ, USA
- Ferziger, J. H. 1998, *Numerical methods for engineering application*, 2<sup>nd</sup> ed., Wiley-Interscience, Canada
- Francesconi, E. and Anghileri, M. 2009, 'A numerical-experimental investigation on crash behaviour of skin panels during a water impact comparing ALE and SPH approaches', 7<sup>th</sup> European LS-DYNA Users Conference, 14-15 May 2009, Salzburg, Austria
- Francesconi, E., Anghileri, M., Castelletti, L. M. L. and Pittofrati, M. 2008, 'Survey of feasible numerical approaches to analyse the behaviour of a composite skin panel during a water impact', 26<sup>th</sup> International Congress of the Aeronautical Sciences, 14-17 September, Anchorage, Alaska, USA
- Gingold, R. A. and Monaghan, J. J. 1977, 'Smoothed particle hydrodynamics - Theory and application to non-spherical stars', Royal Astronomical Society, Monthly Notices, vol. 181, pp. 375-389
- Hughes, K., Campbell, J. and Vignjevic, R. 2008, 'Application of the finite element method to predict the crashworthy response of a metallic helicopter under floor structure onto water', *International Journal of Impact Engineering*, vol. 35, no. 5, pp. 347-362
- Hughes, O. F. 1972, 'Solution of the wedge entry problem by numerical conformal mapping', *Journal of Fluid Mechanics*, vol. 56, no. 1, pp. 173-192
- Jackson, K. E. and Fasanella, E. L. 2005, 'Crash simulation of a vertical drop test of a commuter-class aircraft', *International Journal of Crashworthiness*, vol. 10, no. 2, pp. 173-182
- Jackson, K. E. and Fuchs, Y. T. 2008, 'Comparison of ALE and SPH simulations of vertical drop tests of a composite fuselage section into water', 10<sup>th</sup> International LS-DYNA Users Conference, 8-10 June, Dearborn, MI, US
- Karman, T. v. 1929, *The impact of seaplane floats during landing*, National Advisory Committee for Aeronautics, TN 321, Washington, USA
- Kennedy, J. M. 2009, Ph.D., KBS2 Inc., Burr Ridge, IL, USA
- Kermanidis, T., Labeas, G., Apostopoulos, C. and Michielsen, L. 1998, 'Numerical simulation of composite aircraft structures under impact', 5<sup>th</sup> International Conference on Structures under Shock and Impact, 24-26 June, Thessaloniki, Greece, 591-600
- Kindervater, C. M., Kohlgruber, D. and Johnson, A. 1999, 'Composite vehicle structural crashworthiness - A status of design methodology and numerical simulation techniques', *International Journal of Crashworthiness*, vol. 4, no. 2, pp. 213-230

- Korobkin, A. A. and Pukhnachov, V. V. 1988, 'Initial stage of water impact', *Annual Review of Fluid Mechanics*, vol. 20, pp. 159-185
- Lacome, J. L. 2004, 'Smoothed particle hydrodynamics method in LS-DYNA', 3<sup>rd</sup> LS-DYNA Forum, 14-15 October, Bamberg, Germany
- Lacome, J. L. 2009, 'SPH formulations - New developments in LS-DYNA', 7<sup>th</sup> European LS-DYNA Conference 2009, 14-15 May 2009, Salzburg, Austria
- Lepi, S. M. 1998, *Practical guide to finite elements*, Marcel Dekker, USA
- Libersky, L. D., Petschek, A. G., Carney, T. C., Hipp, J. R. and Allahdadi, F. A. 1993, 'High strain lagrangian hydrodynamics', *Journal of Computational Physics*, vol. 109, pp. 67-75
- Liu, G. R. 2002, *Mesh free methods for fluid dynamics problems*, CRC Press
- Liu, G. R. and Liu, M. B. 2003, *Smoothed particle hydrodynamics - a meshfree particle method*, World Scientific Publishing, Singapore
- LSTC 2005, 'LS-DYNA theory manual', *Livermore Software Technology Corporation*
- LSTC 2007, 'LS-DYNA keyword user's manual', *Livermore Software Technology Corporation*
- Lu, C. and He, Y. 1998, 'Nonlinear fluid-structure interaction during two dimensional water impact', 3<sup>rd</sup> International Conference on nonlinear mechanics, 17-20 August, Shanghai, China, 513-517
- MathWorks 2009, *MATLAB - Image and Video Processing*, <[www.mathworks.com](http://www.mathworks.com)>
- Matthew 2009, *Importance of total energy conservation*, LS-DYNA User Group Blog, <<http://tech.dir.groups.yahoo.com/group/LS-DYNA/>>
- May, A. 1970, 'A review of water entry theory and data', *Journal of Hydronautics*, vol. 4, no. 4, pp. 140-142
- Mayo 1945, *Analysis and modifications of theory for impact of seaplanes on water*, NASA Langley Research Center, Report No NACA-TR-810, NACA Annual Report 31, pp. 71-82
- McCarthy, M. A., Harte, C. G., Wiggenraad, J. F. M., Michielsen, A. L. P. J., Kohlgruber, D. and Kamoulakos, A. 2000, 'Finite element modelling of crash response of composite aerospace sub-floor structures', *Computational Mechanics*, vol. 26, no. 3, pp. 250-258
- McGehee, J. R., Hathaway, M. E. and Vaughan, V. L. 1959, *Water landing characteristics of a re-entry capsule*, NASA Langley Research Center, Memorandum 5-23-59L, Hampton, VA USA
- Mei, X., Liu, Y. and Yue, D. K. P. 1999, 'On the water impact of general two-dimensional sections', *Applied Ocean Research*, vol. 21, pp. 1-15

- Monaghan, J. J. 1988, 'An introduction to SPH', *Computer Physics Communications*, vol. 48, pp. 89-96
- Monaghan, R. J. 1952, *A review of the essentials of impact force theories for seaplanes and suggestions for approximate design formulae*, Aeronautical Research Council, Rep. Mem. 2720, London, UK
- Oger, G., Doring, M., Alessandrini, B. and Ferrant, P. 2006, 'Two-dimensional SPH simulations of wedge water entries', *Journal of Computational Physics*, vol. 213, pp. 803-822
- Ortiz, R., Portemont, G., Charles, J. L. and Sobry, J. F. 2002, 'Assessment of explicit FE capabilities for full scale coupled fluid/structure aircraft ditching simulations', 23<sup>rd</sup> International Congress of the Aeronautical Sciences, 8-13 September, Toronto, Canada
- Pentecote, N. and Kindervater, C. M. 1999, 'Airframe water impact analysis using a local/global methodology', American Helicopter Society 55<sup>th</sup> Annual Forum, 25-27 May, Montreal, Canada, 1633-1643
- Pentecote, N. and Vigliotti, A. 2003a, 'Crashworthiness of helicopters on water: Test and simulation of a full-scale WG30 impacting on water', *International Journal of Crashworthiness*, vol. 8, no. 6, pp. 559-572
- Pentecote, N., Kohlgruber, D. and Kamoulakos, A. 2003b, 'Simulation of water impact problems using the smoothed particle hydrodynamics method', International Conference on Technological Innovation for Land Transportation (TILT), 2-4 December, Lille, France
- RAFAEL 2005, *Rotorcraft external airbag protection system (REAPS)*, <<http://defense-update.com/products/r/reaps.htm>>
- Randhawa, H. S. and Lankarani, H. M. 2003, 'Finite element analysis of impacts on water and its application to helicopter water landing and occupant safety', *International Journal of Crashworthiness*, vol. 8, no. 2, pp. 189-200
- Sareen, A. K., Smith, M. R. and Hashish, E. 1999, 'Crash analysis of an energy absorbing subfloor during ground and water impacts', American Helicopter Society 55<sup>th</sup> Annual Forum, 25-27 May, Montreal, Canada
- Schwer, L. E. 2009, Ph.D., Schwer Engineering & Consulting Services, Windsor, CA, USA
- Seddon, C. M. and Moatamedi, M. 2006, 'Review of water entry with applications to aerospace structures', *International Journal of Impact Engineering*, vol. 32, no. 7, pp. 1045-1067
- Shao, S. 2008, 'Incompressible SPH simulation of water entry of a free-falling object', *International Journal for Numerical Methods in Fluids*, vol. 59, no. 1, pp. 91-115
- Shoji, H., Minegishi, M., Miyaki, H. and Iwasaki, K. 2008, 'Hydrodynamic impact estimation of transport fuselage structure with vertical drop water impact tests', 49<sup>th</sup>

AIAA/ASME/ASCE/AHS/ASC Structures, Structural Dynamics, and Materials Conference, 7-10 April, Schaumburg, IL, USA

Stellingwerf, R. F. and Wingate, C. A. 1993, 'Impact modelling with smooth particle hydrodynamics', Smooth Particle Hydrodynamics in Astrophysics, Trieste, Italy

Stenius, I. 2006, *Finite element modelling of hydroelasticity in hull-water impacts*, KTH Centre for Naval Architecture, Stockholm, Sweden

Stubbs, S. M. 1967, *Dynamic model investigation of water pressures and accelerations encountered during the landings of the Apollo spacecraft*, NASA, TN D - 3980, Washington DC, USA

Taylor, A. P. 2002, 'Developments in the application of LS-DYNA to fluid structure interaction (FSI) problems in recovery system design and analysis', 7<sup>th</sup> International LS-DYNA Users Conference, 19-21 May, Detroit, USA

THK 2006, Linear Ball Slide. THK Co. Ltd.  
<<http://www.thk.com/eng/products/class/linearballslide/index.html>>

ThomasNet 2009. *Linear motion guide operates in medium to low vacuum*. Thomas Publishing Company. <<http://news.thomasnet.com/fullstory/492631>>

Thompson, W. C. 1972, *Ditching investigation of a 1/30-scale dynamic model of a heavy jet transport airplane*, NASA Langley Research Centre, L-7841

Thuis, H. G. S. J., Vries, H. P. J. D. and Wiggenraad, J. F. M. 1995, 'Sub-floor skin panels for improved crashworthiness of helicopters in case of water impact', American Helicopter Society 51<sup>st</sup> Annual Forum, 9-11 May, Fort Worth, Texas USA, pp. 600-607

Thuis, H. G. S. J. and Wiggenraad, J. F. M. 1994, 'A tensor skin concept for crashworthiness of helicopters in case of water impact', American Helicopter Society 50<sup>th</sup> Annual Forum, 11-13 May, Washington DC, USA, pp. 547-555

Tutt, B. A. and Taylor, A. P. 2004, 'The use of LS-DYNA to simulate the water landing characteristics of space vehicles', 8<sup>th</sup> International LS-DYNA Users Conference, 2-4 May, Detroit, USA

Ubels, L. C. and Wiggenraad, J. F. M. 2002, *Increasing the survivability of helicopter accidents over water*, National Aerospace Laboratory NLR, NLR-TP-2002-110

Vignjevic, R. 2004, *Review of development of the smooth particle hydrodynamics (SPH) method*, Cranfield University, UK

Vignjevic, R. and Meo, M. 2001, 'Simulation of helicopter under-floor structure impact on water', *International Journal of Crashworthiness*, vol. 6, no. 3, pp. 425 - 443

Vignjevic, R. and Meo, M. 2002, 'A new concept for a helicopter sub-floor structure crashworthy in impacts on water and rigid surfaces', *International Journal of Crashworthiness*, vol. 7, no. 3, pp. 321-330

Wagner 1932, 'Phenomena associated with impact and gliding on a liquid surface', *Journal of Applied Mathematics and Mechanics*, vol. 12, no. 4, pp. 193-215

Wiggenraad, J. F. M., Santoro, D., Lepage, F., Kindervater, C. and Manez, H. C. 2001, *Development of a crashworthy composite fuselage concept for commuter aircraft*, National Aerospace Laboratory NLR, NLR-TP-2001-108

Wiggenraad, J. F. M., Michielsen, A. L. P. J., Santoro, D., Lepage, F., Kindervater, C. and Beltran, F. 2000, *Development of a crashworthy composite fuselage structure for a commuter aircraft*, National Aerospace Laboratory NLR, NLR-TP-99532

Wittlin, G., Schultz, M. and Smith, M. R. 2000, 'Rotary wing aircraft water impact test and analyses correlation', American Helicopter Society 56<sup>th</sup> Annual Forum, 19-21 January, Virginia, USA

Wittlin, G., Smith, M. and Richards, M. 1997, 'Airframe water impact analysis using a combined MSC/DYTRAN-DRI/KRASH approach', American Helicopter Society 53<sup>rd</sup> Annual Forum, 29 April-1 May, Virginia Beach, VA, USA, pp. 1138-1150

Yettou, E.-M., Desrochers, A. and Champoux, Y. 2006, 'Experimental study on the water impact of a symmetrical wedge', *Fluid Dynamics Research*, vol. 38, pp. 47-66

Zhang, Q., Qin, Q. and Wang, J. 1993, 'A theoretical model on coupled fluid structure impact', *Applied Mathematical Modelling*, vol. 17, no. 1, pp. 25-33

Zhao, R. and Faltinsen, O. 1993, 'Water entry of two-dimensional bodies', *Journal of Fluid Mechanics*, vol. 246, pp. 593-612

This page is intentionally blank

## **Appendix I**

### **Curve Shifting for Experimental Analysis**

The raw displacement data obtained from point specification in Tracker<sup>®</sup> was often out-of-phase in time due to varied lengths of video strips which all begin with  $t$  set to 0 s. Therefore, appropriate adjustments were made to shift the displacement-time histories such that they all followed the same temporal variation. This made it possible to identify any outliers, and also average the displacement data between all three curves for each test configuration.

Figure 90 graphs the raw data obtained from Tracker<sup>®</sup> and the results of the curve shifts which makes the data suitable for further analysis.

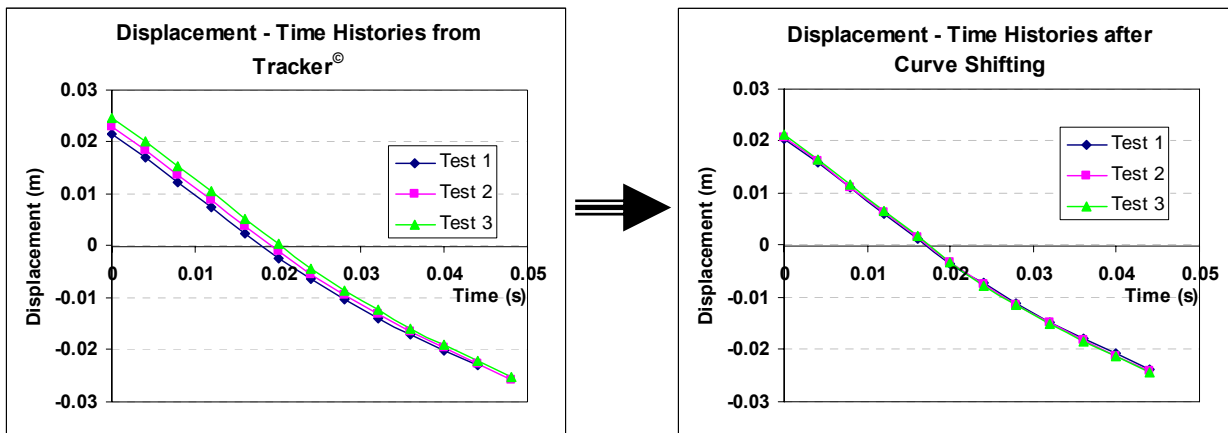


Figure 90: Curve shifting for experimental data processing

The only outlier that was identified from the entire data set is plotted in Figure 91. This was for the heavy impactor with a 35° deadrise angle and dropped from a height of 50 mm. It can clearly be seen that the Test 1 curve does not follow the trend shown by the other two tests.

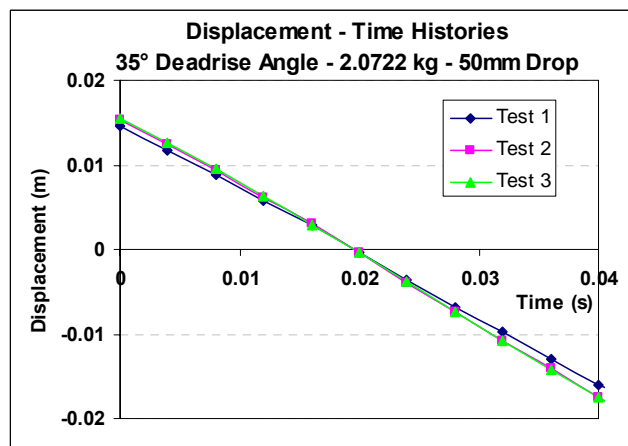


Figure 91: Identification of an outlier within an experimental data set

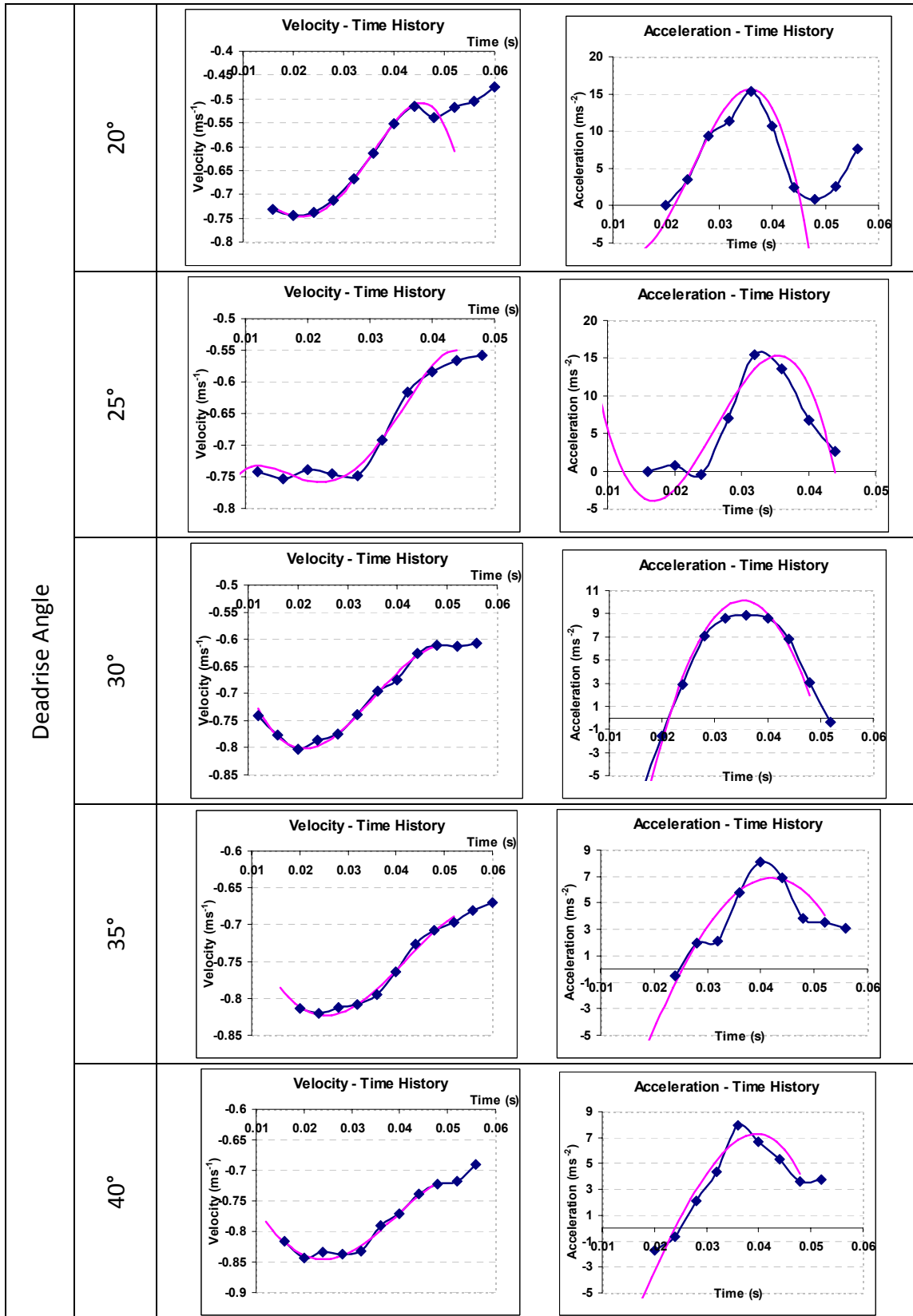


## **Appendix II**

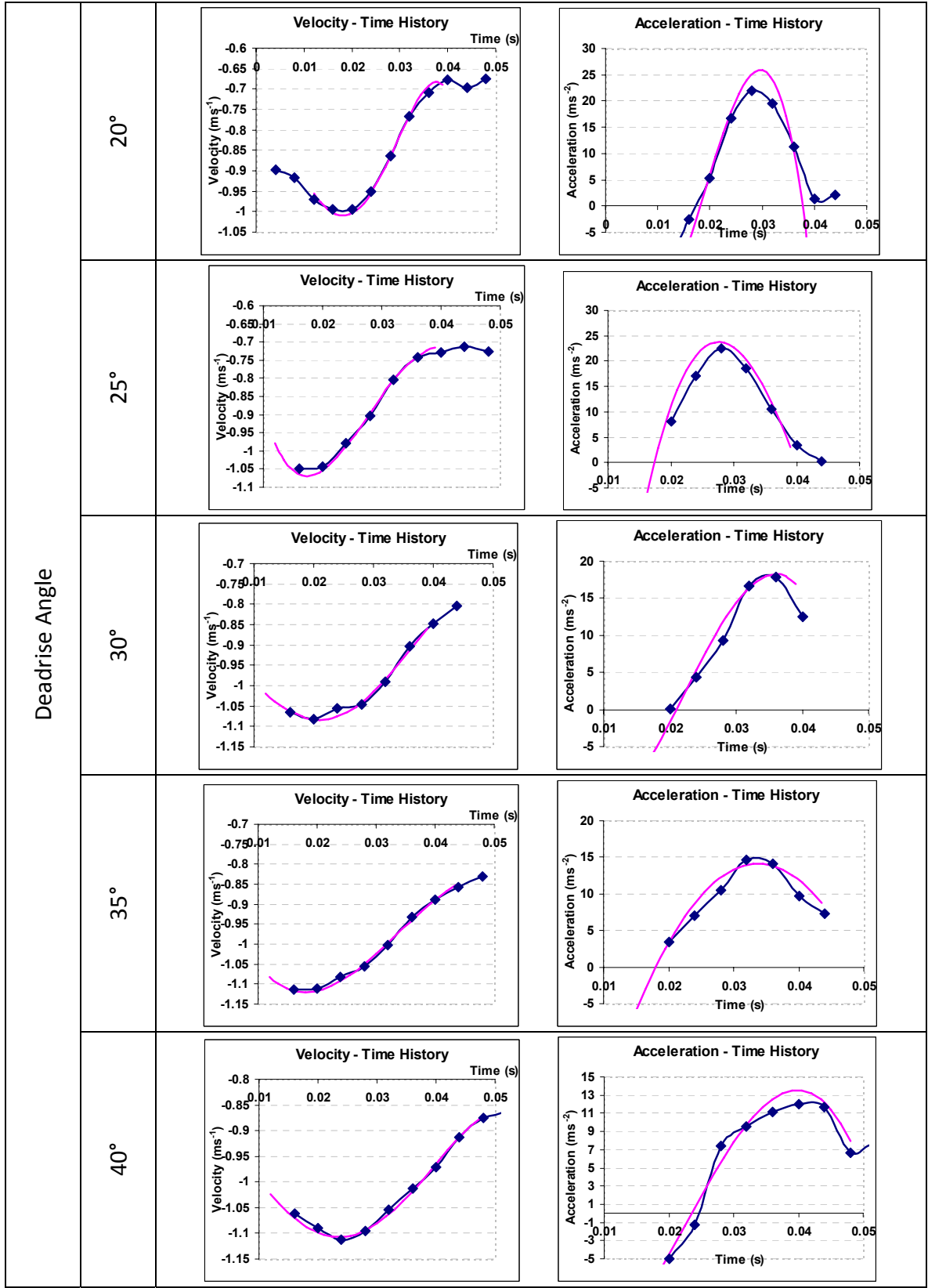
### **Experimental Test Results**

Velocity and acceleration-time histories for all the test configurations are plotted using both the discrete method and polynomial approximations. The plots of the discrete method are obtained from the average of the three different displacement data sets for each configuration, excluding any identifiable outliers.

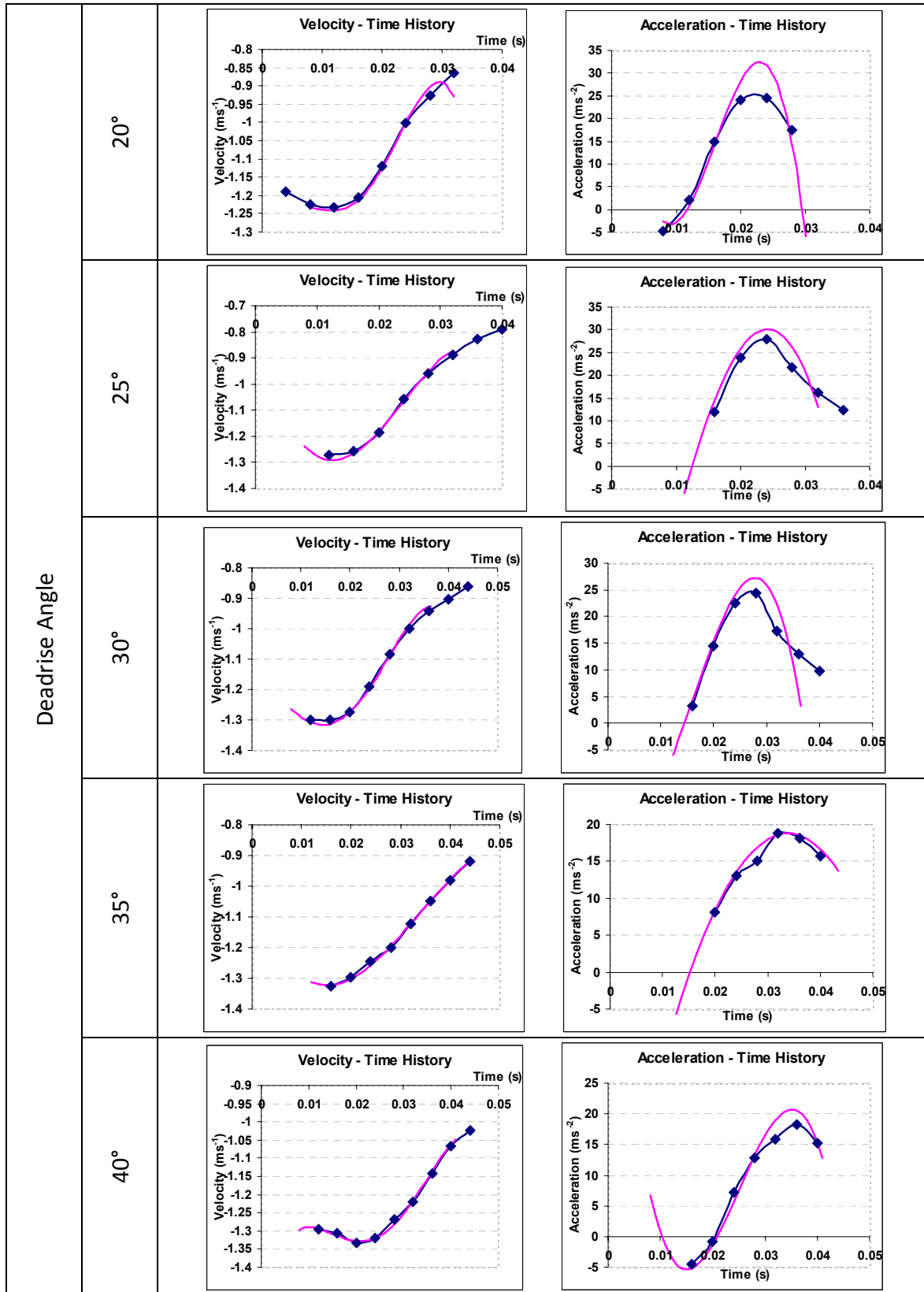
# Light Impactor - 50 mm Drop Height



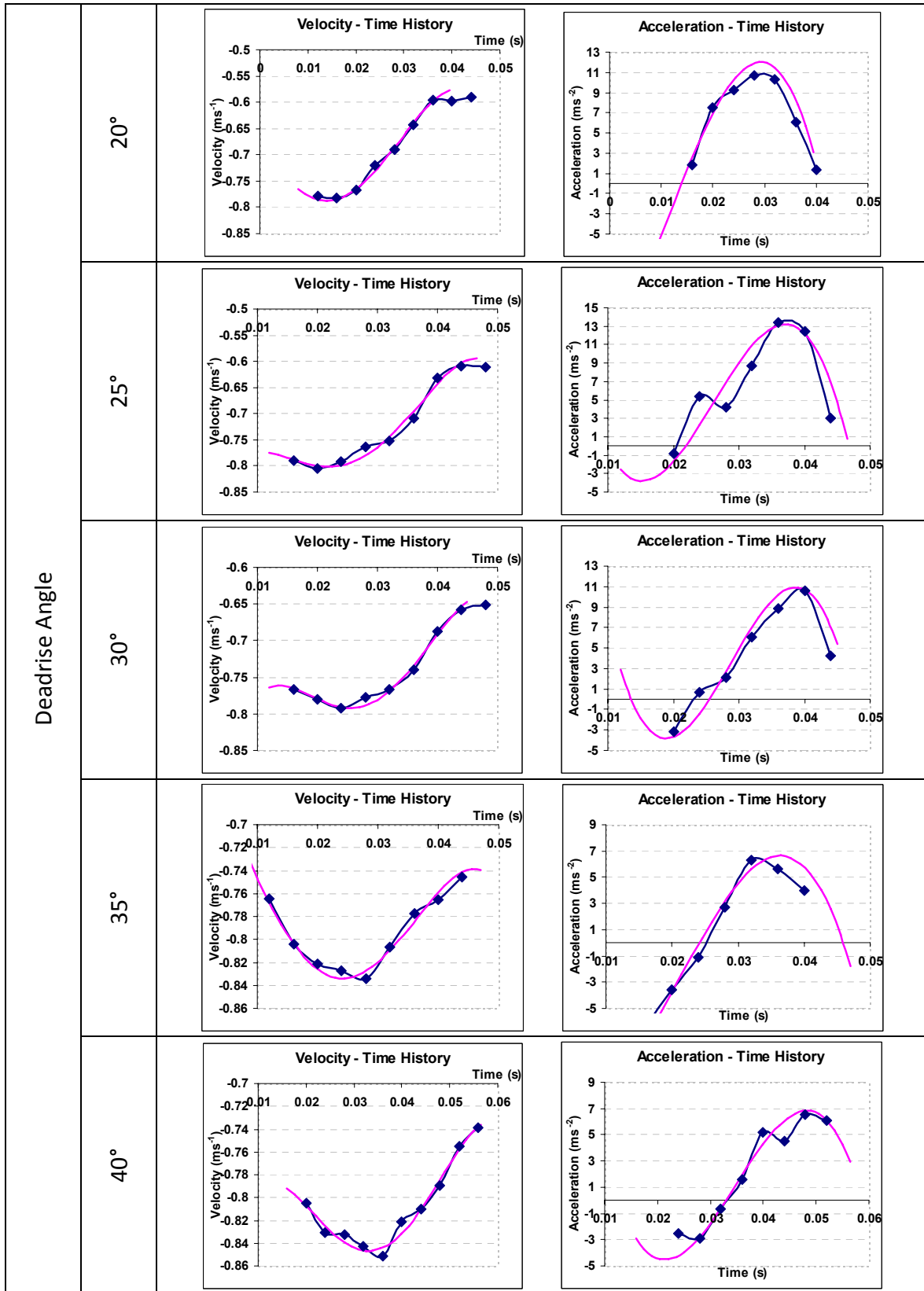
# Light Impactor - 100 mm Drop Height



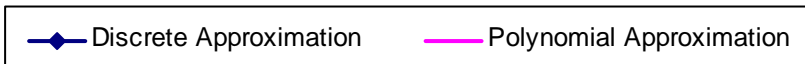
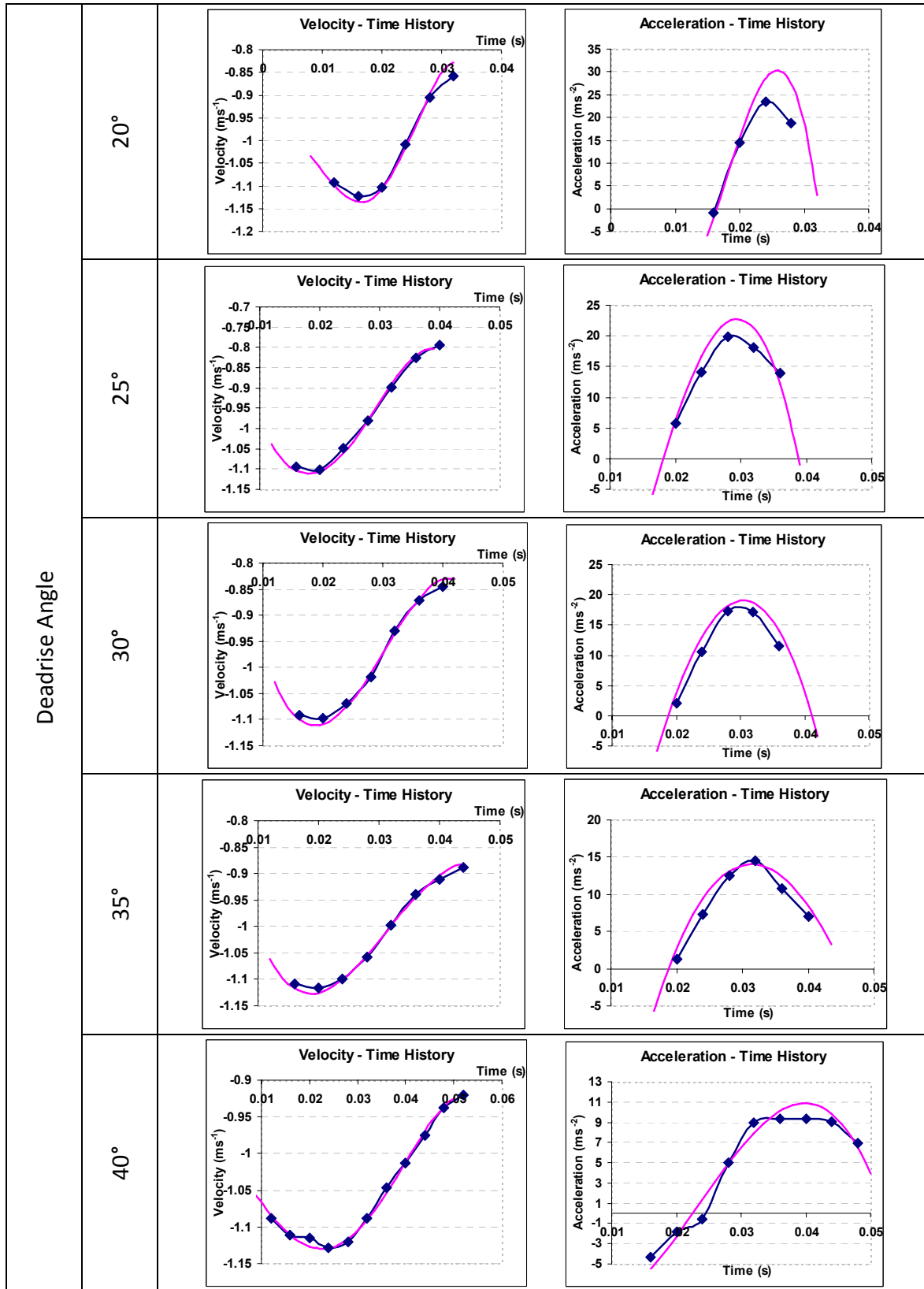
# Light Impactor - 150 mm Drop Height



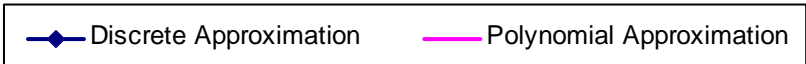
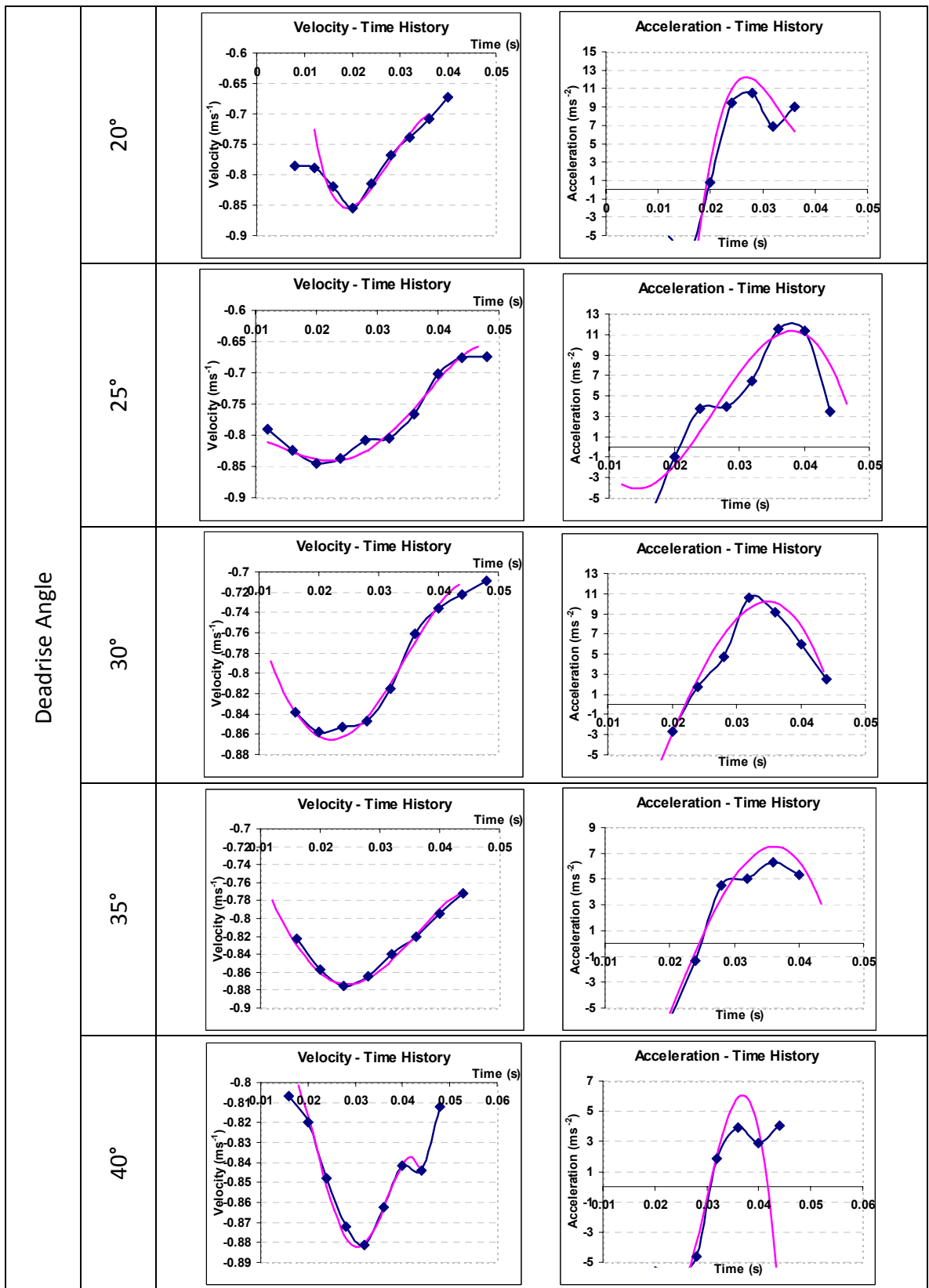
# Intermediate Impactor - 50 mm Drop Height



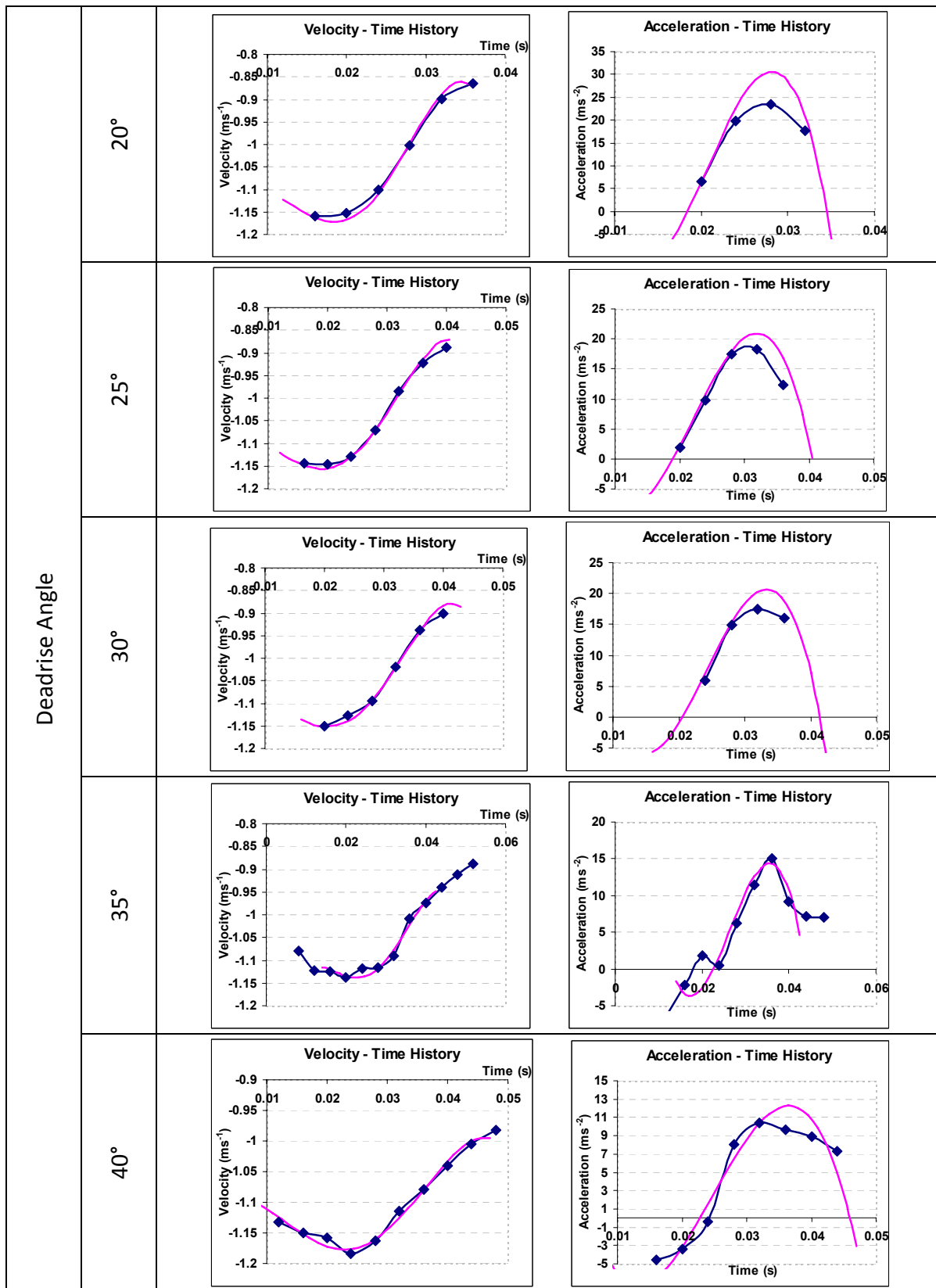
### Intermediate Impactor - 100 mm Drop Height



### Heavy Impactor - 50 mm Drop Height



**Heavy Impactor - 100 mm Drop Height**

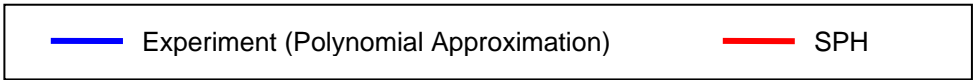
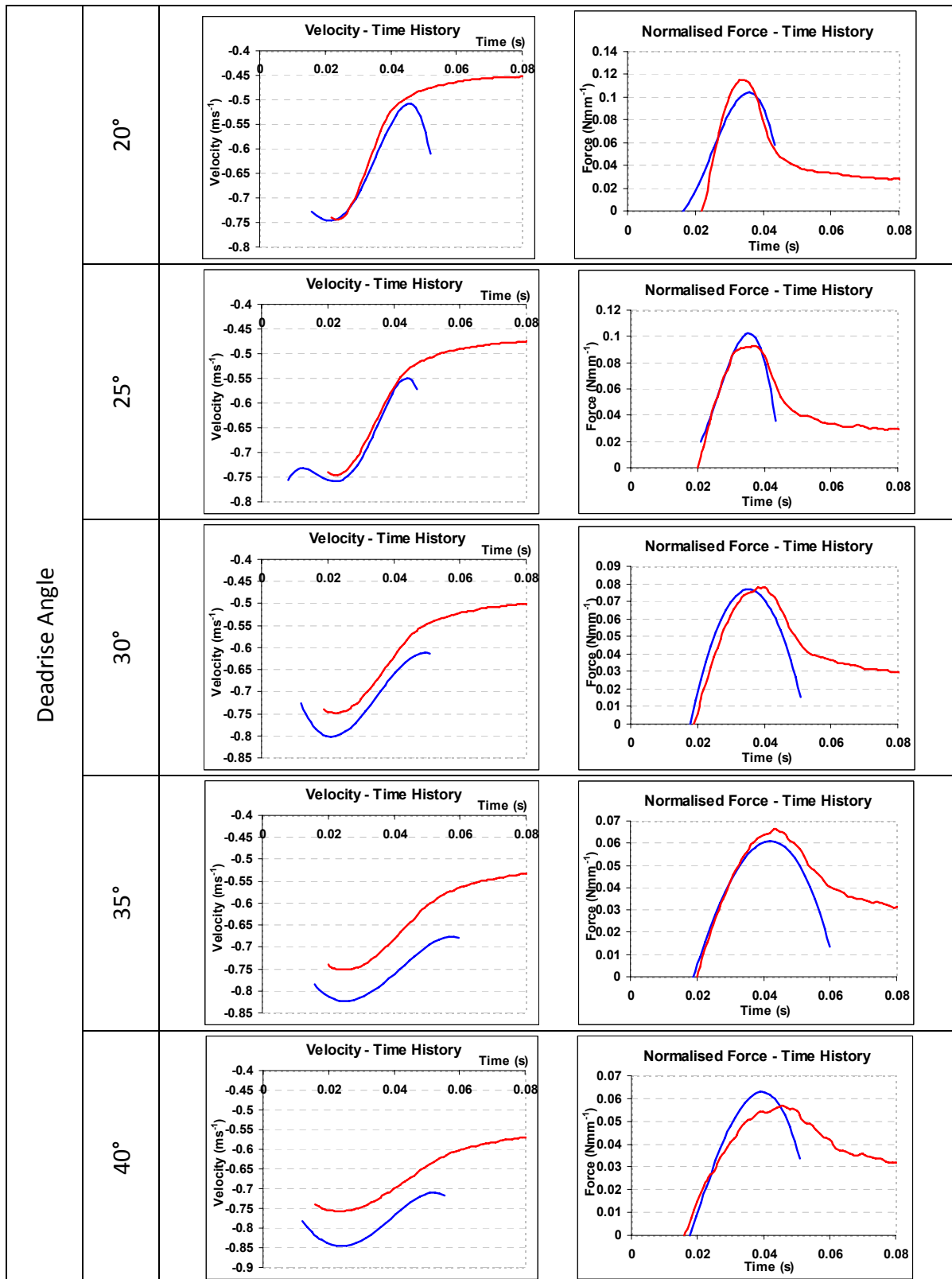




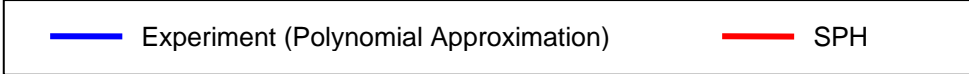
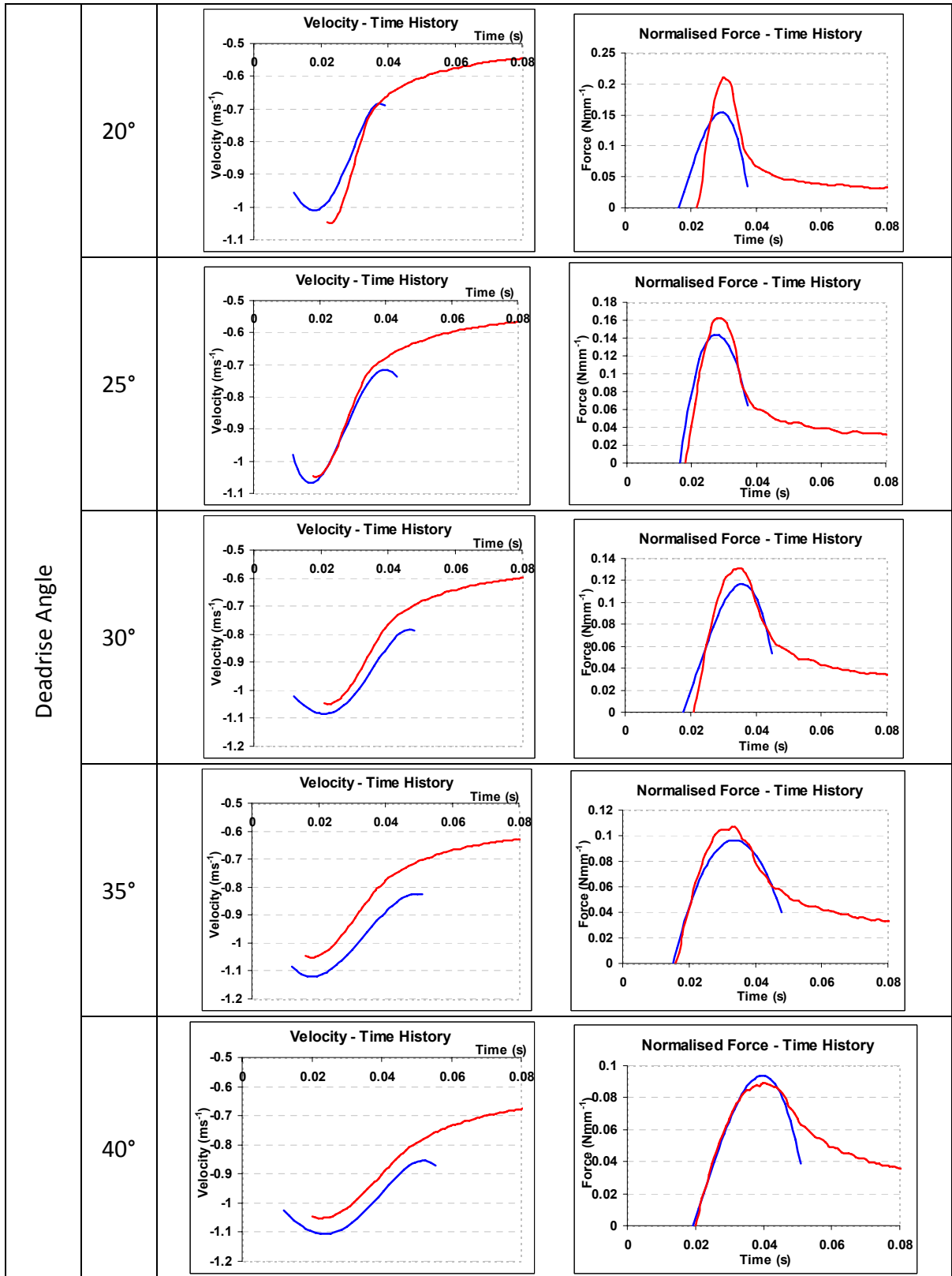
## **Appendix III**

# **Correlation between Experiment and Simulations**

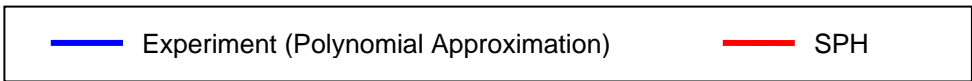
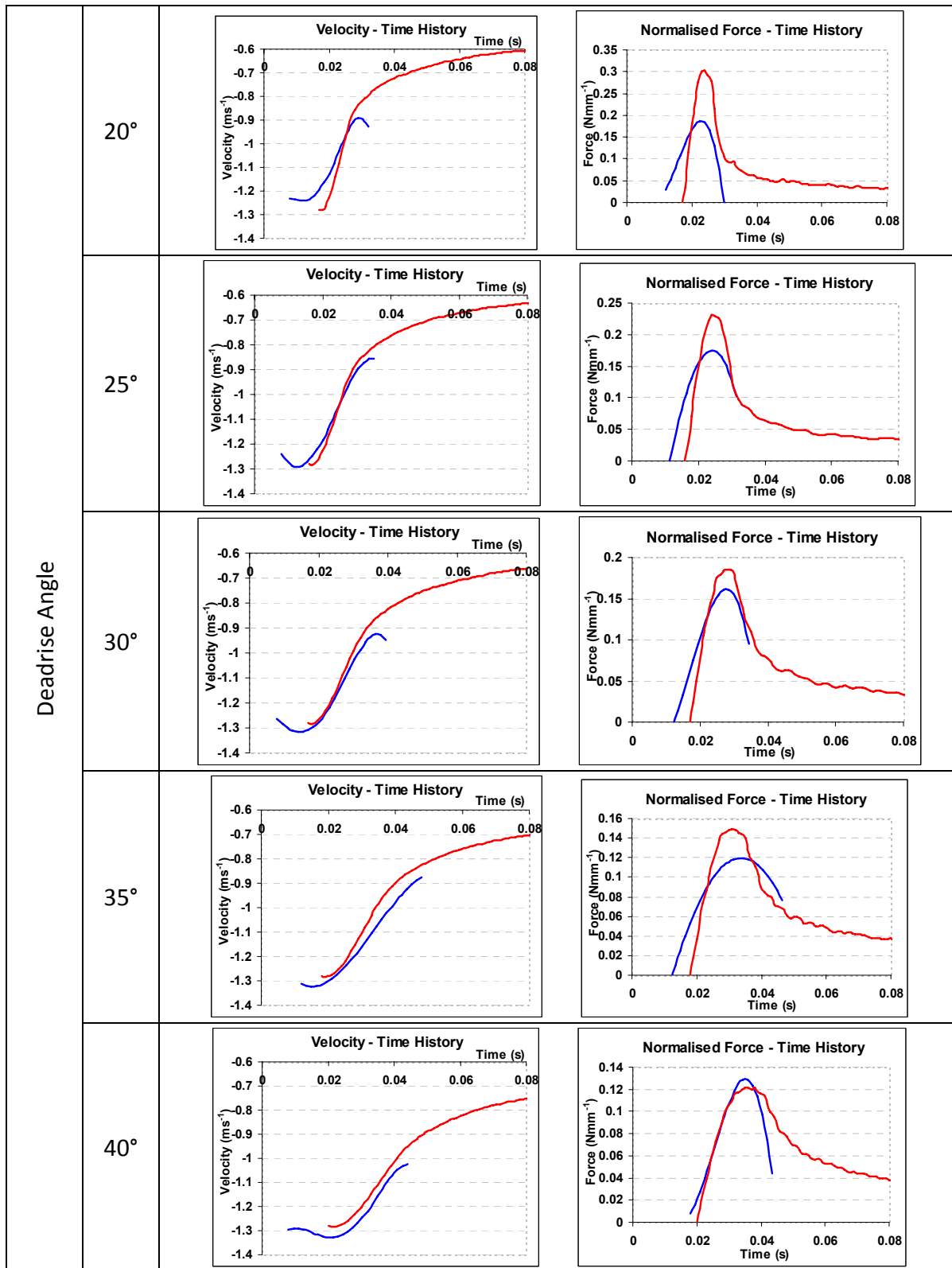
# Light Impactor - 50 mm Drop Height



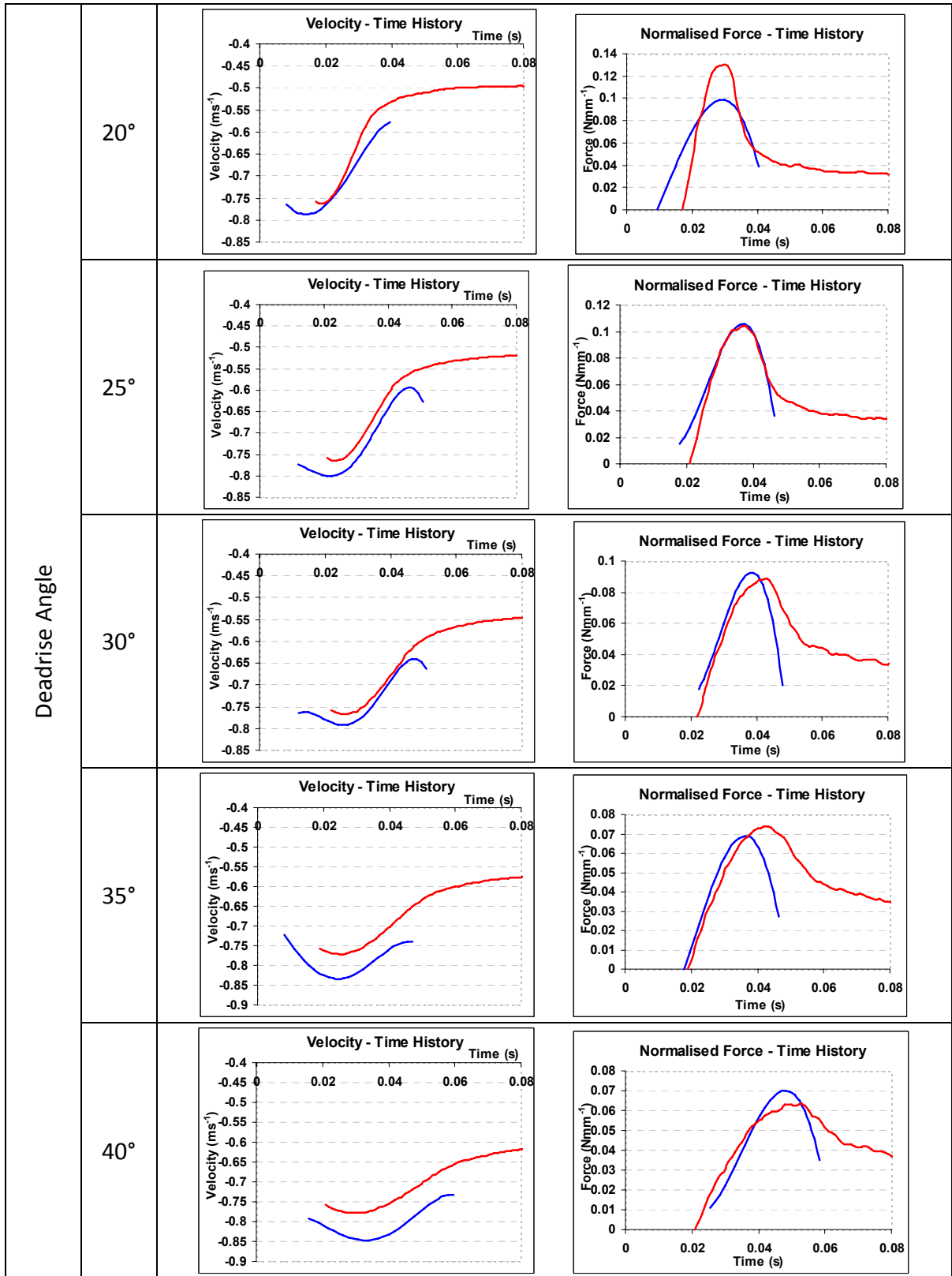
# Light Impactor - 100 mm Drop Height



# Light Impactor - 150 mm Drop Height

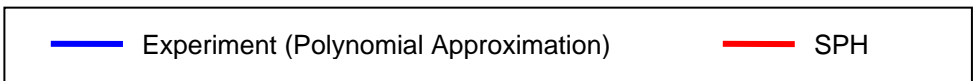
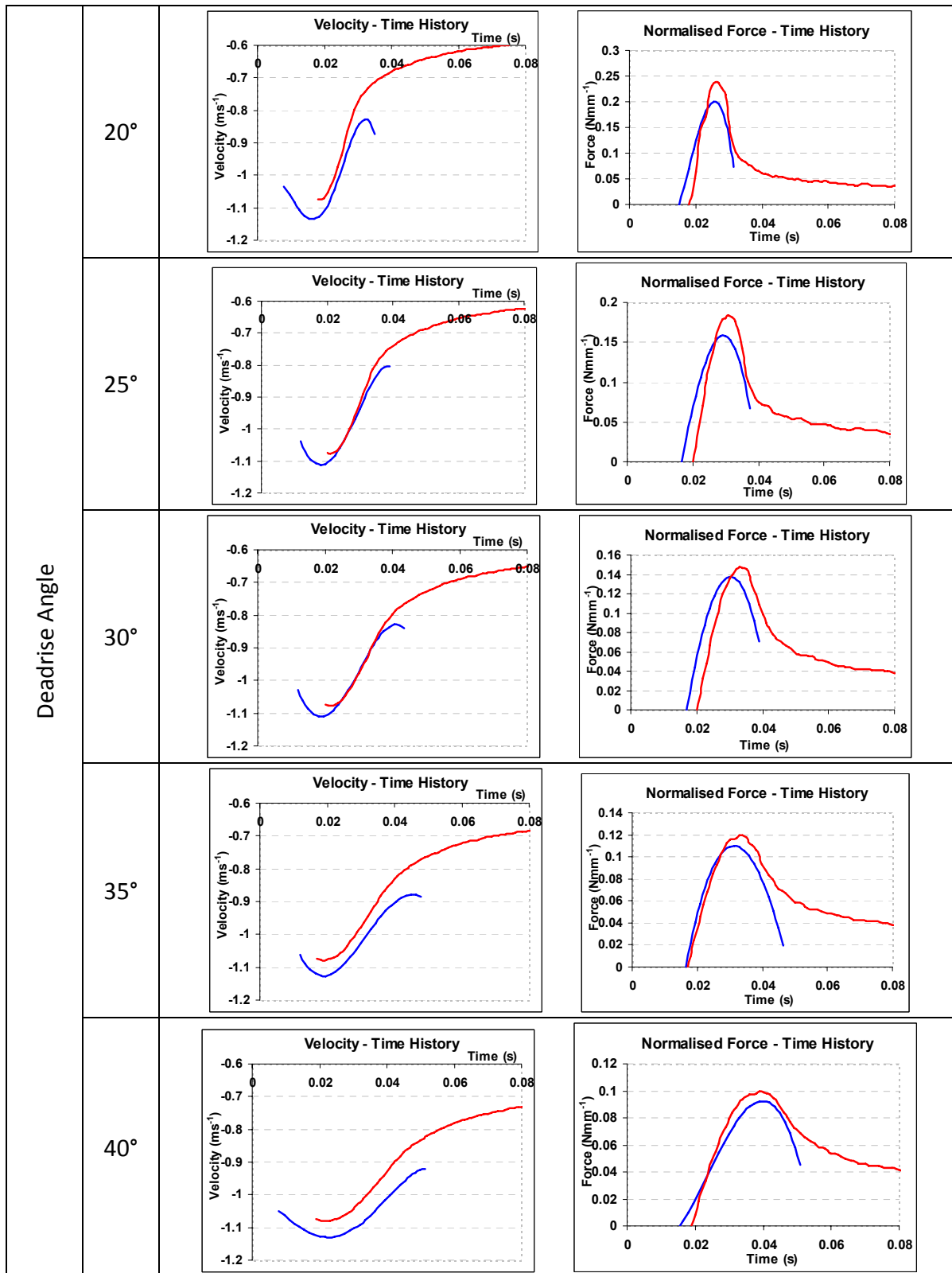


# Intermediate Impactor - 50 mm Drop Height

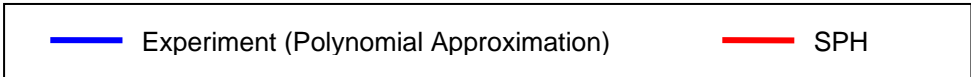
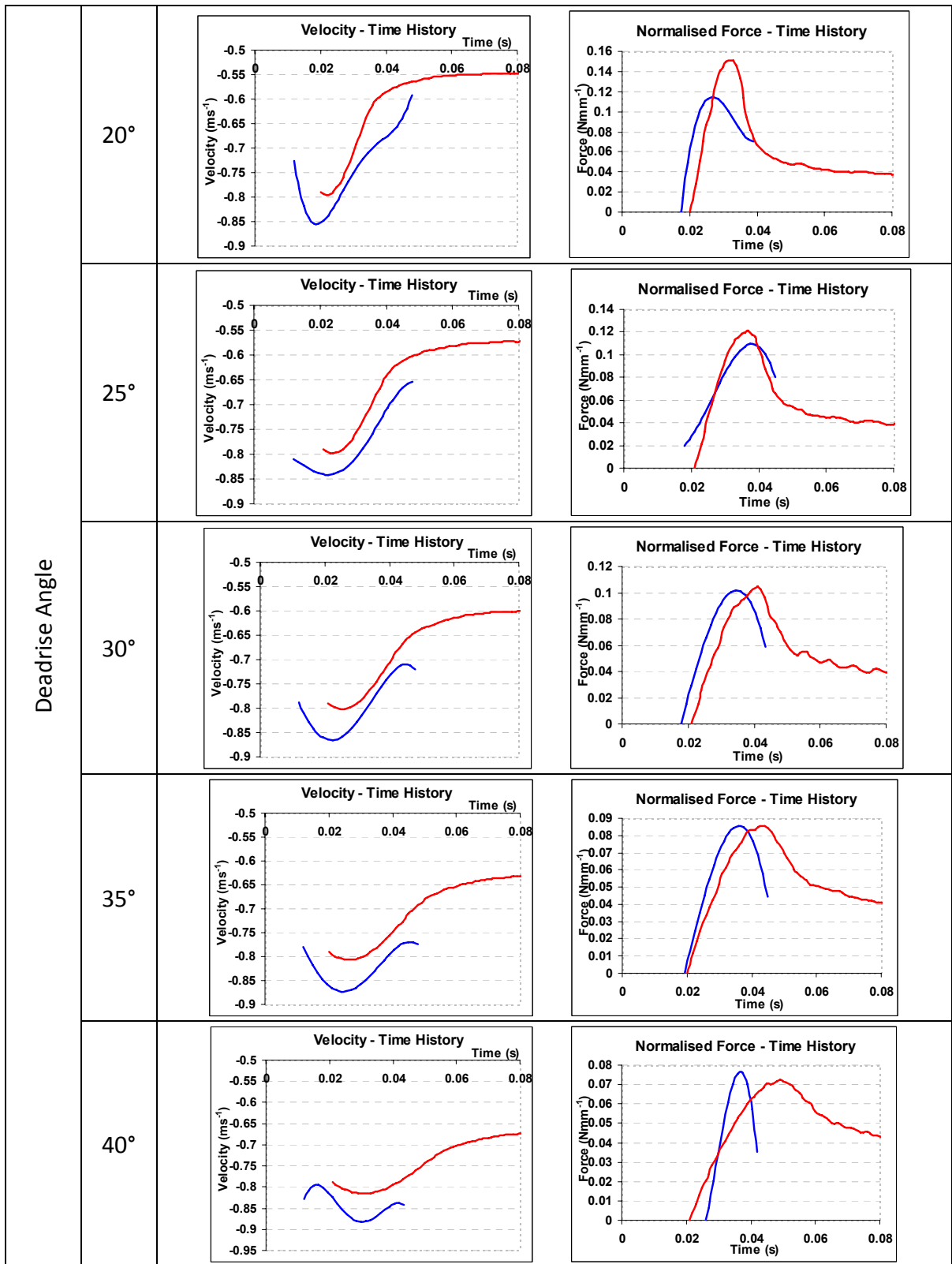


— Experiment (Polynomial Approximation)      — SPH

# Intermediate Impactor - 100 mm Drop Height



# Heavy Impactor - 50 mm Drop Height



# Heavy Impactor - 100 mm Drop Height

